

# **Energy-Efficient System Design for Future Wireless Communications**

A thesis submitted for the degree of Doctor of Philosophy

(PhD)

by

**Adrian Garcia Rodriguez**

Communications and Information Systems Research Group

Department of Electronic and Electrical Engineering

University College London

**May 2016**



## Statement of Originality

I, Adrian Garcia Rodriguez confirm that the work presented in this thesis is my own. Where information has been derived from other sources, I confirm that this has been indicated in the thesis.

Signed:

Date:



## Abstract

The exponential growth of wireless data traffic has caused a significant increase in the power consumption of wireless communications systems due to the higher complexity of the transceiver structures required to establish the communication links. For this reason, in this Thesis we propose and characterize technologies for improving the energy efficiency of multiple-antenna wireless communications.

This Thesis firstly focuses on energy-efficient transmission schemes and commences by introducing a scheme for alleviating the power loss experienced by the Tomlinson-Harashima precoder, by aligning the interference of a number of users with the symbols to transmit. Subsequently, a strategy for improving the performance of space shift keying transmission via symbol pre-scaling is presented. This scheme re-formulates complex optimization problems via semidefinite relaxation to yield problem formulations that can be efficiently solved. In a similar line, this Thesis designs a signal detection scheme based on compressive sensing to improve the energy efficiency of spatial modulation systems in multiple access channels. The proposed technique relies on exploiting the particular structure and sparsity that spatial modulation systems inherently possess to enhance performance.

This Thesis also presents research carried out with the aim of reducing the hardware complexity and associated power consumption of large scale multiple-antenna base stations. In this context, the employment of incomplete channel state information is proposed to achieve the above-mentioned objective in correlated communication channels. The candidate's work developed in Bell Labs is also presented, where the feasibility of simplified hardware architectures for massive antenna systems is assessed with real channel measurements. Moreover, a strategy for reducing the hardware complexity of antenna selection schemes by simplifying the design of the switching procedure is also analyzed.

Overall, extensive theoretical and simulation results support the improved energy efficiency and complexity of the proposed schemes, towards green wireless communications systems.



## Acknowledgements

While the authorship of this thesis is unipersonal, many important people have contributed to it from multiple angles and should be thanked accordingly.

First, I would like to thank my supervisor Dr. Christos Masouros. Reaching this point would not have been possible without your guidance and patience throughout all the stages of this process. I am indebted by your personal and professional support during these years and I understand that everything that comes from now, including this work, has been possible thanks to you. Being your PhD student has been a privilege. I would like to thank Prof. Lajos Hanzo for the technical discussions about the contents introduced in Chapter 4 of this Thesis, which were greatly improved thanks to his suggestions. I would also like to acknowledge Prof. Izzat Darwazeh and Dr. Kai-Kit Wong for sharing their expertise during these years.

My internship in Bell Labs Dublin has significantly enriched this experience, since I have met excellent researchers and people that have helped to broaden and improve my view. Particularly, I would like to thank Dr. Pawel Rulikowski and Dr. Vijay Venkateswaran for allowing me to collaborate in their project and learn from them. I explicitly express my gratitude for acquiring the channel measurements employed in Chapter 8 and the technical advice regarding hardware specifics in Chapter 7. I would also like to say thanks to Dr. Efstratios Doumanis, Dr. David López Pérez, Dr. Lei Guan, Mr. Ray Kearney, Dr. Senad Bulja, Dr. Holger Claussen, Dr. Stepan Kucera and Dr. Florian Pivit for both their technical and non-technical discussions, which have greatly contributed to this project.

I would also like to show my gratitude to my friends and UCL colleagues, since these years of work would have been much harder without their company and support. Having met them and learned from them has made this adventure a pleasure. I would particularly like to acknowledge Dr. Francesco Renna for sharing both of his exceptional technical and personal qualities with me. I would also like to say special thanks to Mr. Pierluigi Vito Amadori, Mr. Sergio García Gil, Mr. Ayoze Amaro García and Dr. Iván Pérez Álvarez for accompanying me during this long trip, as real friends would do. I also appreciate the insightful conversations with Mr. Jure Sokolić and Dr. João De Castro Mota.

Finally, this thesis is dedicated to my parents and family, since achieving this goal would not have been possible without their devoted support.



# Contents

<b>List of Figures</b>	<b>15</b>
<b>List of Tables</b>	<b>21</b>
<b>List of Abbreviations</b>	<b>23</b>
<b>List of Symbols and Operators</b>	<b>27</b>
<b>1 Introduction</b>	<b>29</b>
1.1 Aim and Motivation . . . . .	31
1.2 Main Contributions . . . . .	32
1.3 Thesis Organization . . . . .	34
1.4 Publications . . . . .	36
<b>2 Energy Efficiency in Multiple Antenna Wireless Communications Systems</b>	<b>39</b>
2.1 Multiple-Input Multiple-Output (MIMO) Communications . . . . .	39
2.1.1 Fundamentals and Preliminaries . . . . .	39
2.1.2 Precoding in MIMO Systems . . . . .	42
2.1.3 Energy Efficiency in MIMO Wireless Communications . . . . .	45
2.2 Large Scale Antenna Systems (LSAS) . . . . .	47
2.2.1 System Model of LSAS . . . . .	47
2.2.2 Achievable Sum Rates with Linear Detection in LSAS . . . . .	48
2.2.3 Acquisition of Channel State Information (CSI) in LSAS . . . . .	51
2.2.4 Fundamental Challenges of LSAS . . . . .	53
2.3 Enhancing the Energy Efficiency of Multiple Antenna Systems . . . . .	58
2.3.1 Antenna and BeamSpace Selection . . . . .	59
2.3.2 Spatial Modulation . . . . .	61

2.3.3	Hybrid Analog-Digital Precoding and Detection for LSAS . . . . .	66
<b>3</b>	<b>Power-Efficient Tomlinson-Harashima Precoding</b>	<b>69</b>
3.1	Introduction . . . . .	69
3.2	Power-Efficient THP (PE-THP) by Adaptive Symbol Scaling . . . . .	71
3.2.1	Conventional THP . . . . .	71
3.2.2	Overview of Complex Domain Interference Optimized THP (CIO-THP) . . . . .	73
3.2.3	Proposed Zero Forcing Power-Efficient THP (ZF PE-THP) . . . . .	74
3.2.4	Definition of the Scaling Factors in PE-THP . . . . .	75
3.2.5	Expansion of Optimization Regions with PE-THP . . . . .	78
3.3	Power Loss Analysis . . . . .	80
3.4	Power Consumption Analysis . . . . .	83
3.4.1	Complexity analysis . . . . .	83
3.4.2	Power Efficiency Maximization . . . . .	85
3.5	Results and Discussion . . . . .	87
3.6	Conclusions . . . . .	93
<b>4</b>	<b>Pre-Scaling for Space Shift Keying via Semidefinite Programming</b>	<b>95</b>
4.1	Introduction . . . . .	95
4.2	Space Shift Keying with Pre-Scaling . . . . .	97
4.2.1	MED Maximization . . . . .	99
4.2.2	Power Minimization . . . . .	99
4.3	Pre-Scaling Optimization for SSK via Semidefinite Programming . . . . .	100
4.3.1	MED Maximization . . . . .	100
4.3.2	Power Minimization . . . . .	102
4.3.3	Effect of the Optimization on the Received Constellation . . . . .	102
4.3.4	Measuring the Impact of the Problem Relaxation . . . . .	103
4.4	Robust Design: Worst-Case Robustness to Imperfect CSI . . . . .	105
4.4.1	MED Maximization . . . . .	107
4.4.2	Power Minimization . . . . .	108
4.5	Results and Discussion . . . . .	109
4.6	Conclusions . . . . .	116

<b>5</b>	<b>Compressive Sensing Based Detection for Spatial Modulation in Large Scale Antenna Systems</b>	<b>119</b>
5.1	Introduction . . . . .	119
5.2	Preliminaries . . . . .	121
5.2.1	System Model of the Multiple Access Channel (MAC) . . . . .	121
5.2.2	Multiple Access Spatial Modulation . . . . .	122
5.2.3	Large Scale Antenna Systems (LSAS) and Low-Complexity Detection . . . . .	123
5.3	Straightforward Application of CS Algorithms for SM Detection . . . . .	124
5.4	Proposed Spatial Modulation Matching Pursuit (SMMP) . . . . .	126
5.5	Complexity Analysis . . . . .	131
5.5.1	Complexity of the Least Squares Problem . . . . .	131
5.5.2	Overall Complexity of the Proposed Algorithm . . . . .	133
5.6	Convergence Rate of Iterative Least Squares Algorithms in LSAS . . . . .	135
5.7	Energy Efficiency . . . . .	139
5.8	Results and Discussion . . . . .	140
5.9	Conclusions . . . . .	148
<b>6</b>	<b>Low-Complexity Large Scale Antenna Systems: Incomplete Channel State Information</b>	<b>149</b>
6.1	Introduction . . . . .	149
6.2	System Model . . . . .	151
6.2.1	TDD System Model and CSI Acquisition . . . . .	151
6.2.2	Physically-Constrained Channel Model for 2D Antenna Arrays . . . . .	153
6.3	Relaxing the CSI Acquisition: Incomplete CSI . . . . .	155
6.3.1	Distribution of the CSI on the Antenna Array . . . . .	157
6.3.2	Implications of the Acquisition of Incomplete CSI . . . . .	160
6.4	CSI Error Under Incomplete CSI . . . . .	162
6.5	Complexity Analysis . . . . .	167
6.5.1	CSI Acquisition Stage . . . . .	167
6.5.2	Data Transmission (Downlink) Stage . . . . .	168
6.5.3	Data Reception (Uplink) Stage . . . . .	169
6.5.4	Total Complexity . . . . .	170

6.6	Achievable Rates and Energy Efficiency . . . . .	170
6.6.1	Downlink Achievable Rates with Incomplete CSI . . . . .	170
6.6.2	Energy Efficiency Model . . . . .	171
6.7	Results and Discussion . . . . .	173
6.8	Conclusions . . . . .	180
<b>7</b>	<b>Low-Complexity Large Scale Antenna Systems: Reduced-Connectivity</b>	
	<b>Antenna Selection</b>	<b>183</b>
7.1	Introduction . . . . .	183
7.2	Preliminaries . . . . .	185
7.2.1	Downlink System Model . . . . .	185
7.2.2	Antenna Selection Benchmarks . . . . .	186
7.2.3	Channel State Information Acquisition for AS Systems . . . . .	187
7.2.4	Sources of Losses in the RF Switching Matrices of AS . . . . .	190
7.3	Fully-Flexible (FF) Switching for Antenna Selection . . . . .	191
7.4	Partially-Connected Switching Architectures and Resulting AS Constraints	196
7.4.1	Optimization constraints for AS with Instantaneous CSI . . . . .	198
7.4.2	Optimization constraints for AS with Power-Based CSI . . . . .	200
7.4.3	Implications of Reducing Connectivity . . . . .	201
7.4.4	Practical Hardware Implementation for PB-AS in LSAS . . . . .	202
7.5	Performance Analysis: Degradation due to Limited Switching Connectivity	204
7.5.1	Ergodic Capacity Approximation for FF-AS . . . . .	204
7.5.2	Ergodic Capacity Approximation for PC-AS . . . . .	206
7.6	Energy Efficiency with Insertion Losses . . . . .	209
7.7	Results and Discussion . . . . .	210
7.8	Conclusions . . . . .	216
<b>8</b>	<b>Realistic Large Scale Antenna Systems: Channel Measurements and</b>	
	<b>Hybrid Precoding Revisited under Realistic RF Modeling</b>	<b>219</b>
8.1	Introduction . . . . .	219
8.2	Channel Measurements: Campaign and Analysis . . . . .	220
8.2.1	Measurement Campaign . . . . .	220
8.2.2	Measurements Analysis . . . . .	223

8.3	LSAS with a Reduced Number of RF Chains in Realistic Propagation Scenarios . . . . .	231
8.3.1	Antenna Selection (AS) . . . . .	232
8.3.2	Eigenspace Selection . . . . .	235
8.4	Hybrid Analog-Digital Precoding Revisited under Realistic RF Modeling	237
8.4.1	Hybrid Precoding Systems . . . . .	238
8.4.2	Fully-Connected Analog Beamforming Network . . . . .	239
8.4.3	DFT Analog Beamforming Networks via Butler Matrices . . . . .	241
8.4.4	Static Insertion Losses (IL) . . . . .	242
8.4.5	Energy Efficiency . . . . .	243
8.4.6	Results and Discussion . . . . .	244
8.5	Conclusions . . . . .	247
<b>9</b>	<b>Conclusions</b>	<b>249</b>
9.1	Summary and Conclusions of the Thesis . . . . .	249
9.2	Future Work . . . . .	254
	<b>Appendices</b>	<b>259</b>
	Appendix A. Proof of Theorem 4.4.1 . . . . .	259
	Appendix B. Proof of Proposition 5.6.1 . . . . .	261
	Appendix C. Proof of Theorem 5.6.1 . . . . .	262
	Appendix D. Proof of Theorem 6.4.1 . . . . .	263
	Appendix E. Proof of Corollary 6.4.1.2 . . . . .	265
	Appendix F. Computation of the Joint Probabilities in (7.38) . . . . .	267
	<b>List of References</b>	<b>269</b>



# List of Figures

1.1	Thesis Structure. . . . .	34
2.1	Block diagram with the basic elements of a MIMO digital communication system. . . . .	40
2.2	Classification of the precoding techniques. . . . .	43
2.3	Illustration of the channel hardening effect. Achievable sum rates vs. $N$ for $K = \{2, 6\}$ and $\rho_{\text{ul}} = 1/K$ . Marked lines denote the average sum rates and shaded areas denote the 90% confidence intervals of the instantaneous sum rates $R_{\text{sum}}^{\text{ul}}$ in (2.14). . . . .	50
2.4	TDD operation protocol. Each symbol slot represents a time/frequency resource. . . . .	51
2.5	Illustration of the (a) pilot contamination effect and (b) inter-cell interference produced by the pilot contamination effect. . . . .	54
2.6	Schematic of the $4 \times 16$ planar antenna array employed for the channel measurements in Bell Labs. . . . .	57
2.7	Block diagram of a transmit antenna selection (AS) system. . . . .	60
2.8	Block diagram and physical interpretation of a beamspace MIMO system. . . . .	61
2.9	Illustration of the transmission process in spatial modulation. . . . .	62
2.10	Comparison between the architectures of (a) a conventional MIMO transmitter and (b) a spatial modulation transmitter. . . . .	63
2.11	Nomenclature and characteristics of different SM-based systems. . . . .	64
2.12	Illustration of the uplink of a LSAS with SM. The mobile terminals only activate a subset of antennas for transmission towards the BS. . . . .	65
2.13	Simplified block diagram of a hybrid analog-digital precoding system. . . . .	66
3.1	Block diagram of the proposed PE-THP. . . . .	72

3.2	Regions that contain all possible values for the optimized constellation symbols in (a) the first user of PE-THP (CIO-THP) and (b) PE-THP for users $2 \leq k \leq \tilde{K}$ . . . . .	76
3.3	Visualization of the regions with the possible solutions of the optimization process for (a) $\tilde{K} = 1$ and (b) $\tilde{K} = 2$ . . . . .	79
3.4	BER vs. SNR for THP, CIO-THP and PE-THP for $N = K = 4$ antennas and both 4-QAM and 16-QAM. . . . .	88
3.5	Power loss vs. SNR for THP, CIO-THP and (a) PE-THP with $\tilde{K} = 2$ or (b) PE-THP with $\tilde{K} = 4$ for different received SNR thresholds and 4-QAM modulation. . . . .	89
3.6	BER vs. power loss for THP, CIO and PE-THP. $N = K = 4$ , 4-QAM, SNR = 29 dB and varying thresholds $\gamma_k$ . . . . .	90
3.7	BER vs. power loss for THP, CIO-THP and PE-THP. $N = K = 4$ , 4-QAM, $\gamma = 15$ dB and varying SNR. . . . .	91
3.8	Number of operations in kflops vs. $\gamma_k$ for THP, CIO-THP and PE-THP systems with $N = K = 4$ antennas and 4-QAM. . . . .	92
3.9	Total power consumption vs. $\tilde{K}$ for different $P_t$ . THP-based systems with $N = K = 8$ , 16-QAM modulation and $\gamma = \gamma_A$ . . . . .	92
4.1	Block diagram of SSK transceiver with pre-scaling. . . . .	98
4.2	Impact of pre-scaling in the received constellations for a $(4 \times 1)$ -element MISO system. (a) Conventional SSK and (b) Pre-scaled SSK. . . . .	102
4.3	BER vs. SNR for both $(2 \times 2)$ and $(4 \times 3)$ MIMO systems. . . . .	110
4.4	BER vs. SNR for a $(4 \times 2)$ MIMO system. . . . .	111
4.5	Empirical CDF of the transmission power for $(4 \times 2)$ and $(4 \times 3)$ MIMO systems. . . . .	112
4.6	Average transmission power vs MED thresholds for (a) $(4 \times 2)$ and (b) $(4 \times 3)$ MIMO systems. . . . .	114
4.7	Probability of feasibility vs. MED thresholds for (a) $(4 \times 2)$ and (b) $(4 \times 3)$ MIMO systems. . . . .	115
4.8	Empirical PDF of the MED of a $(4 \times 2)$ MIMO system under imperfect CSI conditions with $\tau = 0.01$ and $d = 1$ for (a) SSK, (b) SSK-CR, (c) SSK-GED, (d) SSK-SDR, and (e) robust SSK-SDR. . . . .	116

5.1	BER vs. SNR for $N = 128$ , $\bar{K} = S = 16$ , $n_t = 4$ , $n_a = 1$ , $i_{\max} = 2$ , $\tilde{S} = S$ and $S_e = 64$ bpcu. . . . .	141
5.2	BER vs. SNR for $N = 128$ , $\bar{K} = 16$ , $n_t = 7$ , $n_a = 2$ , $i_{\max} = 3$ , $\tilde{S} = S = 2\bar{K}$ and $S_e = 96$ bpcu. . . . .	142
5.3	BER vs. SNR for $N = 128$ , $\bar{K} = S = 32$ , $n_t = 4$ , $n_a = 1$ , $i_{\max} = 3$ , $\tilde{S} = S$ and $S_e = 128$ bpcu with (a) perfect and (b) imperfect CSI ( $\tau = 0.25$ ). . . . .	142
5.4	BER vs. $t_e$ for $N = 128$ , $\bar{K} = 16$ , $n_t = 4$ , $\tilde{S} = S$ , SNR = 6 dB, $i_{\max} = 2$ and $S_e = 64$ bpcu. . . . .	144
5.5	BER vs. complexity for $N = 128$ , $\bar{K} = S = 16$ , $n_t = 4$ , $n_a = 1$ , SNR = 6 dB, $S_e = 64$ bpcu, $i_{\max} = 2$ , $\tilde{S} = S$ with different LS methods. . . . .	145
5.6	BER vs. complexity for $N = 128$ , $\bar{K} = S = 8$ , $n_t = 4$ , $n_a = 1$ , SNR = 2 dB, $S_e = 32$ bpcu, $i_{\max} = 2$ , $\tilde{S} = S$ with different LS methods. . . . .	146
5.7	Energy efficiency vs. number of users $\bar{K}$ to achieve BER = $10^{-3}$ . $N = 128$ , $n_t = 4$ , $n_a = 1$ . $P_\psi = 20$ mW. . . . .	146
5.8	Energy efficiency vs. number of users $\bar{K}$ to achieve BER = $10^{-3}$ . $N = 128$ , $n_t = 4$ , $n_a = 1$ . $P_\psi = 10$ mW . . . . .	147
6.1	(a) Example of CSI distribution for $M_h = 4$ , $M_v = 3$ and $N_c = 7$ . (b), (c) Basic CSI distribution patterns. Black and white elements represent antennas with and without acquired CSI respectively. . . . .	156
6.2	Block diagram of the proposed transmission scheme. Black and white antennas represent elements with and without acquired CSI respectively. . . . .	161
6.3	$\Delta_k$ vs. inter-antenna spacing for azimuth sector angles of $\pi$ , $\pi/4$ and $\pi/8$ radians (URA) and $\pi/4$ (ULA). $N = 144$ , $N_c = N/2$ and $K = 16$ . . . . .	165
6.4	$\Delta_k$ vs. ratio of antennas with CSI ( $N_c/N$ ) for different inter-antenna spacings $d$ . $N = 144$ and $K = 16$ . . . . .	166
6.5	Spectral efficiency per user ( $S_k$ ) vs. SNR for $L = 10.9\lambda^2$ . $N = 144$ and $N = 72$ , $K = 12$ and $N_c = N/2$ for incomplete CSI acquisition. . . . .	174
6.6	Spectral efficiency per user ( $S_k$ ) vs. ratio of antennas with CSI ( $N_c/N$ ). $N = 144$ , $K = 12$ and SNR = 10 dB. . . . .	175
6.7	Spectral efficiency per user ( $S_k$ ) vs. inter-antenna distance ( $d/\lambda$ ). $N = 144$ , $K = 12$ and SNR = 10 dB. . . . .	176

6.8	(a) Precoding-related complexity and (b) total complexity per frame for increasing $N_c$ . $K = 12$ users, $\eta_{\text{coh}} = 140$ , $\eta_{\text{tr}} = K = 12$ and $\eta_{\text{dl}} = 7 \times 14$ .	177
6.9	Energy efficiency vs. sum spectral efficiency for $L = 10.9\lambda^2$ . $N = 144$ and $N = 72$ , $K = 12$ .	178
6.10	Energy efficiency vs. ratio of antennas with CSI ( $N_c/N$ ) for a microcell scenario and varying inter-antenna distance $d$ . $N = 144$ , $K = 12$ and SNR = 10 dB.	179
6.11	Energy efficiency vs. ratio of antennas with CSI ( $N_c/N$ ) for a femtocell scenario and varying inter-antenna distance $d$ . $N = 144$ , $K = 12$ and SNR = 10 dB.	179
7.1	Block diagrams of FF architectures: (a) a conventional $4 \times 8$ switching matrix with each input port connected to every output port (FF-FC) and (b) a switching matrix minimizing the number of internal connections (FF-MC).	192
7.2	Illustrative block diagrams for the PC switching architectures of (a) $\lfloor \frac{N}{M} \rfloor \geq 2$ and (b) $\lfloor \frac{N}{M} \rfloor < 2$ .	197
7.3	Block diagram of different hardware implementations for measuring channel power. (a) One parallel power meter chain per antenna and (b) limited number of power meter chains with additional switches.	203
7.4	Theoretical and simulated ergodic capacities (bits/s/Hz) vs. $M$ . $N = 8$ , $K = 2$ and $\rho = 10$ dB.	208
7.5	Sum rates (bits/s/Hz) vs. $M$ for DPC and ZF with FF and PC switching matrices. $N = 128$ , $K = 16$ , $\rho = 15$ dB and $\eta_{\text{dl}}/\eta_{\text{coh}} = 1$ .	211
7.6	Sum rates (bits/s/Hz) vs. $M$ for DPC and ZF with FF and PC switching matrices. $N = 128$ , $K = 16$ , $\rho = 15$ dB and $\eta_{\text{coh}} = 200$ .	212
7.7	Sum rates (bits/s/Hz) vs. $N$ for DPC and ZF with FF and PC switching matrices. $M = 32$ , $K = 16$ , $\rho = 15$ dB and $\eta_{\text{coh}} = 200$ .	213
7.8	Insertion losses (dB) introduced by different switching architectures vs. $M$ . $N = 128$ and basic switching losses given in Table 7.1.	213
7.9	Total system's power consumption vs. $M$ with $N = 128$ , $P_t = 30$ dBm and $P_{\text{dyn}} = \gamma(P_t/100)$ for $\gamma = \{0.5, 5\}$ .	215

7.10	Energy efficiency $\varepsilon$ vs. $M$ for a ZF precoding system with $N = 128$ , $P_t = 46$ dBm, $\eta_{\text{coh}} = 200$ and $\rho = 15$ dB. . . . .	216
8.1	Overview of the measurement area in Bell Labs Stuttgart. . . . .	221
8.2	Schematic of the rectangular base station antenna array with $N = 64$ antennas. . . . .	222
8.3	$ \mathbb{E}\{\mathbf{h}_l\} $ vs. BS antenna index. . . . .	224
8.4	(a) MSE vs. measurement position index and, (b) $ \mathbf{h}_k $ vs. BS antenna index for two consecutive measurements with identical BS and MS physical positions and a randomly selected subcarrier. . . . .	225
8.5	Normalized channel power (dBW) vs. column antenna index for the $M_v = 4$ rows of the BS planar array for (a) LOS, (b) NLOS and, (c) LOS with multipath scenarios. . . . .	226
8.6	Magnitude of the entries of the channel covariance matrix $\mathbf{R}_k = \mathbb{E}\{\mathbf{h}_k^H \mathbf{h}_k\}$ of a randomly selected user $k$ with NLOS propagation. . . . .	228
8.7	Summative eigenvalue function (%) of the channel covariance matrices vs. number of selected eigenvalues of the acquired measurements with (a) noise, and (b) without noise. . . . .	229
8.8	CDF of the singular value spread $\bar{\kappa}$ for (a) LOS, (b) NLOS and (c) LOS with multipath scenarios. $K = 4$ . . . . .	230
8.9	Ergodic spectral efficiency with ZF precoding (bits/s/Hz) vs. $M$ with and without AS for LOS, LOS with multipath and NLOS channels. . . . .	233
8.10	Different implementations of the AS scheme. (a) $N$ RF chains and $N_{\text{PA}} = N$ PAs, (b) $M < N$ RF chains and $N_{\text{PA}} = M$ PAs and, (c) $M < N$ RF chains and $N_{\text{PA}} = N$ PAs. . . . .	234
8.11	Block diagram of a transceiver architecture with a reduced number of RF chains via phase shifting network. . . . .	236
8.12	Ergodic ZF achievable rates vs. $M$ for different reduced-RF schemes and $\rho = -5$ dB. (a) $K = 4$ users and (b) $K = 8$ users. . . . .	237
8.13	Block diagram of a hybrid precoding system comprised of digital precoding and a fully-connected analog beamforming network (FC-ABFN). . .	239
8.14	Block diagram of a $4 \times 4$ Butler matrix. . . . .	242

8.15	Sum spectral efficiency (bits/s/Hz) vs. $\bar{\rho}$ . $N = 64$ , $K_{\{1,2,3\}} = 4$ , $b_{\{1,3\}} = 10$ and $b_2 = 12$ . . . . .	245
8.16	Sum spectral efficiency (bits/s/Hz) vs. $\bar{\rho}$ . $N = 128$ , $K_{\{1,2,3\}} = 4$ and varying number of RF chains. . . . .	245
8.17	Energy efficiency (Mbits/Joule) vs. $\bar{\rho}$ . $N = 128$ , $K_{\{1,2,3\}} = 4$ and varying number of RF chains. $B = 20$ MHz and $P_{\text{out}} = 46$ dBm. . . . .	246
9.1	Empirical CDF and limit condition condition number for (a) $N = 128$ , $ \mathcal{L}  = 8$ and (b) $N = 128$ , $ \mathcal{L}  = 32$ . . . . .	262

# List of Tables

2.1	Different power consumption models employed in the literature for the calculation of the energy efficiency in MIMO systems. . . . .	46
3.1	Optimization constraints $\tilde{\Phi}(\alpha_k^r, \alpha_k^i)$ for selected modulations . . . . .	78
3.2	Approximate complexity in number of floating-point operations in the transmit signal generation of a PE-THP transmitter. . . . .	85
4.1	Mean ( $\mu$ ) and standard deviation ( $\sigma$ ) of $\mathcal{F}_{4,1}$ with $P_t = 1$ . . . . .	104
4.2	Average ( $\mu$ ) and standard deviation ( $\sigma$ ) of the computational time employed to compute the transmit pre-scaling factors with optimization-based algorithms. . . . .	111
5.1	Complexity in number of real floating-point operations (flops) to solve a $m \times n$ least squares problem. . . . .	132
5.2	Complexity in number of real floating-point operations (flops) of different large scale MIMO detectors. . . . .	134
5.3	Complexity and BER of a system with $N = 128$ , $\bar{K} = S = \tilde{S} = 12$ , $n_t = 8$ , $i_{\max} = 2$ , SNR = 5 dB and 4-QAM modulation. . . . .	135
6.1	Complexity in number of floating-point operations (flops) of a base station with incomplete CSI. . . . .	170
6.2	Power consumption of micro and femto base stations. . . . .	173
7.1	Basic SPXT switches . . . . .	193
7.2	Insertion losses introduced by the fully-flexible architectures in an AS system with $N = 32$ and $M = 6$ . . . . .	195
8.1	Orientative insertion losses (IL) of the hardware components employed in the design of analog beamforming networks. . . . .	243



# List of Abbreviations

## A

<b>ABFN</b>	Analog Beamforming Network
<b>ADC</b>	Analog-to-Digital Converter
<b>AoA</b>	Angle of Arrival
<b>AS</b>	Antenna Selection
<b>AWGN</b>	Additive White Gaussian Noise

## B

<b>BER</b>	Bit Error Rate
<b>BLAST</b>	Bell Laboratories Layered Space-Time
<b>bpcu</b>	Bits Per Channel Use
<b>BPSK</b>	Binary Phase Shift Keying
<b>BS</b>	Base Station

## C

<b>CAP-MIMO</b>	Continuous Aperture Phased MIMO
<b>CDF</b>	Cumulative Distribution Function
<b>CG</b>	Conjugate Gradient
<b>CIO-THP</b>	Complex Domain Interference Optimized THP
<b>CoSaMP</b>	Compressive Sampling Matching Pursuit
<b>CS</b>	Compressive Sensing
<b>CSI</b>	Channel State Information

## D

<b>DAC</b>	Digital-to-Analog Converter
<b>DFT</b>	Discrete Fourier Transform
<b>DoD</b>	Directions of Departure
<b>DPC</b>	Dirty Paper Coding

<b>DSP</b>	Digital Signal Processor
<hr/>	
<b>F</b>	
<b>FDD</b>	Frequency Division Duplexing
<b>FF</b>	Fully-Flexible
<hr/>	
<b>G</b>	
<b>GSM</b>	Generalized Spatial Modulation
<hr/>	
<b>I</b>	
<b>IL</b>	Insertion Loss
<hr/>	
<b>L</b>	
<b>LOS</b>	Line-Of-Sight
<b>LS</b>	Least Squares
<b>LSAS</b>	Large Scale Antenna System
<hr/>	
<b>M</b>	
<b>MAC</b>	Multiple Access Channel
<b>MED</b>	Minimum Euclidean Distance
<b>MF</b>	Matched Filter
<b>MIMO</b>	Multiple-Input Multiple-Output
<b>MISO</b>	Multiple-Input Single-Output
<b>ML</b>	Maximum Likelihood
<b>MMSE</b>	Minimum Mean Square Error
<b>mmWave</b>	Millimeter Wave
<b>MPD</b>	Message Passing Detection
<b>MRT</b>	Maximum Ratio Transmission
<b>MS</b>	Mobile Station
<b>MSE</b>	Mean Squared Error
<b>MU-MIMO</b>	Multi-User MIMO
<hr/>	
<b>N</b>	
<b>NLOS</b>	Non-Line-Of-Sight
<b>NP</b>	Non-Polynomial
<hr/>	
<b>O</b>	

<b>OFDM</b>	Orthogonal Frequency Division Multiplexing
<hr/>	
<b>P</b>	
<b>P2P</b>	Peer-to-Peer
<b>PAPR</b>	Peak-to-Average Power Ratio
<b>PB</b>	Power-Based
<b>PC</b>	Partially-Connected
<b>PDF</b>	Probability Density Function
<hr/>	
<b>Q</b>	
<b>QAM</b>	Quadrature Amplitude Modulation
<hr/>	
<b>R</b>	
<b>RF</b>	Radio Frequency
<b>RZF</b>	Regularized Zero Forcing
<hr/>	
<b>S</b>	
<b>SDP</b>	Semidefinite Programming
<b>SDR</b>	Semidefinite Relaxation
<b>SINR</b>	Signal-to-Interference-plus-Noise Ratio
<b>SM</b>	Spatial Modulation
<b>SMMP</b>	Spatial Modulation Matching Pursuit
<b>SNR</b>	Signal-to-Noise Ratio
<b>SPST</b>	Single-Pole Single-Throw
<b>SSK</b>	Space Shift Keying
<b>SSK-GED</b>	SSK Guaranteed Euclidean Distance
<b>SSK-MMD</b>	SSK Maximum Minimum Distance
<b>SVD</b>	Singular Value Decomposition
<hr/>	
<b>T</b>	
<b>TDD</b>	Time Division Duplexing
<b>THP</b>	Tomlinson-Harashima precoding
<b>TPS</b>	Transmit Pre-Scaling
<hr/>	
<b>U</b>	
<b>ULA</b>	Uniform Linear Array

**URA**                      Uniform Rectangular Array

**V**  
-----  
**VP**                      Vector Perturbation

**Z**  
-----  
**ZF**                      Zero Forcing

# List of Symbols and Operators

$ \cdot $	Absolute value of a complex number or determinant of a matrix
$(\cdot)^T$	Transpose of a vector or matrix
$(\cdot)^H$	Hermitian transpose of a vector or matrix
$(\cdot)^{-1}$	Inverse of a matrix
$(\cdot)^\dagger$	Moore-Penrose pseudoinverse of a matrix
$p \bmod L$	Modulo operation for a real number $p$ with base $L$
$\text{diag}(\cdot)$	Diagonal of a matrix
$\text{rank}(\cdot)$	Rank of a matrix
$\sim$	Indicates “distributed as”
$\mathcal{CN}(\cdot, \cdot)$	Complex normal statistical distribution
$\mathcal{U}(\cdot)$	Uniform statistical distribution
$\mathcal{CW}(\cdot, \cdot)$	Complex Wishart distribution
$\mathbb{E}\{\cdot\}$	Statistical expectation
$\lfloor \cdot \rfloor$	Floor function
$\lceil \cdot \rceil$	Ceiling function
$\llbracket \cdot \rrbracket$	Rounding function
$\mathbb{C}$	Set of complex numbers
$\mathbb{R}$	Set of real numbers
$\mathbb{Z}$	Set of integer numbers
$\mathbb{H}$	Set of Hermitian matrices
$\mathbb{B}$	Set of binary matrices
$\text{Re}(\cdot)$	Real component of a complex number
$\text{Im}(\cdot)$	Imaginary component of a complex number
$\mathcal{O}(\cdot)$	Complexity order
$\otimes$	Kronecker product
$\ \cdot\ _p$	$\ell_p$ norm of a vector or matrix
$\ \cdot\ _F$	Frobenius norm of a vector or matrix
$Q(\cdot)$	Q-function

$(\cdot)!$	Factorial of a real number
$\subseteq$	Subset operator
$\subset$	Strict subset operator
$\emptyset$	Empty set
$\mathbf{A} \succeq 0$	Positive semidefinite matrix $\mathbf{A}$
$\cup$	Union of sets
$\cap$	Intersection of sets
$(\cdot)^c$	Complement of a set
$\in$	$\mathcal{X} \in \mathcal{Y}$ indicates that $\mathcal{X}$ takes values from the set $\mathcal{Y}$
$\infty$	Infinity
$\det(\cdot)$	Determinant of a matrix
$\text{Tr}(\cdot)$	Trace of a matrix
$\binom{a}{b}$	Binomial coefficient indexed by $a$ and $b$
$\triangleq$	Equality by definition
$\text{supp}(\cdot)$	Identification of the indices corresponding to the non-zero entries
$\min(\cdot)$	Minimum entry of a vector
$\arg \min(\cdot)$	Index of the minimum entry in a vector
$\max(\cdot)$	Maximum entry of a vector
$\arg \max(\cdot)$	Index of the maximum entry in a vector
$\lambda_{\max}(\cdot)$	Maximum singular value of a matrix
$\lambda_{\min}(\cdot)$	Minimum singular value of a matrix
$\sigma_{\max}(\cdot)$	Maximum eigenvalue value of a matrix
$\sigma_{\min}(\cdot)$	Minimum eigenvalue value of a matrix
$\text{var}(\cdot)$	Variance of random variables
$\text{cov}(\cdot)$	Covariance of random variables
$\forall$	“For all”
$\gamma(\cdot, \cdot)$	Lower incomplete gamma function

# Chapter 1

## Introduction

The design of spectrally efficient wireless communications has been a key focus of both academia and industry for the past generations of mobile communications standards due to the need of providing service to an exponentially increasing number of mobile devices while satisfying their data rate requirements [1]. However, the impact that the achievable rate increase has on the power consumption of both mobile units and base stations has arisen as one of the main issues in the development of novel communication systems. Specifically, the power consumption of the mobile stations has become a major concern because battery technologies have not been able to scale up with the increasingly higher energy requirements, hence significantly affecting the battery lifetime [2]. Moreover, the total energy consumption of the mobile and wired networks has also attracted much interest recently as it has currently grown up to 3% of the global power consumption and it is expected to keep increasing in the following years [3–5]. Indeed, 5G communication systems and beyond are not only anticipated to provide high data rates, but they are also expected to do that in a power-efficient manner [2, 6]. To study the trade-off between power consumption and achievable rates, the focus of researchers has shifted towards a metric that combines them: the energy efficiency [2, 7].

The energy efficiency essentially characterizes the relationship between the total power consumption of a communication system and its spectral efficiency. Hence, the maximization of this parameter provides a solution to the energy problem and it is

expected to determine the characteristics of the wireless communications systems deployed in the future [8]. This area of research is commonly referred to as green wireless communications and it has motivated several industrial initiatives such as the SMART 2020 report or the GreenTouch consortium [8–10]. In fact, due to its importance, novel technologies whose main aim is to improve the energy efficiency of wireless communications have been developed. Among these alternatives, the employment of multiple antennas, also known as multiple-input multiple-output (MIMO) communications, has been shown to be one of the most relevant options to satisfy the future energy efficiency requirements [2].

Although generally MIMO communications have been used with the sole purpose of maximizing the achievable rates, more recent strategies based on the same principle have shown that their use is also convenient for maximizing the energy efficiency. For instance, large scale or massive MIMO technologies suggest to incorporate a large number of antennas at the base stations to increase the transmission rates while maintaining a constrained transmission power [11, 12]. This is possible because the large number of antennas facilitates achieving unprecedented spatial resolutions, simultaneously diminishing harmful communication effects such as the channel noise or the inter-user interference [11, 12]. However, the approach conventionally adopted in current MIMO standards of dedicating one radio frequency (RF) chain per antenna constitutes a major bottleneck for the practical deployment of these systems due to the large complexity and power consumption of the related circuitry, which also severely affects the analog-digital data interfaces [13–15]. Furthermore, the consideration of higher frequency bands such as millimeter wave also poses novel system-level design challenges due to the generally larger power consumption of hardware components required at those frequencies, e.g. the analog-to-digital converters (ADCs) [16, 17].

Understanding the importance of the above problems, technologies such as space shift keying (SSK) [18], spatial modulation (SM) [19] or hybrid precoding and detection [20] have been proposed with the objective of enhancing the overall energy efficiency and reducing the number of hardware components implemented at the transceivers. This aim is generally achieved by reducing the number of RF chains while exploiting the

availability of multiple antennas to improve the data rates. Still, both the characterization and development of energy-efficient strategies are at an early stage, since critical aspects such as the propagation characteristics with large arrays are still under study [21]. Overall, the flourishing area of green communications poses a significant number of exciting open questions and research opportunities, which constitute the focus of this Thesis.

## 1.1 Aim and Motivation

In spite of comprising the core of a number of technologies considered for future energy-efficient communications, a number of aspects involved in the design of multiple antenna systems have not been fully optimized as yet [6, 22]. Indeed, the design of modern transmission schemes such as spatial modulation require the application of innovative strategies for enhancing their performance, hence motivating the development of novel approaches for exploiting the potential of multiple antenna designs.

Similarly, the understanding of channel propagation and the design of large scale antenna systems (LSAS) are at a premature state [12, 13]. This drives research focused on providing insights on their real performance and exploring the system-level differences when compared with small-scale antenna systems. Amongst the important differences, analyzing the impact of dedicating one RF chain per antenna element or increasing the size of the physical structure required for deploying an excessive number of antennas are particularly relevant, since the promising gains offered by LSAS rely on specific assumptions that might not be satisfied in practical systems [11].

Simultaneously, the above analyses motivate research focused on solving the specific problems that arise in LSAS such as their excessive analog hardware and signal processing complexities, which greatly harm their energy efficiency [13]. In this line, the implementation of strategies traditionally employed for MIMO systems such as antenna selection might alleviate the above-mentioned problems [23]. However, the substantial differences between LSAS and small-scale MIMO designs prompts the design of original solutions as well as introducing modifications to existing schemes with the aim of

facilitating the practical deployment of these systems.

## 1.2 Main Contributions

This Thesis aims at characterizing and enhancing the energy efficiency of both small and large scale multiple antenna communications systems by proposing and evaluating various schemes with this objective. Specifically, the main contributions of this work can be summarized as follows:

- Design of a power-efficient scheme for Tomlinson-Harashima precoding (THP) that relies on the adjustment of the transmit constellation symbols depending on the known inter-user interference to pre-subtract (Chapter 3). The results indicate that the proposed scheme is capable of reducing the transmission power of conventional THP to less than 50% of its original value for the small scale antenna systems considered, while approximately preserving its average performance.
- Formulation and solution of computationally tractable optimization problems via semidefinite programming (SDP) for enhancing the minimum Euclidean distance (MED) of the received symbols in SSK transmission (Chapter 4). Robust optimization problems accounting for imperfect channel state information (CSI) acquisition are also designed. The results demonstrate the signal-to-noise ratio (SNR) enhancements offered by the proposed optimization algorithms, which can be larger than 3 dB with respect to conventional SSK transmission for the small scale MIMO scenarios considered.
- Design of a detector based on compressive sensing (CS) for spatial modulation (SM) systems in the large scale multiple access channel (Chapter 5). The results for the scenarios explored demonstrate that the proposed CS-based detector can provide performance gains in the order of 2 – 3 dB when compared with linear detection algorithms of comparable complexity.
- Design of a strategy for reducing the signal processing and the hardware complexities of massive antenna arrays deployed in physically constrained structures by

incomplete CSI acquisition (Chapter 6). The designed scheme exploits the severe correlation experienced between the channels of neighbour antenna elements for relaxing the CSI requirements. The results obtained for space-constrained arrays demonstrate that both the number of RF hardware components and the digital signal processing load can be approximately halved at a moderate performance loss that depends on the system's SNR, hence improving the resultant system's energy efficiency.

- Evaluation of multiple RF switching implementations for AS systems and design of a switching architecture for reducing their hardware complexity (Chapter 7). Relevant technical specifications such as the insertion losses (ILs) of various RF switching matrices are analyzed. The results show that the slight performance loss introduced by the architecture with a reduced number of internal switches is clearly counterbalanced by its implementation benefits and IL reductions, which can be in the order of 2-3 dB for the LSAS with a reduced number of RF chains explored in this Thesis.
- Analysis of the propagation in LSAS based on channel measurements and assessment of various strategies for reducing the analog hardware complexity in realistic scenarios (Chapter 8). The characteristics of the communications channels in LSAS are determined by analyzing channel measurements acquired in Bell Labs with a massive antenna array. The performance of strategies for reducing the excessive analog hardware complexity of these systems such as antenna selection is also assessed. The results show that realistic massive MIMO channels experience severe variations in the power received along the antenna array due to its large dimensions, hence motivating the deployment of solutions with reduced hardware complexity in LSAS.
- Proposal of a model for evaluating under realistic RF losses the performance of hybrid analog-digital precoding and detection systems (Chapter 8). The introduced model accounts for the practical operation of the hardware components involved in the RF stage of hybrid schemes and bridges the gap between theoretical works and

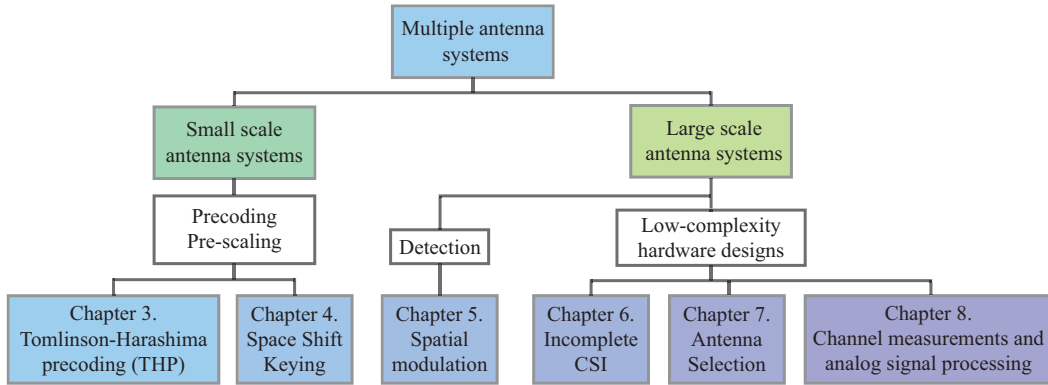


**Figure 1.1:** Thesis Structure.

practical hybrid RF designs. The results substantially differ from those found in the existing literature and demonstrate the importance of adopting a holistic RF and digital perspective in the design of hybrid precoding and detection systems. In particular, it is demonstrated that increasing the number of RF chains does not always enhance the rate performance of hybrid precoding and detection systems due to the larger power losses introduced in the RF signal processing stage.

### 1.3 Thesis Organization

Subsequent to this introductory Chapter, this Thesis is organized following the structure illustrated in Fig. 1.1 and described in the sequel.

Chapter 2 provides a comprehensive review of multiple antenna technologies that constitute the basis of future energy-efficient wireless communication systems. In particular, this chapter describes the principles of MIMO systems with particular emphasis on signal precoding and detection. The most relevant schemes for reducing the analog hardware complexity and enhancing energy efficiency of both small- and large scale MIMO systems are also identified, since they constitute the foundation of this Thesis.

Chapter 3 introduces a scheme for enhancing the energy efficiency of Tomlinson-Harashima precoding (THP). The considered approach reduces the power loss introduced in this non-linear precoding procedure by aligning the symbols to convey with the known interference to mitigate. The attainable power savings and the additional

signal processing required by the proposed strategy are quantified in this chapter.

Chapter 4 presents an energy-efficient pre-scaling scheme for MIMO space shift keying (SSK) transmission systems. The proposed strategy aims at modifying the transmission symbols to maximize the minimum Euclidean distance (MED) at the receiver side. This is achieved by relaxing the original optimization problems via semidefinite relaxation (SDR) to achieve a computationally efficient solution. The impact of this relaxation on the system performance is characterized and a related scheme with robustness against channel state information (CSI) imperfections is also introduced.

Chapter 5 introduces a detector based on the compressive sensing (CS) principles for spatial modulation (SM) and generalized spatial modulation (GSM) systems in the multiple access channel (MAC). The proposed detector exploits the sparsity inherent to SM-type communications and the particular structure of the MAC to enhance the performance and energy efficiency of conventional MIMO detectors in the large scale regime. The complexity of the proposed CS-based detector is thoroughly studied and the close relationship between CS and MIMO detection is also discussed.

Chapter 6 is dedicated to reduce the analog hardware and signal processing complexities in large scale antenna systems (LSAS). The proposed strategy consists on exploiting the large inter-antenna correlation that arises in physically constrained arrays for reducing the number of RF chains or the signal processing load. These objectives are achieved by collecting CSI for a subset of antennas and, subsequently, deriving the CSI of the remaining nearby antennas via simple linear interpolation. The resultant performance-complexity trade-off is characterized in this chapter.

Chapter 7 proposes to reduce the RF complexity and power losses of antenna selection (AS) systems via partially-connected (PC) switching networks. Different implementations of RF switching matrices are analyzed and the performance loss due to having a limited connectivity between the RF chains and the antenna ports is characterized.

Chapter 8 presents research carried out with the aim of characterizing practical LSAS. Insights about the large scale propagation channel are presented based on the data extracted from a measurement campaign carried out in Bell Labs Dublin. The feasibility

of reducing the RF hardware in realistic propagation scenarios is also assessed. In this context, this chapter also proposes a realistic model for characterizing the operation of hybrid analog-digital precoding systems.

Chapter 9 concludes this Thesis by summarizing the contents and the conclusions derived throughout. Moreover, future research lines within the framework of this Thesis are also presented.

Finally, mathematical proofs of the analyses developed throughout this Thesis are provided in Appendices A-F.

## 1.4 Publications

The work developed throughout this Thesis has resulted in the following publications at the time of submission:

### Book Chapters

- [B1] C. Masouros and A. Garcia-Rodriguez, “Chapter 5: Large Scale Antenna Systems,” to be published by The Institution of Engineering and Technology (IET) in the book “5G Wireless Technologies”. Edited by: Angeliki Alexiou.

### Journals

- [J1] A. Garcia-Rodriguez, C. Masouros and P. Rulikowski, “Reduced Switching Connectivity for Power-Efficient Large Scale Antenna Selection,” *submitted to IEEE Transactions on Communications*, May 2016. [Online]. Available: <http://arxiv.org/abs/1605.01549>.
- [J2] A. Garcia-Rodriguez, V. Venkateswaran, P. Rulikowski and C. Masouros, “Hybrid analog-digital precoding revisited under realistic RF modeling,” *submitted to IEEE Wireless Communications Letters*. [Online]. Available: <http://arxiv.org/abs/1604.08123>.

- [J3] A. Garcia-Rodriguez and C. Masouros, "Exploiting the increasing correlation of space constrained massive MIMO for CSI relaxation," *IEEE Transactions on Communications*, vol. 64, no. 4, pp. 1572-1587, April 2016.
- [J4] A. Garcia-Rodriguez, C. Masouros and L. Hanzo, "Pre-scaling optimization for space shift keying based on semidefinite relaxation," *IEEE Transactions on Communications*, vol. 63, no. 11, pp. 4231-4243, November 2015.
- [J5] A. Garcia-Rodriguez and C. Masouros, "Low-complexity compressive sensing detection for spatial modulation in large-scale multiple access channels," *IEEE Transactions on Communications*, vol. 63, no. 7, pp. 2565-2579, July 2015.
- [J6] A. Garcia-Rodriguez and C. Masouros, "Power loss reduction for MMSE-THP with multidimensional symbol scaling," *IEEE Communications Letters*, vol. 18, no. 7, pp. 1147-1150, July 2014.
- [J7] A. Garcia-Rodriguez and C. Masouros, "Power-efficient Tomlinson-Harashima precoding for the downlink of multi-user MISO systems," *IEEE Transactions on Communications*, vol. 62, no. 6, pp. 1884-1896, June 2014.

### **International Conferences**

- [C1] A. Garcia-Rodriguez, C. Masouros and L. Hanzo, "Power-efficient space shift keying transmission via semidefinite programming" in IEEE International Conference on Communications (ICC), May 2016.
- [C2] A. Garcia-Rodriguez and C. Masouros, "Exploiting the tolerance of massive MIMO to incomplete CSI for low-complexity transmission" in IEEE Global Communications Conference (GLOBECOM), pp. 1-6, December 2015.
- [C3] A. Garcia-Rodriguez and C. Masouros, "Energy-efficient spatial modulation in massive MIMO systems by means of compressive sensing," in IEEE International Conference on Communications (ICC), pp. 4541-4546, June 2015.
- [C4] A. Garcia-Rodriguez and C. Masouros, "Low-complexity compressive sensing detection for multi-user spatial modulation systems," in IEEE International Confer-

ence on Acoustics, Speech and Signal Processing (ICASSP), pp. 2999-3003, April 2015.

- [C5] A. Garcia-Rodriguez and C. Masouros, “Optimizing interference as a source of signal energy with non-linear precoding,” invited paper in IEEE International Wireless Communications and Mobile Computing Conference (IWCMC), pp. 809-814, August 2014.

### **Industrial Technical Reports**

- [TR1] A. Garcia-Rodriguez, V. Venkateswaran and P. Rulikowski, “Large Scale Antenna Systems: Channel Measurements and Low-Complexity Designs,” *Alcatel-Lucent Bell Labs Technical Report*, October 2015.

## Chapter 2

# Energy Efficiency in Multiple Antenna Wireless Communications Systems

This chapter presents a review of the state of the art in the research areas relevant to this Thesis. In particular, the focus is placed on multiple antenna strategies designed with the objective of enhancing the energy efficiency of wireless communications. Due to the broad scope of the work, this introductory chapter concentrates on offering a broad overview of the research related to the contributions of this Thesis, while a detailed analysis of the specific state of the art is provided in each chapter separately.

### 2.1 Multiple-Input Multiple-Output (MIMO) Communications

#### 2.1.1 Fundamentals and Preliminaries

Multiple-Input Multiple-Output (MIMO) technologies appeared due to the necessity of scaling up the communication rates and improving the reliability of wireless communications [24, 25]. Essentially, the use of multiple antennas enables the transmission of

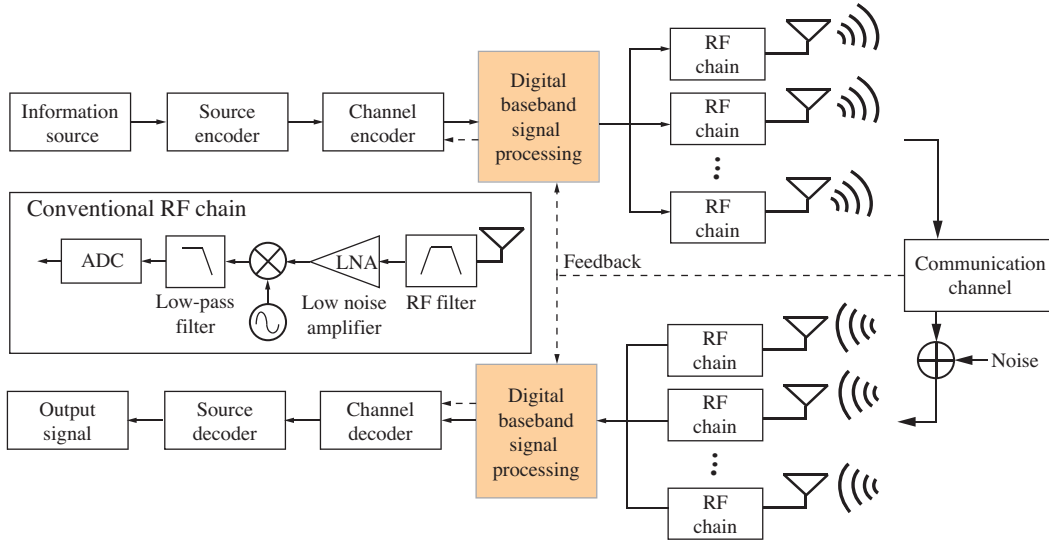


**Figure 2.1:** Block diagram with the basic elements of a MIMO digital communication system.

parallel data streams that are spatially multiplexed. Formally, a downlink MIMO transmission channel with  $N$  transmit antennas and  $K$  receiving antennas can be described by

$$\mathbf{y} = \mathbf{H}\mathbf{x} + \mathbf{n}, \quad (2.1)$$

where  $\mathbf{y} \in \mathbb{C}^{K \times 1}$  is a vector that represents the received signal and  $\mathbf{x} \in \mathbb{C}^{N \times 1}$  contains the symbols transmitted by the  $N$  transmit antennas. Moreover,  $\mathbf{n} \in \mathbb{C}^{K \times 1} \sim \mathcal{CN}(\mathbf{0}, \sigma^2 \mathbf{I}_K)$  denotes the standard additive white-gaussian noise vector with variance  $\sigma^2$ , and  $\mathbf{H} \in \mathbb{C}^{K \times N}$  is the channel matrix whose complex coefficients  $h_{m,n}$  represent the channel gain between the  $n$ -th transmit antenna and the  $m$ -th receive antenna. In the above,  $\mathbf{I}_K$  represents the  $K \times K$  identity matrix and the symbol  $\sim$  indicates “distributed as”. Usually, the communication channel  $\mathbf{H}$  is assumed to follow a frequency flat Rayleigh fading at microwave frequencies, which can correspond to a subcarrier if orthogonal frequency-division multiplexing (OFDM) is used. Hence, the channel matrix is often characterized as  $\mathbf{H} \sim \mathcal{CN}(\mathbf{0}, \mathbf{I}_K \otimes \mathbf{I}_N)$ , where  $\otimes$  denotes the Kronecker product [26, Section 4.6]. A block diagram illustrating the fundamental elements of a MIMO digital communication is shown in Fig. 2.1 [27]. Here, the additional RF chains and antennas required for MIMO transmission are explicitly represented, since they can have a strong influence on the system’s energy efficiency as detailed in Sec. 2.1.3 [28].

**Capacity:** The capacity of the MIMO communication channel can be obtained when both the transmitter and the receiver have perfect instantaneous channel state information (CSI) and it can be expressed as [24]

$$C = \sum_{i=1}^{n_{\min}} \log \left( 1 + \frac{P_i^* \lambda_i^2}{N_0} \right) \text{ bits/s/Hz}, \quad (2.2)$$

where  $\lambda_i$  as the  $i$ -th ordered singular value  $\lambda_1 \geq \lambda_2 \geq \dots \geq \lambda_{n_{\min}}$  of the channel matrix  $\mathbf{H}$  with  $\lambda_{n_{\min}}$  singular values and  $N_0$  denotes the one-sided noise spectral density. The non-zero singular values  $\lambda_i$  are usually referred to as an eigenmode of the channel  $\mathbf{H}$  and each one of them can support an independent data stream. Moreover,  $\mathbf{P}^* = [P_1^*, \dots, P_{n_{\min}}^*]^T$  represents the optimum power allocation vector at the transmitter [24]

$$P_i^* = \left( \mu - \frac{N_0}{\lambda_i^2} \right)^+. \quad (2.3)$$

In the above expressions,  $(\cdot)^T$  denotes the transpose operator,  $(p)^+ = \max(0, p)$ , and  $\mu$  is selected so that the total transmit power constraint  $\sum_i P_i^* = P_t$  is satisfied. The optimal power allocation represented in (2.3) is achieved through water filling, i.e., by allocating more power to the better conditioned channels and less (or even zero) to the worse conditioned ones [24].

**Multiplexing gain:** The increase in the rates of a MIMO system can also be characterized by its multiplexing gain  $r$ , which is defined as [29]

$$\lim_{\text{SNR} \rightarrow \infty} \frac{R(\text{SNR})}{\log(\text{SNR})} = r, \quad (2.4)$$

where  $R(\text{SNR})$  represents the data rate of a communication system for a given transmit signal-to-noise (SNR) [29,30]. In essence, the multiplexing gain characterizes the increase in the degrees of freedom provided by the MIMO channel.

**Diversity gain:** The deployment of multiple antennas can also reduce the average error probability of the communication system. For instance, transmitting signals with identical information exploiting the additional communication paths provided by the multiple antennas is a useful strategy against fading conditions [29]. The characteriza-

tion of this effect is given by the diversity gain  $d$ , which is defined as [30]

$$\lim_{\text{SNR} \rightarrow \infty} \frac{\log P_e(\text{SNR})}{\log(\text{SNR})} = -d, \quad (2.5)$$

where  $P_e(\text{SNR})$  denotes the average error probability at a fixed SNR. In general, there exists a trade-off between the diversity and the multiplexing gains of a MIMO system, since the communication paths are employed with the separate purposes of enhancing the link reliability or the data rates, respectively. The interested reader is referred to [29] for a detailed analysis of this trade-off.

### 2.1.2 Precoding in MIMO Systems

Intuitively, MIMO technologies require additional signal processing at the transmitters and/or the receivers to separate independent data streams. These schemes are classified in detection, precoding and joint transmit and receive techniques depending on whether the signal processing is carried out at the receiver, at the transmitter or at both communication sides, respectively.

Generally, precoding techniques are conventionally employed in the downlink of multi-user scenarios with a single base station (BS), whereas detection schemes are implemented in the uplink. Amongst other reasons, this is because the signal processing load at the mobile devices is usually constrained due to the limitations in the batteries and signal processors. Due to their importance in this Thesis, precoding techniques are reviewed in this section.

In general, precoding techniques translate a significant part of the signal processing load from the mobile units to the BS in broadcast channel scenarios where channel state information is available at the transmitter [31]. Precoding schemes can be classified as linear and nonlinear, according to the transformation that the original information symbols undergo before being transmitted as shown in Fig. 2.2 [32]. Linear precoding techniques are a low complexity means of pre-canceling the interference at the transmitter by taking advantage of the knowledge that the BS has of both the channel and the symbols to transmit [33–38]. Nonlinear precoding schemes have a higher signal

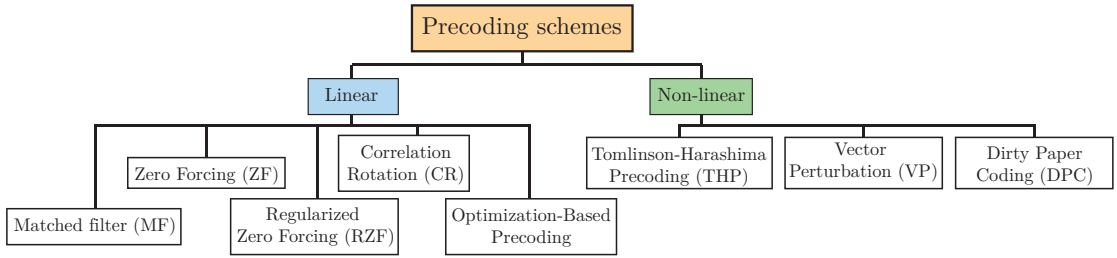


**Figure 2.2:** Classification of the precoding techniques.

processing complexity but also enhance the maximum achievable rates [31, 39–44].

### 2.1.2.1 Linear or Closed-Form Precoding

Closed-form precoding techniques aim at separating the different user streams by employing a precoding matrix  $\mathbf{F}$  that is applied to the vector of input symbols  $\mathbf{u} \in \mathbb{C}^{K \times 1}$ . Formally, the linear precoding process can be expressed as

$$\mathbf{x} = \frac{\mathbf{F}}{\sqrt{\gamma}} \mathbf{u}, \quad (2.6)$$

where the definition of the precoding matrix  $\mathbf{F} \in \mathbb{C}^{N \times K}$  depends on the selection of precoder and the normalization constant  $\gamma$  ensures that the average transmission power is constrained to  $\mathbb{E} \{ \mathbf{x}^H \mathbf{x} \} \leq P_t$ . Here,  $(\cdot)^H$  denotes the conjugate transpose and  $\mathbb{E} \{ \cdot \}$  represents the statistical expectation. The fundamental linear precoding schemes are matched filtering (MF), zero forcing (ZF) and regularized zero forcing (RZF):

- Matched filtering (MF), also known as maximum ratio transmission (MRT), is the simplest precoding strategy [45]. The precoding matrix of the MF precoder is defined as

$$\mathbf{F} = \mathbf{H}^H. \quad (2.7)$$

The performance of this precoder is generally poor as the effect of the multi-user interference is not explicitly mitigated [24].

- Zero forcing (ZF) fully eliminates interference at the cost of enhancing the pre-detection noise at the receivers. Essentially, the effect of the channel over the

transmission symbols is compensated prior transmission by setting [33]

$$\mathbf{F} = \mathbf{H}^\dagger = \mathbf{H}^H (\mathbf{H}\mathbf{H}^H)^{-1}, \quad (2.8)$$

where  $(\cdot)^{-1}$  and  $(\cdot)^\dagger$  denote the inverse and the Moore-Penrose pseudoinverse matrices, respectively [46].

- Regularized zero forcing (RZF) precoding improves the performance of the ZF precoder by maximizing the signal-to-interference-plus-noise ratio (SINR) instead of just focusing on mitigating the inter-user interference. This is accomplished by regularizing the precoding matrix by a factor  $\vartheta$  that is conventionally set to satisfy the minimum mean square error (MMSE) criterion. Mathematically, the precoding matrix is defined as [33]

$$\mathbf{F} = \mathbf{H}^H (\mathbf{H}\mathbf{H}^H + \vartheta \mathbf{I}_N)^{-1}, \quad (2.9)$$

where the optimal regularization factor for a single-cell scenario is given by  $\vartheta_{\text{opt}} = N\sigma^2$  [33].

### 2.1.2.2 Non-Linear Precoding

In contrast with linear precoding techniques, the signal processing operations that non-linear precoders perform to obtain the output signal at the transmitter cannot be characterized via closed-form expressions. The fundamental non-linear precoders are:

- Dirty paper coding (DPC). These techniques are able to achieve the capacity of the communication channel [47]. However, their complexity is too high, involving codes of infinite length and sphere searches with complexity that grows exponentially with the number of users [48, 49].
- Vector perturbation (VP). This precoder perturbs the user data before transmission in a way such that the normalization constant of the ZF precoder is reduced [39]. This modification allows increasing the performance of the linear precoders

as the noise effect at the receivers is diminished. However, this comes at the cost of a significant signal processing complexity, since an integer-lattice least squares (LS) optimization problem is required to be solved [39, 50]

- Tomlinson-Harashima precoding (THP). This nonlinear technique is the focus of Chapter 3 and it is based on successively subtracting the known interference at the transmitter [31]. This precoding scheme is more practical since, while offering a reduced performance when compared with DPC and VP, its complexity is also significantly reduced [31, 39]. Still, a power loss that harms the transmission's energy efficiency, which is particularly pronounced for low-order constellations, is introduced in the signal generation process [31, 51, 52]. Alleviating this power loss is the fundamental objective of the schemes proposed in [53–56]. However, these strategies require to convey additional information to the receivers prior data transmission [53, 56], do not accurately characterize how to determine essential parameters to optimize performance [54], or have limited performance improvements due to being applied to a single user [55]. These shortcomings motivate the technique proposed in Chapter 3 of this Thesis, which provides an alternative solution to overcome the power loss problem.

### 2.1.3 Energy Efficiency in MIMO Wireless Communications

The optimization of the energy efficiency has attracted much interest due to the concern on controlling the power consumption while the rates grow exponentially [2, 4, 57, 58]. The energy efficiency  $\varepsilon$  is defined as

$$\varepsilon = \frac{R}{P_{\text{tot}}}, \quad (2.10)$$

where here  $R$  can refer to the sum rates, the spectral efficiency or the throughput, and  $P_{\text{tot}}$  is the total system power. There exist a variety of models for the total system power consumption  $P_{\text{tot}}$  required for downlink transmission and a summary of these can be found in Table 2.1. These different models or slight variations will be employed throughout this Thesis for computing the total power consumption and energy efficiency

**Table 2.1:** Different power consumption models employed in the literature for the calculation of the energy efficiency in MIMO systems.

Ref.	Formulation	Parameters
[64]	$\begin{cases} P_{\text{tot}}^{\text{DL}} = \left( \frac{T_{\text{data}}^{\text{DL}}}{T_{\text{Coher}}} + \alpha_1 \right) \cdot P^{\text{BS}} + \alpha_2 \cdot P^{\text{MS}} \\ P_{\text{tot}}^{\text{UL}} = \left( \frac{T_{\text{data}}^{\text{UL}}}{T_{\text{Coher}}} + \alpha_3 \right) \cdot P^{\text{MS}} \end{cases}$	$\alpha_{\{1,2,3\}}$ : Overhead signaling parameter $P^{\text{MS}}$ : Transmit power mobile station $P^{\text{BS}}$ : Transmit power base station
[5, 60]	$P_{\text{tot}}^{\text{DL}} = \frac{\frac{P^{\text{BS}}}{\eta(1-\sigma_{\text{feed}})} + P_{\text{RF}} + P_{\text{sta}}}{(1-\sigma_{\text{DC}})(1-\sigma_{\text{cool}})(1-\sigma_{\text{MS}})}$	$\eta$ : Power amplifier efficiency $\sigma_{\text{feed}}$ : Lossy factor antenna feeder $P_{\text{RF}}$ : Power consumption RF chains $P_{\text{sta}}$ : Idle power consumption $\sigma_{\text{DC}}$ : Lossy factor DC-DC supply $\sigma_{\text{cool}}$ : Lossy factor cooling system $\sigma_{\text{MS}}$ : Lossy factor power supply
[2]	$P_{\text{tot}}^{\text{DL}} = \gamma + \beta R$	$\gamma, \beta$ : Constants $R$ : System rate
[57]	$P_{\text{tot}}^{\text{DL}} = \frac{P^{\text{BS}}}{\eta} + M_{\text{a}} P_{\text{dyn}} + P_{\text{sta}}$	$M_{\text{a}}$ : Number of active antennas $P_{\text{dyn}}$ : Dynamic power consumption $P_{\text{sta}}$ : Static power consumption
[40, 65]	$P_{\text{tot}}^{\text{DL}} = \left( \frac{\xi}{\eta} \right) P^{\text{BS}} + M_{\text{a}} P_{\text{dyn}} + C \cdot p_c$	$\xi$ : Peak-to-average power ratio (PAPR) $C$ : Complexity in kflops $p_c$ : Power per $10^3$ operations in a DSP

efficiency of the schemes under consideration. Note that the power consumption models for the uplink of MIMO systems are not as advanced as those developed for the downlink [59]. It should also be highlighted that the power consumption model introduced in [5, 60] is probably the most accurate one, since it is the result of a specific campaign for characterizing the power consumption of existing cellular BSs. Indeed, this model has been adopted by numerous works (e.g., [61–63]).

The optimization of the energy efficiency has been the subject of extensive analysis in the related literature. Illustrative examples aim at highlighting the importance of considering the power consumption of the RF circuitry on the resultant energy efficiency [57, 58, 61, 66]. The optimization of the system’s energy efficiency is also considered in [4, 57, 59, 65, 67, 68] and references therein. Overall, these works highlight a specific concern: the critical impact of incorporating a large number of antennas and analog hardware components on the resultant system’s power consumption and, subsequently, on the energy efficiency. Due to their importance in the context of this Thesis, these massive antenna systems constitute the focus of the following section.

## 2.2 Large Scale Antenna Systems (LSAS)

Massive or large scale antenna systems (LSAS) are currently regarded a key solution for enhancing the spectral efficiency of the communication systems at microwave frequencies [11, 12, 69]. These systems rely on incorporating a large number of antennas at the base stations, which also becomes necessary at millimeter wave (mmWave) frequencies between 30 and 300 GHz, where the signal attenuation is larger than at microwave bands [16, 70]. Note that the increased path loss at higher frequencies also promotes placing BSs closer to the users, i.e. increasing cell densification. Essentially, this results in an interplay between the technologies that will be employed to increase capacity in future networks: small cell solutions [71], massive MIMO [11], and mmWave technologies [17]. This section presents the characteristics and challenges behind LSAS with particular focus on their analysis for microwave frequencies, since they constitute one of the main research areas of this Thesis.

### 2.2.1 System Model of LSAS

Consider the uplink of a single-cell scenario comprised of a BS equipped with  $N$  antennas and  $K \ll N$  single-antenna autonomous users. Due to the reciprocity principle, the uplink channel in the baseband model can be described as the Hermitian transpose of the downlink channel under time division duplex (TDD) operation [72]<sup>1</sup>. In this setting, the uplink channel matrix  $\mathbf{G} \triangleq \mathbf{H}^H \in \mathbb{C}^{N \times K}$  can be expressed as [11]

$$\mathbf{G} \triangleq \mathbf{H}^H = \mathbf{Z}\mathbf{D}^{1/2}, \quad (2.11)$$

where the entries of  $\mathbf{Z} \in \mathbb{C}^{N \times K}$  represent the small (fast) fading effect and they are typically assumed to be independent and identically distributed (i.i.d.) following a complex-normal distribution with zero mean and unit variance,  $z_{n,m} \sim \mathcal{CN}(0, 1)$ , when Rayleigh fading is assumed. The diagonal matrix  $\mathbf{D} \in \mathbb{R}^{K \times K}$  represents the large

<sup>1</sup>Channel reciprocity can be violated if the analog hardware components of the RF transceivers are not accurately calibrated [13]. The interested reader is referred to [13, 73] and references therein for a number of strategies developed with the purpose of continuously calibrating the hardware mismatches produced in the communication system.

(slow) fading and its diagonal coefficients,  $\mathbf{d} = [d_1, \dots, d_K]^T$ , incorporate the effect of both geometric and shadow fading between the mobile stations (MSs) and the BS. The amplitude factor  $d_k$  of the  $k$ -th user is defined as

$$d_k = \frac{z_k}{r_k^\rho}, \quad (2.12)$$

where  $z_k$  corresponds to the standard log-normal shadowing,  $10 \log z_k \sim \mathcal{CN}(0, \sigma_{\text{shad}}^2)$ , with standard deviation  $\sigma_{\text{shad}}$ ,  $r_k$  is the distance between the BS and the  $k$ -th user, and  $\rho$  represents the decay exponent. Typical values in the literature for these parameters are  $\rho = 3.8$  and  $\sigma_{\text{shad}} = 8$  dB [74, 75].

In the uplink, the BS receives a baseband complex signal  $\mathbf{y}_{\text{ul}} = [y_1, \dots, y_N]^T$  which reads as

$$\mathbf{y}_{\text{ul}} = \sqrt{\rho_{\text{ul}}} \cdot \mathbf{G} \cdot \mathbf{x}_{\text{ul}} + \bar{\mathbf{n}}. \quad (2.13)$$

Here,  $\mathbf{x}_{\text{ul}} \in \mathbb{C}^{K \times 1}$  is the vector of transmit symbols from the single-antenna mobile units,  $\rho_{\text{ul}}$  is proportional to the uplink SNR and the noise entries are i.i.d. with unit variance,  $\bar{n}_k \sim \mathcal{CN}(0, 1)$ . Moreover, it is considered that the symbols transmitted by the mobile users satisfy  $\mathbf{x}_{\text{ul}} \sim \mathcal{CN}(\mathbf{0}, \mathbf{I}_K)$  for the capacity derivations in the sequel [11].

### 2.2.2 Achievable Sum Rates with Linear Detection in LSAS

This section shows that even the simplest linear precoding and detection schemes become asymptotically optimal in the realm of LSAS. Specifically, this is demonstrated by considering that the number of antennas at the BS tends to infinity and that there is a large number of scattering centers [11, 74]. The achievable sum rate in the uplink of a generic multi-user MIMO (MU-MIMO) system is given by [11]<sup>2</sup>

$$R_{\text{sum}}^{\text{ul}} = \log_2 \det (\mathbf{I}_K + \rho_{\text{ul}} \mathbf{G}^H \mathbf{G}), \quad (2.14)$$

where  $\det(\cdot)$  denotes the determinant of the argument matrix.

<sup>2</sup>Without loss of generality, this section concentrates on uplink transmission. Similar results can be derived for downlink channels [11, 69].

To derive the achievable rates in LSAS, the fact that  $N \gg K$  in large-scale MIMO systems is exploited, i.e., the uplink channel matrix  $\mathbf{G}$  is a tall matrix. As a consequence of this, the columns of the channel matrix  $\mathbf{G}$  become orthogonal under favorable propagating conditions [74]. Physically, channel orthogonality appears as a result of having a large number of antennas at the BS and can be interpreted as follows: the closer to orthogonal the user channels become, the larger the disparity in the communication channels of different users will be. This facilitates the spatial separation of the data streams received from different users at the BS side, since their channels become distinct. With these restrictions, the following expression is satisfied [11]

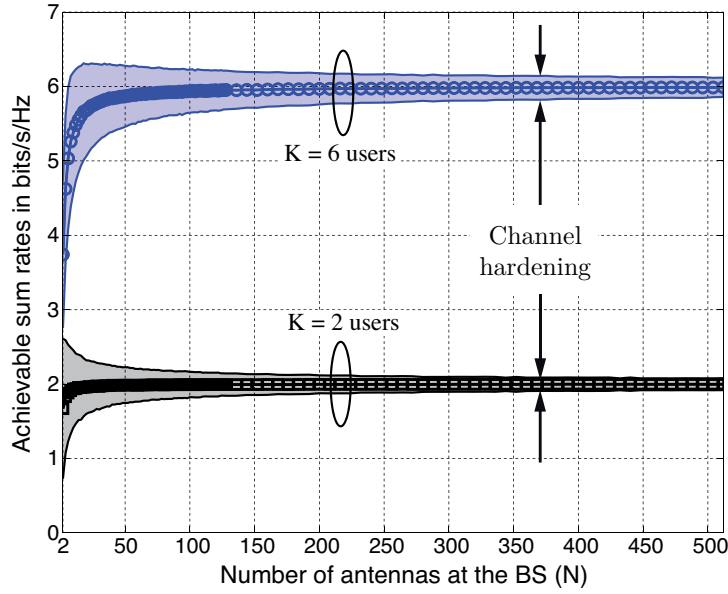
$$\left(\frac{\mathbf{G}^H \mathbf{G}}{N}\right)_{K \ll N} = \mathbf{D}^{1/2} \left(\frac{\mathbf{Z}^H \mathbf{Z}}{N}\right)_{K \ll N} \mathbf{D}^{1/2} \approx \mathbf{D}. \quad (2.15)$$

The above expression can be interpreted in the following way: in the asymptotic limit of large scale MIMO systems and under favorable propagation conditions, only the large scale fading, i.e. shadowing and path loss, has an effect on the communication between the mobile stations and their BS. Incorporating this result into (2.14), the achievable sum rate can be approximated as

$$R_{\text{sum}}^{\text{ul}} \approx \log_2 \det(\mathbf{I}_K + N\rho_{\text{ul}}\mathbf{D}) = \sum_{k=1}^K \log_2(1 + N\rho_{\text{ul}}d_k). \quad (2.16)$$

The last equality provides a nice intuitive interpretation: the transmission channel of an LSAS can be decomposed into  $K$  parallel additive white Gaussian noise channels, where each equivalent link between the  $k$ -th mobile station and the BS has received SNR  $N\rho_{\text{ul}}d_k$ . Note that, since the small-scale parameters do not influence the expression in (2.16), the achievable rates experience reduced temporal variations as the number of BS antennas grows, a phenomenon referred to as channel hardening. In other words, the instantaneous achievable rates approximate the ergodic achievable rates in LSAS [76].

The channel hardening effect is illustrated in Fig. 2.3, which represents both the average of the sum rates  $\mathbb{E}\{R_{\text{sum}}^{\text{ul}}\}$  in (2.14) and their 90% confidence intervals, represented by shaded regions, against  $N$  for the  $K = \{2, 6\}$  cases and  $\rho_{\text{ul}} = 1/K$ . Without loss of generality, this figure considers a channel without path loss, i.e.  $\mathbf{D} = \mathbf{I}_K$  in (2.11).



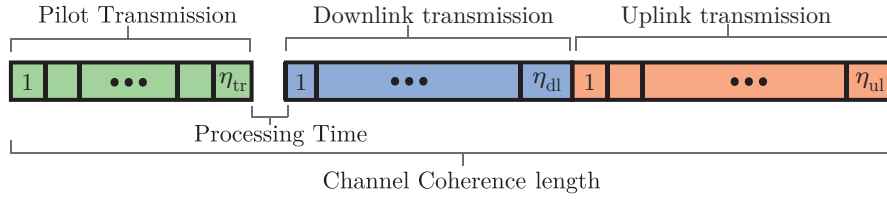
**Figure 2.3:** Illustration of the channel hardening effect. Achievable sum rates vs.  $N$  for  $K = \{2, 6\}$  and  $\rho_{\text{ul}} = 1/K$ . Marked lines denote the average sum rates and shaded areas denote the 90% confidence intervals of the instantaneous sum rates  $R_{\text{sum}}^{\text{ul}}$  in (2.14).

Fig. 2.3 shows that the thickness of the shaded areas representing the 90% confidence intervals is reduced for increasing  $N$ . This is a direct consequence of the channel hardening effect, since the instantaneous sum rates approximate their average value. It can also be observed that the number of BS antennas required to attain channel hardening grows as  $K$  increases, which can be explained by the reduced channel orthogonality of the communication channels from different mobile terminals.

An identical result to (2.16) can be derived if a MF is implemented at the BS under the same conditions, thus verifying that this simple form of detection is optimal. From (2.13) and using (2.15), the post-processed signal after MF detection reads as

$$\mathbf{y} = \mathbf{G}^H \cdot \mathbf{y}_{\text{ul}} = \sqrt{\rho_{\text{ul}}} \mathbf{G}^H \mathbf{G} \cdot \mathbf{x}_{\text{ul}} + \mathbf{G}^H \bar{\mathbf{n}} \approx \sqrt{\rho_{\text{ul}}} N \mathbf{D} \cdot \mathbf{x}_{\text{ul}} + \mathbf{G}^H \bar{\mathbf{n}}. \quad (2.17)$$

The received SNR for the  $k$ -th user in (2.17) is given by  $\text{SNR}_k = N \rho_{\text{ul}} d_k$ , which coincides with that derived in (2.16) and determines the achievable rate for the  $k$ -th user. Alike conclusions can be derived for the ZF and RZF linear detectors [11, 72]. In other words, the performance of linear precoding techniques approaches that obtained with the complex dirty paper coding strategies [11]. In this line, a variety of strategies have



**Figure 2.4:** TDD operation protocol. Each symbol slot represents a time/frequency resource.

been designed with the objective of reducing the signal processing of the large matrix inversions required in the linear ZF and RZF precoding and detection schemes [75,77,78].

### 2.2.3 Acquisition of Channel State Information (CSI) in LSAS

The application of linear precoders and detectors requires knowledge of instantaneous CSI at the BS. Indeed, the duration of the CSI acquisition process justifies the focus of the LSAS literature on TDD operation [11, 74, 79]. This is because the training interval can be proportional to the excessive number of antennas at the BSs in FDD scenarios [79]<sup>3</sup>. Instead, the employment of TDD in massive MIMO systems relies on that the training interval length depends on the number of active terminals and is independent of the number of antennas at the BSs.

Under TDD operation, the channel coherence interval is divided into two phases: pilot training and data transmission and reception. The CSI acquisition sequence is illustrated in Fig. 2.4. First, the BS acquires the CSI via uplink pilots in a process that occupies  $\eta_{tr}$  time/frequency symbol slots. Subsequently, the BS is then ready to transmit or receive data as the instantaneous CSI is available for the design of the precoders and detectors for the downlink and uplink respectively.

The pilot training process starts with each user transmitting its own predefined pilot signals to the BS over  $\eta_{tr} \geq K$  symbols. This condition allows orthogonality between the pilot vector of the  $k$ -th user,  $\boldsymbol{\theta}_k = [\theta_k(1), \dots, \theta_k(\eta_{tr})]^T$ , and the pilot signals of rest

<sup>3</sup>The development of strategies for enabling FDD operation is a flourishing area in the LSAS literature (see, e.g. [80–83] and references therein). However, most of these works assume channel sparsity for reducing the length of the CSI acquisition process, which is yet an hypothesis not confirmed [13].

of the users. In other words, the training pilots should ideally satisfy

$$\boldsymbol{\theta}_i \cdot \boldsymbol{\theta}_j^H = \begin{cases} 1, & \text{if } i = j \\ 0, & \text{if } i \neq j \end{cases}. \quad (2.18)$$

The received signal at the BS after the pilot training phase  $\mathbf{Y}_{\text{tr}} \in \mathbb{C}^{N \times \eta_{\text{tr}}}$  is given by

$$\mathbf{Y}_{\text{tr}} = \sqrt{\rho_{\text{ul}}}\mathbf{G}\boldsymbol{\Theta} + \bar{\mathbf{N}}, \quad (2.19)$$

where  $\boldsymbol{\Theta} \in \mathbb{C}^{K \times \eta_{\text{tr}}}$  is defined as  $\boldsymbol{\Theta} = [\boldsymbol{\theta}_1, \dots, \boldsymbol{\theta}_K]^T$ ,  $\bar{\mathbf{N}} \in \mathbb{C}^{N \times \eta_{\text{tr}}}$  is an AWGN matrix formed by i.i.d. standard gaussian entries and  $\rho_{\text{ul}}$  is the uplink SNR [72].

The received pilots are then processed by correlating them with the pilots already available at the BS. Mathematically, the least squares channel estimate  $\tilde{\mathbf{G}} \in \mathbb{C}^{N \times K}$  can be expressed as [84–86]

$$\tilde{\mathbf{G}} = \mathbf{Y}_{\text{tr}}\boldsymbol{\Theta}^H = (\sqrt{\rho_{\text{ul}}}\mathbf{G}\boldsymbol{\Theta} + \bar{\mathbf{N}})\boldsymbol{\Theta}^H = \sqrt{\rho_{\text{tr}}}\mathbf{G} + \bar{\mathbf{N}}\boldsymbol{\Theta}^H, \quad (2.20)$$

where  $\rho_{\text{tr}}$  is a constant proportional to the SNR of the training phase [72]. Other estimation methods such as MMSE can also be applied provided that the statistics of the channel are known in advance [85]. From (2.20), the BS is also capable of estimating the downlink channel by considering channel reciprocity, i.e.,  $\tilde{\mathbf{H}}_{\text{dl}} = \tilde{\mathbf{G}}^H$ .

The CSI acquisition process can limit the global performance of practical massive MIMO systems due to the necessity of satisfying  $\eta_{\text{tr}} \geq K$ . Hence, one of the most active areas of research is focused on reducing the acquisition time or the complexity of estimating the communication channel [85, 87]. Indeed, the coherence time might not be long enough in realistic multi-cell scenarios to provide orthogonality between the pilots of different cells without significantly degrading the performance. This entails that non-orthogonal pilots have to be employed, which in turn generates the so-called pilot contamination effect [74]. Since pilot contamination is usually considered the ultimate performance limit of LSAS [11], this aspect is analyzed separately in Sec. 2.2.4, where the fundamental challenges of LSAS are identified.

## 2.2.4 Fundamental Challenges of LSAS

### 2.2.4.1 Pilot Contamination

The limited coherence time of realistic transmission channels forces the employment of non-orthogonal pilot sequences between the terminals of different cells in TDD scenarios. As a consequence, the BS—which would only ideally receive channel information about the intra-cell users—acquires inaccurate CSI during the training phase because it cannot decorrelate the pilot signals generated from the users of other cells. The worst-case scenario where the same pilot sequences are re-used in all cells is usually considered in the literature [74]. Specifically, under these conditions the LS estimate obtained at the  $l$ -th BS can be expressed as [84]

$$\tilde{\mathbf{G}}_{ll} = \sqrt{\rho_{\text{tr}}}\mathbf{G}_{ll} + \underbrace{\sqrt{\rho_{\text{tr}}}\sum_{i \neq l} \mathbf{G}_{il}}_{\text{Inter-cell interference}} + \bar{\mathbf{N}}_l, \quad (2.21)$$

where  $\mathbf{G}_{il} \in \mathbb{C}^{N \times K}$  denotes the channel between the mobile stations of the  $i$ -th cell and the  $l$ -th BS,  $\bar{\mathbf{N}}_l \in \mathbb{C}^{N \times K}$  represents the standard AWGN at the  $l$ -th BS with i.i.d. entries  $\bar{n}_{ij} \sim \mathcal{CN}(0, 1)$ , and  $\sqrt{\rho_{\text{tr}}}$  is a constant proportional to the SNR of the training phase. The pilot contamination process is illustrated in Fig. 2.5(a). In this simplified scenario two arbitrary users with the same training sequence affect the channel estimate obtained by the BS in Cell 1, since this BS is not able of decorrelate their sequences.

The simplest precoding strategy, i.e. the MF, can be employed to illustrate the effect of the pilot contamination in the downlink. This precoder is able to achieve the sum rates in the uplink (and, similarly, downlink) of LSAS as shown in Sec. 2.2.2, and its simplicity contributes to understand the effect of the pilot contamination in multi-cell scenarios. Specifically, consider a multi-cell system comprised of  $L$  cells. The received signal at the mobile units in the  $l$ -th cell in such a system is given by

$$\mathbf{y}_l = \sqrt{\rho_{\text{dl}}}\mathbf{H}_l\mathbf{x}_l + \underbrace{\sqrt{\rho_{\text{dl}}}\sum_{i \neq l} \mathbf{H}_l\mathbf{x}_i}_{\text{Inter-cell interference}} + \mathbf{n}_l, \quad (2.22)$$

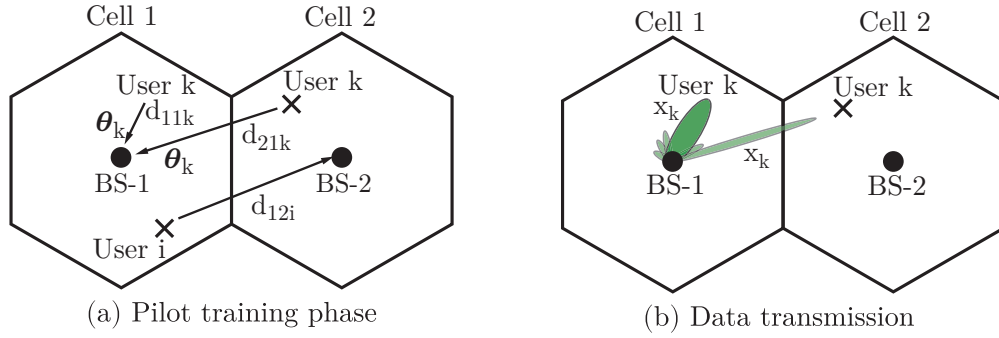


**Figure 2.5:** Illustration of the (a) pilot contamination effect and (b) inter-cell interference produced by the pilot contamination effect.

where  $\mathbf{y}_l \in \mathbb{C}^{K \times 1}$  is the composite signal received by the  $K$  users positioned in the  $l$ -th cell,  $\mathbf{x}_i \in \mathbb{C}^{N \times 1}$  denotes the signal transmitted by the  $i$ -th BS and  $\rho_{\text{dl}}$  is proportional to the downlink SNR. Moreover,  $\mathbf{n}_l$  is the noise received by the MS in the  $l$ -th cell with independent i.i.d. components following  $n_{ij} \sim \mathcal{CN}(0, 1)$ . Note that effect of the inter-cell interference is explicitly shown in (2.22), since each mobile user receives information from all  $L$  BSs. When a MF precoder  $\tilde{\mathbf{F}} = \tilde{\mathbf{G}}_{ll} \triangleq \tilde{\mathbf{H}}_{ll}^H$  is applied at the transmitter, the signals received at the mobile units of  $l$ -th cell can be subsequently expressed as

$$\mathbf{y}_l = \sqrt{\rho_{\text{dl}}} \sum_{n=1}^L \mathbf{H}_{ln} \tilde{\mathbf{F}}_{ll} \mathbf{u}_l + \mathbf{n}_l = \sqrt{\rho_{\text{dl}}} \sum_{n=1}^L \mathbf{H}_{ln} \left[ \sqrt{\rho_{\text{tr}}} \mathbf{H}_{ll}^H + \sqrt{\rho_{\text{tr}}} \sum_{i \neq n} \mathbf{H}_{in}^H + \bar{\mathbf{N}}_l \right] \mathbf{u}_n + \mathbf{n}_l, \quad (2.23)$$

where  $\mathbf{u}_l \in \mathbb{C}^{K \times 1}$  denotes the data symbols for the users of the  $l$ -th cell and the MF is built by incorporating the channel estimate obtained in (2.21). As  $N$  grows large, products of the form  $\mathbf{H}_{ln} \bar{\mathbf{N}}_j$  can be considered negligible since the noise is always uncorrelated with any other quantity. Moreover, products of the form  $\mathbf{H}_{ln} \cdot \mathbf{H}_{in}^H \forall i \neq l$  are much smaller than the correlated products ( $i = l$ ) for large  $N$ . Using identity (2.15) and the above-mentioned assumptions, the received signal at the mobile units (2.23) can be expressed as

$$\mathbf{y}_l \approx N \sqrt{\rho_{\text{dl}} \cdot \rho_{\text{tr}}} \left( \sum_{n=1}^L \mathbf{D}_{ln} \mathbf{u}_n \right), \quad (2.24)$$

where  $\mathbf{D}_{ln} \in \mathbb{R}^{K \times K}$  is a diagonal matrix containing the large scale fading coefficients between the users of the  $l$ -th cell and the  $n$ -th BS. Particularizing (2.24) for the  $k$ -th user of the  $l$ -th cell, the received symbol at the  $k$ -th mobile station under the large scale

MIMO assumptions is given by

$$y_{lk} \approx N\sqrt{\rho_{\text{dl}} \cdot \rho_{\text{tr}}} \left( d_{llk} \cdot u_{lk} + \sum_{n \neq l} d_{lnk} \cdot u_{nk} \right), \quad (2.25)$$

where  $d_{lnk}$  denotes the large-scale fading between the  $k$ -th terminal of the  $l$ -th cell and the  $n$ -th BS. Instead,  $u_{nk}$  represents the symbol transmitted from the  $n$ -th BS to the  $k$ -th user of that cell. From (2.25), the signal to interference plus noise ratio (SINR) at the  $k$ -th terminal reads as

$$\text{SINR}_k = \frac{d_{llk}^2}{\sum_{n \neq l} d_{lnk}^2}. \quad (2.26)$$

The above expression can be interpreted as follows: in the downlink of multi-cell systems, all BSs partially beamform their signals to the mobile users placed in other cells due to the pilot contamination effect. In other words, an inaccurate estimation of the intra-cell channel generates inter-cell interference. This effect is depicted in Fig. 2.5(b), where it can be seen that the BS-1 partially beamforms its signal to the mobile user that shares a common pilot sequence in the adjacent cell. Note that increasing the pilot power does not increase the SINR as  $\rho_{\text{tr}}$  does not appear in (2.26), which is a consequence of the pilot re-use in the different cells [11]. Moreover, it can be concluded that the small-scale fading, the noise in the channel acquisition procedure, and the uncorrelated noise at the receivers vanish in the large scale antenna limit, since they do not intervene in the final SINR of the system [72, 79, 84].

The mitigation of pilot contamination is one of the most active research areas in LSAS. Although not extensively described in here for reasons of space, two alternative approaches are conventionally adopted in the literature for alleviating pilot contamination: 1) identifying the differences between the intra-cell signals from the exterior ones in order to separate them during the pilot training stage [79, 88–93], and 2) modifying the CSI acquisition protocols [94, 95]. The interested reader is referred to the above-mentioned mentioned works for further discussion.

### 2.2.4.2 Non-Ideal Hardware

The large number of antennas required in LSAS promotes the employment of cheaper analog hardware components that might introduce signal distortions and imperfections, hence affecting the performance provided by realistic LSAS [96]. An extensive analysis of the hardware impairments is provided in [64], where the impairments are incorporated via several additional noise sources when compared to the conventional MIMO system model: one at the BS and an additional one in each mobile terminal. These sources model the combined effect of non-idealities such as I/Q imbalance, imperfect analog filters, or non-linear power amplifiers [64, 96]. Specifically, the model that incorporates the above hardware non-idealities for the uplink data transmission in a single-user setup can be expressed as [64]

$$\mathbf{y} = \mathbf{g}(u + \varpi_t) + \varpi_r + \bar{\mathbf{n}}, \quad (2.27)$$

where both the hardware impairments at the BS,  $\varpi_r$ , and the mobile terminal,  $\varpi_t$ , are comprised of i.i.d. Gaussian random variables as per the central limit theorem [64, 97]. In the above expression,  $u \in \mathbb{C}$  denotes the symbol transmitted by the user,  $\mathbf{g} \in \mathbb{C}^{N \times 1}$  represents the communication channel and  $\bar{\mathbf{n}}$  is the AWGN vector with i.i.d. entries following  $\bar{n}_i \sim \mathcal{CN}(0, \sigma^2)$ . A fundamental conclusion derived in [64] is that cheaper components can be employed at the BSs without noticing a significant decrease in the performance of the system. This facilitates the deployment of LSAS, since the number of components at their BSs notably increases w.r.t. conventional MU-MIMO [13]. The interested reader is referred to [98–100] and references therein for more information regarding hardware non-idealities in LSAS.

### 2.2.4.3 Inter-Antenna Correlation due to Space Constraints

The large number of antennas that massive MIMO technologies advocate entails that the physical space dedicated to allocate the antennas must also grow if they operate on the same frequency bands [11, 101]. However, a limit in the maximum number of antennas can appear due to the existence of physical restrictions at the BS structure. Consider for instance an antenna array with  $N = 64$  elements and transmitting at a

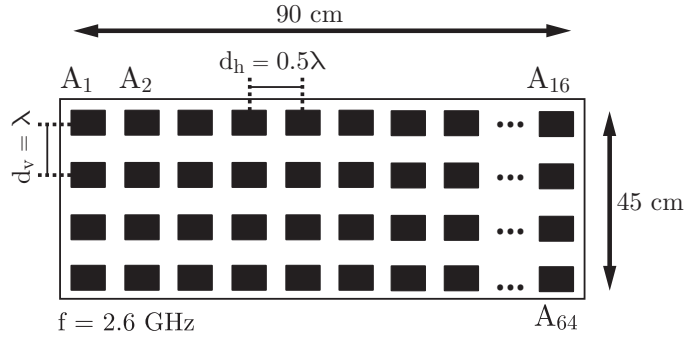


**Figure 2.6:** Schematic of the  $4 \times 16$  planar antenna array employed for the channel measurements in Bell Labs.

typical frequency of  $f = 2.6$  GHz [102]. This results in a wavelength of  $\lambda = c/f \approx 11.5$  cm, where  $c = 3 \times 10^8$  m/s refers to the speed of light. If  $d \geq 0.5\lambda$  is considered to mitigate inter-antenna correlation and mutual coupling [103,104], placing the antennas in a traditional uniform linear array (ULA) topology seems impractical in the above example, since the size of the resultant array would at least be  $d_t = N\lambda/2 \approx 3.68$  meters. This antenna size is significantly larger than the physical structures currently employed, hence complicating their deployment.

The above observation motivates the deployment of other antenna topologies such as planar, cylindrical, spherical, or even irregular arrays [12,21,105]. For instance, the dimensions of the above antenna array with  $N = 64$  dual-polarized antenna elements distributed in a planar arrangement with  $N_h = 16$  horizontal antennas ( $d_h = 0.5\lambda$ ) and  $N_v = 4$  vertical antennas ( $d_v = \lambda$ ) would occupy an approximate area of  $92 \times 46$  cm<sup>2</sup>. Indeed, this specific array topology is shown in Fig. 2.6, since it coincides with that employed in Bell Labs for performing the channel measurements analyzed in Chapter 8. Note that placing a larger number of antennas horizontally is conventional due to the interest of having finer resolutions in azimuth than in elevation [73,106]. Moreover, larger vertical inter-antenna distances are promulgated to improve spatial resolution in the elevation domain.

In spite of the above, there might be scenarios where the massive antenna arrays have to be constrained to the physical space occupied by today's BSs. Intuitively, LSAS deployments would require packing more antenna elements in constrained physical spaces, hence generating inter-antenna distances smaller than  $d \leq 0.5\lambda$ . These

reduced inter-antenna spacings can generate severe spatial correlation and mutual coupling between the antenna elements [25, 104, 107–110], whose study for LSAS is considered in [101, 111, 111–113]. Interestingly, [111] shows that, in contrast with the result shown in (2.16), favourable propagation conditions are not attained when asymptotically increasing the number of antennas in a fixed physical space. In spite of this, an increased spatial correlation might also provide opportunities for reducing the hardware and signal processing complexities of LSAS. Indeed, spatial channel correlation has been leveraged in [114] and references therein for reconfiguring the physical location of the antenna elements with the purpose of maximizing performance. Alternatively, the scheme developed in Chapter 6 concentrates on exploiting severe inter-antenna correlation for reducing the complexity of space-constrained massive BSs.

#### **2.2.4.4 Analog Hardware Complexity in LSAS**

As highlighted throughout this chapter, the excessive number of antennas implemented in massive MIMO BSs come at the cost of an equally large number of RF chains. Therefore, the circuit power consumption is increased in LSAS w.r.t. conventional systems, which can degrade the energy efficiency as indicated in Sec. 2.1.3. A number of works have placed special emphasis on the additional power consumption required by the electronic components of LSAS [4, 61, 115, 116]. In a similar line, the analog hardware complexity of LSAS is burdensome due to the large number of RF components required. Therefore, providing effective solutions to these crucial problems is essential for the practical deployment of energy- and cost-efficient LSAS. Due to their relevance for this Thesis, the most relevant alternatives for reducing the complexity of LSAS are introduced in Sec. 2.3.

### **2.3 Enhancing the Energy Efficiency of Multiple Antenna Systems**

As detailed in the previous section and Sec. 2.1.3, increasing the number of antennas might not enhance the system's energy efficiency, since the additional power consumed

by the RF chains may actually produce the opposite effect. Therefore, two complementary aspects required for enhancing the energy efficiency of multiple antenna systems should be considered: 1) understanding the evolution of the actual achievable rates with increasing number of antennas in real communication systems and 2) employing schemes with reduced analog hardware and signal processing complexities. This Thesis presents contributions in both areas, i.e. the realistic propagation channels of LSAS are analyzed in Chapter 8, and a variety of strategies are proposed throughout with the aim of reducing the total power consumption. With the purpose of motivating the reduced-complexity schemes introduced in this Thesis, the following sections describe a number of main alternatives for reducing the hardware and signal processing complexities of multiple antenna systems.

### 2.3.1 Antenna and Beamspace Selection

The selection of a subset of antennas  $M < N$  based on their channel conditions has been posed as a feasible alternative for reducing the complexity in both small and large scale MIMO systems [23, 117, 118]. Intuitively, the selection procedure exploits that separate antenna elements experience different propagation characteristics. Therefore, the fundamental objective consists in choosing  $M$  antenna elements that maximize a given performance metric such as the achievable rates or the energy efficiency. These designs are commonly referred to as antenna selection (AS) schemes and they facilitate reducing the number of RF chains  $M$  at the expense of a performance loss when compared with full-RF MIMO transmitters and receivers [23, 117–123]. The block diagram of an AS system is shown in Fig. 2.7, where the additional switching matrix required for selecting the subset of antennas is explicitly shown.

The characterization and development of AS systems have been the focus of intensive research. For instance, a vast number of sub-optimal AS algorithms for reducing the complexity of the optimal selection have been proposed in the related literature (see, e.g. [118, 124–128] and references therein). Numerous performance analyses in terms of attainable rates and diversity of these algorithms for transmit and receive AS are also

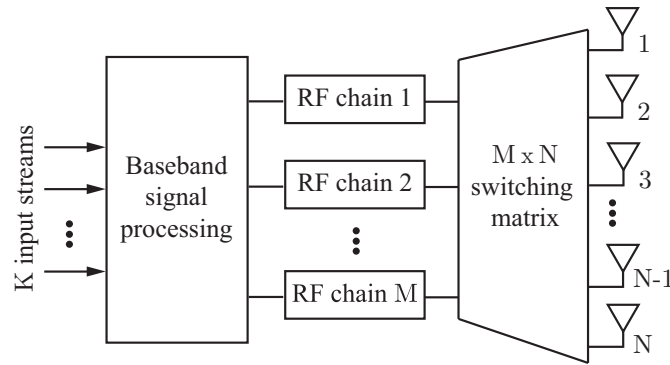


**Figure 2.7:** Block diagram of a transmit antenna selection (AS) system.

available [23,117–123]. Moreover, there are several works studying different aspects of AS systems such as the acquisition of channel state information (CSI) [129–131], their energy efficiency improvements [132–134], or their practical implementation aspects [135,136]. The application of AS to LSAS has also attracted significant attention recently due to the interest in reducing the colossal number of RF chains required [21,137–146]. In turn, the large number of RF chains and antenna ports also pose new challenges in the design of the essential RF switching matrix that implements the AS, which have been identified in [146,147]. While these works propose schemes for reducing the complexity of RF switching matrices, they only concentrate on specific implementations with a fixed number of RF chains and do not perform an accurate characterization of the savings attained. Since AS constitutes one of the best candidates for reducing the hardware complexity in LSAS [148], Chapter 7 analyzes and proposes a variety of RF switching hardware implementations for obtaining further complexity savings in AS systems. In this line, Chapter 8 studies the performance of AS in real propagation environments with a massive antenna array.

At this point it should be noted that a similar approach to antenna selection can be applied in the beamspace domain by performing a transformation of the channel such that the physical space is divided into orthogonal beams [149,150]. Essentially, this transformation can be performed via discrete lens arrays [103,151], Butler matrices [152–154], or any other solution that performs a discrete Fourier transform (DFT) of the channel response [103,149,155]. The basic block diagram and the intuitive interpretation of beamspace MIMO systems is shown in Fig. 2.8, where it can be observed that only a

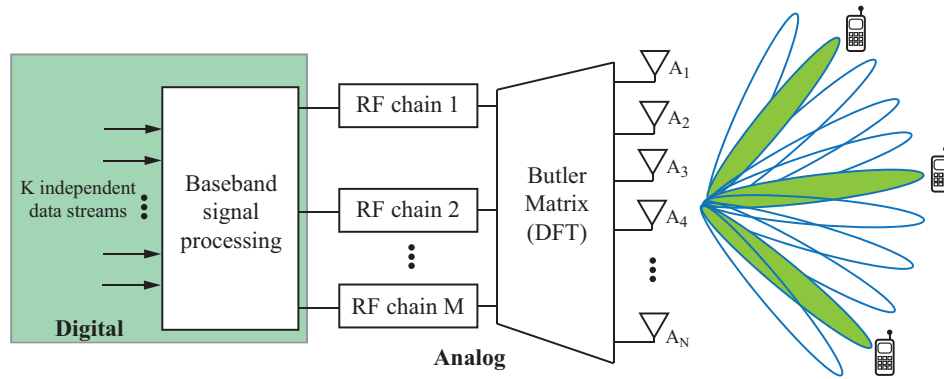


**Figure 2.8:** Block diagram and physical interpretation of a beamspace MIMO system.

subset of coloured beams is active. Consequently, the number of RF chains can be reduced in directional communication channels where signals are received (or transmitted) from a reduced number of physical directions, i.e. sparse channels in the physical domain such as those found at mmWave frequencies [156]. Intuitively, these reduced RF-chain schemes select specific physical directions instead of antenna elements, as conventionally done in AS. These approaches are conventionally referred to as beamspace selection schemes, and their operation in realistic systems is also considered in Chapter 8.

### 2.3.2 Spatial Modulation

Spatial modulation (SM) transmitters and receivers aim at reducing the number of RF chains by activating a subset of antennas  $M < N$  depending on the input bit stream [19, 157, 158]. The essential idea behind SM is to, apart from using conventional modulation methods to transmit information, encoding additional information onto the antenna indexes. This generates a 3-dimensional constellation: the first two signal dimensions corresponding to the conventional  $Q$ -QAM symbols and an additional spatial dimension given by the antenna indexes employed to convey the selected modulation symbol. The operation principle of conventional SM is illustrated in Fig. 2.9 for a system with  $N = 4$  and  $Q = 4$  and can be described as follows:

- The antennas serve as a source of information and the number of antennas determines the number of bits that can be encoded in the spatial dimension. For

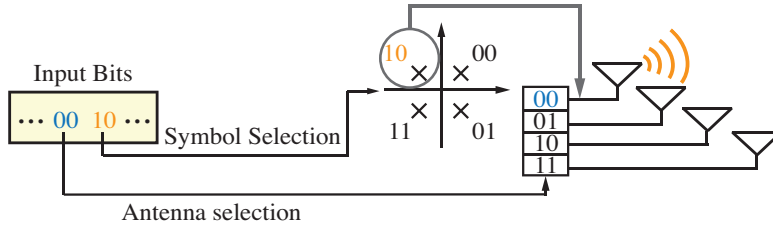


**Figure 2.9:** Illustration of the transmission process in spatial modulation.

instance, the scheme of Fig. 2.9 conveys  $\log_2(N) = \log_2(4) = 2$  bits through the antenna index.

- The remaining bits are subsequently employed to select the modulation symbol. Therefore, the number of bits that can be simultaneously transmitted in bits per channel use (bpcu) depends on both the modulation order and the number of transmit antennas via  $\log_2(N) + \log_2(Q)$ . Specifically, the transmit signal of single-RF SM transmitter adopts the form

$$\mathbf{x} = [0 \cdots s_l^q \cdots 0]^T, \quad (2.28)$$

where  $s^q$  is the  $q$ -th symbol of the transmit constellation  $\mathcal{Q}$  and  $l \in \{1, \dots, N\}$  denotes the index of the active antenna. Note that a large number of entries in the transmitted vector of (2.28) are zero-valued.

- The channel is used as a modulator, i.e., its output (the signal at the receiver) will be different depending on the antenna employed for transmission. For this to hold, SM ideally assumes that the antennas are sufficiently well separated so that there is no spatial correlation between them, and a scenario with sufficient scattering.
- Ideal SM transmission assumes that the receiver has instantaneous CSI knowledge. This channel knowledge is exploited to estimate both the transmitted signal and the active antennas. For instance, the optimal maximum likelihood (ML) detection is given by [159]

$$\left(\hat{l}, \hat{s}^q\right) = \arg \min_{l,q} (\mathbf{y} - \mathbf{h}_l s^q), \quad (2.29)$$

where, in coherence with (2.1),  $\mathbf{y} \in \mathbb{C}^{K \times 1}$  is the received signal,  $\mathbf{h}_l$  represents

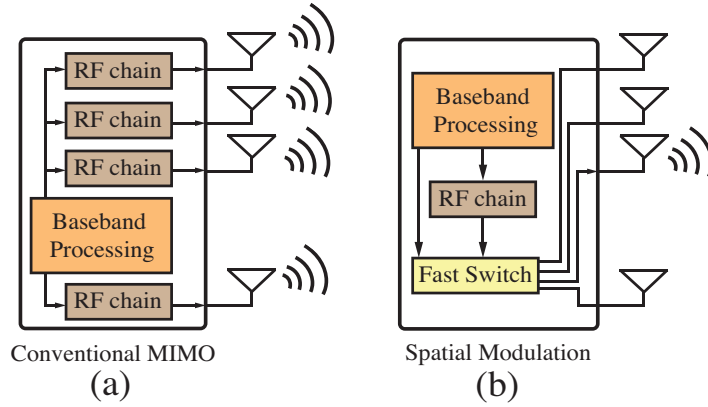


**Figure 2.10:** Comparison between the architectures of (a) a conventional MIMO transmitter and (b) a spatial modulation transmitter.

the  $l$ -th column of the downlink channel matrix, and  $\hat{l} \in \{1, \dots, N\}$  and  $\hat{s}^q \in \mathcal{Q}$  denote the estimated active antenna index and the estimated constellation symbol, respectively.

Overall, the above operation allows decreasing the number of RF chains employed in conventional MIMO transmission, since only one antenna is simultaneously active [19, 157, 158]. This is explicitly shown in Fig. 2.10, where the block diagrams of both conventional MIMO and SM transmitters are represented. Fig. 2.10 explicitly shows that spatial modulation transmitters require a fast switch that varies at the symbol rate, which constitutes one of the main bottlenecks of these systems [19, 157, 158]. Also note that the RF hardware benefits come at the cost of a reduced attainable spectral efficiency  $S_e$  when compared with MIMO transmitters, where  $S_e$  increases linearly with the number of transmit antennas as  $N \log_2(Q)$ . In spite of this, the energy efficiency trade-off can still be favourable for spatial modulation systems, depending on the relative power consumption of the RF chains w.r.t. the transmission power [62, 160–162].

There exists a conglomerate of uncoded SM systems that have different denominations according to their modulation order or their number of active antennas as depicted in Fig. 2.11<sup>4</sup>. This figure highlights in color the schemes where this Thesis has made contributions on: space shift keying (SSK) and spatial modulation (SM). Specifically,

<sup>4</sup>The concept of SM can also be extended to incorporate both space and time dimensions via dispersion matrices that occupy a number of transmission blocks [163, 164]. For reasons of brevity, this Thesis concentrates on conventional SM, where only the spatial dimension as a means of conveying information is considered.

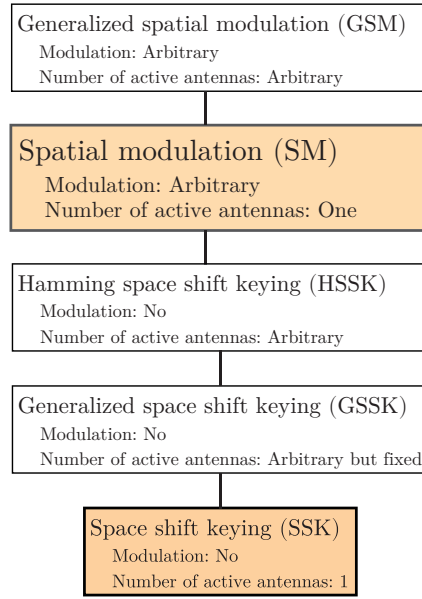


**Figure 2.11:** Nomenclature and characteristics of different SM-based systems.

SSK constitutes a low-complexity version of SM where the information is only conveyed via the spatial-constellation diagram, i.e.  $s^q = 1, \forall q$  in (2.28) [18]. The theoretical characterization of the error rates of both SSK and SM has been performed in [18, 165, 166]. Additionally, there are three research areas in SSK and SM particularly related to this Thesis, namely, signal detection, signal pre-scaling and the application of the SM principles to the multiple access channel (MAC):

- **Signal detection.** The efforts for enhancing the performance attainable by SSK and SM have been mainly focused on the design of detection algorithms for point-to-point systems [19, 157, 167]. The fundamental objective behind this research line is to reduce the computational complexity of the ML detector in (2.29), while approximating its attainable performance (see, e.g. [168–171] and references therein). Particularly related to this Thesis are [172, 173], where the sparsity of the transmitted signals in SSK and GSSK is leveraged for devising single-user detectors based on compressive sensing (CS). Indeed, Chapter 5 also relies on the principles behind CS for proposing a SM detector, although for scenarios with a multiplicity of users, as detailed below.

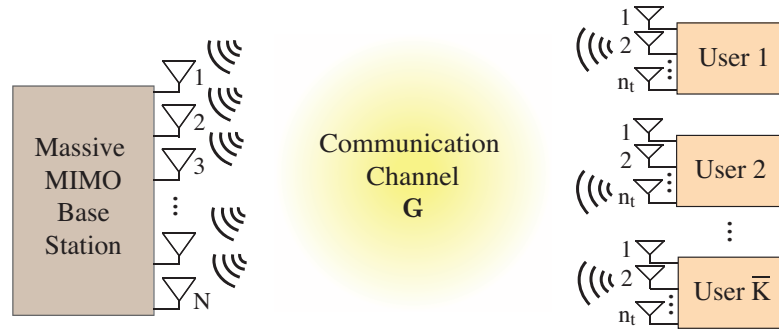


**Figure 2.12:** Illustration of the uplink of a LSAS with SM. The mobile terminals only activate a subset of antennas for transmission towards the BS.

- **Signal pre-scaling.** Although conventional SM systems only consider CSI availability at the receiver for the purpose of detection, a parallel line of research has demonstrated the benefits of exploiting CSI availability at the transmitter. For instance, a number of suboptimal constellation shaping algorithms have been proposed in [163, 174–177]. Similarly, the focus of [178–180] is also placed on developing pre-scaling algorithms, but their application is limited to systems with a single receive antenna. Instead, the schemes developed in [181–184] facilitate the application of symbol pre-scaling to multiple antenna systems. However, these schemes only adapt the transmission power [181, 182], do not devise the candidate pre-scaling factors according to the channel conditions [183], or have a substantial complexity due to the need of solving multiple convex optimization problems before reaching convergence [184]. In order to address the above-mentioned issues, Chapter 4 proposes a pre-scaling strategy for SSK multiple antenna systems based on semidefinite programming.
- **Application of SM to the multiple access channel (MAC).** The works detailed above solely concentrate on point-to-point systems. Instead, contemporary works consider the application of SM to the MAC, where a multiplicity of SM terminals convey information towards a BS, generally considered to incorporate a large number of antennas as shown in Fig. 2.12 [159, 185, 186]. Indeed, the theoretical analyses carried out in [159, 185, 186] demonstrate that SM systems can provide performance improvements over conventional MIMO systems with identical number of RF chains. The extension of SM to multi-user scenarios has been

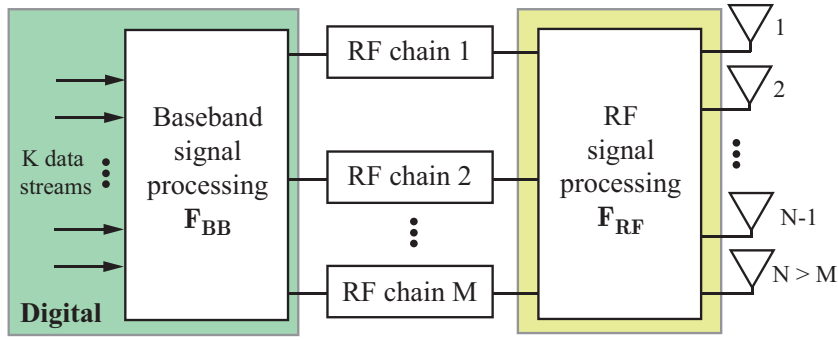


**Figure 2.13:** Simplified block diagram of a hybrid analog-digital precoding system.

also considered in [187–191] for enhancing the performance of conventional point-to-point detection algorithms. Essentially, these detection schemes take advantage of the knowledge that only a given subset of antennas will be active per user. In other words, the transmitted signals have a specific structure. Still, the above algorithms, which have developed contemporarily to this Thesis, do not fully optimize the detection procedure, where additional complexity savings can be achieved. In this line, Chapter 5 designs a detection algorithm for SM with the purpose of providing further complexity and performance benefits in the MAC of LSAS.

### 2.3.3 Hybrid Analog-Digital Precoding and Detection for LSAS

Hybrid analog-digital precoding and detection schemes aim at reducing the number of RF chains by translating part of the signal processing operations to the RF domain [20, 192–195]. Indeed, this approach is crucial in mmWave systems due to the reduced number of degrees of freedom offered by the communication channel and the need for providing beamforming gains [156]. The employment of hybrid precoding and detection at mmWaves is further motivated by the cost of the RF chains at these high frequencies, which is significantly increased w.r.t. the components working below 3 GHz [16, 193]. In practical terms, this introduces a limitation in the number of RF chains that mmWave systems can implement. The composite precoding matrix  $\mathbf{F}$  of hybrid analog-digital precoding systems can be decomposed as [193]

$$\mathbf{F} = \mathbf{F}_{\text{RF}}\mathbf{F}_{\text{BB}}, \quad (2.30)$$

where  $\mathbf{F}_{\text{BB}} \in \mathbb{C}^{M \times K}$  represents the digital baseband precoding matrix and  $\mathbf{F}_{\text{RF}} \in \mathbb{C}^{N \times M}$  characterizes the analog beamforming network (ABFN). The equivalent hardware block diagram of hybrid analog-digital precoding systems is shown in Fig. 2.13. Since  $\mathbf{F}_{\text{RF}}$  admits multiple hardware implementations, additional constraints must be enforced in its definition. Overall, hybrid precoding systems allow reducing both the analog hardware and signal processing complexities at the expense of a reduced flexibility when compared with fully-digital designs [147, 195–197]. The operation of hybrid analog-digital systems in realistic systems is explored in Chapter 8, where the importance of accounting for the particularities of performing part of the signal processing on the RF domain is highlighted.



## Chapter 3

# Power-Efficient

# Tomlinson-Harashima Precoding

### 3.1 Introduction

One of the main factors that reduces the energy efficiency of Tomlinson-Harashima precoding (THP) is the power loss that this system inherently introduces. This power loss is produced by the implementation of the modulo operation at the transmitter and at the receivers as a way of guaranteeing that the transmission power is constrained [51,52]. The power loss acquires a significant importance in low-order modulation systems and it produces an increase in the transmission power caused by the change in the distribution of the transmit symbols after the precoding process [31,51,52].

Several modifications to THP have been examined in previous works with the aim of reducing the power loss. An alternative based on tilting the constellations of the data symbols is analyzed in [53]. The specific tilting angle is adaptively decided at the transmitter depending on the input symbols, and must be conveyed or estimated at the receiver. This reduces the system performance either due to angle estimation errors or the necessity of feedforwarding the angles. A solution to overcome these problems has been proposed in [56], where the authors present an algorithm to optimize the compromise between the performance loss and the power gains, by tilting the trans-

mit constellation. The transmit power can be also reduced for a given performance by modifying the order in which the users are encoded [31]. Particularly, the improvement in the multi-user setting is achieved by performing a reordering of the input data and the rows of the channel matrix according to the Bell Laboratories Layered Space-Time (BLAST) criterion [198]. In [54], a modification of the transmit signal based on the quality-of-service requirements at the receivers is proposed. In this work, a transmit power reduction is proposed after expanding or shrinking the entire user constellations depending on the user requirements. However, this implies that the total transmission power is not constrained and that the optimal expansion factor cannot be known in advance. An alternative technique to reduce the effect of the power loss is complex domain interference optimized THP (CIO-THP) [55]. This strategy is based on modifying the symbol of the first encoded user to optimize the interference in the pre-subtraction process subject to a SNR threshold of the corresponding receiver, therefore reducing the power required for precoding.

The technique proposed in this chapter minimizes the power loss effect by directly scaling the information symbols of *a number of users as opposed to CIO-THP* to better align the resulting interference to the symbols of interest. By doing so, the power to cancel this optimized interference is drastically reduced. In this strategy, the optimum scaling factors are obtained by solving an optimization problem with SNR constraints at the receivers, i.e., the proposed technique can be viewed as a non-trivial enhancement of CIO-THP where expanding the optimization to more users poses new challenges in the design of the optimization problem. Indeed, a change in the definition of the required conditions to ensure a threshold performance at the receivers is necessary due to the use of the modulo operator at the receivers as opposed to CIO-THP where the modulo operator need not be taken into account in the optimization.

## 3.2 Power-Efficient THP (PE-THP) by Adaptive Symbol Scaling

### 3.2.1 Conventional THP

Tomlinson-Harashima precoding (THP) is a nonlinear technique that successively subtracts the known interference at the transmitter [31]. While both minimum mean square error THP (MMSE-THP) and zero forcing THP (ZF-THP) criteria can be applied to define the matrices involved in the precoding process [199], this chapter concentrates on ZF-THP for brevity reasons. The complete block diagram of the proposed power-efficient THP (PE-THP) is shown in Fig. 3.1, where  $\tilde{\mathbf{x}} \in \mathbb{C}^{N \times 1}$  represents the equivalent transmit symbols,  $\mathbf{y} \in \mathbb{C}^{K \times 1}$  denotes the received signals and  $\mathbf{n} \in \mathbb{C}^{K \times 1} \sim \mathcal{CN}(\mathbf{0}, \sigma^2 \mathbf{I}_K)$  denotes the standard additive white-Gaussian noise vector with variance  $\sigma^2$ . In line with conventional ZF-THP, the proposed scheme first lower triangularizes the downlink MISO channel  $\mathbf{H} \in \mathbb{C}^{K \times N}$  by using the LQ decomposition [31]

$$\mathbf{H} = \mathbf{L} \cdot \mathbf{F}^H. \quad (3.1)$$

Here,  $K$  represents the number of single-antenna users,  $N$  is the number of antennas at the BS,  $\mathbf{F}$  is a unitary matrix and  $\mathbf{L}$  is a lower left triangular matrix. Throughout this chapter, the BS is assumed to have a perfect knowledge of the channel  $\mathbf{H}$  and, for simplicity,  $N = K$  is considered as per [31]. By using the resultant matrices from the LQ decomposition, the equivalent THP channel can be represented by the lower left triangular matrix

$$\mathbf{B} = \mathbf{G} \cdot \mathbf{H} \cdot \mathbf{F}, \quad (3.2)$$

where the diagonal matrix of scaling coefficients  $\mathbf{G}$  is obtained from the main diagonal of the matrix  $\mathbf{L}$  as

$$\mathbf{G} = \text{diag} \left( \{ \mathbf{L}^{-1} \}_{n,n} \right). \quad (3.3)$$

The scaling operation is performed by each of the receivers and it ensures that the main diagonal of  $\mathbf{B}$  is formed by ones for correct interference presubtraction. After performing

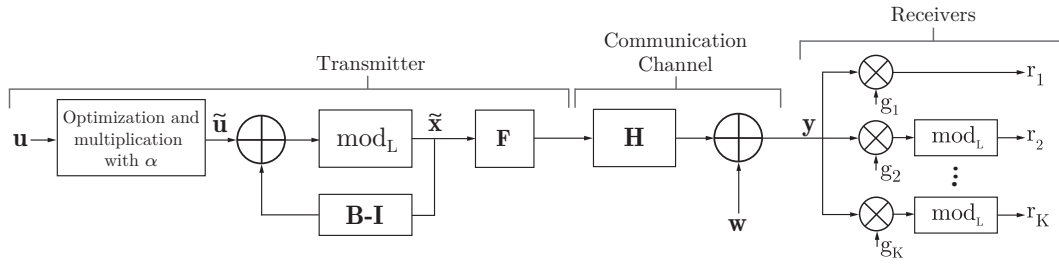


**Figure 3.1:** Block diagram of the proposed PE-THP.

these operations, the resulting MISO channel can be equivalently described as

$$\begin{bmatrix} r_1 \\ r_2 \\ \vdots \\ r_K \end{bmatrix} = \begin{bmatrix} 1 & 0 & \cdots & 0 \\ b_{2,1} & 1 & \cdots & 0 \\ \vdots & \vdots & \cdots & \vdots \\ b_{K,1} & b_{K,2} & \cdots & 1 \end{bmatrix} \begin{bmatrix} x_1 \\ x_2 \\ \vdots \\ x_N \end{bmatrix} + \begin{bmatrix} n_1 \\ n_2 \\ \vdots \\ n_K \end{bmatrix}, \quad (3.4)$$

where  $\mathbf{r} = [r_1, r_2, \dots, r_K]^T$  is the received signal after the THP processing at the receivers.

THP-based systems implement  $\mathbf{B}^{-1}$  at the transmitter to guarantee that the received symbols are interference-free. However, since a straight implementation of this solution increases the transmission power dramatically, a modulo operation is applied to avoid this [31]. The modulo function ensures that the transmitted symbols lie inside the Voronoi region of the original constellation and is given as

$$[p] \bmod_L = p - \left\lfloor \frac{\text{Re}(p) + L/2}{L} \right\rfloor L - i \left\lfloor \frac{\text{Im}(p) + L/2}{L} \right\rfloor L, \quad (3.5)$$

where  $\text{Re}(\cdot)$  and  $\text{Im}(\cdot)$  represent the real and imaginary parts of the input symbol respectively and  $L \in \mathbb{R}^+$  is the base of the modulo operation that depends on the selected modulation as described below. Subsequently, conventional THP obtains the transmitted symbols  $\tilde{x}_k$  as

$$\tilde{x}_k = \left[ u_k - \sum_{l=1}^{k-1} b_{k,l} \tilde{x}_l \right] \bmod_L, \quad k \in \{1, \dots, K\}, \quad (3.6)$$

where  $b_{k,l}$  denotes the  $k, l$ -th coefficient of the matrix  $\mathbf{B}$  and  $u_k$  is the constellation

symbol intended for the  $k$ -th user.

At the receiver, the equalized signal for the  $k$ -th user after the modulo operation is defined as

$$r_k = \begin{cases} g_{1,1} \cdot y_1, & \text{if } k = 1, \\ [g_{k,k} \cdot y_k] \bmod_L, & \text{if } k = \{2, \dots, K\}, \end{cases} \quad (3.7)$$

where, as represented in Fig. 3.1, it can be observed that the receiver of the first encoded user does not implement the modulo operation, since there is no interference to pre-subtract in the precoding process.

In the rest of this chapter, unless stated otherwise, it has been assumed that the original data symbols  $u_k$  are selected from the  $Q$ -QAM constellation  $\mathcal{Q} = \{a_R + ia_I | a_R, a_I \in \{\pm 1, \pm 3, \dots, \pm(\sqrt{Q} - 1)\}\}$ . These symbols are normalized by the factor  $f_{\text{nor}} = \sqrt{2(Q-1)/3}$  to ensure that the average energy of the constellation symbols is independent of the modulation order. Additionally, the base  $L$  of the modulo operation in THP can be easily calculated for  $Q$ -QAM modulations as  $L = \sqrt{Q}/f_{\text{nor}}$ .

### 3.2.2 Overview of Complex Domain Interference Optimized THP (CIO-THP) [55]

The modulo operation in (3.6) introduces a power loss, particularly significant for low-order modulations, due to the resultant uniform distribution of the symbols  $x_k, k \in \{1, \dots, K\}$  [31]. The power loss is formally defined as the ratio

$$\text{PL} = \frac{\mathbb{E}\{P_t\}}{N\mathbb{E}\{E_s\}}, \quad (3.8)$$

where  $E_s$  is the average symbol power of the original constellation and  $\mathbb{E}\{P_t\}$  represents the actual average transmission power after the modulo operation and symbol scaling.

CIO-THP reduces the power loss of conventional THP by scaling the symbol of the first user such that the interfering signals are better aligned with the symbols to transmit [55]. To accomplish this, CIO-THP defines a complex scaling factor  $a = a^r + ia^i$  that modifies the amplitude and phase of the first user's symbol  $u_1$ . The scaling factor is

selected in such a way that the total transmit power  $P_t$  of the modified transmit signal  $\tilde{\mathbf{x}} \in \mathbb{C}^{N \times 1}$  is minimized.

To secure a performance threshold, the norm of the transmit symbol of the first user must be lower bounded. Specifically, the scaling factors  $a$  for different phase-amplitude modulations are deducted in [55] as a function of the SNR required at the receiver  $\gamma$ , which for the first user reads as

$$\text{SNR}_1 = \frac{E_s |a|^2}{g_{1,1}^2 \sigma^2} \geq \gamma. \quad (3.9)$$

Here,  $g_{1,1}$  is the first element of the diagonal matrix  $\mathbf{G}$ ,  $\sigma^2$  denotes the noise variance at each receiver and the factor  $E_s |a|^2$  is the symbol energy after applying the scaling factor  $a = a^r + ia^i$ .

CIO-THP is based on the fact that, since the first user experiences no interference, the modulo operation is not required and the symbol of this user can be scaled arbitrarily subject to a SNR requirement. The scaling of other users is, however, more challenging as described in the following.

### 3.2.3 Proposed Zero Forcing Power-Efficient THP (ZF PE-THP)

Intuitively, the above power gains can be enhanced by allowing the symbols of further users to be scaled and thus adding new variables to the former optimization problem. These new optimization variables correspond to the extra scaling factors that are assigned to a specific number of users  $\tilde{K} > 1$ . Therefore, instead of just scaling the first user as in CIO-THP, the proposed PE-THP considers that the scaling factors can be applied to a larger number of users. This effectively increases the number of variables to optimize, making possible to generally find better solutions to the power minimization problem. Specifically, the adjusted symbols of PE-THP,  $\tilde{u}_k$ , can be expressed as

$$\begin{aligned} \tilde{u}_k &= \alpha_k^r u_k^r + i \alpha_k^i u_k^i, & k \leq \tilde{K} \\ \tilde{u}_k &= u_k, & k > \tilde{K} \end{aligned} \quad (3.10)$$

where  $\alpha_k^r$  and  $\alpha_k^i$  represent the real and imaginary parts of the scaling factor for the  $k$ -th user  $\alpha_k \triangleq \alpha_k^r + i\alpha_k^i$ , which are defined in Sec. 3.2.4. With these modified scaling factors, the precoded signal for the  $k$ -th user is obtained as

$$\tilde{x}_k(\hat{\alpha}_k) = \left[ \tilde{u}_k - \sum_{l=1}^{k-1} b_{k,l} \tilde{x}_l(\hat{\alpha}_{k-1}) \right] \text{mod}_L, \quad k \in \{1, \dots, K\}, \quad (3.11)$$

where  $\hat{\alpha}_{k-1} \in \mathbb{C}^{(k-1)}$  denotes the scaling factors that are applied to the  $k-1$  user symbols previously encoded. The difference in this formulation with respect to the original THP defined in (3.6) resides in that now the user symbols are modified by the scaling factors selected to minimize the transmission power. This in turn affects the interference generated from the users already precoded when generating the  $k$ -th transmit symbol  $\tilde{x}_k(\hat{\alpha}_k)$ . Also note that in PE-THP the processing at the receivers remains identical to the one performed in THP as per (3.7).

### 3.2.4 Definition of the Scaling Factors in PE-THP

Based on (3.11), the main objective of PE-THP is to find the scaling factors that better align the interference with the symbols to transmit to reduce the transmit power. These scaling factors can be calculated by solving the optimization problem

$$\begin{aligned} & \underset{\alpha}{\text{minimize}} \quad \left\{ \sum_{k=1}^K |\tilde{x}_k(\hat{\alpha}_k)|^2 \right\} \\ & \text{subject to } \tilde{\Phi}(\alpha_k^r, \alpha_k^i) \text{ for } 1 \leq k \leq \tilde{K}, \end{aligned} \quad (3.12)$$

where  $\tilde{\Phi}(\alpha_k^r, \alpha_k^i)$  are a set of constraints that depend on the received SNR requirements as detailed in the following. The optimization problem (3.12) has been proven to be convex in [55] for CIO-THP ( $\tilde{K} = 1$ ) under the assumption that the symbol replicas of the extended constellation are given. Note that the same argument holds when more optimization variables are added as this does not affect the conclusions obtained in [55]. Therefore, the solution to the optimization problem can be obtained numerically if the assumption holds by solving a non-linear least squares problem for which there are several algorithms already available [200, 201]. Since the above condition is not always

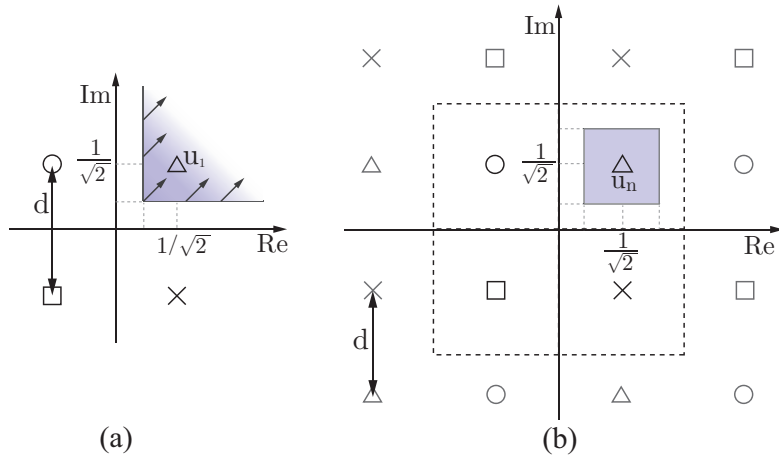


**Figure 3.2:** Regions that contain all possible values for the optimized constellation symbols in (a) the first user of PE-THP (CIO-THP) and (b) PE-THP for users  $2 \leq k \leq \tilde{K}$ .

guaranteed, a low-resolution search can be applied before the execution of the non-linear least squares algorithm for guaranteeing a close-to-optimal solution.

The definition of the constraints in PE-THP differs from the one used in CIO-THP. This is because, in contrast to CIO-THP where the first receiver does not apply the modulo operation, in PE-THP the users  $2 \leq k \leq \tilde{K}$  must execute it to guarantee that the signal to transmit lies inside the boundaries of the Voronoi region. In other words, the scaling factors in PE-THP are not only lower bounded by the received SNR thresholds as depicted in Fig. 3.2(a) for CIO-THP. In this figure, the four constellation symbols for the example of 4-QAM are represented by different geometric figures and  $d$  denotes the minimum Euclidean distance (MED) in the constellation. In fact, decision thresholds must be imposed in all directions around the information symbols in the signal constellation for these users. This is necessary because the signal constellation is infinitely replicated in all directions after applying the modulo function [55]. Hence, since all information symbols are adjacent to different ones in any direction as shown in Fig. 3.2(b), new detection thresholds must be imposed to avoid decoding errors. Note that this new restriction does not affect user 1 since its receiver does not implement the modulo function. Consequently, the first user in PE-THP will only have a lower SNR threshold as it is depicted in Fig. 3.2(a). In this figure, the shaded region represents the set of feasible solutions that satisfy the imposed thresholds.

It is clear from the above that decision thresholds around the symbols for users  $2 \leq k \leq \tilde{K}$  will have both upper and lower limits. For these users, the area that contains all possible solutions for the scaled symbols,  $\psi_k$ , is a square whose center is the original symbol  $u_k$ , and one of its vertices (the closest to the origin) is the symbol that corresponds to the one obtained when multiplying the original user symbol by the minimum scaling factor. This region is represented by the colored area in Fig. 3.2(b). Considering this, a different threshold can be defined by each of the users according to their specific requirements to secure a threshold performance. In particular, for two-dimensional constellations in which all their symbols have the same energy such as 4-QAM the scaling factors must satisfy

$$\begin{aligned} |\alpha_k^{r,i}| &\geq \beta_k, \text{ for } k = 1 \\ \beta_k &\leq |\alpha_k^{r,i}| \leq 2 - \beta_k, \text{ for } 2 \leq k \leq \tilde{K} \end{aligned} \quad (3.13)$$

where the modulation-dependent parameter  $\beta_k$  is defined as

$$\beta_k \triangleq \sqrt{\gamma_k g_{k,k}^2 \sigma^2 / E_s}. \quad (3.14)$$

Here,  $\gamma_k$  represents the performance threshold at the  $k$ -th receiver and  $E_s$  is the energy of the constellation symbol without considering the scaling factor effect. These constraints guarantee that the distance between any of the solutions obtained by the optimization problem and the boundaries of the Voronoi region is equal or greater than the minimum required to satisfy the receiver's threshold performance as shown in Fig. 3.2(b). As an illustrative example, the resulting optimization constraints  $\alpha_k^r, \alpha_k^i$  are calculated in Table 3.1 for the most practical binary phase-shift keying (BPSK), 4-QAM and 16-QAM modulations, although extension to higher-order modulations is straightforward. It should be pointed out that in general the constraints  $\gamma_k$  are a function of the distance between symbols  $d$ . The reason for this is that the average error rate in these cases depends on the distances between neighboring symbols rather than just on the absolute symbol power. Indeed, the constants that limit the upper and lower bounds for the scaling factors in these constellations vary depending on the energy of the real and

**Table 3.1:** Optimization constraints  $\tilde{\Phi}(\alpha_k^r, \alpha_k^i)$  for selected modulations

	Optimization Constraints $\tilde{\Phi}(\alpha_k^r, \alpha_k^i)$
BPSK	$\alpha_1^r \geq \sqrt{\gamma_1 g_{1,1}^2 \sigma^2}$ and $\alpha_1^i : \text{N/A}, \quad k = 1$ $\sqrt{\gamma_k g_{k,k}^2 \sigma^2} \leq \alpha_k^r \leq 2 - \sqrt{\gamma_k g_{k,k}^2 \sigma^2}$ and $\alpha_k^i : \text{N/A}, \quad 2 \leq k \leq \tilde{K}$
4QAM	$\alpha_1^r \geq \sqrt{\gamma_1 g_{1,1}^2 \sigma^2}$ and $\alpha_1^i \geq \sqrt{\gamma_1 g_{1,1}^2 \sigma^2}, \quad k = 1$ $\sqrt{\gamma_k g_{k,k}^2 \sigma^2} \leq \alpha_k^r \leq 2 - \sqrt{\gamma_k g_{k,k}^2 \sigma^2}$ and $\sqrt{\gamma_k g_{k,k}^2 \sigma^2} \leq \alpha_k^i \leq 2 - \sqrt{\gamma_k g_{k,k}^2 \sigma^2}, \quad 2 \leq k \leq \tilde{K}$
16QAM	$\beta_k^{\{r,i\}} \triangleq \sqrt{\gamma_k g_{k,k}^2 \sigma^2 / E_s^{\{r,i\}}}$ $k = 1 \left\{ \begin{array}{ll} \beta_1^r \leq \alpha_1^r \leq 2 - \beta_1^r & \text{and} \quad \beta_1^i \leq \alpha_1^i \leq 2 - \beta_1^i & \text{for } u_1 = \{\pm 1 \pm i\} / \sqrt{10} \\ \alpha_1^r \geq \beta_1^r + 2/3 & \text{and} \quad \beta_1^i \leq \alpha_1^i \leq 2 - \beta_1^i & \text{for } u_1 = \{\pm 3 \pm i\} / \sqrt{10} \\ \beta_1^r \leq \alpha_1^r \leq 2 - \beta_1^r & \text{and} \quad \alpha_1^i \geq \beta_1^i + 2/3 & \text{for } u_1 = \{\pm 1 \pm 3i\} / \sqrt{10} \\ \alpha_1^r \geq \beta_1^r + 2/3 & \text{and} \quad \alpha_1^i \geq \beta_1^i + 2/3 & \text{for } u_1 = \{\pm 3 \pm 3i\} / \sqrt{10} \end{array} \right.$ $1 < k \leq \tilde{K} \left\{ \begin{array}{ll} \beta_k^{\{r,i\}} \leq \alpha_k^{\{r,i\}} \leq 2 - \beta_k^{\{r,i\}} & \text{for } \text{Re}(u_k) = 1/\sqrt{10} \text{ or } \text{Im}(u_k) = 1/\sqrt{10} \\ \beta_k^{\{r,i\}} + 2/3 \leq \alpha_k^{\{r,i\}} \leq 4/3 - \beta_k^{\{r,i\}} & \text{for } \text{Re}(u_k) = 3/\sqrt{10} \text{ or } \text{Im}(u_k) = 3/\sqrt{10} \end{array} \right.$

imaginary parts of the symbols to scale  $E_s^{\{r,i\}}$ . Further, to maintain the coherence with the objective of reducing the transmit power, the lower threshold of the scaling factors is fixed to  $|\alpha_k^{\{r,i\}}|^2 = 1$  in badly conditioned channels where it is impossible to guarantee a certain threshold at the receivers without increasing the total transmission power.

### 3.2.5 Expansion of Optimization Regions with PE-THP

To illustrate the expanded optimization domains for PE-THP, a visual analysis of the signal generation process in CIO-THP and PE-THP is represented in Fig. 3.3 for  $N = K = 3$ . In this figure,  $u_k, k \in \{1, \dots, K\}$ , are the original symbols for each user,  $\tilde{x}_k, n \in \{1, \dots, K\}$ , represent the transmit symbol of the  $k$ -th user, and the regions  $\psi_k, k \in \{1, \dots, K\}$ , represent the possible scaled symbols  $\tilde{\mathbf{u}}$  when the entire set of feasible solutions to the optimization problem (3.12) is considered. Moreover, according to (3.11), each of the possible scaled symbols  $\tilde{\mathbf{u}}$  generates a different transmit signal  $\tilde{\mathbf{x}}$ , represented by the colored regions  $\chi_k, k \in \{1, \dots, K\}$ . In other words, the shaded regions illustrate all the signals that could be transmitted when considering the scaling factors that satisfy the optimization constraints. In this illustrative example,  $u_1 = (-1 + i)\sqrt{\frac{1}{2}}$ ,  $u_2 = (1 - i)\sqrt{\frac{1}{2}}$ ,  $u_3 = (-1 - i)\sqrt{\frac{1}{2}}$  are represented by the circles in each of the sub-figures.

First, in Fig. 3.3(a) the precoding operation is depicted for CIO-THP. It can be seen that the area that includes all the feasible symbols for the first user,  $\psi_1$ , is lower bounded by  $\Upsilon_1 = \beta_1 u_1^r = \beta_1 u_1^i$  in accordance with (3.10) and (3.13). When a solution (point)

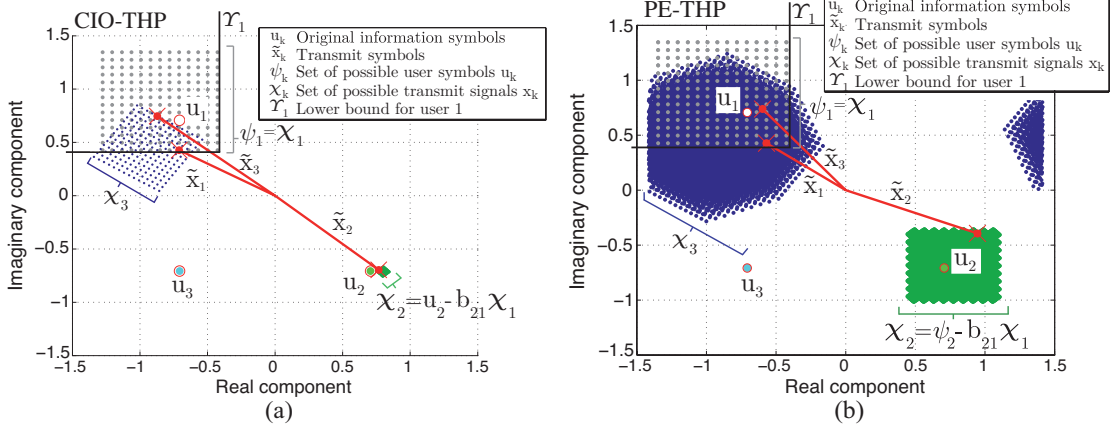


**Figure 3.3:** Visualization of the regions with the possible solutions of the optimization process for (a)  $\tilde{K} = 1$  and (b)  $\tilde{K} = 2$ .

$\tilde{x}_1$  of the region  $\psi_1 = \chi_1$  is selected, specific transmit symbols  $\tilde{x}_{\{2,3\}}$  of the sets  $\chi_{\{2,3\}}$  are also chosen by conventional THP encoding. Here,  $\chi_k$  represent the set of possible transmit signals for the  $k$ -th user generated by the different scaling factors that can be selected for the symbol of the first user. Mathematically, the set  $\chi_k$  of the  $k$ -th user depends on the previous ones as  $\chi_k = \psi_k - \sum_{l=1}^{k-1} b_{k,l} \chi_l$ , i.e., more feasible solutions to the transmit symbols  $\tilde{x}_k$  can be obtained as the size of the first region increases. The function of the optimization process is to find the solution that minimizes the total transmission power ( $P_t = 0.948$ ). The final transmit symbols  $\tilde{x}_k$  are also included in Fig. 3.3(a), represented by the red dots.

The idea behind PE-THP is to increase the size of the regions  $\chi_k$  from which the transmit symbols are selected to improve the results of the optimization. This effect is noticeable in Fig. 3.3(b) where the proposed technique has been applied to  $\tilde{K} = 2$  optimized users. In this figure, it can be seen that now the regions  $\chi_{\{2,3\}}$  are larger compared to the ones in CIO-THP. This is caused by the possibility of also modifying the symbol of the second user  $u_2$ , which in turn not only increases the range of possible constellation symbols for this user in the expanded region  $\psi_2$ , but also the ranges of transmit symbols for both users 2 and 3 in the regions  $\chi_{\{2,3\}}$ . In other words, now there are more degrees of freedom to select the transmit symbol of the third user  $\chi_3 = f(u_3, \chi_{\{1,2\}})$  as the space occupied by the previous regions is larger. As a result, the total

transmission power  $P_t = 0.82$  of the solutions  $\tilde{x}_{\{1,2,3\}}$  obtained in PE-THP is smaller than in CIO-THP due to the more relaxed optimization involved.

### 3.3 Power Loss Analysis

The power loss analysis of this section builds upon the one in [55]. Therefore, to avoid extensive repetition the power loss of the proposed technique is shown by leaning on the key results from [55] and highlighting the differences in the analysis for PE-THP. In particular, the Gaussian-Modulo distribution is employed, since it provides an accurate approximation to the probability density function (PDF) of the output symbols of a THP system where an adaptive symbol scaling of the first user is performed [55]. Here, this approach is extended to derive an upper bound of the power loss in the more generic case of PE-THP.

Without considering the modulo operation, in PE-THP the transmit symbols are generated as the subtraction between the scaled user symbols and the interference from the previously encoded users as shown in (3.6). Since the interference term is influenced by the lower triangular matrix  $\mathbf{B}$ , in the Gaussian-Modulo approximation the entries  $b_{k,n}$  are approximated as  $b_{k,n} \sim \mathcal{CN}(0, \sigma_{k,N}^2)$  with variance [55]

$$\sigma_{k,N}^2 = \frac{1}{2(N-k+1)}, \quad (3.15)$$

In this expression and for the rest of the sections a frequency flat Rayleigh fading channel  $\mathbf{H} \sim \mathcal{CN}(\mathbf{0}, \frac{1}{KN} \mathbf{I}_K \otimes \mathbf{I}_N)$  is considered to facilitate a direct comparison with [55].

Following the Gaussian-Modulo analysis [55], the distribution of the real or imaginary parts of the transmit symbols in CIO-THP and PE-THP can be approximated as  $\tilde{x}_k \sim \mathcal{CN}(\pm \tilde{\mu}_{k,\tilde{K},N}, \tilde{\sigma}_{n,\tilde{K},N}^2)$  for the case of 4-QAM. Here, the upper bound of the variance

$$\tilde{\sigma}_{k,\tilde{K},N}^2 = \frac{1}{2(N-k+1)} \left[ |\bar{\alpha}_{1,\tilde{K}}|^2 + \sum_{l=2}^{k-1} \left( \tilde{\mu}_{l,\tilde{K},N}^2 + \tilde{\sigma}_{l,\tilde{K},N}^2 \right) \right] \quad (3.16)$$

has to be computed iteratively due to the dependence of the transmit symbol of the

$k$ -th user on the previously encoded ones. The constant  $|\bar{\alpha}_{1,\tilde{K}}|^2$  denotes the average scaling factor for the first user which, as opposed to CIO-THP, varies with the number of optimized users  $\tilde{K}$ . It should be remarked that in PE-THP the scaling factors are determined on an instantaneous basis to minimize the total transmit power. Therefore, the use of the average value  $|\bar{\alpha}_{1,\tilde{K}}|^2$  to approximate the variance of the transmit signal provides an upper bound to the real variance since this symbol-by-symbol dependence is not included. It should be also noted that, from (3.16), the main difference in PE-THP with respect to the previous approaches is that the average value,  $\tilde{\mu}_{n,\tilde{K},N}$ , of the transmit symbols is further reduced due to the increased range of feasible solutions to the optimization problem. What is more, it is precisely this term the one that reflects the improvement of the proposed technique since its value depends on the additional scaling factors introduced by PE-THP (c.f. [55]).

The effect of the modulo operation in the transmit signal also has to be considered to obtain an approximation of the power loss in PE-THP. Specifically, the tails of the PDF of  $\tilde{x}_k$  that fall outside the Voronoi region of the constellation are folded back inside its limits, an effect that can be modeled by adding replicas of the original Gaussian PDF in the centers of the extended constellation symbols [55]. Formally, the resulting Gaussian-Modulo distribution for the considered 4-QAM constellation is given by

$$\begin{aligned}
 \hat{p}_{[x]}(x, \tilde{\sigma}_{k,\tilde{K},N}^2) &= \sum_{l=-1}^1 p \left( x, \mu = \tilde{\mu}_{k,\tilde{K},N} + \frac{4l}{\sqrt{2}}, \tilde{\sigma}_{k,\tilde{K},N}^2 \right) \Big|_0^{\sqrt{2}} \\
 &\quad + p \left( x, \mu = -\tilde{\mu}_{k,\tilde{K},N} + \frac{4l}{\sqrt{2}}, \tilde{\sigma}_{k,\tilde{K},N}^2 \right) \Big|_0^{\sqrt{2}}, \quad (3.17)
 \end{aligned}$$

where it is assumed that a good approximation of the resulting PDF can be obtained by considering a limited number ( $L_{\text{lim}} = 6$ ) of overlapping distributions.

From the distribution of the transmit symbols (3.17), it is possible to determine the second moment  $P_{k,\tilde{K},N} = \mathbb{E} \left\{ ([\tilde{x}_k] \bmod_L)^2 \right\}$  of the distribution for the  $k$ -th user by solving

$$P_{k,\tilde{K},N} = 4 \sum_{l=-1}^1 \int_0^{\sqrt{2}} x^2 \cdot p \left( x, \mu = \pm \tilde{\mu}_{k,\tilde{K},N} + \frac{4l}{\sqrt{2}}, \tilde{\sigma}_{k,\tilde{K},N}^2 \right) dx. \quad (3.18)$$

Here, the symmetry between the real and imaginary parts of the transmit symbols have

been exploited to obtain (3.18). The above result holds for the 4-QAM constellation assumed throughout this work with Voronoi region defined in the two-dimensional space  $\tilde{\nu} \in [-\sqrt{2}, \sqrt{2}]$ . However, note that this analysis can be directly applied to other constellations by modifying the limits of the Voronoi region and the centers of the replicas. As a result of the above analysis, the Gaussian-Modulo approximation of the power loss for PE-THP systems with a 4-QAM modulation can be expressed as

$$L_{\tilde{K},N}^{\text{PE-THP}} = \frac{\bar{\alpha}_{1,\tilde{K}}^2}{N} + \frac{4}{N} \times \sum_{k=2}^M \sum_{l=-1}^1 \int_0^{\sqrt{2}} x^2 p\left(x, \mu = \pm \tilde{\mu}_{k,\tilde{K},N} + \frac{4l}{\sqrt{2}}, \tilde{\sigma}_{k,\tilde{K},N}^2\right) dx, \quad (3.19)$$

where it has been considered that the transmit power of a  $Q$ -QAM constellation without the power loss effect is  $P_t^{\text{no-PL}} = 1$ . In this expression, the mean value  $\mu$  for the  $k$ -th user and the average scaling factor for the first user  $|\bar{\alpha}_{1,\tilde{K}}|^2$  are obtained via Monte Carlo simulations due to the difficulty of determining these analytically. Finally, the solution of the integral in (3.19) can be expressed as

$$L_{\tilde{K},N}^{\text{PE-THP}} = \frac{\bar{\alpha}_{1,\tilde{K}}^2}{N} + \frac{2}{\sqrt{2\pi}N} \sum_{k=2}^K \sum_{l=-1}^1 \left\{ 2\tilde{\sigma} \left[ e^{-\frac{\mu^2}{2\tilde{\sigma}^2}} - (\sqrt{2} + \mu)e^{-\frac{(\mu-\sqrt{2})^2}{2\tilde{\sigma}^2}} \right] + \sqrt{2\pi}(\tilde{\sigma}^2 + \mu^2) \left[ \text{erf}\left(\frac{2 - \sqrt{2}\mu}{2\tilde{\sigma}}\right) + \text{erf}\left(\frac{\mu}{\sqrt{2}\tilde{\sigma}}\right) \right] \right\}, \quad (3.20)$$

where  $\text{erf}(x)$  denotes the error function defined as  $\text{erf}(x) = \frac{2}{\sqrt{\pi}} \int_0^x e^{-t^2} dt$ .

Note that in (3.20), the dependence of the power loss with  $\tilde{K}$  and  $N$  is implicitly included in both the average value of the transmit symbols,  $\tilde{\mu}_{k,\tilde{K},N}$ , and the average scaling factor for the first user,  $\bar{\alpha}_{1,\tilde{K}}$ . Since this dependence is intractable analytically, in the following a semi-empirical approximation to the power loss in terms of  $\tilde{K}$  and  $N$  is introduced. This approximation is based on a second-order polynomial expression of the form

$$L_{\tilde{K},N}^{\text{PE-THP}} \simeq c_{20}\tilde{K}^2 + c_{02}N^2 + c_{11}N\tilde{K} + c_{10}\tilde{K} + c_{01}N + c_{00}, \quad (3.21)$$

where the constants  $c_{kl} \in \Re$  are determined via least-squares curve fitting to the original formula [202]. This expression shows the direct relationship between the power loss and the design parameters  $\tilde{K}$  and  $N$ . The constants  $c_{kl}$  depend on the modulation

order  $Q$  and the performance thresholds  $\gamma$ . As shown in the sequel, by appropriate selection of  $c_{kl}$ , the approximation closely resembles the real behavior of the power loss for a wide range of scenarios.

### 3.4 Power Consumption Analysis

Although the total transmission power may be reduced, PE-THP tends to have a higher complexity compared to THP, which therefore introduces a trade-off between transmit power and complexity. This extra signal processing complexity is caused by the necessity of solving the optimization problem defined in (3.12). In this section, the resulting complexity for PE-THP is calculated and this result is used to compare its power efficiency with THP to evaluate the above mentioned trade-off. Towards this end, the power consumption is computed by following a standard model as specified in Sec. 2.1.3. Specifically, the total power consumption is modelled as [40, 65]

$$P_{\text{tot}} = \left( \frac{\xi}{\eta} \right) P_t + N \cdot P_{\text{dyn}} + p_c \cdot C, \quad (3.22)$$

where  $P_t$  refers to the transmission power and the rest of variables involved in (3.22) are defined in Table 2.1. Throughout, a scenario-dependent transmit power  $P_t$  is considered, whereas the efficiency factor corresponds to the one of a class-A amplifier,  $\eta = 0.35$ , which is commonly used in this setting due to the linearity required to transmit a  $Q$ -QAM signal [203].  $\xi$  represents the average the modulation-dependent peak to average power ratio (PAPR). The power consumed by the RF chain of each antenna adopts a reference value of  $P_{\text{dyn}} = 34.4$  mW [40, 65] and  $p_c$ , which accounts for the power consumption per  $10^3$  operations ( $C$ ), is chosen as  $p_c = 5.76$  mW/kOps as per the Virtex-5 FPGA family from Xilinx [204].

#### 3.4.1 Complexity analysis

To calculate the overall complexity of the THP and PE-THP processes, the number of floating-point operations (flops) required in a system where  $N = K$  has been determined.

The results are detailed in Table 3.2 where, for simplicity, it has been assumed that a multiplication (division) has the same complexity as a summation (subtraction). This is a common assumption in the literature for this kind of analysis [205]. In addition, the operations required to calculate the Hessian of a complex matrix are assumed negligible with respect to the rest of the computations.

Table 3.2 shows that PE-THP increases the signal processing load due to the optimization problem required to compute the optimum scaling factors. The solution of this optimization problem can be obtained by solving a nonlinear least squares problem whose complexity can be divided into two parts: the one that depends on the minimization algorithm itself, and another one that corresponds to the number of times that (3.12) must be evaluated in the optimization process:

- The complexity of the minimization process can be estimated as  $\mathcal{O}(S_{\text{it}} \cdot S_{\text{par}})$ , where  $S_{\text{it}}$  is the number of iterations and  $S_{\text{par}}$  refers to the number of parameters to optimize [206]. In PE-THP, the parameters to optimize are the real and imaginary parts of the scaling factors. Therefore, their number can be expressed as a function of the number of users whose symbols will be modified, i.e.,  $S_{\text{par}} = 2K$ . On the contrary, the number of iterations of the minimization algorithm are problem-dependent.
- Regarding the complexity of evaluating (3.12), the number of operations that must be computed in each function evaluation can be directly extracted from Table 3.2. The number of function evaluations,  $S_{\text{ev}}$ , are dependent on the specific scenario.

According to the results of Table 3.2, the complexity of the minimization algorithm can be considered negligible compared to the rest of the process. The reason for this is that both the number of parameters to optimize and the average number of iterations is not in the order of the rest of operations such as the number of function evaluations  $S_{\text{ev}}$ . Moreover, the optimization algorithm requires an initial approximation that is provided by performing a low-resolution search prior the execution of the Trust-Region-Reflective algorithm. This previous step is not considered in the complexity analysis since, although performed for simplicity, it is only necessary for those scenarios where

**Table 3.2:** Approximate complexity in number of floating-point operations in the transmit signal generation of a PE-THP transmitter.

<b>PE-THP</b>	
<i>Operation</i>	<i>Complexity in flops</i>
qr( <b>H</b> ) [205]	$C_1 \simeq (16/3) N^3$
$\mathbf{G} = \text{diag}(\{\mathbf{L}^{-1}\}_{k,k})$	$C_2 = N$
$\mathbf{B} = \mathbf{G} \cdot \mathbf{H} \cdot \mathbf{F}$	$C_3 = 8N^3 - 2N^2$
$S_{\text{ev}} \times \begin{cases} \tilde{x}_k = \left[ \tilde{u}_k - \sum_{l=1}^{k-1} b_{k,l} \tilde{x}_l \right] \text{mod}_L, \\ P_t = \tilde{\mathbf{x}}^H \cdot \tilde{\mathbf{x}} \end{cases}$	$C_4 \simeq S_{\text{ev}} \times (4N^2 + 4N) + S_{\text{ev}} \times (7N)$
Trust-Region-Reflective minimization [206]	$C_6 = \mathcal{O}(2N \cdot S_{it})$
$\mathbf{s} = \mathbf{F}\mathbf{x}$	$C_7 = 8N^2 - 2N$
<b>Total</b>	$C_{\text{PE-THP}} \simeq (40/3) N^3 + (10 + S_{\text{ev}})N^2 + 11S_{\text{ev}}N$

the encoded symbol replicas are modified w.r.t. conventional THP [55]. Therefore, the number of operations required by the PE-THP scheme is approximated as

$$C_{\text{PE-THP}} \simeq C_{\text{THP}} + S_{\text{ev}} \cdot (4N^2 + 12N). \quad (3.23)$$

Here, the average number of function evaluations,  $S_{\text{ev}}$ , can be computed via Monte Carlo simulations to derive the average complexity of the proposed technique. To extract the information about the dependence of  $S_{\text{ev}}$  with  $N$  and  $\tilde{K}$ , a second-order polynomial expression such as the one shown in (3.21) will be used in the sequel. This simpler expression provides a good approximation to the Monte Carlo results and it facilitates determining the dependence between the overall complexity and the above-mentioned parameters.

### 3.4.2 Power Efficiency Maximization

For given performance requirements, a natural approach in the design of a communication system is to devise a scheme that minimizes the power consumption as defined in (3.22). Indeed, it is clear that the power loss contributes to the overall power consumption as the power required by the power amplifier  $P_{\text{PA}}$  is affected by the increase in the transmit power. For this reason, the reduction in the power loss that the proposed technique introduces provides a valid alternative to improve the power consumption in

THP-based systems. However, the complexity of the signal processing in PE-THP increases with the number of optimized users  $\tilde{K}$  due to the additional operations required to solve the optimization problem defined in (3.12). Therefore, an analysis of the trade-off between the reduction in the transmit power and the additional signal processing consumption is necessary to determine the best number of users  $\tilde{K}$  to optimize.

### 3.4.2.1 THP

The uniform approximation to the power loss [52] and the above complexity analysis can be used to calculate total power consumption of a THP system,  $P_{\text{tot}}^{\text{THP}}$ . Substituting these into (3.22), the total power consumption of a THP system can be expressed as

$$P_{\text{tot}}^{\text{THP}} \simeq P_{\text{p}} \cdot \frac{\left(\frac{\xi}{\eta}\right) \left(1 + \frac{Q}{Q-1}(K-1)\right)}{K} + N \cdot P_{\text{dyn}} + p_{\text{c}} \cdot \frac{(40/3)N^3 + 10N^2 + 11N}{10^3}, \quad (3.24)$$

where  $P_{\text{p}}$  is the intended transmission power without considering the power loss effect.

### 3.4.2.2 PE-THP

The optimization of the overall power consumption in PE-THP has an additional degree of freedom w.r.t. THP, i.e., the number of optimized users  $\tilde{K}$ . Therefore, to minimize this metric and select the best number of users to scale  $\tilde{K}$  it is necessary to understand the dependence of the power loss and the complexity of the proposed technique with  $N$  and  $\tilde{K}$ . However, since in PE-THP the theoretical approximations of these quantities do not have an analytic form as a function of  $\tilde{K}$  and  $N$ , this work resorts to a curve fitting approximation based on the Monte Carlo simulation results to obtain the desired closed-form expression

$$P_{\text{tot}}^{\text{PE-THP}} \simeq P_{\text{p}} \cdot \left(\frac{\xi}{\eta}\right) \cdot P_{\text{PL}}(\mathbf{c}_{\text{PL}}) + N \cdot P_{\text{dyn}} + p_{\text{c}} \cdot \frac{(40/3)N^3 + (10 + P_{\text{S}}(\mathbf{c}_{\text{S}}))N^2 + 12P_{\text{S}}(\mathbf{c}_{\text{S}})N}{10^3}. \quad (3.25)$$

Here,  $P_{\text{PL}}(\mathbf{c}_{\text{PL}})$  and  $P_{\text{S}}(\mathbf{c}_{\text{S}})$  represent the second-order polynomial approximation to the power loss and  $S_{\text{ev}}$  respectively with the set of coefficients  $\mathbf{c} = [c_{20}, c_{02}, \dots, c_{00}]^{\text{T}}$ . Note that, as mentioned above, the coefficients  $\mathbf{c}$  of the polynomial approximation vary with the modulation order  $Q$  and the specific performance thresholds  $\gamma$ . Once computed, these coefficients can be used to determine the overall power consumption for given  $P_{\text{p}}$ ,  $\tilde{K}$  and  $N$ , therefore providing a method to select the best number of users to optimize for a variety of scenarios. Indeed, for given rate requirements, the maximum power efficiency w.r.t.  $\tilde{K}$  is found by minimizing  $P_{\text{t}}^{\text{PE-THP}}$ , i.e. directly by taking the derivative of the differentiable expression in (3.25). Specifically, the optimum number of users to scale according to PE-THP is selected as

$$\tilde{K}_{\text{opt}} = \left\lceil \left[ \arg \left\{ \frac{\partial P_{\text{tot}}^{\text{PE-THP}}}{\partial \tilde{K}} = 0 \right\} \right] \right\rceil, \quad (3.26)$$

subject to  $\frac{\partial^2 P_{\text{tot}}^{\text{PE-THP}}}{\partial^2 \tilde{K}} > 0,$

where  $\lceil \cdot \rceil$  denotes the rounding operator to the closest integer and  $\tilde{K}_{\text{opt}} \in \{1, \dots, K\}$ .

### 3.5 Results and Discussion

To evaluate the improvement of the proposed technique with respect to the previous alternatives, numerical results have been obtained by performing Monte Carlo simulations in MATLAB<sup>®</sup>. Since they are the central subject of study of this Thesis, the simulation results compare the performance and power-related aspects of THP, CIO-THP and PE-THP with ZF. It should also be noted that, although not explicitly included here for reasons of brevity, the proposed technique can be adapted to the MMSE-THP by considering the appearance of the interference at the receivers [199]. The simulation scenario assumes a transmitter with 4-QAM and 16-QAM modulations, a flat Rayleigh fading channel which is perfectly known at the BS and  $N = K$ . It is noted that the structure of the receivers is identical for PE-THP and THP. Moreover, the optimization problem that must be solved in the PE-THP scheme has been implemented via a two-step procedure as detailed in Sec. 3.2: a low-resolution linear search

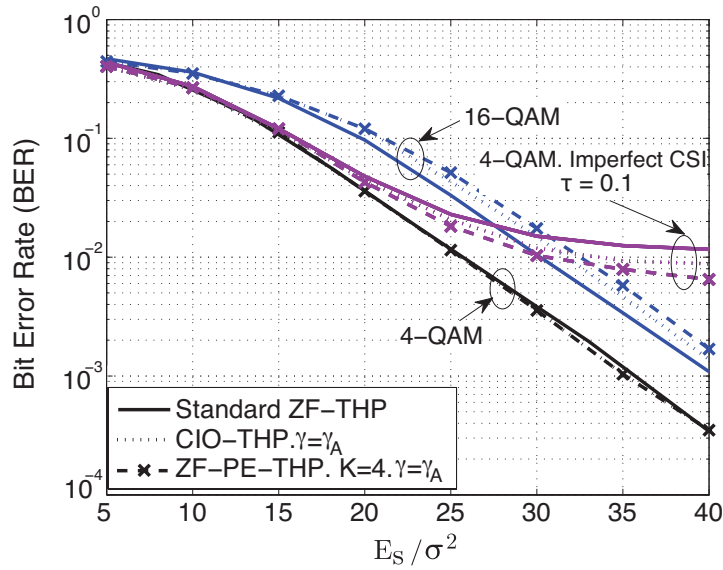


**Figure 3.4:** BER vs. SNR for THP, CIO-THP and PE-THP for  $N = K = 4$  antennas and both 4-QAM and 16-QAM.

and a subsequent nonlinear least squares problem. The average number of iterations and function evaluations, which are required to determine the algorithmic complexity, are also calculated via Monte Carlo simulations. Moreover, the thresholds  $\gamma_k$ ,  $k \in \{1, \tilde{K}\}$  guaranteeing that the bit error rate (BER) performance is approximately preserved are referred to as  $\gamma_A$  for notational convenience. In the following,  $\text{SNR} = E_s/\sigma^2$ , where  $E_s$  denotes the energy per symbol prior scaling.

The results of Fig. 3.4 show the BER against increasing levels of SNR for THP, CIO-THP and PE-THP with  $N = K = 4$  antennas and  $\tilde{K} = 4$  optimized users. It can be observed that both CIO-THP and PE-THP are able to approximately preserve the performance of conventional THP in spite of the scaling procedure. A slight degradation in the performance of PE-THP w.r.t. conventional THP and CIO-THP for 16-QAM can be observed in this figure. This effect is caused by the existence of tighter optimization constraints in this modulation. Additionally, the performance of the systems under study with imperfect CSI is also shown in Fig. 3.4. The imperfect CSI has been modeled following [207], where the channel estimation error is controlled by a parameter,  $\tau \in [0, 1]$ , that determines the accuracy of the acquired CSI, i.e.,  $\tau = 0$  corresponds to perfect CSI and  $\tau = 1$  implies that only statistical information is available. From the results of this figure, it can be seen that the performance is deteriorated in a similar way

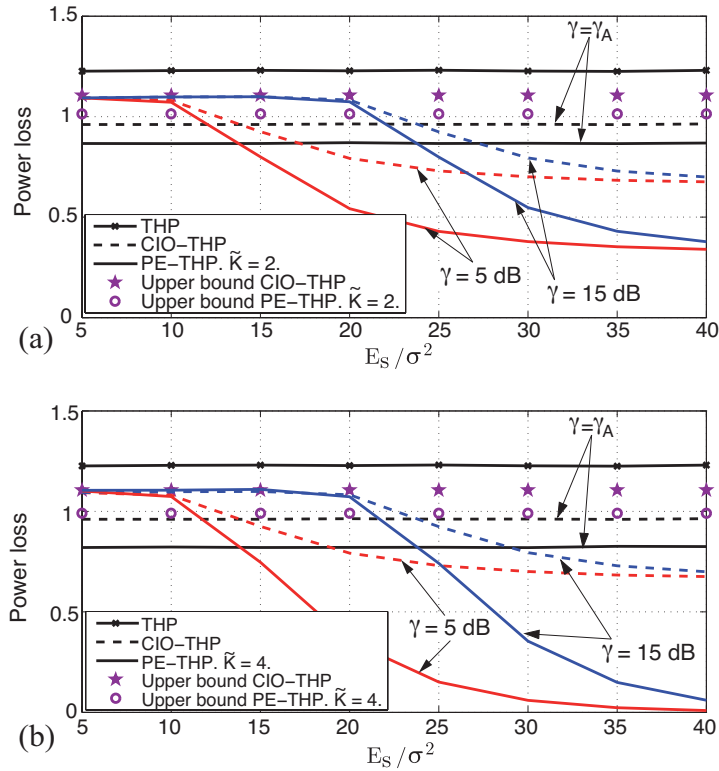


**Figure 3.5:** Power loss vs. SNR for THP, CIO-THP and (a) PE-THP with  $\tilde{K} = 2$  or (b) PE-THP with  $\tilde{K} = 4$  for different received SNR thresholds and 4-QAM modulation.

for both conventional THP and the proposed scheme when  $\tau = 0.1$ . In general, Fig. 3.4 proves that the performance of the PE-THP system can approximate the one of a standard THP transmitter while, as demonstrated in the following, it is able to reduce its transmission power.

Fig. 3.5 shows the power loss for different THP systems with  $N = K = 4$  antennas and a 4-QAM modulation as a function of the SNR. The results also include the theoretical upper bounds as derived in section V. For ease of comparison, Fig. 3.5(a) includes the results for  $\tilde{K} = 2$  optimized users whereas the number of optimized users rises up to  $\tilde{K} = 4$  in Fig. 3.5(b). From the observation of the results for PE-THP with  $\tilde{K} = 2$  and  $\tilde{K} = 4$ , it can be concluded that the power loss decreases with the number of optimized users independently of the selected threshold. Moreover, it is also shown that the power loss is reduced as the SNR grows when a specific threshold  $\gamma$  is determined. This effect is due to the possibility of further reducing the transmit power since, from Table 3.1,

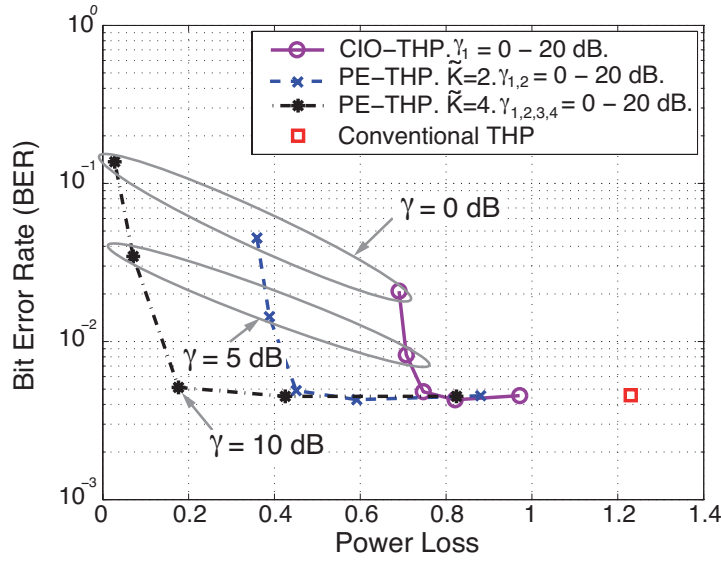


**Figure 3.6:** BER vs. power loss for THP, CIO and PE-THP.  $N = K = 4$ , 4-QAM, SNR = 29 dB and varying thresholds  $\gamma_k$ .

the range of values that the scaling factors can adopt in PE-THP depend on the noise level at the receivers. Savings in the transmit power up to 33% and 15% w.r.t. THP and CIO-THP respectively can be observed when the received performance thresholds are fixed as a function of the SNR ( $\gamma_k = \gamma_A$ ).

Fig. 3.6 studies the trade-off between the performance and power loss of the THP, CIO-THP and PE-THP systems with varying thresholds  $\gamma_k$ ,  $N = K = 4$ , 4-QAM, and SNR = 29 dB. Significant gains in power for the proposed scheme of over 90% and 85% with respect to THP and CIO-THP can be observed for SNR thresholds where the power optimization is relaxed without harming performance, in the region of uncoded BER below  $10^{-2}$ . Performance is, however, affected for lower performance thresholds, where evidently BER can not be guaranteed.

The performance vs. power loss trade-off is also depicted in Fig. 3.7 for THP, CIO-THP and PE-THP systems in the same scenario of  $N = K = 4$  and 4-QAM but under different SNR conditions. Again, significant power savings for the proposed scheme can be observed at high SNR values where the performance is not damaged. These power gains tend to diminish for decreasing SNR values. From Figs. 3.6 and 3.7 it can be seen that the proposed scheme offers significant power savings in the medium to high

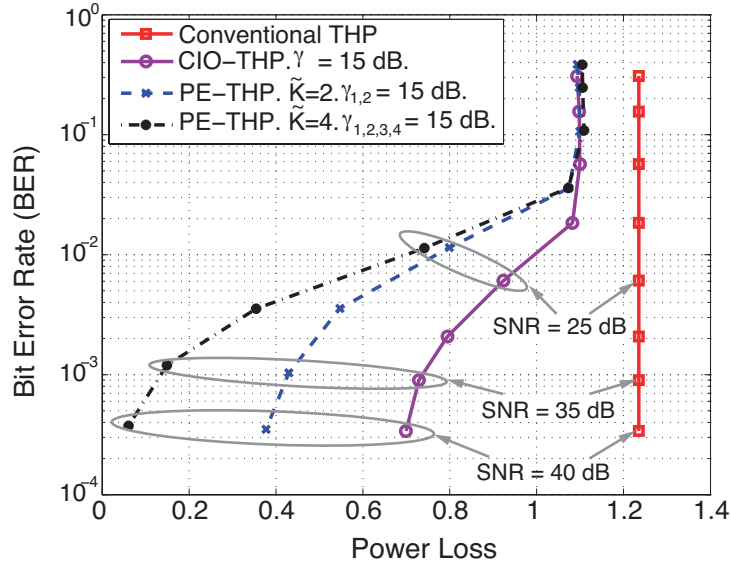


**Figure 3.7:** BER vs. power loss for THP, CIO-THP and PE-THP.  $N = K = 4$ , 4-QAM,  $\gamma = 15$  dB and varying SNR.

SNR regions where the power optimization is most effective, yielding a much reduced transmission power.

The complexities of THP, CIO-THP and PE-THP are shown in Fig. 3.8 for the case of 4-QAM and increasing  $\gamma_k$ . It can be seen that the number of operations required to solve the optimization problem increases as the thresholds  $\gamma_k$  lower down. This effect can be explained by taking into account that the range of possible solutions increases when  $\gamma_k$  is made smaller, therefore complicating the minimization process since a larger number of function evaluations  $S_{ev}$  is required.

Fig. 3.9 depicts the normalized power consumption as a function of  $\tilde{K}$  for different intended transmit powers  $P_t$  in a system with  $N = K = 8$ , 16-QAM and  $\gamma = \gamma_A$ , hence guaranteeing an approximate performance. Typical transmit power budgets corresponding to LTE BS, Picocell BS and WiFi BS are selected for reference to practical systems [5]. Moreover, Fig. 3.9 also includes the power consumption approximation described in (3.25). The polynomial coefficients obtained in these scenarios are  $\mathbf{c}_{PL} = [0.01, -0.0018, 0, -0.12, 0.04, 0.88]^T$  and  $\mathbf{c}_S = [0.51, 1.25, -0.1, 8.77, 0, 86, -3.24]^T$  for the power loss and for  $S_{ev}$  respectively. It can be seen that the second-order polynomial expression closely matches the empirical results for any  $\tilde{K}$  and  $N$ , therefore making

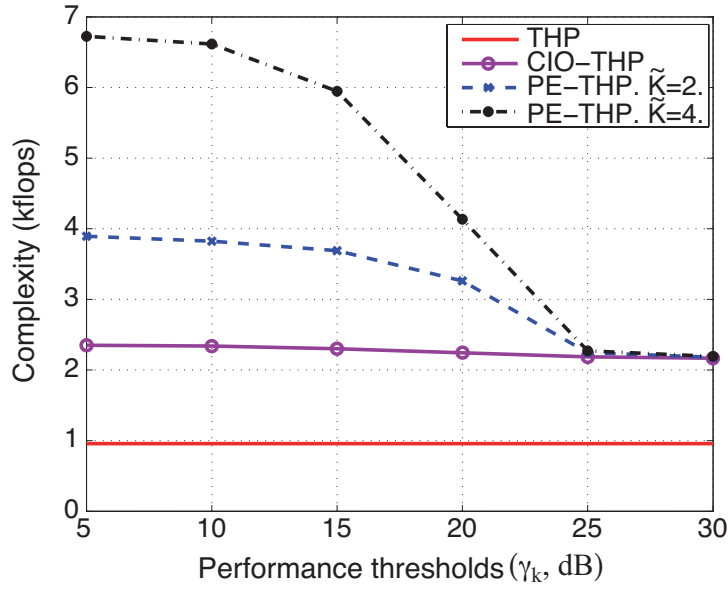


**Figure 3.8:** Number of operations in kflops vs.  $\gamma_k$  for THP, CIO-THP and PE-THP systems with  $N = K = 4$  antennas and 4-QAM.

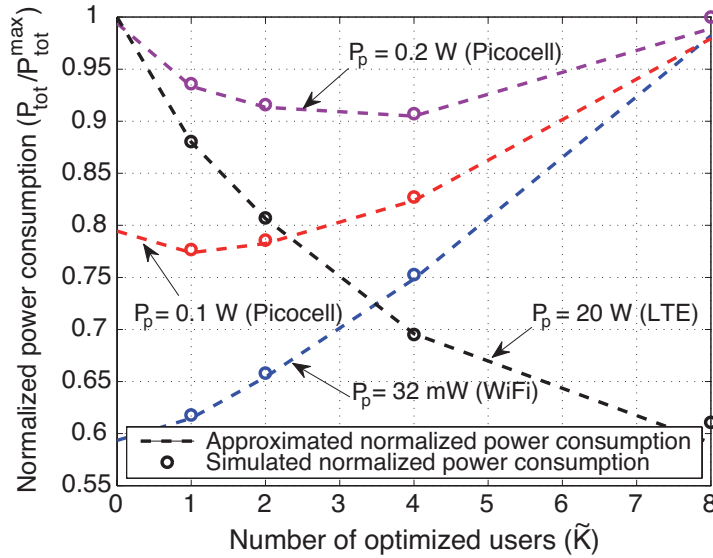


**Figure 3.9:** Total power consumption vs.  $\tilde{K}$  for different  $P_t$ . THP-based systems with  $N = K = 8$ , 16-QAM modulation and  $\gamma = \gamma_A$ .

possible to select the best number of users to optimize without having to compute the results for all possible combinations of these parameters. It can also be observed that the optimum  $\tilde{K}$  to minimize the overall power consumption, which corresponds to the minimum in each curve, increases as  $P_p$  does. Based on these results, it can be concluded that the proposed technique is most useful w.r.t. THP and CIO-THP in the higher

transmit power scenarios of the LTE BS and Pico BS, where the power consumed by the power amplifier  $P_{\text{PA}}$  dominates over the signal processing consumption.

### 3.6 Conclusions

In this work, a power efficient THP scheme has been proposed. Based on a power consumption analysis, it has been concluded that it is possible to improve the results of the previous approaches in terms of power loss by scaling the original user symbols. It has been confirmed that the proposed technique can maintain the error rates of THP and CIO-THP while, at the same time, decreasing their power loss. In this line, the benefits of both CIO-THP and PE-THP have been shown to be particularly significant at large SNRs, where transmission power savings larger than 50% have been demonstrated.

*Critique:* The above-mentioned enhancements come at the cost of a higher computational complexity. Indeed, there exists a trade-off between performance and complexity: while complexity increases when a higher number of users are scaled, this also entails that the known interference can be better aligned with the symbols to transmit, hence further reducing the transmission power. This suggests that the proposed scheme is particularly suitable for MIMO setups with a small number of antennas, where the signal processing complexity increase is constrained. Moreover, note that the optimal scaling factors might be re-utilized without the need of solving again the optimization problem if the channel remains constant, e.g., by implementing a lookup table for the possible input symbol combinations. This aspect promotes the application of the proposed scheme in slowly varying channels and in small scale MIMO systems, where the number of possible input symbol combinations is reduced.



## Chapter 4

# Pre-Scaling for Space Shift Keying via Semidefinite Programming

### 4.1 Introduction

Both space shift keying (SSK) and spatial modulation (SM) aim for reducing the analog hardware complexity of conventional spatial multiplexing [18,19,158,167]. Specifically, SSK and SM rely on encoding information into the active antenna indices, which allows reducing the number of radio frequency (RF) chains employed for transmission, when compared to the family of classic spatial multiplexing schemes [19,158,167]. The essential objective behind reducing the number of RF chains is to enhance the system's energy efficiency by lowering down the total power consumption [2].

While the development of strategies for improving the attainable performance has been mostly concentrated on techniques at the receiver side [168–171], a parallel line of research proposes to exploit the availability of channel state information (CSI) at the transmitter for devising constellation shaping schemes [163,174–177]. In this context, [174] analyzes the design of amplitude and phase constellations for minimizing the average bit error probability of SM, whereas [175] analytically studies the achievable

transmit diversity order under different design conditions. SSK's particular characteristic of solely carrying information in the spatial domain has also been exploited for the design of constellation shaping strategies in [163, 176, 177].

The maximization of the minimum Euclidean distance (MED) in the resultant SSK and SM constellations via symbol pre-scaling has been the focus of [178–180]. In particular, the pre-scaling strategies developed in [178, 179] rely on forcing the received SM constellation to resemble a classic quadrature amplitude modulation (QAM) constellation from an inter-symbol distance perspective. However, the employment of the regimes in [178, 179] may severely affect the system's signal-to-noise ratio (SNR) due to the stringent requirement of inverting the channel coefficients, which may become critical for ill-conditioned channels. The scheme introduced in [180] mitigates this problem by solely applying a phase shift by the pre-scaling procedure. However, the above designs only consider a single antenna at the receiver, which in turn simplifies both the characterization and shaping of the received SM constellation.

The application of pre-scaling strategies to the more intricate systems with multiple antennas at both communication ends has been promulgated in [181–184, 208]. In particular, the schemes of [181, 182] propose opportunistic power allocation methods for both SSK and generalized SSK for the sake of improving their performance, which implies that only the amplitude of the transmit signals is modified. By contrast, simultaneous phase and amplitude pre-scaling is considered in the constellation randomization (CR) technique of [183]. This low-complexity scheme relies on generating  $D_s$  complex-valued scaling factors off-line, and subsequently employing those specific scaling factors that maximize the MED. The schemes introduced in [184], which were developed in parallel to the work described in this chapter [209], further improve the performance by employing a successive convex approximation technique for solving the resultant optimization problems for maximizing the MED. Subsequent to this work, [208] has proposed algorithms with the similar objectives of maximizing the MED and minimizing the bit error rate (BER) of SM systems. However, the schemes devised in [208] for maximizing the MED only concentrate on  $2 \times K$  MIMO systems. Interestingly, the authors in [208] show that a criterion designed for directly minimizing the BER can provide noticeable

improvements over schemes that solely aim at maximizing the MED.

Against the above contributions, this chapter considers the optimization of the pre-scaling factors for SSK transmission via semidefinite programming. Specifically, the original non polynomial (NP)-hard optimization problems are recast for the sake of maximizing the performance of SSK transmissions via semidefinite relaxation (SDR). This guarantees the applicability of the proposed pre-scaling designs to multi-antenna aided receivers by carefully adapting the schemes introduced in [178–180]. Additionally, this contribution aims at improving the performance of the strategy developed in [183] by taking into account the channel conditions in the design of the pre-scaling vectors, while reducing the signal processing complexity of the algorithms advocated in [184], where multiple convex optimization problems have to be solved before reaching convergence.

## 4.2 Space Shift Keying with Pre-Scaling

The system model considered throughout this chapter is comprised of a transmitter having  $N$  antennas, and a receiver equipped with  $K$  antennas, as shown in Fig. 4.1. The SSK transmitter activates a single antenna based on the input bit stream, hence conveying a total of  $\lfloor \log_2(N) \rfloor$  bits per channel use, where  $\lfloor \cdot \rfloor$  denotes the floor function. Combining (2.1) and (2.28), the received signal  $\mathbf{y} \in \mathbb{C}^{K \times 1}$  can be expressed as

$$\mathbf{y} = \mathbf{H}\mathbf{W}\mathbf{e}_n + \mathbf{n} = \mathbf{h}_n w_n + \mathbf{n}, \quad (4.1)$$

where  $\mathbf{e}_n \in \mathbb{C}^{N \times 1}$  is the  $n$ -th column of the identity matrix  $\mathbf{I}_N$ , and  $\mathbf{n} \in \mathbb{C}^{K \times 1} \sim \mathcal{CN}(\mathbf{0}, \sigma^2 \mathbf{I}_K)$  denotes the ubiquitous additive white-Gaussian noise vector. Moreover,  $\mathbf{H} \in \mathbb{C}^{K \times N} \sim \mathcal{CN}(\mathbf{0}, \mathbf{I}_K \otimes \mathbf{I}_N)$  represents the Rayleigh communication channel considered in the following and  $\mathbf{W} \in \mathbb{C}^{N \times N} = \text{diag}(\mathbf{w})$  is a diagonal matrix, with its  $n$ -th diagonal coefficient given by  $w_n$  and satisfying  $\mathbf{w}^H \mathbf{w} = N$ , unless stated otherwise. Note that the single-RF chain benefit of SSK transmission is preserved when pre-scaling is employed, and that the pre-scaling coefficients that determine the amplitude and phase of the transmitted symbols solely rely on the instantaneous channel coefficients, but not

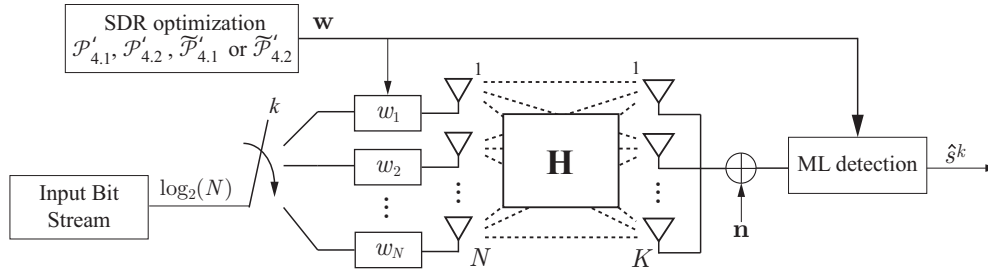


**Figure 4.1:** Block diagram of SSK transceiver with pre-scaling.

on the alphabet and input bits.

The optimal detection strategy of the receiver obeys the maximum likelihood (ML) criterion of

$$\hat{n} = \arg \min_n \|\mathbf{y} - \mathbf{h}_n \hat{w}_n\|^2, \quad (4.2)$$

where  $\mathbf{h}_n$  is the  $n$ -th column of  $\mathbf{H}$  and  $\hat{w}_n$  denotes the  $n$ -th pre-scaling coefficient estimated at the receiver side. In the following it has been assumed that the pre-scaling coefficients  $\hat{w}_n$  and  $w_n$  are computed independently at both the transmit and the receive sides based on the perfect channel estimates. Hence, no feedforwarding of the pre-scaling coefficients prior to data transmission is required.

The performance of the SSK transmission scheme considered is determined by the pairwise error probabilities [165]

$$P(\mathbf{e}_k \rightarrow \mathbf{e}_m | \mathbf{H}) = Q \left( \sqrt{\frac{1}{2\sigma^2} \|\mathbf{h}_k w_k - \mathbf{h}_m w_m\|^2} \right), \forall m \neq k, \quad (4.3)$$

where  $m, k \in \{1, \dots, N\}$  denote the specific index of the antenna activated for transmission and  $Q(\cdot)$  represents the  $Q$ -function. It can be seen from (4.3) that the detection performance of SSK is conditioned by the MED of the received constellation symbols [165], which is given by

$$\text{MED} = \min_{m,k} \|\mathbf{h}_k w_k - \mathbf{h}_m w_m\|^2, \forall m \neq k. \quad (4.4)$$

The efficient design of the SSK pre-scaling coefficients based on the above metric constitutes the focus of this contribution.

### 4.2.1 MED Maximization

An appealing technique of improving the attainable performance of conventional SSK transmission relies on maximizing the MED, while satisfying the maximum power constraint. In this particular case, the optimal pre-scaling vector  $\mathbf{w}_{\text{opt}}$  can be obtained as a solution of the optimization problem

$$\begin{aligned} \mathcal{P}_{4.0} : \underset{\mathbf{w}}{\text{maximize}} \quad & \min_{\substack{m,k \\ m \neq k}} \left( \|\mathbf{h}_k w_k - \mathbf{h}_m w_m\|^2 \right) \\ \text{subject to} \quad & \|\mathbf{w}\|^2 \leq (P_t N). \end{aligned} \quad (4.5)$$

The constraint in (4.5) ensures having an average transmission power per channel use of  $\mathbb{E}\{w_n^H w_n\} = P_t$ ,  $\forall n \in \{1, \dots, N\}$ . The more tractable epigraph problem form of (4.5) is given by

$$\begin{aligned} \mathcal{P}_{4.1} : \underset{\mathbf{w}, d}{\text{maximize}} \quad & d \\ \text{subject to} \quad & \|\mathbf{h}_k w_k - \mathbf{h}_m w_m\|^2 \geq d, \quad \forall m \neq k \\ & \|\mathbf{w}\|^2 \leq (P_t N). \end{aligned} \quad (4.6)$$

Here,  $d$  represents the MED. Note that the above optimization problem is not convex w.r.t. the optimization variable  $\mathbf{w}$  due to the existence of non-convex quadratic constraints [210, 211].

### 4.2.2 Power Minimization

A problem of similar character to the above consists of procuring the pre-scaling factors that minimize the average transmission power, while satisfying a given MED threshold  $d$ . This optimization problem can be expressed as

$$\begin{aligned} \mathcal{P}_{4.2} : \underset{\mathbf{w}}{\text{minimize}} \quad & \|\mathbf{w}\|^2 \\ \text{subject to} \quad & \|\mathbf{h}_k w_k - \mathbf{h}_m w_m\|^2 \geq d, \quad \forall m \neq k. \end{aligned} \quad (4.7)$$

### 4.3 Pre-Scaling Optimization for SSK via Semidefinite Programming

The NP-hard nature of the nonconvex quadratically constrained quadratic problems  $\mathcal{P}_{4.1}$  and  $\mathcal{P}_{4.2}$  motivates the development of potentially suboptimal reformulations [210–212]. In particular, the optimization problems  $\mathcal{P}_{4.1}$  and  $\mathcal{P}_{4.2}$  are recast as semidefinite programs by exploiting their resemblance to the sensor network location problem [210, 213], where the aim is to maximize the MED between adjacent sensor nodes.

#### 4.3.1 MED Maximization

This section concentrates on reformulating the non-convex optimization constraints of  $\mathcal{P}_{4.1}$  via semidefinite relaxation [211]. First, the number of meaningful constraints in the second line of  $\mathcal{P}_{4.1}$  and  $\mathcal{P}_{4.2}$  is determined. In particular, the number of non-identical constraints is given by

$$N_c = \sum_{i=1}^N (N - i) = \frac{N(N - 1)}{2}, \quad (4.8)$$

where the fact that for any  $x_i, x_j, i \neq j$ , the operation  $\|x_i - x_j\|$  is equivalent to  $\|x_j - x_i\|$  has been considered, which makes unnecessary to analyze the symmetrical terms. Moreover, the left-hand side of the quadratic constraints can be decomposed as

$$\|\mathbf{h}_k w_k - \mathbf{h}_m w_m\|^2 = \sum_{i=1}^K \|h_{(k,i)} w_k - h_{(m,i)} w_m\|^2, \quad (4.9)$$

where  $h_{(k,i)}$  refers to the  $i$ -th entry of  $\mathbf{h}_k$ . The  $i$ -th term of the summation in (4.9) can be re-formulated as [213]

$$\|h_{(k,i)} w_k - h_{(m,i)} w_m\|^2 = \text{Tr} \left( \mathbf{e}_{(k,m)}^{(i)} \left( \mathbf{e}_{(k,m)}^{(i)} \right)^H \mathbf{w} \mathbf{w}^H \right) = \text{Tr} \left( \mathbf{A} \mathbf{E}_{(k,m)}^{(i)} \right), \quad (4.10)$$

where  $\mathbf{A} \triangleq \mathbf{w} \mathbf{w}^H$ ,  $\mathbf{E}_{(k,m)}^{(i)} \triangleq \mathbf{e}_{(k,m)}^{(i)} \left( \mathbf{e}_{(k,m)}^{(i)} \right)^H$ , and  $\mathbf{e}_{(k,m)}^{(i)} \in \mathbb{C}^{N \times 1}$  is a vector with two non-zero entries in the positions specified by  $k$  and  $m$

$$\mathbf{e}_{(k,m)}^{(i)} = [0, \dots, h_{(k,i)}, \dots, -h_{(m,i)}, \dots, 0]^T. \quad (4.11)$$

Let  $\mathbf{E}_{(k,m)}$  be defined as

$$\mathbf{E}_{(k,m)} \triangleq \sum_{i=1}^K \mathbf{E}_{(k,m)}^{(i)}. \quad (4.12)$$

Note that  $\mathbf{E}_{(k,m)} \in \mathbb{H}^N$ ,  $\forall k \neq m$ , where  $\mathbb{H}^N$  represents the set of  $(N \times N)$ -element complex-valued Hermitian matrices. Then, by substituting (4.9), (4.10) and (4.12) into (4.6),  $\mathcal{P}_{4.1}$  can be recast as

$$\begin{aligned} \mathcal{P}_{4.1} : \quad & \underset{\mathbf{A}}{\text{maximize}} \quad d \\ & \text{subject to} \quad \text{Tr}(\mathbf{E}_{(k,m)}\mathbf{A}) \geq d, \forall k \neq m \\ & \quad \quad \quad \text{Tr}(\mathbf{A}) \leq (P_t N) \\ & \quad \quad \quad \mathbf{A} \succeq 0, \text{rank}(\mathbf{A}) = 1. \end{aligned} \quad (4.13)$$

Here,  $\mathbf{A} \succeq 0$  indicates that  $\mathbf{A}$  is positive semidefinite, and it has been considered that  $\|\mathbf{w}\|^2 = \text{Tr}(\mathbf{w}\mathbf{w}^H) = \text{Tr}(\mathbf{A})$ . The above optimization problem is equivalent to that formulated in (4.6) and still remains NP-hard. However, a relaxed convex version of  $\mathcal{P}_{4.1}$  can be obtained by dropping the non-convex constraint  $\text{rank}(\mathbf{A}) = 1$ , which results in

$$\begin{aligned} \mathcal{P}'_{4.1} : \quad & \underset{\mathbf{A}}{\text{maximize}} \quad d \\ & \text{subject to} \quad \text{Tr}(\mathbf{E}_{(k,m)}\mathbf{A}) \geq d, \forall k \neq m \\ & \quad \quad \quad \text{Tr}(\mathbf{A}) \leq (P_t N), \mathbf{A} \succeq 0. \end{aligned} \quad (4.14)$$

The optimization problem (4.14) is convex in the optimization variables  $\mathbf{A}$  and  $d$ , which facilitates the employment of efficient convex solvers [211]. At this point, it should be emphasized that the pre-scaling problem (4.14) differs from those conventionally employed for beamforming [214]. Specifically, there exists a larger number of optimization constraints and these are distinct, since the information conveyed by SSK depends on the distance between the symbols received when different antennas are activated. Instead, conventional beamforming problems aim at determining the beamforming vector that maximizes the signal-to-interference-plus-noise ratio (SINR) at the receiver, since

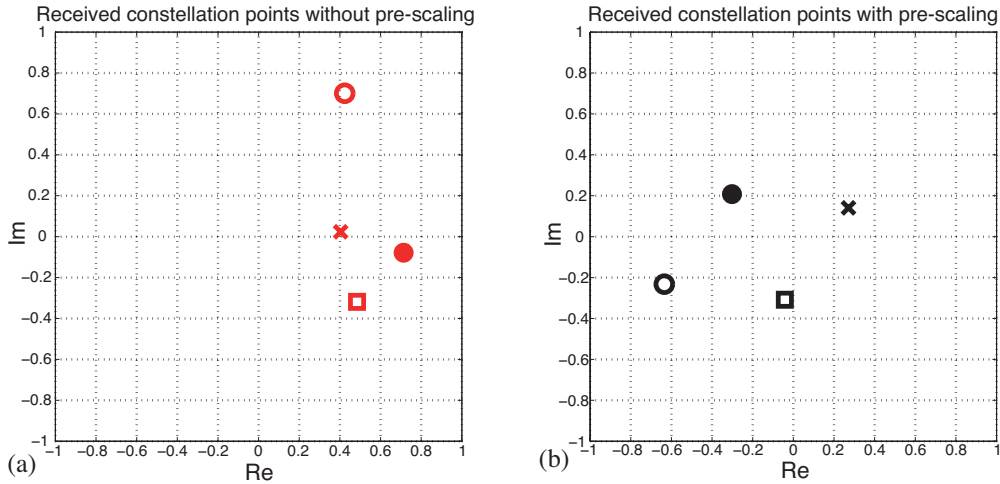


**Figure 4.2:** Impact of pre-scaling in the received constellations for a  $(4 \times 1)$ -element MISO system. (a) Conventional SSK and (b) Pre-scaled SSK.

the information is solely carried out via the traditional amplitude-phase constellations.

### 4.3.2 Power Minimization

Following a procedure akin to that employed for deriving  $\mathcal{P}'_{4.1}$  from  $\mathcal{P}_{4.1}$ , the semidefinite relaxation of  $\mathcal{P}_{4.2}$  yields

$$\begin{aligned}
 \mathcal{P}'_{4.2} : \quad & \underset{\mathbf{A}}{\text{minimize}} \quad \text{Tr}(\mathbf{A}) \\
 & \text{subject to} \quad \text{Tr}(\mathbf{E}_{(k,m)}\mathbf{A}) \geq d, \forall k \neq m, \\
 & \mathbf{A} \succeq 0.
 \end{aligned} \tag{4.15}$$

### 4.3.3 Effect of the Optimization on the Received Constellation

Prior to characterizing the performance of the scheme considered, the effect of solving the optimization problem  $\mathcal{P}'_{4.2}$  in the received constellation is illustrated using an intuitive example. Specifically, Fig. 4.2(a) shows the received constellation, when conventional SSK transmission is employed, whereas Fig. 4.2(b) represents that under the same channel conditions, but applying the pre-scaling coefficients designed following  $\mathcal{P}'_{4.2}$  using  $d = 0.3$ . In both figures, the distinct constellation symbols are illustrated by different geometrical shapes. The larger MED separation experienced by the constella-

tion symbols of Fig. 4.2(b) demonstrates that the approach considered is indeed capable of enhancing the MED, hence improving the overall performance of conventional SSK. Moreover, the average transmission power of  $\mathbb{E}\{P_t\} = 1$  W for SSK is reduced in this particular example to  $\mathbb{E}\{P_t\} = 0.56$  W thanks to the proposed pre-scaling. However, the solutions obtained by solving the relaxed problems might become suboptimal in terms of the attainable MED or the transmission power in  $\mathcal{P}'_{4.1}$  and  $\mathcal{P}'_{4.2}$ , respectively, as a consequence of removing the non-convex rank constraint. The characterization of this aspect in the pre-scaling scheme considered motivates the following analysis.

#### 4.3.4 Measuring the Impact of the Problem Relaxation

The pre-scaling vectors obtained by the SDR of the optimization problems  $\mathcal{P}_{4.1}$  and  $\mathcal{P}_{4.2}$  only coincide with those of  $\mathcal{P}'_{4.1}$  and  $\mathcal{P}'_{4.2}$  when  $\text{rank}(\mathbf{A}) = 1$  [210]. This implies that the pre-scaling vector  $\mathbf{w}$  employed for transmission can be straightforwardly derived as

$$\mathbf{w} = \mathbf{w}_{\text{opt}} = \mathbf{U}\mathbf{\Sigma}^{1/2}, \quad (4.16)$$

where  $\mathbf{w}_{\text{opt}}$  denotes the optimal pre-scaling vector solution to  $\mathcal{P}_{4.1}$  and  $\mathcal{P}_{4.2}$ , while  $\mathbf{U}$  and  $\mathbf{\Sigma}$  correspond to the eigenvectors and eigenvalues of  $\mathbf{A}$  respectively, i.e.,  $\mathbf{A} = \mathbf{U}\mathbf{\Sigma}\mathbf{U}^H$ . However, the above-mentioned ideal condition  $\text{rank}(\mathbf{A}) = 1$  is not always satisfied, and therefore randomization strategies have been employed for finding close-to-optimal solutions [210, 212]. Specifically, the pre-scaling vectors are obtained as [212]

$$\mathbf{w} = c\mathbf{U}\mathbf{\Sigma}^{1/2}\mathbf{v}, \quad (4.17)$$

where  $\mathbf{v}$  is a vector comprised of the exponential random variables characterized by,  $v_i = e^{j\hat{\theta}_i}$ ,  $\hat{\theta}_i \sim \mathcal{U}(0, 2\pi]$ , which are uniformly distributed on the unit circle of the complex plane satisfying  $\mathbb{E}\{\mathbf{v}\mathbf{v}^H\} = \mathbf{I}_N$ . Here, the constant  $c$  guarantees that the problem constraints are satisfied. It should be remarked that the solutions  $\mathbf{w}$  obtained as a result of (4.16) and (4.17) are sub-optimal when  $\text{rank}(\mathbf{A}) \neq 1$ , i.e.,  $\widetilde{\mathbf{W}} \triangleq \mathbf{w}\mathbf{w}^H \neq \mathbf{w}_{\text{opt}}\mathbf{w}_{\text{opt}}^H$  and  $\mathbf{A} \neq \mathbf{w}\mathbf{w}^H$  [210, 212].

**Table 4.1:** Mean ( $\mu$ ) and standard deviation ( $\sigma$ ) of  $\mathcal{F}_{4,1}$  with  $P_t = 1$ .

$N/K$	<i>SSK-SDR</i>		<i>SSK-CR</i>		<i>SSK-MMD</i>		<i>SSK</i>	
	$\mu$	$\sigma$	$\mu$	$\sigma$	$\mu$	$\sigma$	$\mu$	$\sigma$
2/1	1	0	1.27	0.39	1	0	6.35	21.1
4/2	1.4	0.37	1.96	0.55	1.08	0.09	4.66	9.8
4/3	1.31	0.32	1.8	0.43	1.07	0.08	3.03	2.61

An accurate characterization of the impact of the above degradation should rely on contrasting the resultant value of the objective function, namely the MED attained or the optimal transmission power, obtained by the optimization problems  $\mathcal{P}_{4,1}$ ,  $\mathcal{P}_{4,2}$  and their relaxed versions  $\mathcal{P}'_{4,1}$ ,  $\mathcal{P}'_{4,2}$ . This characterization is, however, impractical due to the computational hardness of deriving the optimal solution to the original problems  $\mathcal{P}_{4,1}$  and  $\mathcal{P}_{4,2}$  [210, 212]. Alternatively, the impact of relaxation can be characterized by exploiting that the value,  $f'^*$ , of the objective function delivered by SDR provides a useful bound to the optimal problem [212]. Therefore, a relevant figure of merit  $\mathcal{F}$  can be defined as [212]

$$\mathcal{F}_{\{4,1,4,2\}} = \frac{f'_{\{4,1,4,2\}}}{f_{\{4,1,4,2\}}}, \quad (4.18)$$

where  $f'_{\{4,1,4,2\}}$  denotes the specific value of the objective function in  $\mathcal{P}'_{\{4,1,4,2\}}$ , when the solution directly retrieved by the solver  $\mathbf{A}$  is employed, while  $f_{\{4,1,4,2\}}$  corresponds to the particular value of the objective function obtained after applying (4.16) or (4.17), i.e. by employing  $\widetilde{\mathbf{W}} \triangleq \mathbf{w}\mathbf{w}^H$ . In the above expressions, the subscripts refer to the optimization problem considered, i.e.,  $\mathcal{P}_{4,1}$  or  $\mathcal{P}_{4,2}$ . At this point it should be clarified that the solutions retrieved by the solver  $\mathbf{A}$  are different from those obtained after randomization  $\widetilde{\mathbf{W}}$  when  $\text{rank}(\mathbf{A}) \neq 1$ . The figure of merit  $\mathcal{F}$  in (4.18) can also be generalized both to SSK and to CR-aided SSK (SSK-CR) [183], as well as to SSK maximum minimum distance (SSK-MMD) [209] to determine the solution's proximity to the optimal one.

Table 4.1 characterizes both the expectation and the standard deviation of  $\mathcal{F}_{4,1}$ , explicitly quantifying the degradation of the solutions provided by the schemes considered in this work. In this particular case,  $f'_{4,1}$  and  $f_{4,1}$  correspond to the MED obtained by employing  $\mathbf{A}$  and  $\widetilde{\mathbf{W}}$  respectively. Note that  $\mathcal{F}_{4,1} \geq 1$ , since the MED bound  $f'_{4,1}$

obtained by the solver is always larger than or equal to the MED  $f_{4.1}$  attained after randomization.  $D_s = 20$  candidate scaling vectors are considered for SSK-CR [183, 209]. Remarkably, the results of Table 4.1 show that both the proposed semidefinite relaxation (SSK-SDR) and SSK-MMD always achieve the optimal solution for  $N = 2$ , which is a consequence of the Shapiro-Barvinok-Pataki bound [184]. It can also be observed that the proposed SSK-SDR pre-scaling is capable of reducing both the expectation and the standard deviation of the figure of merit  $\mathcal{F}$ , when compared to conventional SSK and SSK-CR. In other words, the solutions retrieved by the proposed SSK-SDR are closer to the solution of the optimal problem  $\mathcal{P}_{4.1}$ . Indeed, the results of Table 4.1 indicate that the benefits offered by the proposed SDR-based technique become more pronounced for reduced system dimensions. Simultaneously, it can be seen that the SSK-MMD algorithm, which was published throughout the development of this work [209], is capable of providing better solutions than the proposed SSK-SDR scheme. Nonetheless, in the following it is shown that the closer proximity of the SSK-MMD solutions to the optimal ones is achieved at the expense of a substantial increase in their computational complexity, and that the performance differences remain modest for the small scale antenna systems considered in this chapter.

#### 4.4 Robust Design: Worst-Case Robustness to Imperfect CSI

The acquisition of perfect CSI is generally infeasible due to the presence of noise or finite quantization [215], an aspect not considered in the pre-scaling designs developed in [178–180, 183] and Sec. 4.3. As a consequence, the performance of transmit pre-scaling (TPS) techniques may be dramatically affected, since the actual received constellation symbols will be different from the ones estimated at the transmitter. For this reason, this section conceives robust designs to guarantee the target performance of the system under imperfect CSI conditions. In particular, the design of schemes based on preserving the required performance for the worst case of a bounded CSI error are presented. This illustrative criterion has been selected due to the practicality of considering a given CSI

acquisition error, above which the system's performance is no longer guaranteed [214].

Clearly, following (4.10) and (4.11), the non-availability of perfect CSI should impact the definition of the constraint matrices  $\mathbf{E}_{(k,m)}$  in (4.12) in order to meet the performance target at the receiver. To account for this, the principles behind robust beamforming designs can be exploited to ensure that the target performance of the system is preserved [214]. In particular, the constraint matrices of the robust pre-scaling design can be expressed as [216]

$$\bar{\mathbf{E}}_{(k,m)} = \sum_{i=1}^K \left( \tilde{\mathbf{E}}_{(k,m)}^{(i)} + \mathbf{\Delta}_{(k,m)}^{(i)} \right) = \tilde{\mathbf{E}}_{(k,m)} + \mathbf{\Delta}_{(k,m)}, \quad (4.19)$$

where the CSI uncertainty per receive antenna is modeled via an error matrix  $\mathbf{\Delta}_{(k,m)}^{(i)}$  with a bounded Frobenius norm  $\|\mathbf{\Delta}_{(k,m)}^{(i)}\|_{\text{F}} \leq \epsilon_{(k,m)}^{(i)}$ . For ease of notation and without loss of generality, in the following  $\mathbf{\Delta}_{(k,m)} \triangleq \sum_{i=1}^K \mathbf{\Delta}_{(k,m)}^{(i)}$  and  $\|\mathbf{\Delta}_{(k,m)}\|_{\text{F}} \leq \epsilon_{(k,m)}$ . The constant that upper-bounds the Frobenius norm of the error  $\epsilon_{(k,m)}$  establishes the target performance depending on the accuracy of the available CSI. Moreover,  $\tilde{\mathbf{E}}_{(k,m)}^{(i)}$  corresponds to the constraint matrix for the  $i$ -th receive antenna and, similarly to (4.10)–(4.11), it is given by

$$\tilde{\mathbf{E}}_{(k,m)}^{(i)} = \tilde{\mathbf{e}}_{(k,m)}^{(i)} \left( \tilde{\mathbf{e}}_{(k,m)}^{(i)} \right)^{\text{H}}, \quad (4.20)$$

where  $\tilde{\mathbf{e}}_{(k,m)}^{(i)}$  can be expressed as

$$\tilde{\mathbf{e}}_{(k,m)}^{(i)} = \left[ 0, \dots, \tilde{h}_{(k,i)}, \dots, -\tilde{h}_{(m,i)}, \dots, 0 \right]^{\text{T}}. \quad (4.21)$$

At this point it is noted that the sparse structure of  $\tilde{\mathbf{E}}_{(k,m)}^{(i)}$  must be incorporated into the definition of the error constraint matrix  $\mathbf{\Delta}_{(k,m)}$ . Intuitively, this is because the CSI estimation errors can only affect the non-zero entries of the constraint matrix  $\tilde{\mathbf{E}}_{(k,m)}^{(i)}$ . To account for this,  $\mathcal{C}_{(k,m)}$  is defined as

$$\mathcal{C}_{(k,m)} = \left\{ \mathbf{C} \in \mathbb{C}^{N \times N} \mid c_{r,c} = 0 \ \forall \ ((r \neq k, m) \wedge (c \neq k, m)) \right\}. \quad (4.22)$$

Here,  $\mathcal{C}_{(k,m)}$  represents the set of sparse matrices with non-zero entries determined by  $k$

and  $m$ . In the above expression,  $c_{r,c}$  denotes the  $(r,c)$ -th entry of the matrix  $\mathbf{C}$  and  $\wedge$  represents the logical function “and”. Clearly,  $\tilde{\mathbf{E}}_{(k,m)} \in \mathcal{C}_{(k,m)}$  and  $\mathbf{\Delta}_{(k,m)} \in \mathcal{C}_{(k,m)}$ . The following sections illustrate the procedures for obtaining robust convex formulations of the relevant problems considered in this work.

#### 4.4.1 MED Maximization

Following a procedure similar to the one employed for deriving  $\mathcal{P}'_{4.1}$ , the NP-hard robust pre-scaling optimization problem that maximizes the MED at reception subject to a total power constraint can be expressed as

$$\begin{aligned}
 \tilde{\mathcal{P}}_{4.1} : \quad & \underset{\mathbf{A}}{\text{maximize}} \quad d \\
 & \text{subject to} \quad \min_{\|\mathbf{\Delta}_{(k,m)}\|_F \leq \epsilon_{(k,m)}} \left\{ \text{Tr} \left( \left( \tilde{\mathbf{E}}_{(k,m)} + \mathbf{\Delta}_{(k,m)} \right) \mathbf{A} \right) \right\} \geq d, \\
 & \quad \tilde{\mathbf{E}}_{(k,m)} + \mathbf{\Delta}_{(k,m)} \succeq 0, \quad \mathbf{\Delta}_{(k,m)} \in \mathcal{C}_{(k,m)}, \forall k \neq m. \\
 & \quad \text{Tr}(\mathbf{A}) \leq (P_t N), \\
 & \quad \mathbf{A} \succeq 0, \quad \text{rank}(\mathbf{A}) = 1.
 \end{aligned} \tag{4.23}$$

Note that the constraint matrices of the optimization problem (4.23),  $\tilde{\mathbf{E}}_{(k,m)} + \mathbf{\Delta}_{(k,m)}$ , differ from those of the conventional problem defined in (4.13). Specifically, the constraints consider the worst-case scenario in which the Euclidean distance of the received symbols is minimized for the matrices  $\mathbf{\Delta}_{(k,m)} \in \mathcal{C}_{(k,m)}$  satisfying  $\|\mathbf{\Delta}_{(k,m)}\|_F \leq \epsilon_{(k,m)}$ . Additionally, the fact that the matrices  $\tilde{\mathbf{E}}_{(k,m)} + \mathbf{\Delta}_{(k,m)}$  are positive semidefinite, which follows from their definition in (4.19)–(4.21), has also been considered [214, 216]. Since finding a robust optimization problem that can be efficiently solved by applying standard convex optimization techniques is a key objective of this chapter, the following theorem provides a SDR version of  $\tilde{\mathcal{P}}_{4.1}$ .

**Theorem 4.4.1** Let  $\mathbf{A} \triangleq \mathbf{w}\mathbf{w}^H$ , where  $\mathbf{w}$  represents the pre-scaling vectors to be optimized. Moreover, let  $\tilde{\mathbf{E}}_{(k,m)}$ , be as defined in (4.19)–(4.21), while  $\epsilon_{(k,m)}$  is a predeter-

mined constant. Then, a SDR version of  $\tilde{\mathcal{P}}_{4.1}$  in (4.23) is given by

$$\begin{aligned}
 \tilde{\mathcal{P}}'_{4.1} : & \underset{\mathbf{A}, \mathbf{B}_{(k,m)}}{\text{maximize}} \quad d \\
 \text{s.t.} & \quad -\epsilon_{(k,m)} \|\mathbf{B}_{(k,m)} - \mathbf{A}\|_{\text{F}} - \text{Tr} \left( \tilde{\mathbf{E}}_{(k,m)} (\mathbf{B}_{(k,m)} - \mathbf{A}) \right) \geq d, \\
 & \quad \mathbf{B}_{(k,m)} \succeq 0, \mathbf{B}_{(k,m)} \in \mathcal{B}_{(k,m)}, \forall k \neq m \\
 & \quad \mathbf{A} \succeq 0, \text{Tr}(\mathbf{A}) \leq (P_{\text{t}}N),
 \end{aligned} \tag{4.24}$$

where the optimization variables  $\mathbf{B}_{(k,m)}, \forall k \neq m \in \{1, \dots, N\}$ , are the Lagrangian multipliers of the inner optimization problem contained in  $\tilde{\mathcal{P}}_{4.1}$ , while  $\mathcal{B}_{(k,m)}$  is the set of matrices satisfying  $\mathcal{B}_{(k,m)} = \left\{ \mathbf{B}_{(k,m)} \in \mathbb{C}^{N \times N} \mid \mathbf{B}_{(k,m),\{r,c\}} = \mathbf{A}_{\{r,c\}} \text{ if } \tilde{\mathbf{E}}_{(k,m),\{r,c\}} = 0 \right\}$ . Here,  $(\cdot)_{\{r,c\}}$ , represents the  $r, c$ -th entry of a matrix. Finally, the non-convex constraint of  $\text{rank}(\mathbf{A}) = 1$  has been dropped.

**Proof of Theorem 4.4.1** The proof can be found in Appendix A. □

The robust optimization problem  $\tilde{\mathcal{P}}'_{4.1}$  can be solved with the aid of standard convex techniques and it facilitates the design of pre-scaling vectors robust to imperfect CSI conditions, as shown in Sec. 4.5.

#### 4.4.2 Power Minimization

A similar procedure to the one detailed in Sec. 4.4.1 can be followed to obtain a relaxed robust version of the optimization problem that minimizes the transmission power subject to satisfying the performance thresholds  $\mathcal{P}_{4.2}$ , which can be expressed as

$$\begin{aligned}
 \tilde{\mathcal{P}}'_{4.2} : & \underset{\mathbf{A}, \mathbf{B}_{(k,m)}}{\text{minimize}} \quad \text{Tr}(\mathbf{A}) \\
 \text{s.t.} & \quad -\epsilon_{(k,m)} \|\mathbf{B}_{(k,m)} - \mathbf{A}\|_{\text{F}} - \text{Tr} \left( \tilde{\mathbf{E}}_{(k,m)} (\mathbf{B}_{(k,m)} - \mathbf{A}) \right) \geq d, \\
 & \quad \mathbf{B}_{(k,m)} \succeq 0, \mathbf{B}_{(k,m)} \in \mathcal{B}_{(k,m)}, \forall k \neq m \\
 & \quad \mathbf{A} \succeq 0.
 \end{aligned} \tag{4.25}$$

At this point it should be remarked that the original application of SDR to SSK developed in Sec. 4.3 facilitates the design of TPS schemes exhibiting robustness against imperfect CSI. Also note that with respect to the existing robust designs found in the literature, such as the downlink beamforming schemes of [214,217], the constraint matrices  $\tilde{\mathbf{E}}_{(k,m)}$  of the proposed designs (4.24) and (4.25) depend on the actual channel realization and not on its second-order statistics [214]. This is because the instantaneous MED at the receiver is used as a performance metric instead of the conventional average SNR, an approach that is particularly suited to SSK transmission that substantially modifies the definition of the relevant constraint matrices [178–180,214,217].

## 4.5 Results and Discussion

To evaluate the benefits of the proposed technique, this section presents numerical results based on Monte Carlo simulations of conventional SSK without scaling (termed as SSK in the figures), SSK using the constellation randomization of [183] with  $D_s = 20$  candidate scaling vectors, termed as SSK-CR, the iterative algorithms developed in [184], and the proposed SSK using SDR optimization, namely SSK-SDR. In this section the nomenclature of [184] is maintained for coherence, i.e. the algorithm employed to solve  $\mathcal{P}_{4.1}$  is referred to as the SSK maximum minimum distance (SSK-MMD) regime, whereas  $\mathcal{P}_{4.2}$  is solved via the so-called SSK guaranteed Euclidean distance (SSK-GED) algorithm. Throughout this section the convergence of the above SSK-MMD and SSK-GED algorithms is deemed to be achieved when the Euclidean norm of the error between the input and the output of the convex optimization problem performed every iteration satisfies  $\bar{\xi} \leq 10^{-3}$ . The performance of the systems constructed with the aid of the non-relaxed optimization problems is not shown due to their intractable computational complexity. The channel impulse response follows  $\mathbf{H} \in \mathbb{C}^{K \times N} \sim \mathcal{CN}(\mathbf{0}, \mathbf{I}_K \otimes \mathbf{I}_N)$  and is assumed to be perfectly known at the transmitter and the receiver unless otherwise stated. Without loss of generality, it is assumed that the average transmit power is restricted to  $P_t \leq 1$  for the conventional techniques and for the case of problem  $\mathcal{P}'_{4.1}$  of the proposed scheme, unless stated otherwise. Small-scale MIMO systems are considered,

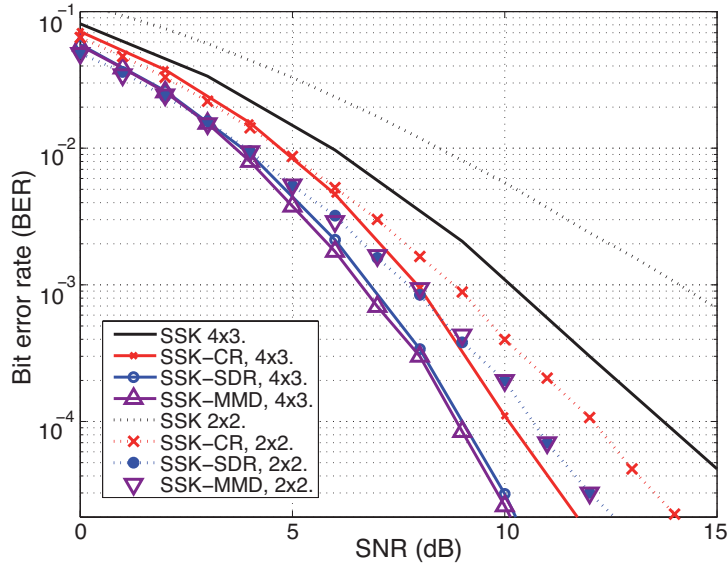


**Figure 4.3:** BER vs. SNR for both  $(2 \times 2)$  and  $(4 \times 3)$  MIMO systems.

since the benefits of the proposed technique are maximized for this regime as discussed in Sec. 4.3.4.

First, the BER performance upon increasing the transmit  $\text{SNR} = 1/\sigma^2$  is characterized for both  $(2 \times 2)$  and  $(4 \times 3)$ -element MIMO systems in Fig. 4.3. In this case, the comparison involves the MED maximization problem  $\mathcal{P}'_{4.1}$  upon varying the noise power. It can be seen in Fig. 4.3 that while SSK-CR improves the conventional SSK transmission by the TPS operation, the proposed scheme further enhances the attainable performance by the proposed optimization. In these particular cases, the performance of both SSK-MMD and SSK-SDR are almost indistinguishable. However, note that this is achieved at the cost of a significantly higher computational complexity for SSK-MMD, since multiple convex optimization problems must be solved, before convergence is achieved. This is explicitly shown in Table 4.2, where both the average and the standard deviation of the computational time required to obtain the transmit pre-scaling factors are portrayed for  $10^4$  channel realizations. These results indicate that SSK-SDR is capable of offering a similar performance at a computational time up to 20 times shorter than that required by the SSK-MMD algorithm [184]. Indeed, it can be observed that the proposed SSK-SDR scheme offers a significantly smaller variation in the computational time required for solving the optimization problems under different

**Table 4.2:** Average ( $\mu$ ) and standard deviation ( $\sigma$ ) of the computational time employed to compute the transmit pre-scaling factors with optimization-based algorithms.

$(N \times K)$	<i>SSK-MMD</i>		<i>SSK-SDR</i>	
	$\mu$	$\sigma$	$\mu$	$\sigma$
$(4 \times 2)$	3.85 sec.	3.9 sec.	0.24 sec.	0.025 sec.
$(4 \times 3)$	4.67 sec.	3.74 sec.	0.23 sec.	0.022 sec.

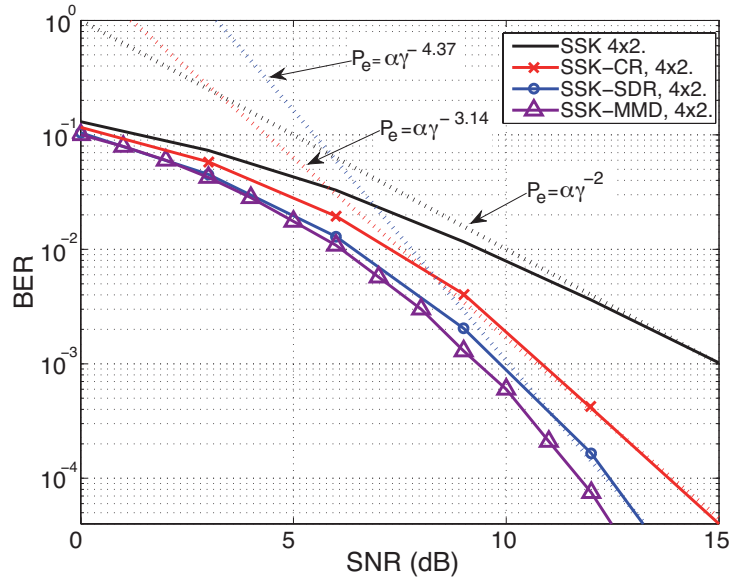


**Figure 4.4:** BER vs. SNR for a  $(4 \times 2)$  MIMO system.

channel conditions.

Similar trends can be observed in Fig. 4.4, where the  $(4 \times 2)$ -element MIMO system is examined. It can be seen that the SSK-MMD algorithm of [184] only offers a slight improvement over the proposed SSK-SDR in the scenario considered. This entails that the proposed SSK-SDR strategy provides the best performance-complexity trade-off, since the SSK-MMD algorithm is significantly more complex as detailed in Table 4.2. Additionally, Fig. 4.4 portrays the high diversity order provided by SSK-SDR thanks to the enhanced MED. This is evidenced by the higher slope of the BER curve in line with the definition of the diversity gain [30].

Fig. 4.5 shows the cumulative distribution function (CDF) of the equivalent transmit

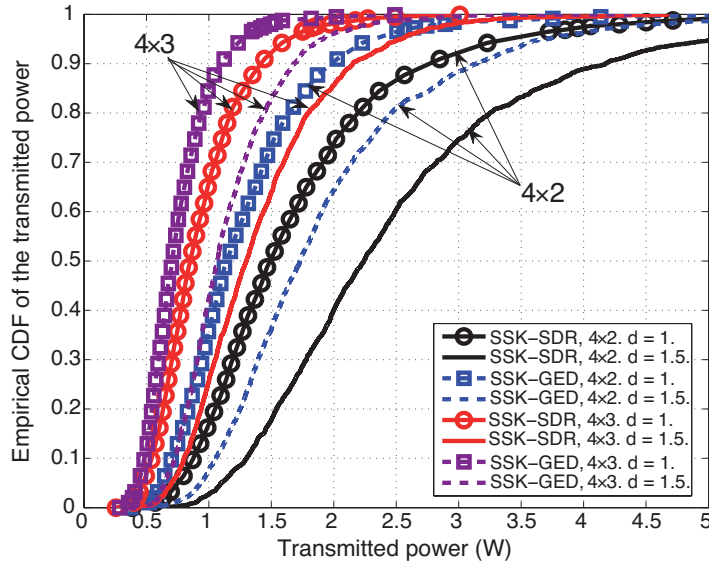


**Figure 4.5:** Empirical CDF of the transmission power for  $(4 \times 2)$  and  $(4 \times 3)$  MIMO systems.

power<sup>1</sup> for problem  $\mathcal{P}'_{4,2}$  and SSK-GED in the  $(4 \times 2)$  and  $(4 \times 3)$ -element MIMO systems, for different values of the MED thresholds  $d$ . It can be observed that the  $(4 \times 3)$ -element MIMO system has a smaller spread in the transmit power values necessitated for guaranteeing the required MED threshold, and this spread tends to increase upon increasing the MED thresholds  $d$ . It is also shown that SSK-GED generally requires less transmission power than SSK-SDR to satisfy a given MED threshold, as further analyzed in the following. It should be noted that the transmit power spread results from the fact that the MED threshold has to be satisfied under different channel conditions, which imposes a transmit power variation.

To prevent repetition, in the following the focus is placed on the power minimization problem for clarity, although it is clear that the MED maximization problem requires a similar solution [214]. In this section, the estimated channel between the transmit antennas and the  $k$ -th receive antenna with imperfect CSI is modeled as [207, 215]

$$\tilde{\mathbf{h}}_k = \sqrt{1 - \tau^2} \mathbf{h}_k + \tau \mathbf{q}_k, \quad (4.26)$$

<sup>1</sup>Without loss of generality, we employ the equivalent transmit power defined as  $\text{Tr}(\mathbf{w}\mathbf{w}^H)$  for the results shown in the sequel. Note that the actual average transmit power is given by  $P_t = \text{Tr}(\mathbf{w}\mathbf{w}^H)/N$ , since only one antenna is simultaneously active for transmission.

where  $\tilde{\mathbf{h}}_k \in \mathbb{C}^{N \times 1}$  denotes the imperfect CSI estimate available at the transmitter and  $\mathbf{q}_k \sim \mathcal{CN}(\mathbf{0}, \mathbf{I}_N)^2$ . Here,  $\tau$  is a parameter that determines the quality of the instantaneous acquired CSI ranging from perfect CSI ( $\tau = 0$ ) to the unavailability of the instantaneous CSI ( $\tau = 1$ ). Here,  $\epsilon_{(k,m)} = \epsilon = 2\tau = 0.02, \forall k \neq m$  for the robust optimization problem  $\tilde{\mathcal{P}}'_{4,2}$ . The value of  $\epsilon$  has been fixed similarly to [216] for illustrative purposes and without loss of generality. For the cases of SSK and SSK-CR, the scaling vector is multiplied by an appropriate factor in order to increase the separation between the estimated received constellation symbols and to guarantee that the MED constraint is satisfied with the aid of the available CSI estimate (not the true channel). However, note that the actual received symbols are different from the ones estimated at the transmitter due to the effect of the imperfect CSI. As a result, achieving the true MED attained by the non-robust designs in the presence of imperfect CSI cannot be guaranteed. By contrast, the robust schemes are able to guarantee that the MED thresholds are satisfied, as detailed in Sec. 4.4. For practical reasons and without loss of generality, the transmitter has a maximum transmission power of 20 Watts for a given channel realization and the solutions having higher power requirements are treated as infeasible. This constraint is realistic due to the technical limitations of the power amplifiers and it only takes effect for certain badly conditioned channels, since usually the transmission power is considerably lower, as shown in Fig. 4.6.

Fig. 4.6 illustrates the average transmit power in Watts required for increasing MED thresholds using SSK, SSK-CR, SSK-GED and the power minimization problems  $\mathcal{P}'_{4,2}$  and  $\tilde{\mathcal{P}}'_{4,2}$  for  $(4 \times 2)$  and  $(4 \times 3)$ -element MIMO systems. The results of Fig. 4.6 show that the proposed strategies are able to outperform SSK-CR while, simultaneously, SSK-GED is able to provide better solutions in the considered scenarios. Note that the SSK-GED approach is, however, significantly more complex than the proposed SSK-SDR. The enhancements offered by the pre-scaling techniques are a direct consequence of the solutions being closer to the optimal ones, as detailed in Sec. 4.3.4. In this case, the transmission power required to satisfy a given MED threshold can be reduced when

---

<sup>2</sup>It should be noted that the worst-case robust design proposed in Sec. 4.4 is particularly suitable for imperfect CSI models with a bounded error norm. Instead, this section considers a norm-unbounded stochastic error model, since this kind of imperfect CSI characterization is more common and the benefits of the proposed robust design can also be shown.

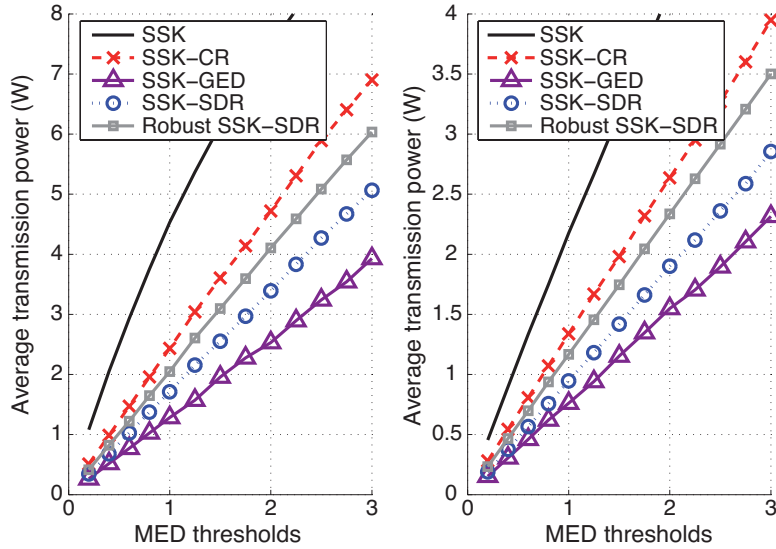


**Figure 4.6:** Average transmission power vs MED thresholds for (a)  $(4 \times 2)$  and (b)  $(4 \times 3)$  MIMO systems.

compared with SSK-CR. Specifically, transmit power savings as significant as 2 Watts for  $d = 3$  in a  $(4 \times 2)$  system w.r.t. SSK-CR can be achieved, while a similar trend can also be observed in the  $(4 \times 3)$  scenario. It can be therefore concluded that the benefits of the pre-scaling designs become more pronounced for large MED thresholds. Moreover, similarly to [216, 218], the results of this figure show the increase in the transmit power necessary to compensate for the CSI uncertainty at the transmitter. In this particular case it can be seen that, in spite of the required transmit power increase, the insightful design offered by the robust SSK-SDR design philosophy still improves upon SSK-CR, where the set of candidate scaling factors is randomly designed. By doing this, the robust SSK-SDR design guarantees that the performance thresholds specified at the receiver are satisfied, while this is not achieved by SSK, SSK-CR, SSK-GED, SSK-SDR and other TPS approaches in the literature [178–180, 183, 184].

The above observation can be explicitly seen in Fig. 4.7(a) and (b), where the probability of feasibility is represented for increasing values of the MED thresholds for the  $(4 \times 2)$  and  $(4 \times 3)$  MIMO systems, respectively. The feasibility probability is defined as  $P(\text{MED} \geq d)$ , provided that the average transmission power required does not exceed 20 Watts for a given channel realization. The remaining cases are considered as infeasible solutions. The same simulation parameters have been used to obtain the results of this

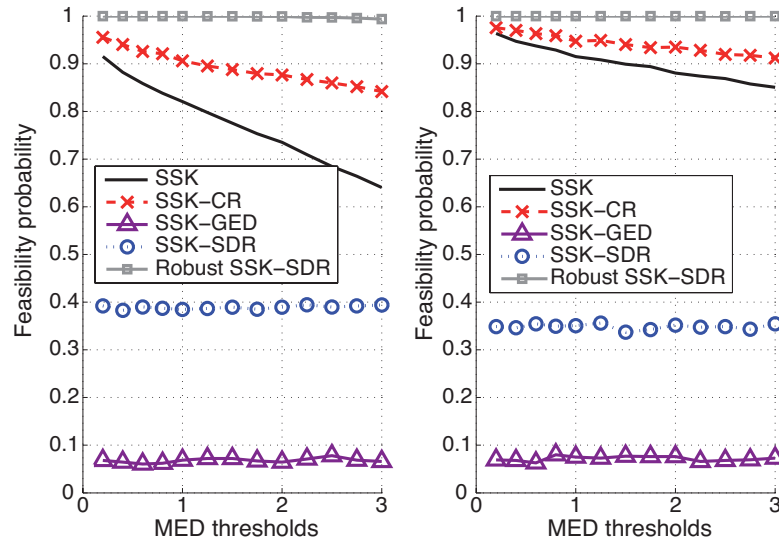


**Figure 4.7:** Probability of feasibility vs. MED thresholds for (a)  $(4 \times 2)$  and (b)  $(4 \times 3)$  MIMO systems.

figure as in Fig. 4.6. By analyzing the results of Fig. 4.7 it can be concluded that the proposed robust strategy offers the highest reliability, since the probability of outage is reduced w.r.t. the non-robust alternatives that do not account for the presence of CSI errors.

A more refined picture of the systems' behaviour considered in this chapter under imperfect CSI conditions is shown in Fig. 4.8, which represents the empirical probability density function (PDF) of the MED at the receiver in a  $(4 \times 2)$  MIMO system in the presence of imperfect CSI by considering the same channel model and conditions as those used in Fig. 4.6. The target MED at the receiver has been set to  $d = 1$  and it is denoted by the red bar in the figures. Note that the red bars are only shown for illustrative purposes and do not represent the PDF over that range. The results of this figure show that the proposed robust SSK-SDR design is capable of guaranteeing the MED thresholds to be exceeded at the receiver. This is in contrast with the pre-scaling designs introduced in [178–180, 183, 184], where achieving the system performance required cannot be guaranteed, as depicted in Fig. 4.8(a), (b), (c) and (d) for the conventional SSK, SSK-CR, SSK-GED, SSK-SDR and designs, respectively. Accordingly, the proposed robust technique enables the application of TPS with MED guarantees in the case of imperfect CSI, which cannot be achieved by the previous approaches. Moreover, the

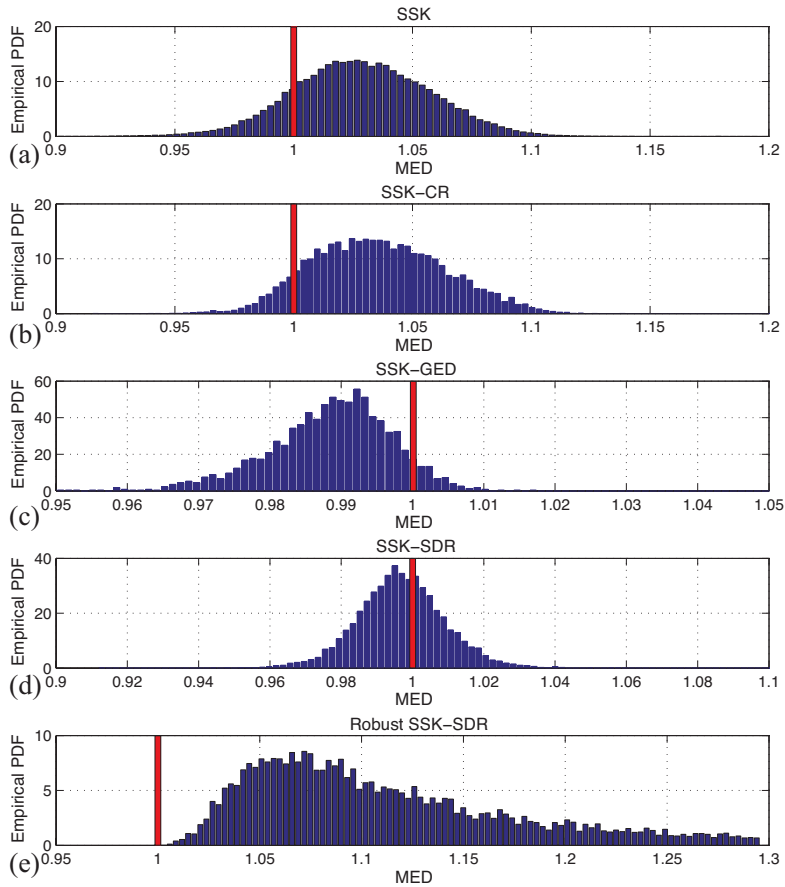


**Figure 4.8:** Empirical PDF of the MED of a  $(4 \times 2)$  MIMO system under imperfect CSI conditions with  $\tau = 0.01$  and  $d = 1$  for (a) SSK, (b) SSK-CR, (c) SSK-GED, (d) SSK-SDR, and (e) robust SSK-SDR.

benefits of the robust design can be clearly seen upon comparing Fig. 4.8(b) and (d). In particular, it can be seen that the robust technique requires less transmission power than SSK-CR, as shown in Fig. 4.6 and, simultaneously, the MEDs at the receiver are significantly enhanced. This improvement comes at the cost of an increased variance in the MED at the receiver w.r.t. the SSK-GED and SSK-SDR designs characterized in 4.8(c) and (d), which, however, have a larger outage probability due to ignoring the impact of inaccurate CSI [218].

## 4.6 Conclusions

This chapter has presented a TPS vector design based on convex optimization for SSK systems. A pair of distinct optimization problems have been introduced, namely

MED maximization under transmit power budget constraints and transmit power minimization under a MED constraint. By invoking SDR, a close-to-optimal TPS has been designed for improving the power efficiency of small scale SSK systems with respect to existing approaches by offering an enhanced performance for a given transmit power budget, or equivalently, a reduced transmit power for achieving a given MED. Indeed, power savings in the order of several Watts have been demonstrated for the systems with stringent performance requirements considered in this chapter. Moreover, a robust design has been developed that is capable of guaranteeing the received MED target in the presence of CSI errors at the transmitter, hence facilitating the use of TPS strategies, when realistic imperfect CSI is available.

*Critique:* It should be noted the scalability of the proposed scheme to spatial modulation with additional signal-constellation points or large-scale antenna systems is limited, since increasing the number of constraints in the optimization problems harms the solutions attained by the relaxed problems [184, 210]. Moreover, while the proposed scheme provides substantial performance improvements over conventional SSK transmission, CSI at the transmitter is required and the peak-to-average power ratio (PAPR) of the transmission is simultaneously increased. Still, significant power savings are expected due to the much reduced transmission power required as shown in the results of this chapter. In the search for larger performance improvements, the later work [208] suggests that performance could be enhanced by considering directly the BER instead of the more limited MED as an optimization metric. However, slight performance improvements are expected for the small-scale systems considered in this chapter, since the advocated solution is already close-to-optimal. Nevertheless, the consideration of this metric for optimizing the performance in large scale antenna systems is of substantial relevance, as explicitly pointed out in Sec. 9.2.



## Chapter 5

# Compressive Sensing Based Detection for Spatial Modulation in Large Scale Antenna Systems

### 5.1 Introduction

Massive MIMO technologies aim at enhancing the spectral efficiency by incorporating a large number of antennas at the base stations (BSs) [11, 72, 101]. This leads to communication systems in which the use of conventional linear detection and precoding techniques becomes optimal in the large scale antenna limit [11, 72]. However, the increased number of radio frequency (RF) chains have a considerable influence on the energy efficiency, hence severely affecting the attainable benefits from this perspective [61]. To alleviate this impact, spatial modulation (SM) poses as a reduced RF-complexity scheme by exploiting the transmit antenna indices as an additional source of information [19, 157, 167].

Up to this point, the literature of SM has mostly focused on developing strategies for point-to-point links [19, 157, 167, 169, 180, 183]. For instance, several low-complexity detectors that approach the performance of the optimal maximum likelihood (ML) estimation have been proposed [170–172, 219]. In this context, the use of a normalized

compressive sensing (CS) detection algorithm as a low-complexity solution for space shift keying (SSK) and generalized space shift keying (GSSK) peer-to-peer (P2P) systems was considered in [172, 173]. In this work, the authors apply a normalization to the channel matrix before the application of the greedy compressive detector to enhance performance. However, the authors restrict its application to single-user SSK and GSSK systems, which constrains its use to low data rate transmission.

More recently, the use of SM has been extended to the multiple access channel (MAC) as a way of enhancing the achievable rates of the conventional single-antenna devices considered in this setting [159, 185, 186]. A number of related works have concentrated on the design of detection schemes to account for the particularities of the large scale MAC. The employment of a message passing detection (MPD) algorithm is proposed in [187, 188] for the MAC with a large number of antennas at the BS. This algorithm offers a performance improvement with respect to conventional MIMO systems with identical attainable spectral efficiency. However, both the storage requirements and the total number of operations are conditioned by the large number of messages transmitted between all the nodes, which must be updated in every iteration [220]. A more complex local search detection algorithm based on finding the local optimum in terms of the maximum likelihood cost is also introduced in [187, 188]. An iterative detector for large scale MAC is developed in [189]. Here, the authors decouple the antenna and symbol estimation processes to reduce the global detection complexity. The algorithm introduced in [190] accounts for the sparsity and signal prior probability of SM transmission in the MAC. In this work, the use of stage-wised linear detection is discarded due to its high complexity and the authors propose a generalized approximate message passing detector. A related approach has been developed in [191] to deal with quantized measurements and spatial correlation. Still, the above algorithms do not fully account for the particularities of iterative detection processes and the complexity benefits that can be obtained by leveraging the principles behind CS algorithms.

This chapter introduces an energy-efficient detector based on CS for the MAC of SM systems with large scale BSs. In particular, it is shown that the signal structure of SM in the MAC can be exploited to provide additional information and improve the per-

formance of CS algorithms [221, 222]. Moreover, the use of a large number of antennas in the MAC eliminate the error floor that greedy CS techniques show in noisy scenarios for practical uncoded bit error rates (BERs) [172]. Indeed, contrary to the common CS knowledge, in this chapter it is demonstrated by means of a thorough complexity analysis that the trade-off between complexity and performance is especially favourable for CS-based detection schemes in scenarios with a large number of receive antennas. Furthermore, in this chapter the energy efficiency and signal processing complexity of the proposed strategy is compared with the conventional zero forcing (ZF) and minimum mean square error (MMSE) linear detectors. In particular, it is shown that the improvements offered by the proposed technique allow enhancing the energy efficiency achieved by these detectors with comparable complexity. In fact, the detailed complexity analysis provides valuable insights regarding the algorithms that must be employed to solve the ZF and MMSE detection problems in large scale SM-MIMO systems.

## 5.2 Preliminaries

### 5.2.1 System Model of the Multiple Access Channel (MAC)

The model considered throughout this chapter characterizes the MAC of a multi-user MIMO system comprised of  $\bar{K}$  mobile stations (MSs) with  $n_t$  antennas each, and a single BS with  $N$  receive antennas as illustrated in Fig. 2.12. The total number of antennas allocated at the MSs is denoted as  $K = \bar{K} \times n_t$ . Similarly to (2.11), the behavior of the multiple access system is described in this chapter by

$$\mathbf{y} = \mathbf{G}\mathbf{x} + \bar{\mathbf{n}}, \quad (5.1)$$

where the relevant variables are identical to those defined in Sec. 2.2.1. In this chapter,  $\bar{\mathbf{n}} \in \mathbb{C}^{N \times 1} \sim \mathcal{CN}(\mathbf{0}, \sigma^2 \mathbf{I}_N)$  and  $\mathbf{G} \in \mathbb{C}^{N \times K} \sim \mathcal{CN}(\mathbf{0}, \mathbf{I}_N \otimes \mathbf{I}_K)$ , unless stated otherwise. As typically assumed in the SM detection literature, the BS is expected to have a perfect knowledge of the communication channel  $\mathbf{G}$  [11, 19].

Throughout this chapter it is assumed that the data symbols transmitted by the

active antennas belong to a normalized  $Q$ -QAM constellation satisfying  $\mathbb{E}\{E_s\} = 1$ , where  $E_s$  refers to the symbol energy. Based on this, the total average signal-to-noise ratio (SNR) of the MAC can be expressed as

$$\text{SNR} = \frac{\mathbb{E}\{\mathbf{x}^H \mathbf{x}\}}{\sigma^2} = \frac{S \cdot \mathbb{E}\{E_s\}}{\sigma^2}, \quad (5.2)$$

where  $\bar{K} \leq S \leq K$  is the total number of antennas simultaneously active amongst the MSs.

### 5.2.2 Multiple Access Spatial Modulation

This section describes the operation of generalized SM transmission with a single RF chain, since particularization to conventional SM is straightforward by letting  $S = \bar{K}$  and forcing the number of antennas per user to be a power of two [167,223]. Throughout this chapter the term SM is employed when referring to both conventional and generalized SM for ease of description. In SM, each transmitter conveys the same constellation symbol by activating a given number of antennas  $n_a$  according to the input bit sequence [19,167,223]. Without loss of generality, in the following it is assumed that the users activate the same number of antennas, i.e.  $S = n_a \times \bar{K}$ . Mathematically, the transmit signal  $\mathbf{x}_{\bar{k}} \in \mathbb{C}^{n_t \times 1}$  of the  $\bar{k}$ -th SM transmitter can be expressed as [167]

$$\mathbf{x}_{\bar{k}} = \left[ 0 \cdots s_{l_1}^q \cdots s_{l_k}^q \cdots 0 \right]^T, \quad (5.3)$$

where  $l_k \in \{1, \dots, n_t\}$  denotes the active antenna index and  $s^q$  represents the  $q$ -th symbol of the transmit constellation  $\mathcal{Q}$ , in coherence with the notation introduced in Sec. 2.3.2. The number of bits that can be encoded on the antenna indices is  $b \triangleq \left\lceil \log_2 \binom{n_t}{n_a} \right\rceil$  [167,223]. Therefore, the number of possible antenna combinations at the transmitter is given by  $r = 2^b$ . This determines the cardinality of  $\mathcal{A}$ , the set comprised of the possible active antenna groups with  $\mathcal{A}_l$  being the  $l$ -th element. Note that there may be invalid antenna groups to preserve an integer length of the bit stream. The composite transmit vector  $\mathbf{x} \in \mathbb{C}^{K \times 1}$  is obtained by concatenating the transmit signals

as  $\mathbf{x} = [\mathbf{x}_1^T \mathbf{x}_2^T \cdots \mathbf{x}_K^T]^T$ . Note that, while a conventional MIMO transmitter is able to convey  $B_{\text{MIMO}} = n_t \cdot \log_2(Q)$  bits, a single SM transmitter encodes  $B_{\text{SM}} = b + \log_2(Q)$  bits in every channel use.

At the receiver, detection schemes exploit the channel knowledge to determine the active antennas and the conveyed constellation symbols [19]. Among these, the optimum detector follows the ML criterion and its output reads as

$$\hat{\mathbf{x}} = \arg \min_{\tilde{\mathbf{s}}_p} \|\mathbf{y} - \mathbf{G}\tilde{\mathbf{s}}_p\|_2^2. \quad (5.4)$$

Here, the signal  $\tilde{\mathbf{s}}_p \in \mathbb{C}^{K \times 1}$  belongs to the set that includes all the possible transmit signals  $\Gamma$  and  $\|\cdot\|_p$  denotes the  $\ell_p$  norm. The cardinality of  $\Gamma$ ,  $|\Gamma| = (Q \times r)^{\overline{K}}$ , exponential with the number of users  $\overline{K}$ , establishes an upper bound on the complexity of SM detection.

### 5.2.3 Large Scale Antenna Systems (LSAS) and Low-Complexity Detection

The large scale MIMO theory focuses on analyzing the benefits of communication systems with a large number of antennas at the BS [11, 72]. One of the fundamental results in this field states that, provided that  $N \gg K$ , the received signal after linear detection  $\mathbf{g} \in \mathbb{C}^{K \times 1}$  satisfies

$$\mathbf{g} = \overline{\mathbf{F}}(\mathbf{G}\mathbf{x} + \overline{\mathbf{n}}) \xrightarrow[N \rightarrow \infty, K = \text{const.}]{\text{a.s.}} \mathbf{x}, \quad (5.5)$$

where  $\overline{\mathbf{F}} \in \mathbb{C}^{K \times N}$  is a linear detection matrix that for the matched filter (MF), ZF and MMSE detectors reads as [33]

$$\overline{\mathbf{F}}^{\text{MF}} = \mathbf{G}^H, \quad (5.6)$$

$$\overline{\mathbf{F}}^{\text{ZF}} = \mathbf{G}^\dagger = (\mathbf{G}^H \mathbf{G})^{-1} \mathbf{G}^H, \quad (5.7)$$

$$\overline{\mathbf{F}}^{\text{MMSE}} = (\mathbf{G}^H \mathbf{G} + \varsigma \mathbf{I})^{-1} \mathbf{G}^H. \quad (5.8)$$

In the above,  $\varsigma = K/\text{SNR}$  [33]. Let  $\mathbf{g}^{\{u\}}$  be the decision vector corresponding to the  $u$ -th user. The sub-optimal but low-complexity approach of decoupling the estimation of the spatial and amplitude-phase modulated symbols is adopted in the sequel [186, 224]. Specifically, the estimated active antenna indices  $\hat{\mathcal{A}}_l$  and the transmitted constellation symbol  $\hat{q}$  for the  $u$ -th user are obtained from (5.5) as

$$\hat{\mathcal{A}}_l = \arg \max_l \left\| \mathbf{g}_{\mathcal{A}_l}^{\{u\}} \right\|_2, \quad (5.9)$$

$$\hat{q} = \mathcal{D} \left( \mathbf{g}_{\hat{\mathcal{A}}_l}^{\{u\}} \right), \quad (5.10)$$

where  $g_{\{\mathcal{A}_l, \hat{\mathcal{A}}_l\}}^{\{u\}}$  represent the entries of the decision vector of the  $u$ -th user  $\mathbf{g}^{\{u\}}$  determined by the sets  $\mathcal{A}_l$  and  $\hat{\mathcal{A}}_l$  respectively, and  $\mathcal{D}$  denotes the demodulation function.

Note that the necessary increase in the number of transmit antennas when SM is employed degrades the performance of the above-mentioned detectors due to the worse conditioning of the channel matrix. For this reason, this chapter proposes a solution inspired by CS to take advantage of the large scale MIMO benefits. In other words, the following sections concentrate on scenarios where  $N \gg K$  does not necessarily hold but  $N \gg \bar{K}$  brings the massive MIMO effect.

### 5.3 Straightforward Application of CS Algorithms for SM Detection

The main issue with the conventional ZF and MMSE linear detectors when applied to SM and generalized SM detection is that the entire channel matrix  $\mathbf{G} \in \mathbb{C}^{N \times M}$  must be employed for detection even though only  $S$  columns contribute to the acquisition of the amplitude-phase signal information. This can be circumvented by exploiting the sparsity of SM signals to further enhance the performance attained by linear detectors. The signals conveyed by SM are defined as  $S$ -sparse because they only contain  $S \ll K$  non-zero entries equal to the number of antennas simultaneously active  $S$  [172]. This property has been exploited by CS to improve signal estimation from compressive measurements. Specifically, CS capitalizes on signal sparsity to guarantee a reliable signal recovery with

efficient algorithms [225,226]. The CS measurements  $\mathbf{y} \in \mathbb{R}^{N \times 1}$  of a sparse signal  $\mathbf{x}$  can be expressed as [226–228]

$$\mathbf{y} = \mathbf{\Phi}\mathbf{x} + \mathbf{e}, \quad (5.11)$$

where  $\mathbf{x} \in \mathbb{R}^{K \times 1}$  represents the original sparse signal,  $\mathbf{\Phi} \in \mathbb{R}^{N \times K}$  is the measurement matrix, and  $\mathbf{e} \in \mathbb{R}^{N \times 1}$  is a measurement error term. Note that the complex-valued system in (5.1) can be straightforwardly re-expressed to resemble the real-valued one in (5.11) [172]. In this chapter, the similarity between (5.1) and (5.11) is exploited to improve the detection performance of the conventional linear MIMO detectors.

In CS, the restricted isometry property (RIP) determines whether signal recovery guarantees are fulfilled or not for any communication channel  $\mathbf{\Phi} = \mathbf{G}$  [226,227]. For the case of the MIMO channel, the RIP of order  $S$  is satisfied for a channel matrix  $\mathbf{G}$  if, for any  $S$ -sparse signal  $\mathbf{x}$ , the relationships

$$(1 - \delta_S)\|\mathbf{x}\|_2^2 \leq \|\mathbf{G}\mathbf{x}\|_2^2 \leq (1 + \delta_S)\|\mathbf{x}\|_2^2 \quad (5.12)$$

hold for a constant  $\delta_S \in (0, 1)$ . For instance, a matrix comprised of independent and identically distributed Gaussian random variables is known to satisfy  $\delta_S \leq 0.1$  provided that  $N \geq cS \log(K/S)$ , with  $c$  being a fixed constant [227]. Note that this kind of channel communication matrix conventionally arises in rich scattering environments with Rayleigh fading [11].

Once the signal measurements are acquired and contrary to the ML detector given in (5.4), the detection of the SM signals in CS relies on the sparsity of SM transmission to generate an estimate. For the case with  $\delta_{2S} < \sqrt{2} - 1$  [228] (5.4) can be solved in a low-complexity CS-inspired fashion as

$$\begin{aligned} & \text{minimize } \|\mathbf{x}\|_1 \\ & \text{subject to } \|\mathbf{G}\mathbf{x} - \mathbf{y}\|_2 \leq \tilde{\mu}, \end{aligned} \quad (5.13)$$

In the above expression the constant  $\tilde{\mu}$  limits the noise power  $\|\tilde{\mathbf{n}}\|_2 \leq \tilde{\mu}$ . Although the above optimization problem can be solved with well-known convex approaches, these

alternatives are often computationally intensive, so faster techniques that offer a trade-off between performance and complexity such as greedy algorithms are commonly used instead [227].

From the vast variety of CS greedy algorithms, this section selects one of the most efficient schemes to approximate the solution of (5.13): the Compressive Sampling Matching Pursuit (CoSaMP) [229]. The CoSaMP is a low-complexity algorithm that goes through an iterative reconstruction process to recover both the active antenna indices and the amplitude-phase information of the transmitted signals. Moreover, this algorithm provides optimal error guarantees for the detection of sparse signals since, similarly to the more complex convex algorithms, a stable signal recovery is guaranteed under noisy conditions with a comparable number of receive antennas [229]. The results obtained in the sequel show that the large number of antennas at the BS motivates the employment of this algorithm for SM detection by performing a thorough complexity analysis as opposed to [172,229]. Moreover, as the structure of the transmitted signals in the MAC is not accounted for in the generic CS detection, the following section proposes an approach specifically tailored for the considered scenarios to improve the detection performance.

## 5.4 Proposed Spatial Modulation Matching Pursuit (SMMP)

One of the key characteristics of conventional greedy CS algorithms is that no prior knowledge of the sparse signal other than the number of non-zero entries is assumed. However, when applied to the proposed scenario, this condition can generate situations in which the output of the detector does not have physical sense. For instance, the detected signal could have more than one active antenna per user, which is not possible when conventional SM modulation is used [19]. This undesired operating condition is caused by the noise and inter-user interference effects that arise in the MAC. To mitigate these, the proposed sub-scheme incorporates additional prior knowledge about the distribution of the non-zero entries in the transmitted signal to further enhance

---

**Algorithm 1** Spatial Modulation Matching Pursuit
 

---

**Input:**  $\mathbf{G}$ ,  $\mathbf{y}$ ,  $S$ ,  $n_a$ ,  $\tilde{S}$ ,  $i_{\max}$ .

1: **Output:**  $\tilde{\mathbf{x}}^{i_{\max}} \triangleq S$ -sparse approximation  
 2:  $\tilde{\mathbf{x}}^0 \leftarrow \mathbf{0}$ ,  $i \leftarrow 0$  {Initialization}  
 3: **while** halting criterion *false* **do**  
 4:    $\mathbf{r} \leftarrow \mathbf{y} - \mathbf{G}\tilde{\mathbf{x}}^i$  {Update residual}  
 5:    $i \leftarrow i + 1$   
 6:    $\mathbf{c} \leftarrow \mathbf{G}^H \mathbf{r}$  {MF to estimate active antenna indices}  
    {7–11: Detect  $n_a$  indices with largest energy per user}  
 7:    $\Omega \leftarrow \emptyset$   
 8:   **for**  $j = 1 \rightarrow \bar{K}$  **do**  
 9:      $\mathcal{M} \leftarrow \{(j-1) \cdot n_t, \dots, j \cdot n_t - 1\}$   
 10:      $\Omega \leftarrow \mathcal{M} (\arg \max \{|\mathbf{c}|_{\mathcal{M}}\}_{n_a}) \cup \Omega$   
 11:   **end for**  
    {12–13: Detect remaining  $\tilde{S} - S$  highest-energy indices}  
 12:    $\mathbf{c}(\Omega) \leftarrow \mathbf{0}$   
 13:    $\Omega \leftarrow \arg \max \{|\mathbf{c}|\}_{(\tilde{S}-S) \cup \Omega}$   
 14:    $\mathcal{T} \leftarrow \Omega \cup \text{supp}(\tilde{\mathbf{x}}^{i-1})$  {Merge supports}  
 15:    $\mathbf{b}|_{\mathcal{T}} \leftarrow \mathbf{G}_{\mathcal{T}}^\dagger \mathbf{y}$  {Least squares problem}  
 16:    $\mathbf{b}|_{\mathcal{T}^c} \leftarrow \mathbf{0}$   
    {17–21: Obtain next signal approximation}  
 17:    $\tilde{\mathbf{x}}^i \leftarrow \mathbf{0}$   
 18:   **for**  $j = 1 \rightarrow \bar{K}$  **do**  
 19:      $\mathcal{M} \leftarrow \{(j-1) \cdot n_t, \dots, j \cdot n_t - 1\}$   
 20:      $\tilde{\mathbf{x}}^i|_{\mathcal{M}(\arg \max \{|\mathbf{b}|_{\mathcal{M}}\}_{n_a})} \leftarrow \max \{|\mathbf{b}|_{\mathcal{M}}\}_{n_a}$   
 21:   **end for**  
 22: **end while**

---

performance [221].

The detection algorithm introduced in this chapter is referred to as spatial modulation matching pursuit (SMMP) to explicitly indicate that it corresponds to a particularization to SM operation of the structured CoSaMP iteration developed in [222]. In particular, SMMP reduces the errors in the identification of the active antennas by exploiting the known distribution of the non-zero entries [221, 222]. This also improves the convergence speed of the algorithm as less iterations are required to determine the active antenna indices. While it is intuitive that the concept behind this strategy could be incorporated to other CS detection algorithms, this section concentrates on the CoSaMP algorithm for clarity.

The pseudocode of the proposed strategy is shown in Algorithm 1 for convenience

and its operation can be described as follows [222, 229]:

1. *Computation of the residual.* The algorithm starts by producing an estimate of the largest components of the transmitted signal to identify the active antennas [229]. For this, SMMP employs the residual signal  $\mathbf{r} \in \mathbb{C}^{N \times 1}$  given by

$$\mathbf{r} \triangleq \mathbf{y} - \mathbf{G}\tilde{\mathbf{x}}^i = \mathbf{G}(\mathbf{x} - \tilde{\mathbf{x}}^i) + \bar{\mathbf{n}}, \quad (5.14)$$

where  $\tilde{\mathbf{x}}^i \in \mathbb{C}^{K \times 1}$  is the approximation of the transmit signal at the  $i$ -th iteration. The residual signal concentrates the energy on the components with a largest error in the estimated received signal  $\tilde{\mathbf{y}} = \mathbf{G}\tilde{\mathbf{x}}^i$  [83, 189].

2. *Generation of the decision metric for determining the active antennas.* Subsequently, the decision metric employed to determine the plausible active antennas  $\mathbf{c} \in \mathbb{C}^{K \times 1}$  is obtained as the output of a MF and can be expressed as

$$\mathbf{c} = \mathbf{G}^H \mathbf{r}. \quad (5.15)$$

3. *Determination of the plausible active antennas from the current residual.* From the decision metric obtained in (5.15), the active antenna estimation process forms a set  $\Omega$  of decision variables with cardinality  $|\Omega| = \tilde{S} \geq S$ . The set  $\Omega$  provides an estimate of the plausible active antennas. Note that these entries do not have to correspond to the  $S$  coefficients with highest estimated energy in the transmitted signal as in the CoSaMP algorithm [229]. For instance, let  $\mathbf{x} = [0, 0, -1, 0 | 0, 1, 0, 0]$  be the signal transmitted in a MAC with  $\bar{K} = S = 2$  users with  $n_t = 4$  antennas each and BPSK modulation. The total number of transmit antennas is  $K = n_t \times \bar{K} = 8$ . Then, the set  $\Omega$  in the conventional CoSaMP algorithm could be formed by any  $S = 2$  entries of the set of integers  $\Upsilon_{\text{CoSaMP}} = \{1, 2, \dots, 8\}$  without any restriction. This contrasts with the considered SMMP algorithm, in which the set  $\Omega$  is formed by at least  $n_a = 1$  entry of the set  $\Upsilon_{\text{SMMP}}^1 = \{1, 2, 3, 4\}$  and another one from  $\Upsilon_{\text{SMMP}}^2 = \{5, 6, 7, 8\}$ . In simple terms, the proposed algorithm forces that at least  $n_a$  entries per user are selected as it exploits the knowledge

that

$$\|\mathbf{x}_{\bar{k}}\|_0 = n_a, \quad \bar{k} \in \{1, \dots, \bar{K}\}, \quad (5.16)$$

where  $\|\cdot\|_0$  determines the number of non-zero entries [225,227]. This is represented in lines 7-11 of Algorithm 1, where the  $\arg \max \{\cdot\}_p$  and  $\max \{\cdot\}_p$  functions return the indices and the entries of the  $p$  components with largest absolute value in the argument vector, and  $\emptyset$  denotes the empty set. The remaining  $\tilde{S} - S$  entries are instead selected as the entries with largest energy independently of the user distribution. These additional entries aim at improving the support detection process by involving the LS problem, which offers an enhanced performance in the antenna identification with respect to the estimate provided by the MF [11].

4. *Determination of the final set of plausible active antennas by incorporating those from the previous iteration.* Once the entries with highest error energy in the current residual have been estimated, the set  $\mathcal{T}$  is obtained as

$$\mathcal{T} \triangleq \Omega \cup \text{supp}(\tilde{\mathbf{x}}^{i-1}), \quad (5.17)$$

where  $\text{supp}(\cdot)$  identifies the indices of the non-zero entries. This set provides a final estimate of the plausible active antennas used for transmission by incorporating the ones considered in the previous iteration [83].

5. *Solution of a linear least squares (LS) problem.* The set  $\mathcal{T}$  determines the columns of the matrix  $\mathbf{G}$  employed for solving the unconstrained linear LS problem given by

$$\underset{\mathbf{b}|_{\mathcal{T}}}{\text{minimize}} \|\mathbf{G}_{\mathcal{T}}\mathbf{b}|_{\mathcal{T}} - \mathbf{y}\|_2^2 \rightarrow \mathbf{b}|_{\mathcal{T}} = \mathbf{G}_{\mathcal{T}}^{\dagger}(\mathbf{G}\mathbf{x} + \bar{\mathbf{n}}), \quad (5.18)$$

where  $\mathbf{b}|_{\mathcal{T}}$  denotes the entries of  $\mathbf{b} \in \mathbb{C}^{K \times 1}$  supported in  $\mathcal{T}$ . This notation differs from  $\mathbf{G}_{\mathcal{T}}$ , which refers to the submatrix obtained by selecting the columns of  $\mathbf{G}$  determined by  $\mathcal{T}$ .

The LS approximation is a crucial step as the complexity reduction and the performance improvement w.r.t. conventional linear alternatives depend on the efficiency of this process [229]. This procedure can also be seen as implementing a ZF de-

detector in which, instead of inverting all the columns of the channel matrix, only the columns that have been previously included in the support are inverted. This allows exploiting the large scale MIMO detection benefits as the equivalent ZF detector generally satisfies  $N \gg 2\tilde{S}$  [72]. Due to the possibility of employing different algorithms to solve LS problems, a detailed analysis of their complexity is developed in Sec. 5.5.1.

6. *Approximation of the transmitted signal.* After solving the LS problem, the signal approximation of the  $i$ -th iteration  $\tilde{\mathbf{x}}^i$  is built by selecting the entries with largest energy at the output of the LS problem based on a user-by-user criterion following (5.16). Finally, the sparse output of the algorithm  $\tilde{\mathbf{x}}^{i_{\text{end}}}$  is obtained after the algorithm reaches the maximum pre-defined number of iterations  $i_{\text{max}}$  or a halting criterion is satisfied [229].

Overall, although sub-optimal for a large but finite number of antennas, the proposed scheme exploits the high performance offered by linear detection schemes together with the structured sparsity inherent to SM transmission to reduce complexity. Indeed, a fundamental difference of the proposed approach with respect to the conventional CS approach is that over-determined scenarios are also considered, i.e., communication systems where  $N \geq K$ . Also note that, although shown via iterative structures in Algorithm 1, the additional operations required in the considered algorithm can be implemented via vector operations with reduced computational time.

Regarding the compromise between complexity and performance of the considered technique, it should be noted that several parameters can be modified to adjust this trade-off [229]:

- *Number of entries detected at the output of the MF ( $\tilde{S}$ ):* The parameter  $\tilde{S}$  determines the dimensions of the LS problem, hence severely affecting the signal processing complexity. It also influences the detection performance since the solution is conditioned by the LS matrix  $\mathbf{G}_{\mathcal{T}}$ .
- *Maximum number of iterations of SMMP ( $i_{\text{max}}$ ):* The total number of iterations

determines the complexity and detection accuracy of the algorithm. This parameter can be used to adjust the performance depending on the computational capability of the BS as shown hereafter.

- *Maximum number of iterations of the iterative LS ( $i_{\max}^{\text{LS}}$ ):* The accuracy of the LS solution is improved in every iteration when iterative algorithms are used [230]. Hence, there exists a trade-off between complexity and performance that can be optimized at the BS depending on the communication requirements. As this parameter greatly affects the global complexity, a detailed study of the required number of iterations is developed in Sec. 5.6.

## 5.5 Complexity Analysis

The analysis of the computational complexity is commonly performed by determining the complexity order. This is the approach adopted in [172, 187, 229] to determine the complexity of the proposed algorithms. Instead, this chapter adopts a more precise approach since, as shown in the following, the complexity order does not provide an accurate characterization of the total number of operations due to the iterative nature of the greedy CS-based algorithms. In fact, as opposed to the results obtained in [172] and [229], it is actually concluded that the LS problem can dominate the global complexity.

### 5.5.1 Complexity of the Least Squares Problem

An efficient implementation of the LS algorithm is required to reduce the complexity of the proposed approach since otherwise it can dominate the total number of floating point operations (flops) [229]. In general, the methods to solve the LS problem can be classified according to their approach to obtain the solution into direct and iterative procedures [230]:

- Direct methods include the QR and the Cholesky decompositions and they are based on producing a system of equations that can be easily solved via backward and forward substitutions. The total number of flops is conditioned by the costly

**Table 5.1:** Complexity in number of real floating-point operations (flops) to solve a  $m \times n$  least squares problem.

<i>Operation</i>	<i>Complexity in flops</i>
$\mathbf{G}^\dagger \mathbf{y}$ via QR decomposition [205, 230] <ul style="list-style-type: none"> <li>– QR decomposition</li> <li>– Intermediate computations and back substitution</li> </ul>	$C_T^{\text{LS}} \simeq 8n^2m - \left(\frac{8}{3}\right)n^3 + 8mn + 4n^2$ <ul style="list-style-type: none"> <li>– <math>C_1 = 8n^2m - \left(\frac{8}{3}\right)n^3</math></li> <li>– <math>C_2 = 4n^2 + 8mn</math></li> </ul>
$\mathbf{G}^\dagger \mathbf{y}$ via Cholesky decomposition [230, 232] <ul style="list-style-type: none"> <li>– <math>\mathbf{C} = \mathbf{G}^H \mathbf{G}</math></li> <li>– Cholesky decomposition</li> <li>– Intermediate computations, forward and backward substitutions</li> </ul>	$C_T^{\text{LS}} \simeq 4n^2m + \left(\frac{4}{3}\right)n^3 + 8mn + 11n^2$ <ul style="list-style-type: none"> <li>– <math>C_1 = 4n^2m</math></li> <li>– <math>C_2 = \left(\frac{4}{3}\right)n^3 + 3n^2</math></li> <li>– <math>C_3 = 8n^2 + 8mn</math></li> </ul>
$\mathbf{G}^\dagger \mathbf{y}$ via Richardson Iteration [205, 229, 230] <ul style="list-style-type: none"> <li>– SVD to compute optimal <math>\bar{\alpha}</math></li> <li>– Richardson iterations</li> </ul>	$C_T^{\text{LS}} \simeq \left(\frac{16}{3}\right)n^3 + i_{\max}^{\text{LS}} \times (24mn + 6n)$ <ul style="list-style-type: none"> <li>– <math>C_1 = \left(\frac{16}{3}\right)n^3</math></li> <li>– <math>C_2 = i_{\max}^{\text{LS}} \times (24mn + 6n)</math></li> </ul>
$\mathbf{G}^\dagger \mathbf{y}$ via Conjugate Gradient [229, 230] <ul style="list-style-type: none"> <li>– Algorithm without initial approximation</li> <li>– Algorithm with initial approximation</li> <li>– Conjugate Gradient iterations</li> </ul>	$C_T^{\text{LS}} \simeq C_{1,\{1,2\}} + i_{\max}^{\text{LS}} \times (16mn + 27n)$ <ul style="list-style-type: none"> <li>– <math>C_{1,1} = 8mn + 7n</math></li> <li>– <math>C_{1,2} = 16mn + 18n</math></li> <li>– <math>C_2 = i_{\max}^{\text{LS}} \times (16mn + 27n)</math></li> </ul>

decompositions that must be performed at the beginning of each channel coherence period [231].

- Iterative methods solve the LS problem by refining an initial solution based on the instantaneous residual [230]. These approaches prevent the storage intensive decompositions required by direct methods, an aspect especially beneficial in the proposed scenario due to the large dimensions of the channel matrix  $\mathbf{G}$ .

The number of flops of the QR decomposition, Cholesky decomposition, Richardson iteration and conjugate gradient (CG) LS algorithms are detailed in Table 5.1. Note that the fact that each complex calculus involves the computation of several real operations have been taken into account in Table 5.1. Moreover, similarly to Chapter 3, it has been considered that a real product (division) has the same complexity of a real addition (subtraction) [205].

Regarding the complexity of the Richardson iteration, note that it depends on a parameter  $0 < \bar{\alpha} < 2/\lambda_{\max}^2(\mathbf{G})$  that determines the convergence rate of the algorithm [230]. In the last expression,  $\lambda_{\max}(\mathbf{A})$  denotes the maximum singular value of an ar-

bitrary matrix  $\mathbf{A}$ . The determination of this parameter becomes necessary if a high convergence speed is required and these additional operations are included in Table 5.1. Concerning the CG algorithm, Table 5.1 shows that the complexity differs depending on the availability of an initial approximation to the LS solution [230]. This difference must be considered because, as opposed to the other detectors, the complexity reduction of the greedy CS-based approach is based on the increasing accuracy of the approximations as the algorithm evolves, hence improving the convergence speed as explained in Sec. 5.4.

The comparison between direct LS methods shows that, even though the QR decomposition is more numerically accurate, it also is more complex than the Cholesky decomposition [231]. Therefore, the Cholesky decomposition is preferred for the considered scenario due to the high dimensions of the matrices involved in the LS problem [231]. Regarding the complexity of iterative methods, the results in Table 5.1 describe the reduction of the complexity order when compared to the direct methods pointed out in [229]. However, this improvement does not guarantee a reduction in the number of operations as the total complexity is highly dependent on the number of iterations required until convergence as shown in Sec. 5.8.

### 5.5.2 Overall Complexity of the Proposed Algorithm

Based on the above analyses, a tight upper bound on the total number of real flops of the ZF and SMMP detectors is shown in Table 5.2. The complexity of the ZF detector is solely determined by the operations required to solve the LS problem. Therefore, the increase in the number of transmit antennas of SM may have a significant impact on the total complexity. This is because, while  $K = \overline{K}$  for the conventional large-scale MIMO scenarios with single-antenna users, the relationship  $K = \overline{K} \times n_t$  is satisfied for SM transmitters in the MAC. However, the performance improvements offered by SM justify the complexity increase at the BS, where computational resources are expected to be available [159].

Additionally, it should be pointed out that the flop calculation for the proposed

**Table 5.2:** Complexity in number of real floating-point operations (flops) of different large scale MIMO detectors.

<i>Detector</i>	<i>Complexity in flops</i>
Zero Forcing detector	
– QR factorization	– $C_{\text{QR}} \simeq 8K^2N - \left(\frac{8}{3}\right)K^3 + 8KN + 4N^2$
– Cholesky factorization	– $C_{\text{Chol}} \simeq 4K^2N + \left(\frac{4}{3}\right)K^3 + 8KN + 11K^2$
– Richardson iteration	– $C_{\text{Rich}} \simeq \left(\frac{16}{3}\right)K^3 + [i_{\text{max}}^{\text{LS}} \times (24KN + 6K)]$
– Conjugate gradient	– $C_{\text{CG}} \simeq (8KN + 7K) + [i_{\text{max}}^{\text{LS}} \times (16KN + 27K)]$
SMMP	$C_{\text{SMMP}} \simeq i_{\text{max}} \times (8KN + 8SN) + C_{\text{LS}}^1 + [(i_{\text{max}} - 1) \times C_{\text{LS}}^{i>1}]$
– Matched filter	– $C_{\text{MF}} = 8KN$
– Least Squares problem	– Least Squares problem ( $C_{\text{LS}}$ )
– First SMMP iteration	– $C_{\text{LS}}^1$ . $C_{\text{T}}^{\text{LS}}$ with $m = N$ , $n = \tilde{S}$ and $C_{1,1}$ for CG.
– Rest of SMMP iterations	– $C_{\text{LS}}^{i>1}$ . $C_{\text{T}}^{\text{LS}}$ with $m = N$ , $n = (\tilde{S} + S)$ and $C_{1,2}$ for CG.
– Compute residual	– $C_{\text{res}} \approx 8SN$

algorithm has been performed for the worst-case scenario in which none of the  $S$  entries from the previous SMMP iteration coincide with the  $\tilde{S}$  coefficients selected at the output of the MF. This means that the average number of operations is generally smaller than the one shown in Table 5.2. In spite of this, this tight upper bound allows us to determine the conditions under which CS-based detection is convenient.

The total number of real flops and the BER for an illustrative LSAS scenario are shown in Table 5.3. The relevant system parameters are  $N = 128$ ,  $\bar{K} = S = \tilde{S} = 12$ ,  $n_{\text{t}} = 8$ ,  $i_{\text{max}} = 2$ , SNR = 5 dB and 4-QAM modulation. The number of CG iterations  $i_{\text{max}}^{\text{LS}}$  is set to ensure the maximum attainable performance. Overall, it can be observed that the SMMP algorithm offers a considerable performance improvement with reduced complexity. The results of Table 5.3, which are further developed in Sec. 5.8, also allow concluding that the use of iterative LS algorithms for conventional linear detection may be able to reduce the detection complexity over a channel coherence time. Note that the solution of the LS problem is not exact in these cases, which influences the resulting BER as shown in Table 5.3. This results in a performance improvement for the conventional ZF detector due to the energy concentration on the components that correspond to the active antennas. In this line, the complexity benefits attained by the use of iterative LS algorithms motivate the study of their convergence speed in the following section.

**Table 5.3:** Complexity and BER of a system with  $N = 128$ ,  $\bar{K} = S = \tilde{S} = 12$ ,  $n_t = 8$ ,  $i_{\max} = 2$ , SNR = 5 dB and 4-QAM modulation.

<i>Detection scheme</i>	<i>Complexity</i>	<i>BER</i>
ZF - Cholesky decomposition	6098 kflops	$2.1 \times 10^{-2}$
ZF - Iterative CG detection	696.5 kflops	$1 \times 10^{-3}$
SMMP - Cholesky decomposition	618.5 kflops	$1.12 \times 10^{-5}$
SMMP - Iterative CG detection	507 kflops	$2.08 \times 10^{-5}$

## 5.6 Convergence Rate of Iterative Least Squares Algorithms in LSAS

The complexity of SMMP highly depends on the number of iterations required to obtain a solution to the LS problem. Although the required number of iterations to achieve convergence cannot be known in advance due to the random nature of the communication channel, this section provides two expressions to determine the number of iterations depending on the required output accuracy: a straightforward but less accurate one based on an asymptotic analysis, and a more complex and precise one that resorts to the cumulative distribution function (CDF) of the channel condition number. This offers a more refined and intuitive approach than the one adopted in [229], since the resultant expressions directly depend on the number of antennas of the communication system. Furthermore, the following study can be used to determine whether it is convenient from a numerical perspective to use iterative LS algorithms to solve the ZF problem when applied to LSAS without SM.

The convergence rate of the iterative LS methods is determined by the condition number of the LS matrix  $\mathbf{G}_{\mathcal{L}} \in \mathbb{C}^{N \times |\mathcal{L}|}$  [229, 230]. Throughout this section,  $\mathcal{L}$  is a set defined as  $\mathcal{L} \triangleq \mathcal{T}$  when the SMMP algorithm is used whereas it is given by  $\mathcal{L} \triangleq \{1, 2, \dots, K\}$  for ZF. The standard condition number  $\Theta \in [1, \infty]$  of the matrix  $\mathbf{G}_{\mathcal{L}}$  is defined as [230, 233]

$$\Theta(\mathbf{G}_{\mathcal{L}}) = \frac{\lambda_{\max}(\mathbf{G}_{\mathcal{L}})}{\lambda_{\min}(\mathbf{G}_{\mathcal{L}})} = \sqrt{\frac{\sigma_{\max}(\mathbf{G}_{\mathcal{L}}^H \mathbf{G}_{\mathcal{L}})}{\sigma_{\min}(\mathbf{G}_{\mathcal{L}}^H \mathbf{G}_{\mathcal{L}})}} = \sqrt{\Xi(\mathbf{W})}, \quad (5.19)$$

where  $\lambda_{\max}(\cdot)$  and  $\lambda_{\min}(\cdot)$  denote the maximum and minimum singular values of the

argument matrix respectively,  $\sigma_{\max}(\cdot)$  and  $\sigma_{\min}(\cdot)$  denote the maximum and minimum eigenvalues, and  $\Xi(\mathbf{W})$  refers to the modified condition number defined in [233]. In the last equality,  $\mathbf{W} \in \mathbb{C}^{s \times s}$  is a Wishart matrix with  $t$  degrees of freedom  $\mathbf{W} \sim \mathcal{CW}_s(t, \mathbf{I}_s)$  defined as [233, 234]

$$\begin{cases} \mathbf{W} \triangleq \mathbf{G}_{\mathcal{L}} \mathbf{G}_{\mathcal{L}}^H, & \text{if } N \leq |\mathcal{L}|, \\ \mathbf{W} \triangleq \mathbf{G}_{\mathcal{L}}^H \mathbf{G}_{\mathcal{L}}, & \text{otherwise.} \end{cases} \quad (5.20)$$

In the above,  $s = \min(N, |\mathcal{L}|)$  and  $t = \max(N, |\mathcal{L}|)$ .

To characterize the convergence rate of iterative LS in setup considered in this chapter, this section elaborates on the results of conventional and LSAS theory related to the distribution of the condition number of complex Gaussian and Wishart matrices [233, 234]. Throughout, the focus is placed CG algorithm for brevity, but similar conclusions can be derived for other iterative LS methods [229, 230]. In particular, the residual generated by each iteration of the CG algorithm satisfies [230]

$$\left\| \mathbf{b}_i - \mathbf{G}_{\mathcal{L}}^\dagger \mathbf{y} \right\|_2 \leq 2 \cdot \varrho^i \cdot \left\| \mathbf{b}_0 - \mathbf{G}_{\mathcal{L}}^\dagger \mathbf{y} \right\|_2, \quad (5.21)$$

where the index  $i$  denotes the iteration number,  $\mathbf{b}_i$  is the LS approximation at the  $i$ -th iteration and  $\varrho$  is defined as

$$\varrho = \frac{\Theta(\mathbf{G}_{\mathcal{L}}) - 1}{\Theta(\mathbf{G}_{\mathcal{L}}) + 1}. \quad (5.22)$$

Based on the above result, an upper bound in the number of CG iterations can be expressed as [230]

$$i^{\text{LS}} < \frac{1}{2} \Theta(\mathbf{G}_{\mathcal{L}}) \cdot \log \left( \frac{2}{\iota} \right), \quad (5.23)$$

where  $\iota$  is the relative error defined as

$$\iota = \frac{\left\| \mathbf{b}_i - \mathbf{G}_{\mathcal{L}}^\dagger \mathbf{y} \right\|_2}{\left\| \mathbf{b}_0 - \mathbf{G}_{\mathcal{L}}^\dagger \mathbf{y} \right\|_2}. \quad (5.24)$$

From the above expressions it can be concluded that the convergence speed of the iterative LS methods increases when a smaller number of entries are selected at the output of the MF in the proposed algorithm. This is because the large number of

antennas available at the BS greatly favours the convergence of the CG due to the reduced condition number of the LS matrix. This is characterized by the following proposition on the convergence of the CG algorithm in the large antenna number limit.

**Proposition 5.6.1** An upper bound in the number of iterations required by the LS CG algorithm to achieve a relative error reduction of  $\iota$  under large-scale MIMO conditions is given by

$$i^{\text{LS}} < \frac{1}{2} \cdot \left| \frac{1 + \sqrt{\beta(|\mathcal{L}|)}}{1 - \sqrt{\beta(|\mathcal{L}|)}} \right| \cdot \log \left( \frac{2}{\iota} \right), \quad (5.25)$$

where the function  $\beta(V), V \in \mathbb{Z}^+$  is defined as

$$\begin{cases} \beta(V) = N/V \text{ if } N \geq V, \\ \beta(V) = V/N \text{ otherwise.} \end{cases} \quad (5.26)$$

**Proof of Proposition 5.6.1** The proof is provided in Appendix B.  $\square$

In spite of being valid in a large number of cases, the probability of requiring a higher number of iterations for certain badly conditioned channels cannot be quantified with the above approximation. For this reason, the analysis of the CDF of the modified condition number  $F_{\Xi}(\hat{\xi}) = P(\Xi \leq \hat{\xi})$  with  $\hat{\xi} \geq 1$  developed in [233] is leveraged in the sequel. Specifically, let  $\boldsymbol{\sigma} \triangleq [\sigma_1, \sigma_2, \dots, \sigma_s]$  be the ordered eigenvalues of the Wishart matrix defined in (5.20) so that  $0 < \sigma_s \leq \dots \leq \sigma_1$ . Moreover, let  $\mathbf{V}(\boldsymbol{\sigma})$  be the Vandermonde matrix with  $m, n$ -th entry  $V_{m,n} = \sigma_n^{m-1}$  [26, Section 4.6]. The CDF of the modified condition number  $\Xi$  of an uncorrelated central Wishart matrix is given by [233, Equation (9)]

$$F_{\Xi}(\hat{\xi}) = \left[ \prod_{m=1}^s (s-m)! \prod_{n=1}^s (t-n)! \right]^{-1} \sum_{t=1}^s \int_0^{\infty} |\boldsymbol{\Upsilon}| d\boldsymbol{\sigma}_s. \quad (5.27)$$

Here,  $|\boldsymbol{\Upsilon}|$  denotes the determinant of the matrix  $\boldsymbol{\Upsilon}$ , whose  $m, n$ -th entry  $v_{m,n}$  is defined

as

$$v_{m,n} = \begin{cases} \gamma(t-s+m+n-1, \widehat{\xi}\sigma_s) - \gamma(t-s+m+n-1, \sigma_s) & , m \neq l \\ V_{m,s}V_{n,s}\sigma_s^{t-s}e^{-\sigma_s} & , m = l \end{cases} \quad (5.28)$$

where  $\gamma(a, b)$  is the lower incomplete gamma function given by  $\gamma(a, b) = \int_0^b e^{-t}t^{a-1}dt$ . Equations (5.27) and (5.28) facilitate estimating the CDF of the condition number of a communication channel, which in turn is necessary to determine the number of LS iterations as shown in the following. Using the above results, the following theorem can be stated:

**Theorem 5.6.1** The probability that a given number of LS iterations  $i_{\max}^{\text{LS}}$  suffices to achieve a relative error reduction of  $\iota$  in the LS CG algorithm is given by

$$P(i^{\text{LS}} \leq i_{\max}^{\text{LS}}) = F_{\Xi} \left( \left[ \frac{2 \cdot i_{\max}^{\text{LS}}}{\log\left(\frac{2}{\iota}\right)} \right]^2 \right). \quad (5.29)$$

**Proof of Theorem 5.6.1** The proof is given in Appendix C.  $\square$

The result of Theorem 5.6.1 characterizes the trade-off between accuracy and complexity of the CG when the number of LS iterations is varied. In other words, (5.29) characterizes the impact of varying the number of iterations of the CG algorithm in the performance of the ZF and the proposed SMMP detector. Overall, the results derived in this section allow concluding that the conditions of large-scale MIMO greatly favor the use of the iterative algorithms thanks to the reduced difference between the maximum and minimum singular values of the communication channel, which in turn ensures a fast convergence [11, 230]. This effect is enhanced by the proposed algorithm due to the operation with a better conditioned matrix than conventional ZF or MMSE detectors. In other words, even though several LS problems are solved when the SMMP algorithm is employed, the overall complexity can be reduced w.r.t. the conventional ZF or MMSE detectors because the dimensions of the LS matrices are smaller and the convergence speed of the iterative algorithm is faster.

## 5.7 Energy Efficiency

The study of the energy efficiency becomes especially important in the uplink of multi-user scenarios due to the necessity of finding energy-efficient schemes that allow increasing the battery lifetime [2]. In particular, the energy efficiency is expressed as the spectral efficiency per milliwatt of total consumed power by using the metric [59, 65, 161, 190]

$$\varepsilon = \frac{S_e}{\sum_{\bar{k}=1}^K P_{\bar{k}}} \text{ subject to } \text{BER} \leq \text{BER}_{\text{obj}}. \quad (5.30)$$

Here,  $\text{BER}_{\text{obj}}$  is the objective average BER,  $S_e$  refers to the spectral efficiency in bits per channel use (bpcu), and  $P_{\bar{k}}$  is the total power consumption of the  $\bar{k}$ -th MS in milliwatts required to achieve a given  $\text{BER}_{\text{obj}}$ . However, as highlighted in Sec. 2.1.3, the power consumption models for the uplink are not as developed as those for the downlink. For this reason, this chapter resorts to the power consumption model and values employed in [59]. The total power consumption per MS can be therefore expressed as [59]

$$P_{\bar{k}} = P_{C,\bar{k}} + P_{\text{PA},\bar{k}} = [n_a P_\psi + P_\Psi] + \left[ \sum_{j=1}^{n_t} \left( \frac{\xi}{\eta} \right) \cdot p_{\bar{k},j} \right]. \quad (5.31)$$

In the previous expression,  $P_{C,\bar{k}} = P_\psi + P_\Psi$  denotes the total circuit power consumption excluding the power amplifier (PA) and it is divided into two components:  $P_\psi$  that represents the circuit power consumption that depends on the number of active antennas per MS,  $n_a$ , and  $P_\Psi$  that corresponds to the static power consumption and it is fixed to a reference value of 5 mW per MS [59]. In particular,  $P_\psi$  comprises the additional power consumption required to activate the circuitry of the RF chains and the digital signal processors for transmission. Both  $P_\psi$  and  $P_\Psi$  are assumed to be identical for all MSs. Moreover,  $P_{\text{PA},\bar{k}} = \sum_{j=1}^{n_t} \left( \frac{\xi}{\eta} \right) \cdot p_{\bar{k},j}$  refers to the power consumption of the PA. In the last expression,  $p_{\bar{k},j}$  refers to the power of the signal that is required to be transmitted by the  $j$ -th antenna, the factor  $\xi$  is the modulation-dependent peak to average power ratio (PAPR) and  $\eta = 0.35$  corresponds to the PA efficiency [65]. Based on the above, the global energy efficiency can be expressed as

$$\varepsilon = \frac{S_e}{\sum_{\bar{k}=1}^K \left\{ [n_a P_\psi + P_\Psi] + \left[ \left( \sum_{j=1}^{n_t} \left( \frac{\xi}{\eta} \right) \cdot p_{\bar{k},j} \right) \right] \right\}}, \text{ subject to } \text{BER} \leq \text{BER}_{\text{obj}}. \quad (5.32)$$

## 5.8 Results and Discussion

Monte Carlo simulations in MATLAB<sup>®</sup> have been designed to characterize the performance and energy efficiency improvements of the proposed technique. To maintain the coherence with the SM literature, a comparison between LSAS and SM systems with identical attainable spectral efficiencies is provided. The performance and energy efficiency results of spatial multiplexing systems with identical number of transmit antennas have not been represented in these figures to avoid congestion and because they exhibit a worse behaviour when compared to the spatial multiplexing systems considered here. In the following, SM-ZF and SM-MMSE refer to the linear ZF and MMSE detectors introduced in Sec. 5.2.3, SM Generic CS denotes the CoSaMP algorithm without the improvement described in Sec. 5.3, and the techniques with MIMO on their description correspond to those of a conventional MIMO scenario without SM. For reasons of brevity, this section concentrates on  $\tilde{S} = S$  for the generic and SMMP CS algorithms. Note that this decision entails a minimization of the computational complexity for the CS-based algorithms following the results of Table 5.2. Additionally, the MPD algorithm is also considered in spite of its increased computational complexity [187]. The performance results, unless stated otherwise, have been obtained with an exact solution of the LS problem via Cholesky decomposition.

Fig. 5.1 characterizes the performance of the above-mentioned detectors in a scenario with  $N = 128$ ,  $\bar{K} = 16$ ,  $n_t = 4$ ,  $n_a = 1$  corresponding to the single active antenna SM, and a resulting spectral efficiency of  $S_e = 64$  bpcu. The results of this figure have been obtained with  $i_{\max} = 2$  iterations of Algorithm 1, which ensures a reduced complexity when compared to the algorithms developed in [187]. Note that an error floor is expected due to the non-feasible solutions produced by the generic CS algorithm. This, however, cannot be appreciated in these results since the large number of antennas considered at the BS moves the error floor to very low BER values [172]. Fig. 5.1 shows that the proposed algorithm is able to reduce the required transmission power by more than 4 dB w.r.t. conventional MIMO with  $n_t = 1$  and 16-QAM to achieve a target BER of  $10^{-4}$ . Moreover, it is portrayed that SMMP approaches the performance of the more complex

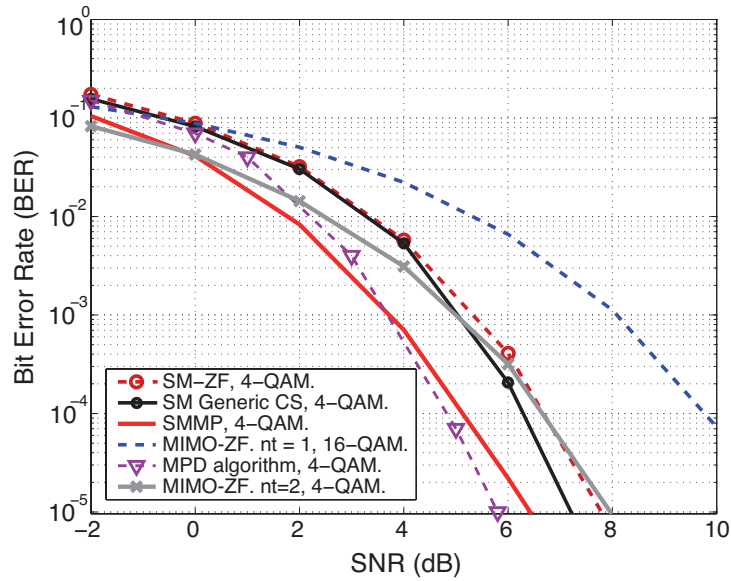


**Figure 5.1:** BER vs. SNR for  $N = 128$ ,  $\bar{K} = S = 16$ ,  $n_t = 4$ ,  $n_a = 1$ ,  $i_{\max} = 2$ ,  $\tilde{S} = S$  and  $S_e = 64$  bpcu.

MPD and outperforms the SM-ZF detector. This is because the proposed strategy is able to iteratively identify the active antenna indices and then perform a selective channel inversion with a matrix of reduced dimensions. Instead, the performance of conventional MIMO with two active antennas per user approaches the performance of SMMP. However, note that in this case the power consumption and complexity of the MSs is increased due to the additional RF chains implemented.

Fig. 5.2 shows the performance of the considered detectors in a scenario with  $N = 128$ ,  $\bar{K} = 16$ ,  $n_t = 7$ , generalized SM with  $n_a = 2$  active antennas per user, and a resulting spectral efficiency of  $S_e = 96$  bpcu. The results of this figure show that generalized SM systems with SMMP detection are capable of improving the performance of conventional MIMO systems employing the same number of RF chains (‘MIMO-ZF.  $n_t = 1$ ’). The use of SMMP also allows outperforming conventional MIMO systems with a pair of RF chains (‘MIMO-ZF.  $n_t = 2$ ’) for the range of practical BERs. Moreover, it can be seen that the SMMP algorithm clearly improves the performance of other linear detectors such as the SM-MMSE detector. In the following, the simulation results are focused on single active antenna SM for reasons of brevity, although it is clear that the resultant conclusions also extend to generalized SM transmission.

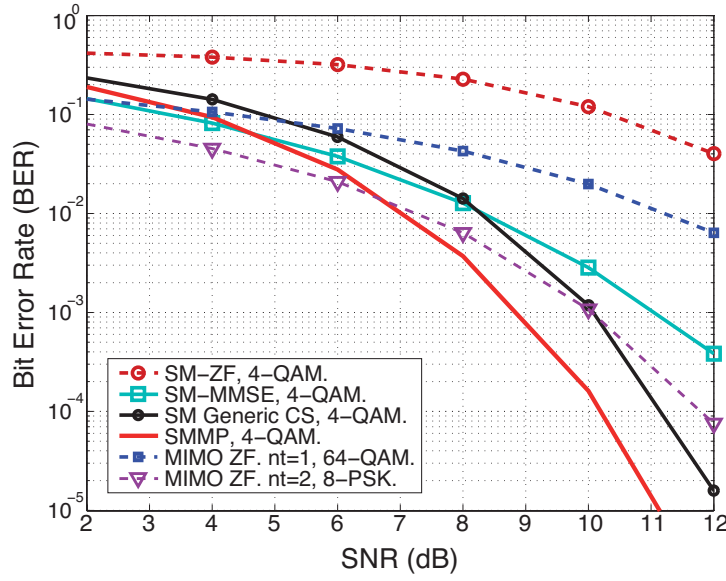


**Figure 5.2:** BER vs. SNR for  $N = 128$ ,  $\bar{K} = 16$ ,  $n_t = 7$ ,  $n_a = 2$ ,  $i_{\max} = 3$ ,  $\tilde{S} = S = 2\bar{K}$  and  $S_e = 96$  bpcu.

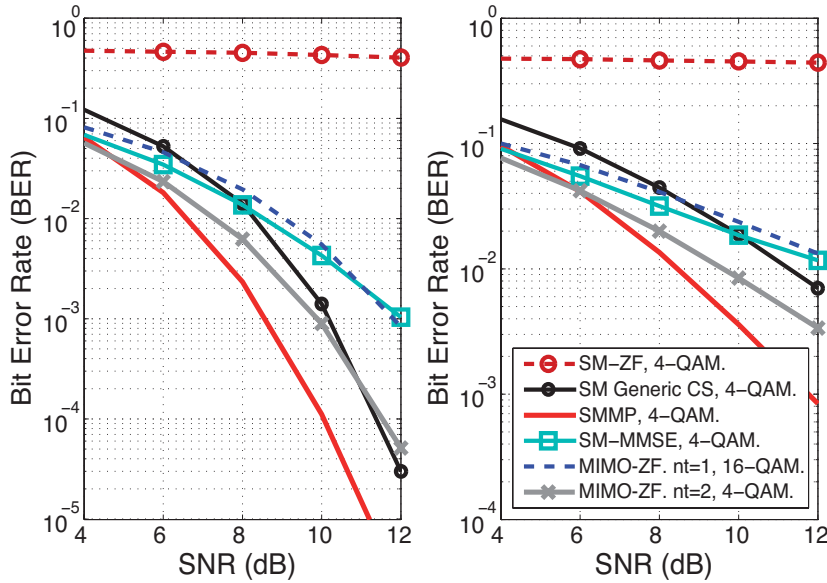


**Figure 5.3:** BER vs. SNR for  $N = 128$ ,  $\bar{K} = S = 32$ ,  $n_t = 4$ ,  $n_a = 1$ ,  $i_{\max} = 3$ ,  $\tilde{S} = S$  and  $S_e = 128$  bpcu with (a) perfect and (b) imperfect CSI ( $\tau = 0.25$ ).

The number of users is increased from  $\bar{K} = 16$  of Fig. 5.1 to  $\bar{K} = 32$  in Fig. 5.3, which shows a scenario especially favourable for the proposed technique. Fig. 5.3 shows that the proposed strategy is able to provide an enhancement of up to three orders of magnitude in the BER at high SNR values w.r.t. conventional large-scale MIMO, and both ZF and MMSE detectors in SM. The performance improvement offered by SM when compared to

conventional MIMO transmission is coherent with the behaviour described in [159,166]. The effect of acquiring inaccurate channel state information (CSI) on the performance is also shown in Fig. 5.3(b). The imperfect CSI is modeled following  $\tilde{\mathbf{G}} = \sqrt{1 - \tau^2}\mathbf{G} + \tau\mathbf{Q}$ , where  $\tau \in [0, 1]$  regulates CSI quality and  $\mathbf{Q} \in \mathbb{C}^{N \times K} \sim \mathcal{CN}(\mathbf{0}, \mathbf{I}_N \otimes \mathbf{I}_K)$  characterizes the channel estimation error [215]. The results of this figure for  $\tau = 0.25$  highlight the robustness of SMMP when compared to traditional CS-based detection, which makes it the best alternative in terms of performance under imperfect CSI.

Although not extensively studied in this chapter for reasons of brevity, the impact of inter-antenna correlation at the MSs plays an important role in the benefits attained by SM over conventional MIMO schemes. Indeed, up to this point it has been considered that the antennas placed at the MSs are uncorrelated, which constitutes the best scenario for SM. However, spatial correlation arises in realistic scenarios due to the limited physical space available at the MSs. Fig. 5.4 characterizes the impact of correlation on the comparison between SM and conventional MIMO. In particular, the simple exponential channel correlation model is employed, i.e. [235,236]

$$\mathbf{G}_{\bar{k}} = \mathbf{Z}_{\bar{k}}\mathbf{R}^{\frac{1}{2}}, \quad (5.33)$$

where  $\mathbf{G}_{\bar{k}} \in \mathbb{C}^{N \times n_t}$ ,  $\bar{k} \in \{1, \dots, \bar{K}\}$  denotes the channel of the  $\bar{k}$ -th user,  $\mathbf{Z}_{\bar{k}} \in \mathbb{C}^{N \times n_t} \sim \mathcal{CN}(\mathbf{0}, \mathbf{I}_N \otimes \mathbf{I}_{n_t})$  and  $\mathbf{R}$  is the exponential correlation matrix, which is assumed identical for all users and is given by [235,236]

$$\mathbf{R} = \begin{pmatrix} 1 & t_e & \dots & t_e^{n_t-1} \\ t_e & 1 & \dots & t_e^{n_t-2} \\ \vdots & \vdots & \dots & \vdots \\ t_e^{n_t-1} & t_e^{n_t-2} & \dots & 1 \end{pmatrix}, \quad (5.34)$$

where  $t_e \in [0, 1]$  is the exponential parameter [235,236]. The evolution of the BER against increasing  $t_e$  is shown in Fig. 5.4 for the same simulation setup illustrated in Fig. 5.1 with SNR = 6 dB. The results of Fig. 5.4 indicate that the performance benefits provided by SM when compared with conventional MIMO transmission vanish for large

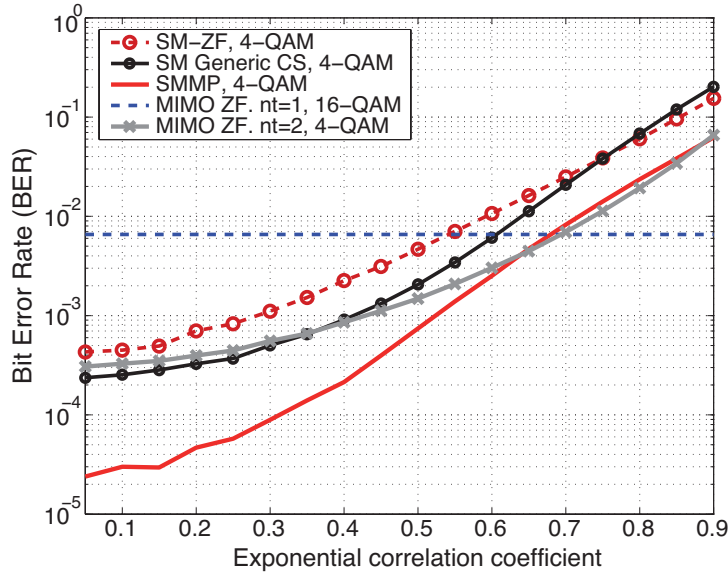


**Figure 5.4:** BER vs.  $t_e$  for  $N = 128$ ,  $\bar{K} = 16$ ,  $n_t = 4$ ,  $\tilde{S} = S$ , SNR = 6 dB,  $i_{\max} = 2$  and  $S_e = 64$  bpcu.

$t_e$ . Indeed, while the proposed scheme shows a robustness against correlation, there is a point ( $t_e \approx 0.7$ ) where incorporating a single antenna at the terminals is more effective. Intuitively, this occurs because identifying the active MS antennas becomes more difficult at the BS due to the similarity of their channels, hence degrading the performance of SM.

Fig. 5.5 shows the trade-off between performance and complexity in real flops for a MAC with  $N = 128$ ,  $\bar{K} = 16$ ,  $n_a = 1$ ,  $S_e = 64$  bpcu,  $i_{\max} = 2$ ,  $\tilde{S} = \bar{K}$  and SNR = 6 dB. The number of antennas per user is  $n_t = 4$  when SM is used, whereas it is  $n_t = 1$  and  $n_t = 4$  for conventional MIMO. Note that the complexity and performance of the CG algorithm varies depending on the number of iterations as explained in Sec. 5.5.1. From the results of this figure it can be concluded that the SMMP approach offers the best performance with a restrained complexity. When compared to LSAS with the same spectral efficiency and alike number of RF chains ('MIMO-ZF,  $n_t = 1$ '), the use of SM increases complexity due to the higher number of antennas at the MSs, but in turn offers a performance improvement of more than two orders of magnitude. This improvement is not as significant with respect to the spatial multiplexing system with the same number of antennas ('MIMO-ZF,  $n_t = 4$ '), where instead the complexity is dramatically reduced. Fig. 5.5 also shows the complexity improvements that can

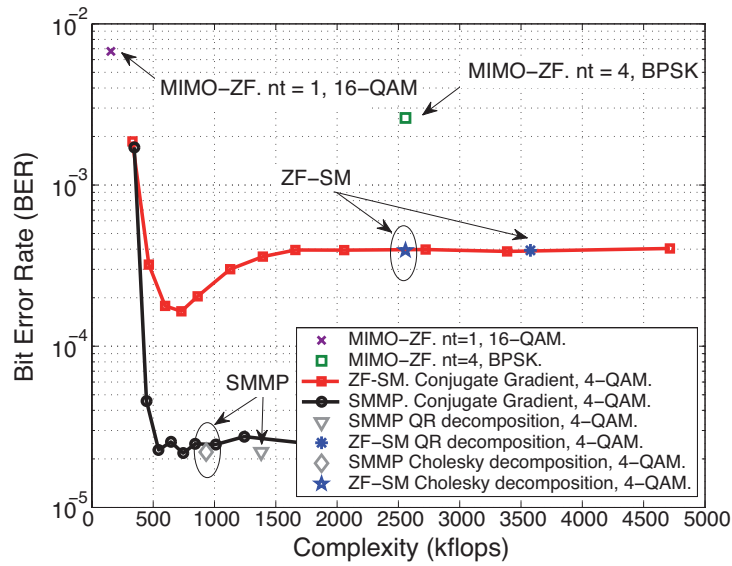


**Figure 5.5:** BER vs. complexity for  $N = 128$ ,  $\bar{K} = \bar{S} = 16$ ,  $n_t = 4$ ,  $n_a = 1$ ,  $\text{SNR} = 6$  dB,  $S_e = 64$  bpcu,  $i_{\max} = 2$ ,  $\tilde{S} = S$  with different LS methods.

be obtained when the iterative CG algorithm termed ‘ZF-SM. Conjugate Gradient’ considered in this chapter is employed to solve the LS problems against traditional direct methods such as ‘ZF-SM. QR decomposition’ and ‘ZF-SM. Cholesky decomposition’ in Fig. 5.5. The number of iterations and, inherently, the complexity can be adjusted depending on the BER required at the BS. This result suggests that the use of the CS-based detection is especially convenient in fast fading scenarios with a reduced channel coherence period. This is because whereas CS-based detection methods perform the same computations in every channel use, the linear detectors solved with direct methods focus the intensive computations at the beginning of the coherence period and reduce their complexity afterwards [4].

A similar conclusion can be obtained from the results of Fig. 5.6, where the focus is on controlling the attainable performance by varying the number of LS iterations in the CG algorithm. Also note that, as opposed to the conclusions achieved in [172, 229], the iterative LS algorithm accounts for 60% of the global detection complexity, hence justifying the need of an accurate complexity characterization. Altogether, it can be concluded that the proposed strategy offers significant performance improvements with similar complexity, when compared with conventional detection schemes in systems with

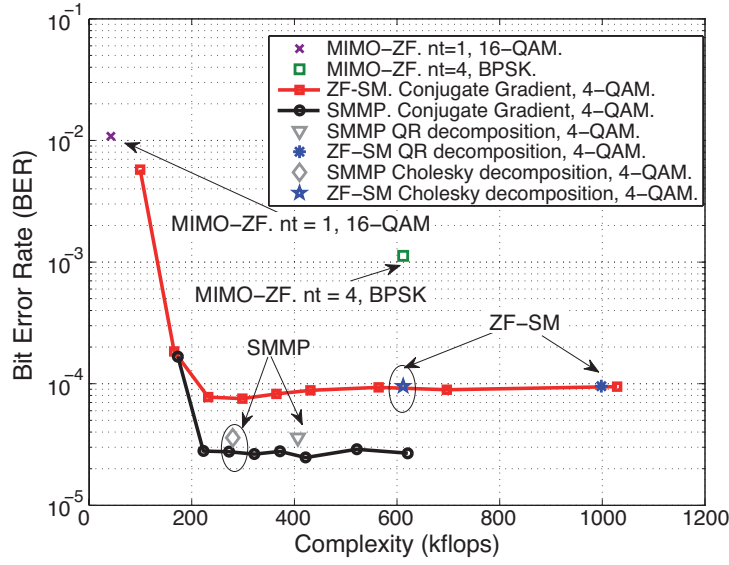


**Figure 5.6:** BER vs. complexity for  $N = 128$ ,  $\bar{K} = \bar{S} = 8$ ,  $n_t = 4$ ,  $n_a = 1$ , SNR = 2 dB,  $S_e = 32$  bpcu,  $i_{\max} = 2$ ,  $\tilde{S} = S$  with different LS methods.

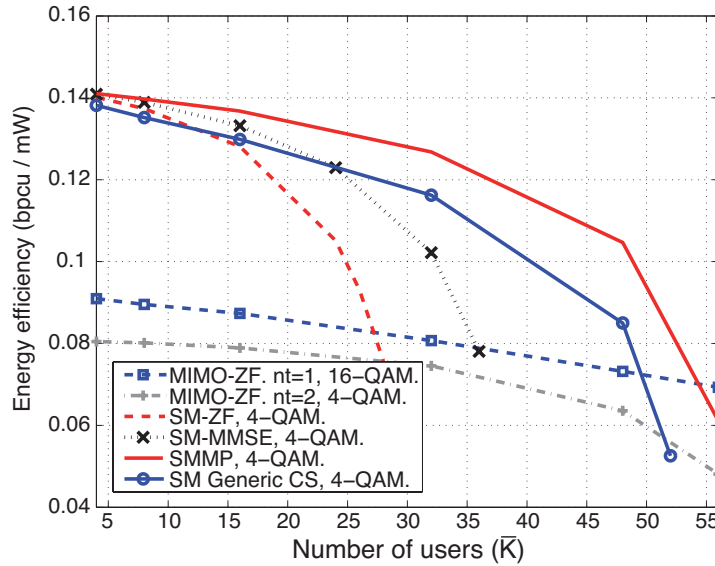


**Figure 5.7:** Energy efficiency vs. number of users  $\bar{K}$  to achieve BER =  $10^{-3}$ .  $N = 128$ ,  $n_t = 4$ ,  $n_a = 1$ .  $P_\psi = 20$  mW.

identical number of antennas.

Regarding the energy efficiency of the CS-based detection, Fig. 5.7 shows this metric for an uncorrelated MAC with  $N = 128$  and a varying number of users. The transmission power is varied depending on the number of users so that  $\text{BER}_{\text{obj}} = 10^{-3}$  in (5.30). The circuit power consumption depending on the number of active antennas is set to a

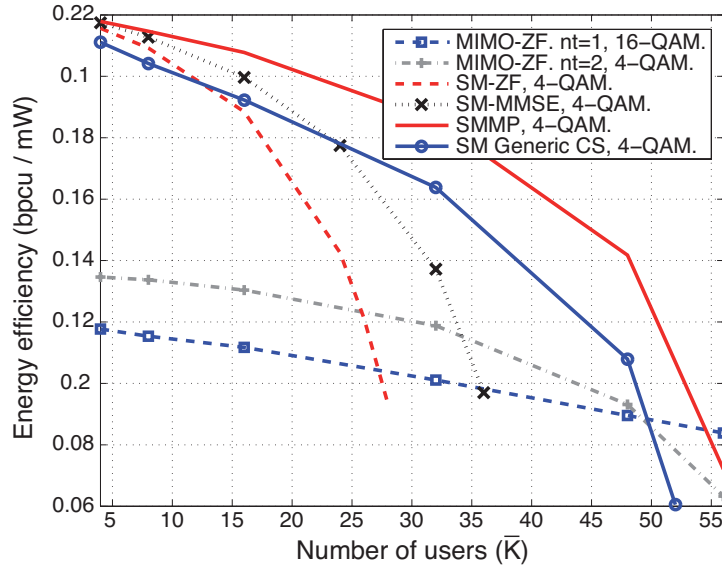


**Figure 5.8:** Energy efficiency vs. number of users  $\bar{K}$  to achieve  $\text{BER} = 10^{-3}$ .  
 $N = 128$ ,  $n_t = 4$ ,  $n_a = 1$ .  $P_\psi = 10$  mW

realistic value of  $P_\psi = 20$  mW [65], and the noise variance is fixed to  $\sigma^2 = 0.01$ . Note that the PAPR factor of the single-antenna users is increased w.r.t. SM due to the use of a higher modulation order  $Q$ . From the results of this figure it can be concluded that the use of SM allows to significantly increase the energy efficiency of conventional LSAS for low and intermediate system loading factors. This improvement due to the reduced circuit power consumption and PAPR was already noticed in [237] for the downlink of small-scale P2P systems. Moreover, the proposed technique outperforms the rest of conventional detectors, hence constituting an energy-efficient alternative in the MAC.

Fig. 5.7 also shows that, in spite of the transmission energy savings that can be obtained when  $n_t = 2$  and 4-QAM are used in MIMO systems, the increased circuit power consumption caused by the higher number of RF chains penalizes the energy efficiency. To show this effect, in Fig. 5.8 we reduce the power consumed by the RF chains  $P_\psi$  to half, i.e.,  $P_\psi = 10$  mW. By doing so, now it can be seen that the use of a MIMO system with  $n_t = 2$  outperforms the option of having single-antenna devices. Still, the energy efficiency of the SM alternatives is significantly higher than the one of MIMO strategies for a low and intermediate number of users due to the reduced transmission power required to compensate the inter-user interference.

## 5.9 Conclusions

In this chapter, a low-complexity detection algorithm for SM has been presented. The proposed strategy is based upon CS by incorporating the additional structure and sparsity of the signals transmitted in the MAC. The results obtained in this chapter indicate that the benefits of the proposed algorithm are maximized when a large number of receive antennas are implemented at the BS, due to its faster convergence and improved performance. Indeed, it has been shown that the proposed CS-based detection for SM can achieve energy efficiency improvements of up to 90% with respect to traditional systems with single-antenna terminals, for the scenarios explored in this chapter.

*Critique:* At this point, it should be noted that SM schemes motivate the employment of single-carrier modulation to fully exploit the additional dimension introduced to the transmit constellation [158]. This might complicate their incorporation to existing mobile standards, where multi-carrier modulations are conventionally employed instead [1]. Furthermore, note that SM systems need larger CSI acquisition periods than systems with single-antenna mobile terminals, due to the larger number of antennas implemented. This could affect the resultant spectral efficiencies in fast varying communication channels. The consideration of more realistic channel models for evaluating the correlation at both the BS and the MSs also seems necessary to assess the attainable performance of SM in practical communications systems.

## Chapter 6

# Low-Complexity Large Scale Antenna Systems: Incomplete Channel State Information

### 6.1 Introduction

One of the fundamental concerns in the deployment of large scale antenna systems (LSAS) relates to fitting an excessive number of antennas in constrained physical spaces [11,101,112]. This leads to an increased inter-antenna correlation due to insufficient antenna separation, which may affect the system capacity unless conveniently approached [11,111,114,150,238]. In this context, the excessive number of antennas deployed in LSAS makes the consideration of these effects critical. The significant power consumption introduced by the additional radio frequency (RF) chains implemented in massive MIMO systems can also have a negative impact on the energy efficiency [61]. Moreover, the collection of accurate channel state information (CSI) complicates the application of LSAS to frequency division duplex (FDD) scenarios. This is because the CSI acquisition time of the conventional FDD approaches can be proportional to the number of antennas allocated at the base station (BS) [11,69].

The above-mentioned challenges have been explored in a number of related works.

For instance, the effects of fitting a massive number of antennas in size-constrained structures have been studied in [101, 111, 112, 239]. Specifically, [101] explores the impact of physical space constraints on the sum rate performance of LSAS, whereas [111] demonstrates that inter-user interference does not vanish in the large antenna limit when the physical size of the antenna array is constrained. The influence of the power consumption of the RF circuitry on the energy efficiency and strategies to reduce the number of electronic components have been considered in [4, 61, 64, 80, 192]. Additionally, several alternatives have been proposed to improve the acquisition of the CSI for both time division duplex (TDD) and FDD systems (see, e.g., [80–82, 87, 88, 240] and references therein). Some of these works exploit the appearance of low-rank channel matrices due to the inter-antenna correlation of massive antenna arrays or finite scattering to enhance the channel estimation process. Particularly related to the strategy developed in this chapter is [241, 242], where the large correlation between adjacent antennas is exploited to optimize the design of the feedback information during the CSI acquisition stage of FDD systems. In line with these contributions, this chapter explores a solution particularly tailored for size-constrained antenna arrays that addresses several of the above-mentioned challenges.

Specifically, this chapter proposes a strategy to optimize the trade-off between the quality of the acquired CSI and the energy efficiency in tightly packed antenna arrays with a large number of antennas. The proposed scheme is based on exploiting inter-antenna correlation to relax CSI acquisition by completely disposing with the CSI of a subset of antennas. This is done by deactivating a number of antennas during the pilot training stage, hence acquiring incomplete information of the global communication channel. After this process, the CSI of the antennas that were inactive during the CSI acquisition stage is obtained by simply averaging the instantaneous CSI of the neighbour antennas that collected this information. As a result, the signal processing load and the power consumption of the RF circuitry during the CSI acquisition process is reduced at the cost of decreasing the accuracy of the channel estimation. Indeed, this benefit holds true for the data transmission stage as well, which motivates studying the effects that the number of antennas without instantaneous CSI has on the performance, computational

load and energy efficiency of size-constrained massive BSs.

In particular, although the collection and use of incomplete CSI has notable implications in the implementation of both TDD and FDD scenarios, this chapter concentrates on TDD systems for both reasons of simplicity and for their practical importance in LSAS [11, 13, 69]. In this setting, it is observed that the transmission performance of massive MIMO BSs deployed in constrained physical spaces is highly tolerant to the acquisition of incomplete CSI. Overall, this translates to significant potential gains in the energy efficiency due to the simultaneous reduction in the number of RF chains and signal processing load offered by the proposed scheme.

## 6.2 System Model

### 6.2.1 TDD System Model and CSI Acquisition

A generic multi-user TDD system comprised of  $K$  single-antenna users and a large scale BS with  $N \gg K$  antennas is considered in this chapter, where the essential results obtained in Chapter 2 are reproduced for convenience. The communication channel follows a block-fading propagation model, hence remaining constant throughout a number of  $\eta_{\text{coh}}$  symbols in which a frame is conveyed, and varying independently between frames [215]. Initially, the CSI is acquired at the BS via the predefined orthogonal training signals transmitted from the mobile stations (MSs) during the first  $\eta_{\text{tr}} \geq K$  symbol slots [79, 243]. Specifically, let  $\mathbf{G} \in \mathbb{C}^{N \times K}$  denote the uplink communication channel matrix in coherence with Chapter 2. Similarly to (2.19), the signal received by the BS during the training stage is given by [79, 84]

$$\mathbf{P} = \sqrt{\rho_{\text{ul}}} \cdot \mathbf{G}\mathbf{\Theta} + \bar{\mathbf{N}}, \quad (6.1)$$

where  $\mathbf{\Theta} \in \mathbb{C}^{K \times \eta_{\text{tr}}}$  represents the orthogonal training signals transmitted by the users,  $\rho_{\text{ul}}$  is the signal-to-noise ratio (SNR) of the reverse channel, and  $\bar{\mathbf{N}} \in \mathbb{C}^{N \times \eta_{\text{tr}}}$  is an additive white Gaussian noise matrix with independent and identically distributed (i.i.d.) entries  $\bar{n}_{i,j} \sim \mathcal{CN}(0, 1)$ . The training signal matrix is given by  $\mathbf{\Theta} = [\boldsymbol{\theta}_1, \dots, \boldsymbol{\theta}_K]^T$ ,

where  $\boldsymbol{\theta}_k \in \mathbb{C}^{\eta_{\text{tr}} \times 1}$  denotes the orthogonal training signal assigned to the  $k$ -th user. The correlation of the received signals during the training stage with the pilot sequences yields the decision metric [72, 79, 84]

$$\hat{\mathbf{P}} = (\sqrt{\rho_{\text{tr}}} \cdot \mathbf{G}\boldsymbol{\Theta} + \bar{\mathbf{N}}) \boldsymbol{\Theta}^{\text{H}} = \sqrt{\rho_{\text{tr}}} \cdot \mathbf{G} + \bar{\mathbf{N}}\boldsymbol{\Theta}^{\text{H}}, \quad (6.2)$$

where  $\rho_{\text{tr}}$  represents the effective training SNR [72] and  $\bar{\mathbf{N}}\boldsymbol{\Theta}^{\text{H}} \sim \bar{\mathbf{N}}$ . The estimated uplink channel can be directly obtained from (6.2) by applying estimation strategies such as those based on minimizing the mean square error (MMSE) [84, 85]. Moreover, provided that channel reciprocity holds, the downlink channel  $\mathbf{H}$  can be straightforwardly obtained as the conjugate transpose of the uplink estimate, i.e.  $\mathbf{H} = \mathbf{G}^{\text{H}}$  [72].

Once the pilot transmission stage is completed, the remaining symbol slots  $\eta_{\text{coh}} - \eta_{\text{tr}}$  of the channel coherence time are used for downlink and uplink data transmission [79, 243, 244]. By particularizing (2.1), the signal received by the  $k$ -th MS during a downlink symbol slot can be expressed as

$$y_k = \sqrt{\rho_{\text{f}}} \cdot \mathbf{g}_k^{\text{H}} \mathbf{x} + n_k, \quad (6.3)$$

where  $\mathbf{x} \in \mathbb{C}^{N \times 1}$  denotes the symbols transmitted by the BS,  $\mathbf{g}_k^{\text{H}} \in \mathbb{C}^{1 \times N}$  represents the downlink communication channel from the BS to the  $k$ -th user,  $\rho_{\text{f}}$  denotes the SNR of the forward link, and  $n_k \sim \mathcal{CN}(0, 1)$  is the standard additive white Gaussian noise. In this massive MIMO setting, linear precoding strategies approach the performance of the more computationally complex non-linear schemes, hence making their use convenient [11, 72]. For this reason, the transmit signal is decomposed as

$$\mathbf{x} = \nu \cdot \mathbf{F}\mathbf{u} = \frac{\mathbf{F}\mathbf{u}}{\sqrt{\mathbb{E}\{\text{Tr}[\mathbf{F}^{\text{H}}\mathbf{F}]\}}}, \quad (6.4)$$

where  $\mathbf{F} \in \mathbb{C}^{N \times K}$  represents an arbitrary linear precoding matrix,  $\mathbf{u} \in \mathbb{C}^{K \times 1}$  denotes the user constellation symbols to be conveyed, and  $\nu = 1/\mathbb{E}\{\sqrt{\text{Tr}[\mathbf{F}^{\text{H}}\mathbf{F}]}\}$  [72]. Here,  $\text{Tr}(\cdot)$  is the trace of a matrix and the normalization constant  $\nu$  guarantees that the average transmission power is constrained to  $P_{\text{t}} = \mathbb{E}\{\mathbf{x}^{\text{H}}\mathbf{x}\} = 1$ . To maintain the focus on the

proposed concept, this chapter concentrates on zero-forcing (ZF) precoding, although it is clear that the benefits of the proposed strategy also apply to other precoding schemes. As indicated in (2.8), the signal transmitted by the ZF precoder is given by

$$\mathbf{x} = \nu \cdot (\tilde{\mathbf{G}}^H)^\dagger \mathbf{u} = \frac{\tilde{\mathbf{G}} (\tilde{\mathbf{G}}^H \tilde{\mathbf{G}})^{-1} \mathbf{u}}{\sqrt{\mathbb{E} \left\{ \text{Tr} \left[ (\tilde{\mathbf{G}}^H \tilde{\mathbf{G}})^{-1} \right] \right\}}}, \quad (6.5)$$

where  $\tilde{\mathbf{G}}^H$  represents the estimate of the downlink channel available at the BS.

### 6.2.2 Physically-Constrained Channel Model for 2D Antenna Arrays

In contrast to previous chapters, where uncorrelated channels were considered, this section describes the physical channel model that will be employed in the following to characterize the particular properties of size-constrained massive MIMO BSs, which constitute the focus of this chapter [84,87,101,111,207]. The consideration of these physically constrained structures is motivated by the possible deployment of future massive MIMO transceivers within the limited spaces of today's BSs. Accordingly, the MIMO arrays might experience transmit correlation and mutual coupling that will be dependent on the increasing number of antenna elements. In particular, since large scale BSs are expected to be implemented in 2D and 3D antenna structures that allow packing more elements in a fixed physical space, this section describes the physical channel model of a planar antenna array [11]. In this study, the effects of mutual coupling are neglected since they can be compensated by impedance matching techniques [245]. Therefore, the propagation channel from the  $k$ -th user to the BS can be expressed as [84,207]

$$\mathbf{g}_k = \mathbf{A}_k^H \mathbf{z}_k, \quad (6.6)$$

where  $\mathbf{z}_k \sim \mathcal{CN}(\mathbf{0}, \mathbf{I}_{D_k})$ ,  $D_k$  corresponds to the number of directions in which the angular domain is divided, and  $\mathbf{A}_k \in \mathbb{C}^{D_k \times N}$  is the steering matrix containing the  $D_k$  transmit steering vectors of the antenna array. The transmit steering matrix of the  $k$ -th user is

given by [101, 207]

$$\mathbf{A}_k = \frac{1}{\sqrt{D_k}} [\mathbf{a}^T(\phi_{k,1}, \theta_{k,1}), \dots, \mathbf{a}^T(\phi_{k,D_k}, \theta_{k,D_k})]^T. \quad (6.7)$$

Here, the directions of departure (DoD) of the  $k$ -th user are characterized by  $\phi_{k,n} \in [\phi_k^{\min}, \phi_k^{\max}]$  and  $\theta_{k,n} \in [\theta_k^{\min}, \theta_k^{\max}]$ , which specify the azimuth and elevation angles of departure respectively. The transmit steering vectors of an arbitrary rectangular array can be expressed as [106]

$$\mathbf{a}(\phi_{k,n}, \theta_{k,n}) = \left[ 1, e^{j2\pi[d_h \sin(\theta_{k,n}) \sin(\phi_{k,n})]}, \dots, e^{j2\pi[(M_h-1)d_h \sin(\theta_{k,n}) \sin(\phi_{k,n}) + (M_v-1)d_v \sin(\theta_{k,n}) \cos(\phi_{k,n})]} \right]. \quad (6.8)$$

Here,  $d_h$  and  $d_v$  denote the inter-antenna spacing in the horizontal and vertical axes normalized by the carrier wavelength  $\lambda$ , and  $M_h$  and  $M_v$  represent the number of antennas allocated in the horizontal and vertical axes respectively. Clearly,  $d_h = d_v$  for the particular case of uniform rectangular arrays (URAs). The total number of antennas is therefore given by  $N = M_h \times M_v$ . Moreover, to provide a fair comparison, this chapter considers that the horizontal and vertical inter-antenna distances at the BS are given by

$$d_{\{h,v\}} = \frac{L_{\{h,v\}}}{(M_{\{h,v\}} - 1)}, \quad (6.9)$$

where  $L_{\{h,v\}}$  denotes the fixed horizontal and vertical lengths of the antenna array. The total surface in which the antennas are deployed is denoted as  $L = L_h \times L_v$ . Note that the above model assumes that there is no spatial correlation between users, a reasonable consideration since the inter-user distance is usually larger than  $\lambda$  [101].

*Remark:* Since the physical space dimensions of the antenna array are predetermined, the above entails that the inter-antenna correlation depends on the total number of antennas installed. This model accurately captures the inter-antenna correlation that arises due to insufficient antenna separation, which constitutes the focus in the following.

*Remark:* Linear antenna arrays can be regarded as a particular

case of the described rectangular array by letting  $M_v = 1$  and setting  $\theta_{k,n} = \pi/2 \forall k \in \{1, \dots, K\}, n \in \{1, \dots, D_k\}$  [101].

### 6.3 Relaxing the CSI Acquisition: Incomplete CSI

The dense deployment of antenna arrays leads to an increased correlation between the antenna elements, which also translates to a larger similarity between the communication channels of closely spaced antennas [11, 101]. This circumstance motivates considering the practicability of collecting the CSI for a subset of antennas during the CSI acquisition stage and analyzing its effects in the operation of the communication system. Formally, let the set that indexes all the antenna elements allocated at the BS be defined as

$$\mathcal{N} = \{1, \dots, N\}. \quad (6.10)$$

Each entry of the set indexes the  $n$ -th antenna of the planar array  $A_n$  as shown in Fig. 6.1(a). Furthermore, let the sets  $\mathcal{B} \subset \mathcal{N}$  and  $\mathcal{C} \subset \mathcal{N}$  be defined as two subsets of  $\mathcal{N}$  satisfying

$$\mathcal{B} \cap \mathcal{C} = \emptyset, \mathcal{B} \cup \mathcal{C} = \mathcal{N}. \quad (6.11)$$

In the previous expressions,  $\subset$ ,  $\cup$  and  $\cap$  denote the subset, union and intersection of sets respectively. Specifically, the subset  $\mathcal{B}$  indexes the antennas whose CSI has been acquired during the pilot training stage, and  $\mathcal{C}$  determines the antennas without instantaneous CSI availability. Subsequently,  $|\mathcal{B}| = N_c \leq N$  and  $|\mathcal{C}| = N - N_c$  determine the number of antennas with and without instantaneous CSI knowledge respectively. Here  $|\cdot|$  denotes the cardinality of a set.

The proposed scheme aims at limiting the collection of instantaneous CSI to a number of antennas  $N_c \leq N$ . Subsequently, the large inter-antenna correlation that arises in tightly packed antenna arrays is exploited to determine the CSI for the rest of antennas. In other words, only the antennas indexed by the subset  $\mathcal{B}$  will be active during pilot signal reception, and the averages of the information acquired will be subsequently used

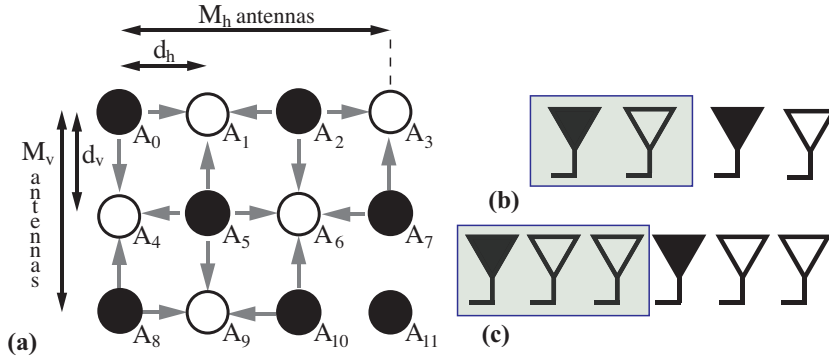


**Figure 6.1:** (a) Example of CSI distribution for  $M_h = 4$ ,  $M_v = 3$  and  $N_c = 7$ . (b), (c) Basic CSI distribution patterns. Black and white elements represent antennas with and without acquired CSI respectively.

as CSI for the remaining antennas for the purposes of precoding and detection. This brings the following critical benefits that will be studied in the following:

- The signal processing load of the channel estimation and signal transmission processes can be dramatically reduced. This can be attained by limiting the number of antennas simultaneously active during pilot reception and by performing an insightful design of the transmit signals.
- The number of receive RF chains activated throughout the pilot training and downlink transmission stages is constrained to  $N_c$ , hence potentially reducing the circuit power consumption of the related circuitry.

At this point it is remarked that the incomplete acquisition process affects the decision metric obtained after pilot correlation in (6.2), which for  $\eta_{\text{tr}} = K$  can be expressed as

$$\hat{\mathbf{P}}|_{[\mathcal{B}, \mathcal{K}]} = \sqrt{\rho_{\text{tr}}} \cdot \mathbf{G}|_{[\mathcal{B}, \mathcal{K}]} + (\bar{\mathbf{N}} \mathbf{\Theta}^H)|_{[\mathcal{B}, \mathcal{K}]}, \quad (6.12)$$

where  $\mathbf{C}|_{[\mathcal{T}_1, \mathcal{T}_2]}$  represents the sub-matrix obtained by selecting the rows given by  $\mathcal{T}_1$  and the columns specified by  $\mathcal{T}_2$ . In this notation, the sets  $\mathcal{K} = \{1, \dots, K\}$  and  $\mathcal{N} = \{1, \dots, N\}$  are commonly employed to select all the columns or rows depending on the context. Similarly,  $\mathbf{c}|_{[\mathcal{T}]}$  is employed to denote the sub-vector obtained by selecting the entries determined by  $\mathcal{T}$ . Throughout this chapter,  $\mathbf{c}_{k,n}$  denotes the  $n$ -th entry of the vector  $\mathbf{c}_k$  for ease of notation.

After the incomplete channel estimation process, the channel of the  $k$ -th user can be expressed as

$$\tilde{\mathbf{g}}_k|_{[\mathcal{B}]} = \hat{\mathbf{g}}_k, \quad (6.13)$$

$$\tilde{\mathbf{g}}_k|_{[\mathcal{C}]} = f\left(\tilde{\mathbf{g}}_k|_{[\mathcal{B}]}\right), \quad (6.14)$$

where  $\hat{\mathbf{g}}_k \in \mathbb{C}^{N_c \times 1}$  denotes the uplink channel of the  $k$ -th user for the antennas with CSI acquired during the training stage (subject to CSI acquisition errors), and  $f(\cdot) : \mathbb{C}^{N_c} \rightarrow \mathbb{C}^{(N-N_c)}$  is a linear function whose definition will be considered in the following.

### 6.3.1 Distribution of the CSI on the Antenna Array

The definition of  $\mathcal{B}, \mathcal{C}$  and  $f(\cdot)$  impacts the performance and complexity of the proposed scheme. Ideally, an optimization problem could be formulated for determining the antennas that collect instantaneous CSI during the pilot training stage. The objective of this problem would be minimizing the effect of the incomplete CSI acquisition on the accuracy of the resulting channel estimate. This however entails significant complexity and is therefore out of the scope of this study, which focuses on a low-complexity CSI distribution and averaging approach. For this reason, this chapter proposes a CSI distribution strategy that leverages on the use of predefined CSI distribution patterns. The considered scheme aims at obtaining a low-complexity solution by exploiting the following intuition: the larger the correlation between the channels without instantaneous CSI and the channels employed to derive their CSI, the smaller the CSI error introduced. In other words, for any antenna deactivated during the training stage, there must be others with their instantaneous CSI available in its proximity. Specifically, the proposed CSI distribution procedure is based on the combination of the two basic CSI distribution patterns shown in Fig. 6.1(b) and (c) with colored subsets. In these figures, the black and white antennas represent the antennas with and without instantaneous CSI acquired during the training stage respectively. These patterns facilitate an efficient distribution of the CSI for the cases  $(N_c/N) \geq (1/3)$  that are explored in the following<sup>1</sup>.

<sup>1</sup>Note that this is adequate since it will be shown that  $(N_c/N) \geq (1/3)$  is required to obtain a satisfactory performance in realistic massive MIMO systems. This is because the double polarized antennas to be employed in future deployments occupy a physical space that might impede placing them arbitrarily close.

**Algorithm 2** Pseudocode of the CSI distribution algorithm

---

**Input:**  $N, N_c, M_h, M_v$

1: **Output:**  $\mathcal{B}, \mathcal{C}$

2:  $\mathcal{B}, \mathcal{C} \leftarrow \emptyset$  {Initialization}

   {3 – 4 : Maximum and minimum number of antennas with instantaneous CSI per row}

3:  $N_{\max} \leftarrow \lceil N_c/M_v \rceil$

4:  $N_{\min} \leftarrow \lfloor N_c/M_v \rfloor$

   {5 – 6 : Number of rows with the maximum and minimum number of antennas with CSI per row}

5:  $M_{\max} \leftarrow (N_c - M_v N_{\min})$

6:  $M_{\min} \leftarrow M_v - M_{\max}$

7:  $\{\mathcal{B}_{\min}, \mathcal{B}_{\max}\} \leftarrow$  Create reference CSI distribution patterns per row with  $N_{\min}$  ( $\mathcal{B}_{\min}$ ) and  $N_{\max}$  ( $\mathcal{B}_{\max}$ ) antennas with CSI by combining the basic patterns shown in Fig. 6.1(b) and (c) and adding additional antennas with CSI where required}

8: **for**  $j = 0 \rightarrow (M_v - 1)$  **do**

9:   **if**  $j < M_{\min}$  **then**

10:      $\mathcal{B} \leftarrow \mathcal{B} \cup \mathcal{B}_{\min}$

11:   **else**

12:      $\mathcal{B} \leftarrow \mathcal{B} \cup \mathcal{B}_{\max}$

13:   **end if**

14:    $\mathcal{B}_{\min} \leftarrow$  {Circular shift of  $\mathcal{B}_{\min}$  to determine the antennas with CSI in the  $j$ -th row for  $j < M_{\min}$ }

15:    $\mathcal{B}_{\max} \leftarrow$  {Circular shift of  $\mathcal{B}_{\max}$  to determine the antennas with CSI in the  $j$ -th row for  $j \geq M_{\min}$ }

16: **end for**

17:  $\mathcal{C} \leftarrow \mathcal{B}^C$

---

The pseudocode of the proposed CSI distribution procedure is shown in Algorithm 2, where  $\emptyset$  represents the empty set,  $(\cdot)^C$  denotes the complement of a set, and  $\lfloor \cdot \rfloor$  and  $\lceil \cdot \rceil$  denote the floor and ceiling functions, respectively. An illustrative example of the application of this strategy is shown in Fig. 6.1(a) for the case of  $M_h = 4$ ,  $M_v = 3$  and  $N_c = 7$ . The application of Algorithm 2 generalizes the CSI distribution process to more complicated cases. Overall, this representative example shows that the proposed CSI distribution aims at maximizing the number of adjacent antennas with acquired CSI for each antenna without this information to efficiently exploit the inter-antenna correlation.

The operation of the proposed CSI distribution algorithm can be described as follows: Initially, the number of antennas per row with instantaneous CSI is determined by assigning a similar number of antennas with CSI per row to evenly distribute the CSI. For instance, Fig. 6.1(a) shows that the first  $M_{\min} = 2$  rows of antennas have  $N_{\min} = 2$

antennas with CSI, whereas the last one has  $N_{\max} = 3$  antennas with CSI. After this, the antennas with CSI are distributed for each row by combining the antenna patterns depicted in Fig. 6.1(b) and (c), and adding antennas with CSI to these to ensure that the total number of antennas with CSI per dimension is the one previously specified. For instance, Fig. 6.1(a) shows that the CSI in the first row of antennas is distributed by consecutively combining two of the antenna patterns described in Fig. 6.1(b), whereas for the CSI distribution in the third row an additional antenna with CSI has been added. Note that the additional antennas with CSI are solely required for the cases  $(N_c/N) > 1/2$ , and that their specific positions have shown to have a negligible performance impact. Subsequently, the patterns are shifted circularly to determine the distribution of the CSI in the following rows. This is illustrated in Fig. 6.1(a), where it can be seen that the CSI distribution of the second row is obtained by shifting the distribution of the previous one. This procedure ensures that the CSI of the antennas is evenly distributed, thus reducing the distance of the antennas with and without instantaneous CSI.

*Remark:* The employment of the basic CSI distribution patterns does not restrict the proposed scheme to a solution with fixed  $N_c$ . Instead, they facilitate analyzing the complexity-performance trade-off that arises for varying  $N_c$ , since different system requirements might motivate the employment of distinct solutions as studied in the following.

After defining the sets  $\mathcal{B}$  and  $\mathcal{C}$ , the remaining step consists on determining the CSI of the antennas that were inactive during the training stage. Let  $\mathcal{T}_n$  denote the  $n$ -th entry of a set. Then, the CSI of the antennas without instantaneous CSI is obtained by averaging the CSI of the closest antennas with this information. Subsequently, the  $\mathcal{C}_n$ -th entry of the channel vector of the  $k$ -th user can be expressed as

$$\tilde{\mathbf{g}}_{k,\mathcal{C}_n} = \frac{1}{M_{\mathcal{C}_n}} \sum_{i=1}^{M_{\mathcal{C}_n}} \hat{\mathbf{g}}_{k,\mathcal{B}_i^{\mathcal{C}_n}}. \quad (6.15)$$

Here,  $M_{\mathcal{C}_n}$  denotes the number of neighbour antennas with indexes  $\mathcal{B}^{\mathcal{C}_n} \subset \mathcal{B}$  employed to average the CSI for the  $\mathcal{C}_n$ -th antenna. In other words, the CSI of a given antenna without instantaneous CSI knowledge is obtained by averaging the CSI of the antennas

belonging to  $\mathcal{B}^n$ . The global estimated communication channel with incomplete CSI after the averaging operations can be therefore expressed as

$$\tilde{\mathbf{G}} = \mathbf{L}^H \hat{\mathbf{G}}, \quad (6.16)$$

where  $\hat{\mathbf{G}} \in \mathbb{C}^{N \times K}$  is the estimated channel matrix formed by the entries that correspond to the antennas active during the training stage, which are given by  $\hat{\mathbf{g}}_k|_{[\mathcal{B}]}$ , and zeros elsewhere. Moreover,  $\mathbf{L} \in \mathbb{R}^{N \times N}$  describes how the available CSI is combined to obtain the CSI for the rest of the antennas. This matrix is referred to as the CSI averaging matrix and its  $n$ -th column is given by

$$\mathbf{L}|_{[\mathcal{N},n]} = \begin{cases} \mathbf{I}|_{[\mathcal{N},n]}, & \forall n \in \mathcal{B}, \\ \frac{1}{M_n} \mathbf{r}_{\mathcal{B}^n}, & \forall n \in \mathcal{C}, \end{cases} \quad (6.17)$$

where  $\mathbf{I}|_{[\mathcal{N},n]} \in \mathbb{Z}^{N \times 1}$  denotes the  $n$ -th column of an  $N \times N$  identity matrix, and  $\mathbf{r}_{\mathcal{B}^n} \in \mathbb{Z}^{N \times 1}$  is a vector with all its entries set to zero except for those found in the positions given by the set  $\mathcal{B}^n$ , which are equal to one. Similarly to (6.15),  $M_n$  corresponds to the number  $|\mathcal{B}^n|$  of antennas employed for interpolating the CSI of the  $n$ -th antenna. Note that  $\mathbf{L} = \mathbf{I}_N$  when complete CSI is acquired.

*Remark:* Although more intricate strategies can be implemented, this chapter focuses on the simple averaging operation for reasons of illustration and for not detracting the attention from the basic principle introduced here. Moreover, this operation is especially practical due to both the hardware and the signal processing advantages detailed hereafter.

### 6.3.2 Implications of the Acquisition of Incomplete CSI

The averaging of the CSI has several implications on a range of communication aspects such as the signal processing load or the hardware complexity that are considered in this section.

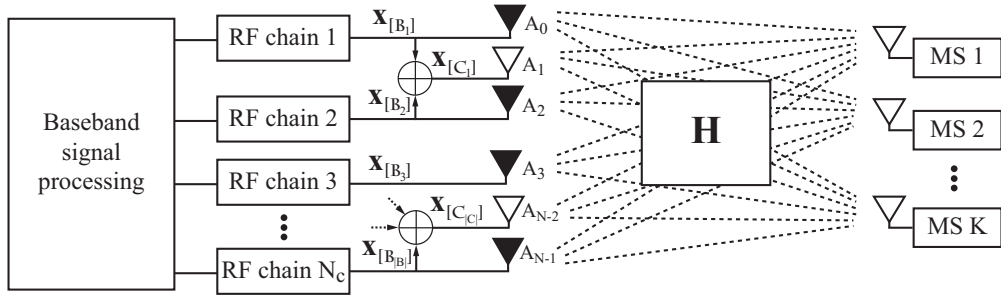


**Figure 6.2:** Block diagram of the proposed transmission scheme. Black and white antennas represent elements with and without acquired CSI respectively.

### 6.3.2.1 Dimensionality Reduction of the Received Training Signals

Inherently, the dimensions of the received training signals are reduced when incomplete CSI is acquired. An immediate consequence of this is that only  $N_c \leq N$  RF chains remain active during the pilot training stage, which facilitates reducing the total power consumption of standard channel estimation approaches [79]. Simultaneously, the computational complexity of the CSI estimation process is reduced due to the smaller dimensions of the acquired pilot signals. Particularly, apart from a decrease in the complexity of the conventional pilot correlation process shown in (6.2), the dimensionality reduction can be particularly beneficial when complex channel estimation strategies are employed due to the polynomial dependence of their complexity on  $N_c$  [85, 87]. This comes at the cost of introducing an error in the channel estimate, which clearly depends on the inter-antenna distance, the quality of the acquired CSI, and the number of antennas with instantaneous CSI as studied in Sec. 6.4.

### 6.3.2.2 Data Transmission Stage: Reduced RF-Chain Implementation

The differences in the estimated channel with full and incomplete CSI have a direct effect on the achievable rates of the system that will be explored in Sec. 6.7. However, the incomplete acquisition of CSI also produces an interesting relationship between the

signals transmitted from the different antennas, which can be re-expressed as

$$\mathbf{x} = \nu \cdot \mathbf{F}\mathbf{u} \iff \begin{cases} \mathbf{x}|_{[\mathcal{B}]} = \frac{\mathbf{F}|_{[\mathcal{B},\mathcal{K}]} \cdot \mathbf{u}}{\mathbb{E} \left\{ \sqrt{\text{Tr}[\mathbf{F}^H \mathbf{F}]} \right\}}, \\ \mathbf{x}|_{[\mathcal{C}]} = \left( \mathbf{L}|_{[\mathcal{B},\mathcal{C}]} \right)^H \cdot \mathbf{x}|_{[\mathcal{B}]}. \end{cases} \quad (6.18)$$

for the conventional matched filter (MF), ZF and regularized ZF precoding schemes. The above expression entails that the signals of the antennas that were deactivated during the training stage can be obtained by combining the signals generated for the antennas whose CSI was acquired. This has a direct consequence on the signal processing load per transmitted symbol, since the signal generation for the set  $\mathcal{C}$  can be done in the analog domain by signal splitting and combining to avoid the computation of  $\mathbf{x}|_{[\mathcal{C}]}$  in the baseband processing stage. This dispenses with the need of  $N - N_c$  RF chains w.r.t. conventional designs as shown in Fig. 6.2.

## 6.4 CSI Error Under Incomplete CSI

First, it should be clarified that in the following the term imperfect CSI is employed when solely describing CSI acquisition errors, whereas the term incomplete CSI is reserved for the cases in which the CSI of a subset of antennas is not acquired. The acquisition of incomplete and imperfect CSI impacts on the quality of the channel estimated and the resulting performance of precoding and detection schemes. For this reason, this section concentrates on characterizing the error introduced by the proposed strategy in the channel estimation process. The channel estimate generated after incomplete CSI acquisition for the  $k$ -th user (6.16) can be re-expressed as [72]

$$\tilde{\mathbf{g}}_k = \mathbf{g}_k - \bar{\mathbf{g}}_k, \quad (6.19)$$

where  $\bar{\mathbf{g}}_k \in \mathbb{C}^{N \times 1}$  represents the error introduced by the acquisition of incomplete and imperfect CSI. Similarly to the previous chapters, the imperfect estimate of the

communication channel for the antennas with CSI is characterized as [207, 215]

$$\widehat{\mathbf{g}}_k|_{[\mathcal{B}]} = \left( \mathbf{A}_k^H \left( \sqrt{1 - \tau_k^2} \mathbf{z}_k + \tau_k \mathbf{q}_k \right) \right) \Big|_{[\mathcal{B}]}, \quad (6.20)$$

where  $\mathbf{q}_k \sim \mathcal{CN}(0, \mathbf{I}_{D_k})$  is independent of  $\mathbf{z}_k$  [207, 215] and  $\tau_k$  is a variable that models the quality of the acquired CSI. The stochastic imperfect CSI model employed in (6.20) facilitates the derivation of intuitive expressions for characterizing the behaviour of the proposed scheme. In particular,  $\tau_k = 0$  indicates that perfect CSI is collected, whereas  $\tau_k = 1$  corresponds to the case where only statistical information is available at the transmitter. Moreover, the error of the channel after the averaging operation for a relevant antenna without CSI is clearly conditioned by its position on the antenna array, the inter-element spacing, and the number of antennas selected for averaging. In the following the impact of the incomplete and imperfect CSI acquisition on the accuracy of the channel estimation is modeled by using the channel error factor [231]

$$\Delta_k = \frac{\mathbb{E} \left\{ \|\bar{\mathbf{g}}_k\|_2^2 \right\}}{\mathbb{E} \left\{ \|\mathbf{g}_k\|_2^2 \right\}} = \frac{\mathbb{E} \left\{ \|\mathbf{g}_k - \tilde{\mathbf{g}}_k\|_2^2 \right\}}{\mathbb{E} \left\{ \|\mathbf{g}_k\|_2^2 \right\}}. \quad (6.21)$$

Specifically, since the focus of this chapter is placed on physically-constrained systems, the following theorem details the behaviour of the above metric for the channel model introduced in Sec. 6.2.2.

**Theorem 6.4.1** Let the communication channel be described as  $\mathbf{g}_k = \mathbf{A}_k^H \mathbf{z}_k$  with  $\mathbf{z}_k \sim \mathcal{CN}(\mathbf{0}, \mathbf{I}_{D_k})$  for a given  $\mathbf{A}_k$ . Also let  $\widehat{\mathbf{g}}_k|_{[\mathcal{B}]} \in \mathbb{C}^{N_c \times 1}$  be the noisy channel estimate of the channel modeled by following (6.20). Moreover, consider the channel of the antennas without CSI to be computed by averaging the imperfect CSI from the nearby antennas as described in Sec. 6.3. Then, the channel error factor is given by

$$\begin{aligned} \Delta_k = & \frac{1}{N} \sum_{n \in \mathcal{B}} \tau_k^2 \mathbf{R}_k|_{[n,n]} + \frac{1}{N} \sum_{n \in \mathcal{C}} \left[ \mathbf{R}_k|_{[n,n]} + \frac{1}{(M_n)^2} \sum_{i \in \mathcal{B}^n} \mathbf{R}_k|_{[i,i]} \right. \\ & \left. - \frac{2\sqrt{1 - \tau_k^2}}{M_n} \operatorname{Re} \left( \sum_{i \in \mathcal{B}^n} \mathbf{R}_k|_{[n,i]} \right) + \frac{2}{(M_n)^2} \operatorname{Re} \left( \sum_{i,j \in \mathcal{B}^n, i > j} \mathbf{R}_k|_{[j,i]} \right) \right], \end{aligned} \quad (6.22)$$

where  $\mathbf{R}_k$  is the correlation matrix of the channel of the  $k$ -th user given by  $\mathbf{R}_k =$

$\mathbb{E} \{ \mathbf{g}_k \mathbf{g}_k^H \} = \mathbf{A}_k^H \mathbf{A}_k$ . Moreover,  $\mathcal{B}^n$  and  $M_n$  represent the indices and total number of antennas employed for computing the CSI of the  $n$ -th antenna as defined in Sec. 6.3 respectively.

**Proof of Theorem 6.4.1** The proof of Theorem 6.4.1 is provided in Appendix D.  $\square$

The above theorem characterizes the impact of applying the proposed strategy based on the entries of the channel correlation matrix of the true channel, the number of antennas with and without instantaneous CSI, the number of antennas employed for the averaging operation, and the quality of the acquired CSI. In the following, a set of relevant corollaries based on the results of Theorem 6.4.1 are derived.

**Corollary 6.4.1.1** *Dependence of  $\Delta_k$  on  $\tau_k$ .* The channel error factor  $\Delta_k$  is an increasing function of the imperfect CSI parameter  $\tau_k$  for transmitters in which the channels of the neighbour antennas are strongly correlated, i.e., those channels satisfying  $\text{Re} \left( \sum_{i \in \mathcal{B}^n} \mathbf{R}_k|_{[n,i]} \right) > 0$ .

**Proof of Corollary 6.4.1.1** The proof follows from the analysis of the terms in (6.22) influenced by the factor  $\tau_k$

$$t_1 = \frac{1}{N} \sum_{n \in \mathcal{B}} \tau_k^2 \mathbf{R}_k|_{[n,n]}, \quad n \in \mathcal{B}, \quad (6.23)$$

and

$$t_2 = -\frac{2\sqrt{1-\tau_k^2}}{M_n} \text{Re} \left( \sum_{i \in \mathcal{B}^n} \mathbf{R}_k|_{[n,i]} \right), \quad n \in \mathcal{C}. \quad (6.24)$$

Clearly, both terms are increasing functions of  $\tau_k$  provided that  $\text{Re} \left( \sum_{i \in \mathcal{B}^n} \mathbf{R}_k|_{[n,i]} \right) > 0$ , which holds true when the channels of the adjacent antennas are severely correlated.  $\square$

Note that the above corollary corroborates the intuition that the collection of imperfect CSI during the training stage influences the quality of the channel approximation generated for the antennas deactivated throughout this process. This can be explained by the dependence of  $t_2$  on  $\tau_k$ .

Additionally, it is also intuitive that the channel error factor  $\Delta_k$  is an increasing function of the inter-antenna distance  $d$  for the ranges typically considered, since the

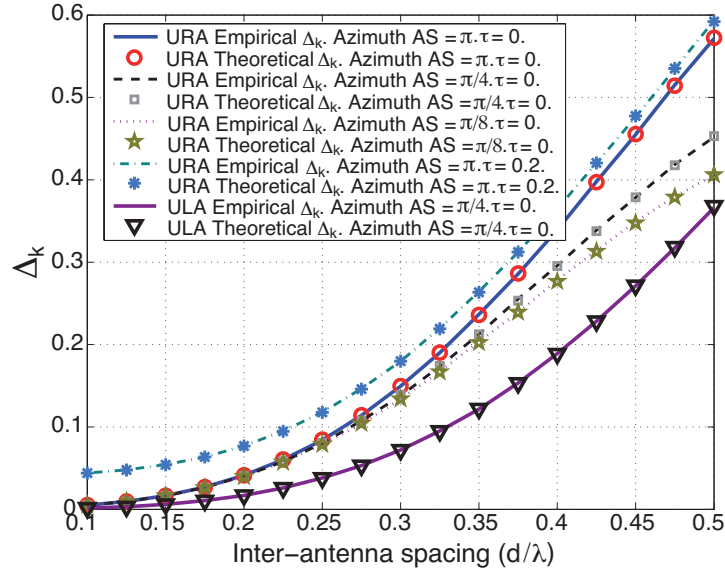


**Figure 6.3:**  $\Delta_k$  vs. inter-antenna spacing for azimuth sector angles of  $\pi$ ,  $\pi/4$  and  $\pi/8$  radians (URA) and  $\pi/4$  (ULA).  $N = 144$ ,  $N_c = N/2$  and  $K = 16$ .

inter-antenna correlation depends on this parameter. However, explicitly showing this for the physical channel model described in Sec. 6.2.2 and a general case is infeasible due to the complexity of the expressions involved. For this reason, the following corollary explores the particular case of a uniform linear array (ULA) with reduced angle spreads, which can arise naturally as manifested by the one-ring correlation model [25].

**Corollary 6.4.1.2** *Dependence of  $\Delta_k$  on  $d$ .* Let the antennas at the BS be placed in a ULA configuration. Moreover, consider that perfect CSI is acquired for the active antennas during the training stage,  $N/N_c \geq 2$  and small angle spreads such that  $\sin(\phi) \approx \phi$  and  $\cos(\phi) \approx (1 - \phi^2/2)$ . Then, the channel error factor  $\Delta_k$  is a monotonically increasing function of the inter-antenna spacing  $d$ .

**Proof of Corollary 6.4.1.2** The proof of Corollary 6.4.1.2 is given in Appendix E.  $\square$

The above observation can be explicitly seen in Fig. 6.3, which represents the variation of the theoretical and empirical metric  $\Delta_k$  in (6.21) for increasing values of inter-antenna spacing when the channel model of Sec. 6.2.2 is employed. The theoretical results in Fig. 6.3 and Fig. 6.4 have been obtained by direct application of (6.22). These results consider transmitter with either  $M_h = M_v = 12$  (URA) or  $M_v = 1$  and  $M_h = 144$  (ULA) antennas,  $N_c = N/2$ , and  $K = 16$  users. The number of angular directions is

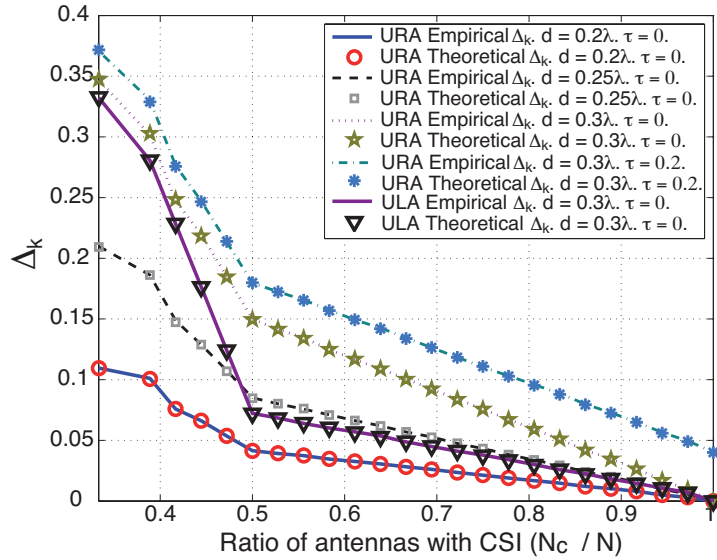


**Figure 6.4:**  $\Delta_k$  vs. ratio of antennas with CSI ( $N_c/N$ ) for different inter-antenna spacings  $d$ .  $N = 144$  and  $K = 16$ .

arbitrarily set to  $D_k = 50$  in (6.7) [84], and the elevation angles of departure are equidistributed within sector angles of  $\pi/3$  radians. Note that, while other arbitrary choices for  $D_k$  could be adopted, the modification of this parameter does not modify the trends and conclusions derived in the following. The different azimuth angle spreads,  $\pi$ ,  $\pi/4$  and  $\pi/8$  radians, characterize the effects of having a limited angle spread on the proposed scheme. For simplicity,  $\tau_k = \tau, \forall k \in \{1, \dots, K\}$ . In this figure and throughout this chapter the number of antennas whose CSI is averaged are selected depending on the number of antennas with CSI as follows. On the one hand, for the cases in which  $(N_c/N) \geq (1/2)$ , only the CSI of the vertically and horizontally adjacent antennas with CSI is averaged. On the other hand, when the number of antennas with CSI is further reduced so that  $(N_c/N) < (1/2)$ , the CSI of the diagonally adjacent antennas is employed to guarantee that the CSI of a sufficient number of antennas is averaged. Altogether, it can be seen that the error of the channel generated after the averaging operation decreases as the antenna inter-spacing is reduced. This can be explained by the larger correlation experienced between neighbour antennas, which also increases when the angle spread is constrained.

The evolution of  $\Delta_k$  for a varying number of antennas with CSI is shown in Fig. 6.4 for the same setup of Fig. 6.3. This figure considers an azimuth angle spread of

$\pi$  radians for the URA BS and of  $\pi/4$  for the ULA BS, and different inter-antenna spacings  $d$ . From the results of this figure it can be concluded that small variations in the number of antennas with CSI strongly influence the error for  $N_c/N < (1/2)$ , whereas this impact is reduced for  $N_c/N \geq (1/2)$ . Intuitively, the reason for this behaviour is related to the number of antennas whose CSI is averaged for a given antenna without CSI, and it is especially pronounced for the ULA BS. Furthermore, it can be seen that the theoretical derivation closely resembles the empirical results in both Fig. 6.3 and Fig. 6.4 with perfect ( $\tau_k = 0$ ) and imperfect CSI ( $\tau_k = 0.2$ ).

## 6.5 Complexity Analysis

This section characterizes the improvements offered by the proposed strategy regarding the signal processing load. Specifically, it is shown that the smaller number of antennas simultaneously active during the CSI acquisition procedure reduces the number of required signal processing operations for channel estimation and precoding. This section follows the analysis of [244] for reasons of reference.

The signal processing operations performed in a TDD communication system can be divided into three different stages, namely CSI acquisition stage, downlink signal transmission, and uplink signal reception as illustrated in Fig. 2.4 [243, 244]. These stages correspond to the communication phases in which the channel coherence time is divided and their respective lengths determine the global complexity as shown in the following.

### 6.5.1 CSI Acquisition Stage

Throughout this stage, the BS receives the pilot signals transmitted by the MSs and uses these to estimate the communication channel [79, 243, 244]. For simplicity, it is considered that the coherence time of the long-term statistics is significantly larger than the channel coherence time. The above entails that a significant portion of the operations to perform the channel estimation after the pilot correlation process remain

valid for a large number of coherence blocks. This makes the pilot correlation process dominate the complexity per coherence block [85]. The total number of real floating-point operations (flops) of this procedure as performed in (6.2),  $C^{\text{tr}}$ , depends on the training length in number of symbols  $\eta_{\text{tr}}$  and is given by [205, 232, 244]

$$C^{\text{tr}} = 8N_c K \eta_{\text{tr}} \stackrel{(a)}{=} 8N_c K^2, \quad (6.25)$$

where (a) holds because it is considered that orthogonality between the pilot training signals of the system users is preserved by letting  $\eta_{\text{tr}} = K$  [244]. Similarly to the previous chapters in this Thesis, the common assumption that real multiplications (divisions) have the same complexity of real additions (subtractions) has been followed [205]. Moreover, it is also considered that complex additions and multiplications involve two and six real floating-point operations respectively [205, 232].

### 6.5.2 Data Transmission (Downlink) Stage

The complexity of the downlink stage is determined by the operations required to generate the precoding matrix at the beginning of each coherence period, and the operations to generate the transmitted signal in every channel use [244]. For the sake of brevity, in the following it is considered that the ZF precoding matrix is computed via the conventional singular value decomposition (SVD) approach. Other strategies such as the Cholesky decomposition have been shown to offer similar complexity results for the scenarios considered in this chapter [231]. In particular, let  $\tilde{\mathbf{G}}^{\text{H}} = \mathbf{U}\mathbf{\Sigma}\mathbf{V}^{\text{H}}$  be the SVD of the estimated downlink channel matrix. Here,  $\mathbf{U} \in \mathbb{C}^{K \times K}$  and  $\mathbf{V} \in \mathbb{C}^{N \times N}$  are unitary matrices comprised of the left and right singular vectors of  $\tilde{\mathbf{G}}^{\text{H}}$  respectively, and  $\mathbf{\Sigma} \in \mathbb{C}^{K \times N}$  is a diagonal matrix containing the ordered singular values of  $\tilde{\mathbf{G}}^{\text{H}}$ . The pseudo-inverse precoding matrix can be subsequently obtained from the SVD as  $(\tilde{\mathbf{H}}^{\text{H}})^{\dagger} = \mathbf{V}\mathbf{\Sigma}^{-1}\mathbf{U}^{\text{H}}$ . The complexity of this process is given by

$$C_{\text{inv}}^{\text{dl}} = C_{\text{SVD}}^{\text{dl}} + C_{\text{div}}^{\text{dl}} + C_{\text{mult}}^{\text{dl}} = (24K^3 + 16K^2N) + K + (2KN + 8K^2N), \quad (6.26)$$

where  $C_{\text{SVD}}^{\text{dl}}$  characterizes the complexity of performing a complex SVD,  $C_{\text{div}}^{\text{dl}}$  refers to the complexity of dividing the  $K$  real diagonal elements of  $\mathbf{\Sigma}$ , and  $C_{\text{mult}}^{\text{dl}}$  accounts for the operations required to multiply a complex full matrix with a real diagonal matrix and two full complex matrices [205]. Note that this computationally intensive operation only has to be performed at the beginning of each channel coherence period, since the result stays valid as long as the channel remains approximately constant.

In conventional MIMO systems, the pseudo-inverse matrix must be multiplied with the symbols to be transmitted to generate the final precoded signal  $\mathbf{x} \in \mathbb{C}^{N \times 1}$  [244]. However, the proposed strategy obtains the signal output of  $N - N_c$  antennas by splitting and combining the signal components of  $\mathbf{x}|_{[\mathcal{B}]} \in \mathbb{C}^{N_c \times 1}$  in the analog domain, hence reducing the dimensions of the required matrix-vector multiplication<sup>2</sup>. Based on this observation, the complexity of computing the precoding signal can be expressed as

$$C_{\text{pr}}^{\text{dl}} = 8N_c K \eta_{\text{dl}}, \quad (6.27)$$

where  $\eta_{\text{dl}}$  denotes the number of symbol periods assigned to downlink transmission. The complexity benefits offered by the proposed in the precoding stage can be clearly observed in (6.27), since the resulting signal processing load is a linear function of the number of antennas with acquired CSI,  $N_c$ . Combining (6.26) and (6.27), the global complexity of the precoding process during a channel coherence period can be expressed as

$$C^{\text{dl}} = C_{\text{inv}}^{\text{dl}} + C_{\text{pr}}^{\text{dl}} \approx 24K^3 + 24K^2N + 8N_c K \eta_{\text{dl}}. \quad (6.28)$$

### 6.5.3 Data Reception (Uplink) Stage

The operations to be performed during the data reception stage mirror the ones to be performed during data transmission. In the case of TDD systems, the detection matrix is readily obtained from the precoding one by exploiting channel reciprocity and the relationship  $(\tilde{\mathbf{H}}^{\text{H}})^{\dagger} = (\tilde{\mathbf{H}}^{\dagger})^{\text{H}}$ . Therefore, the complexity of the uplink stage can be

<sup>2</sup>The computational load of the signal generation process can also be reduced when each antenna has its dedicated RF chain [246].

**Table 6.1:** Complexity in number of floating-point operations (flops) of a base station with incomplete CSI.

<i>Communication phase</i>	<i>Complexity in flops</i>
CSI acquisition stage – Pilot correlation	– $C^{\text{tr}} = 8N_c K \eta_{\text{tr}}$
Downlink stage – Signal generation – Precoding matrix	– $C_{\text{pr}}^{\text{dl}} = 8N_c K \eta_{\text{dl}}$ – $C_{\text{inv}}^{\text{dl}} = (24K^3 + 16K^2N) + K + (2KN + 8K^2N)$
Uplink stage – Signal detection	– $C^{\text{ul}} = 8NK \eta_{\text{ul}}$
Total complexity	– $C_{\text{tot}} \approx 24K^3 + 24K^2(N + N_c/3) + 8K(N_c \eta_{\text{dl}} + N \eta_{\text{ul}})$

computed as

$$C^{\text{ul}} = 8NK \eta_{\text{ul}}, \quad (6.29)$$

where  $\eta_{\text{ul}}$  stands for the number of symbol periods assigned to the uplink stage.

#### 6.5.4 Total Complexity

The total complexity is given by

$$C_{\text{tot}} \simeq C^{\text{ul}} + C^{\text{dl}} + C^{\text{tr}}, \quad (6.30)$$

where, in general,  $C^{\text{ul}} \ll C^{\text{dl}}$  since more time resources are conventionally allocated to the downlink transmission, i.e.,  $\eta_{\text{ul}} \ll \eta_{\text{dl}}$  [1]. This entails that the operations performed during the downlink stage dominate the global complexity, which maximizes the benefits of the proposed scheme due to the reduced complexity required for precoding as shown in Table 6.1. The complexity with full CSI corresponds to  $N_c = N$  in all expressions above.

## 6.6 Achievable Rates and Energy Efficiency

### 6.6.1 Downlink Achievable Rates with Incomplete CSI

This section concentrates on the effects that the use of incomplete CSI has on the spectral and energy efficiency of the communication system. With this purpose and

following [215], the ergodic downlink sum rates of the communication system are defined as

$$R_{\text{sum}} = \frac{\eta_{\text{dl}}}{\eta_{\text{coh}}} \cdot \mathbb{E} \left\{ \sum_{k=1}^K R_k \right\}, \quad (6.31)$$

where  $\varphi = \eta_{\text{dl}}/\eta_{\text{coh}}$  accounts for the loss in the time dedicated to downlink transmission due to the required CSI acquisition and uplink stages. Moreover, a set of ergodic achievable rates  $\mathbb{E}\{R_k\}$  can be expressed as [72]

$$\mathbb{E}\{R_k\} = B \log_2(1 + \gamma_k) = BS_k, \quad (6.32)$$

where  $B$  stands for the system bandwidth,  $S_k$  represents the achievable spectral efficiency of the  $k$ -th user, and  $\gamma_k$  refers to the associated SINR for the  $k$ -th user given by [72, 79]

$$\gamma_k = \frac{\nu^2 |\mathbb{E}\{\mathbf{g}_k^H \mathbf{f}_k\}|^2}{\frac{1}{\rho_f} + \nu^2 \text{var}(\mathbf{g}_k^H \mathbf{f}_k) + \nu^2 \sum_{i \neq k} \mathbb{E}\{|\mathbf{g}_k^H \mathbf{f}_i|^2\}}, \quad (6.33)$$

where  $\mathbf{f}_k \in \mathbb{C}^{N \times 1}$  corresponds to the  $k$ -th column of the precoding matrix  $\mathbf{F}$ . The availability of incomplete and imperfect CSI impacts on the resultant SINR  $\gamma_k$  via the precoding vectors  $\mathbf{f}_k$ . This chapter employs the above sum rate expression to study the improved energy efficiency of the proposed approach in the following.

## 6.6.2 Energy Efficiency Model

Since the proposed technique presents reduced hardware and signal processing complexities, this section relies on one of the energy efficiency models introduced in Sec. 2.1.3 to characterize these improvements. Specifically, the energy efficiency is expressed in this chapter as [4, 57, 60, 61, 116]

$$\epsilon = \frac{R_{\text{sum}}}{P_{\text{tot}}}, \quad (6.34)$$

where  $R_{\text{sum}}$  refers to the system achievable sum rates in bits per second defined in (6.31) and  $P_{\text{tot}}$  denotes the total power in Watts consumed during transmission, which can be

further decomposed as [5, 61]

$$P_{\text{tot}} = \frac{P_{\text{PA}} + P_{\text{RF}} + P_{\text{BB}}}{(1 - \sigma_{\text{DC}})(1 - \sigma_{\text{MS}})(1 - \sigma_{\text{cool}})}. \quad (6.35)$$

Here,  $\sigma_{\text{DC}}$  and  $\sigma_{\text{MS}}$  characterize the losses of the DC-DC and main power supplies whereas  $\sigma_{\text{cool}}$  refers to the active cooling losses as detailed in Sec. 2.1.3 [60]. These losses scale linearly with the power consumption of the electronic components and an accurate characterization of their values has been provided in [5, 60] for different BSs. Moreover,  $P_{\text{PA}}$  denotes the average power required by the power amplifiers (PAs) and is given by

$$P_{\text{PA}} = \frac{P_{\text{t}}}{\eta}, \quad (6.36)$$

where  $\eta$  corresponds to the PA efficiency and  $P_{\text{t}}$  refers to the power required at the output of the power amplifiers. Note that only  $N_{\text{c}}$  PAs are required to generate the output signals as shown in Fig. 6.2. Moreover,  $P_{\text{RF}}$  denotes the active power consumption of the electronic components in the RF chains without accounting for that of the power amplifiers. Therefore,  $P_{\text{RF}}$  can be further expressed as

$$P_{\text{RF}} = N_{\text{c}}(P_{\text{DAC}} + P_{\text{mix}} + P_{\text{filt}}) + P_{\text{syn}}, \quad (6.37)$$

where  $P_{\text{syn}}$  represents the power consumed by the frequency synthesizer, and  $P_{\text{DAC}}$ ,  $P_{\text{mix}}$  and  $P_{\text{filt}}$  denote the power consumption of the digital-to-analog converters (DACs), signal mixers and filters included in each RF chain respectively [61, 247]. Additionally,  $P_{\text{BB}} = p_{\text{c}}C$  corresponds to the power consumption of the digital signal processor (DSP). Here,  $p_{\text{c}}$  determines the power consumption per real flop and  $C$  refers to the average number of real flops per second determined in Sec. 6.5. Since  $P_{\text{RF}}$  depends on the transmission power, it should be noted that the power consumption of the RF circuitry components for the different BSs has been approximated by scaling the data available in [247], which is considered to correspond to a macro BS, by a proportionality factor that relates to the BSs currently deployed [5, 60].

**Table 6.2:** Power consumption of micro and femto base stations.

<i>Parameter</i>		<i>Micro</i>	<i>Femto</i>
Total transmission power [5],	$P_t$	38 dBm	17 dBm
Power amplifier efficiency [57],	$\varsigma$	0.38	
Digital-to-analog converter [5, 247],	$P_{\text{DAC}}$	7.8 mW	0.46 mW
Signal mixer [5, 247],	$P_{\text{mix}}$	15.2 mW	0.9 mW
Signal filtering [5, 247],	$P_{\text{filt}}$	10 mW	0.6 mW
Frequency synthesizer [5, 247],	$P_{\text{syn}}$	25 mW	1.5 mW
Computational efficiency [116],	$p_c^{-1}$	12.8 Mflops / mW	
DC-DC losses [5],	$\sigma_{\text{DC}}$	0.075	0.09
Main supply losses [5],	$\sigma_{\text{MS}}$	0.09	0.11
Cooling losses [5],	$\sigma_{\text{cool}}$	0	0

## 6.7 Results and Discussion

To demonstrate the performance and complexity of the proposed strategy, this section presents numerical results obtained via Monte Carlo simulations. The simulation setup consists of a BS with a planar array comprised of  $N$  antennas, a transmission channel following the physical channel model described in Sec. 6.2.2, and  $K$  single-antenna receivers. For a fair comparison, all transmitters have the same physical size independently of  $N$ . The channel model considers the practical case of imperfect CSI acquisition unless otherwise stated, an equal number of angular directions  $D_k = 50$  in (6.7), and that the angle spread of the azimuth and elevation angles of departure is fixed to  $\pi$  and  $\pi/6$  radians respectively [106]. The imperfect CSI scenario is modeled considering MMSE estimation for the active antennas after the pilot training stage as per (6.12)–(6.14) with  $\rho_{\text{tr}} = 15$  dB [72]. The azimuth and elevation angles of departure of each user are considered to be independent and to follow a random uniform distribution within the relevant angle spread [101, 207]. The following results consider a standard LTE frame with a duration of 10 milliseconds comprised of 10 subframes with 14 OFDM symbols each [1]. For the complexity and energy efficiency results of this section, we arbitrarily consider a short channel coherence block comprised of  $\eta_{\text{coh}} = 140$  time/frequency symbol slots. Moreover, the uplink-downlink configuration 4 of LTE

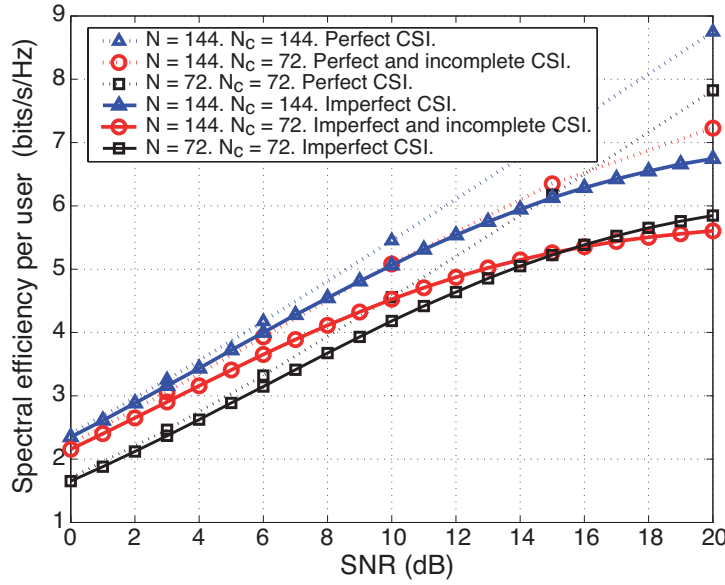


**Figure 6.5:** Spectral efficiency per user ( $S_k$ ) vs. SNR for  $L = 10.9\lambda^2$ .  $N = 144$  and  $N = 72$ ,  $K = 12$  and  $N_c = N/2$  for incomplete CSI acquisition.

TDD is followed, in which a total of 7 subframes are used for downlink transmission [1]. This determines the time spent for CSI acquisition and data transmission, which in turn influences the signal processing complexity and the achievable sum rates as per (6.30) and (6.31) respectively.

The performance of the communication systems considered in this chapter can be observed in Fig. 6.5, where a comparison of the spectral efficiency per user in (6.32) is shown for increasing levels of SNR. In this figure, the antennas are deployed in an area of  $L = 10.9\lambda^2$  and both systems with complete and incomplete CSI are considered. In the following, the number of users is fixed to  $K = 12$ , and the performance for  $N = 144$  ( $M_h = M_v = 12$ ) and  $N = 72$  ( $M_h = 9, M_v = 8$ ) antennas with full CSI is depicted as a reference. This establishes an inter-antenna distance  $d = 0.3\lambda$  in Fig. 6.5 for the cases of  $N = 144$ . Moreover, it is considered that  $N_c/N = 1/2$  for the case of incomplete CSI acquisition. Overall, the results of Fig. 6.5 show that the proposed strategy operates close to a system with  $N$  antennas, full CSI and the same number of RF chains for the low-to-intermediate SNR region. Note that the large number of antennas implemented massive MIMO systems also motivate their operation in this region due to their improved spectral efficiency and the need of limiting the total power consumption [61, 72]. This

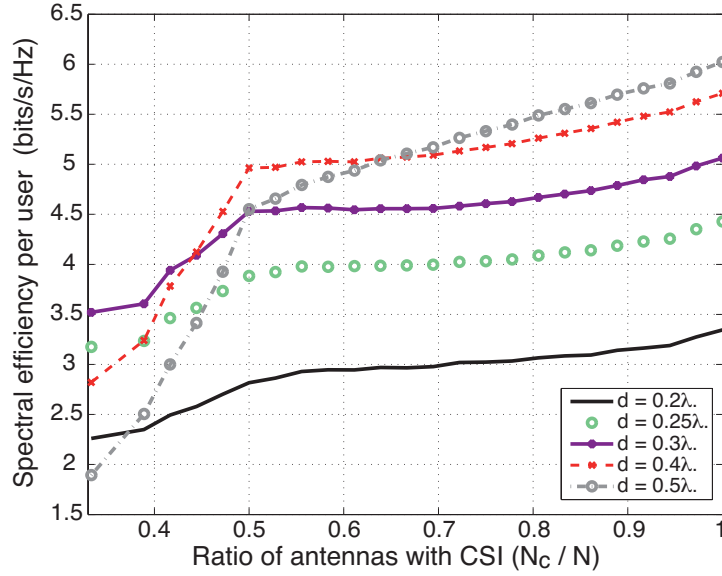


**Figure 6.6:** Spectral efficiency per user ( $S_k$ ) vs. ratio of antennas with CSI ( $N_c/N$ ).  $N = 144$ ,  $K = 12$  and SNR = 10 dB.

validates the benefits of using incomplete CSI in this range as well as the employment of the proposed scheme based on the basic CSI distribution patterns shown in Fig. 6.1. It can also be observed that the performance of the incomplete CSI scheme is limited by the errors introduced by the averaging procedure at high SNRs when perfect CSI is considered. Moreover, it can be seen that the consideration of imperfect CSI also bounds the performance of conventional transmission strategies at high SNRs, hence minimizing the differences between the schemes with full and incomplete CSI.

The effect of  $N_c$  on the performance of the proposed strategy can be observed in Fig. 6.6, where the spectral efficiency vs. the percentage of antennas with CSI is shown for a fixed SNR of 10 dB. From the results of this figure it can be concluded that a larger number of antennas with CSI is required as the inter-antenna spacing increases to reach a given percentage of the ultimate performance obtained when  $(N_c/N) = 1$ . This result is intuitive since the communication channels of the different antennas exhibit a lower correlation for larger antenna separations, hence degrading the performance of the proposed scheme due to the errors introduced by the averaging procedure. In spite of this, it can be seen that activating half of the antennas during the training stage for  $d = 0.3\lambda$  suffices to achieve 75% of the maximum system throughput with full CSI and  $d = 0.5\lambda$ , where the occupied area is larger.

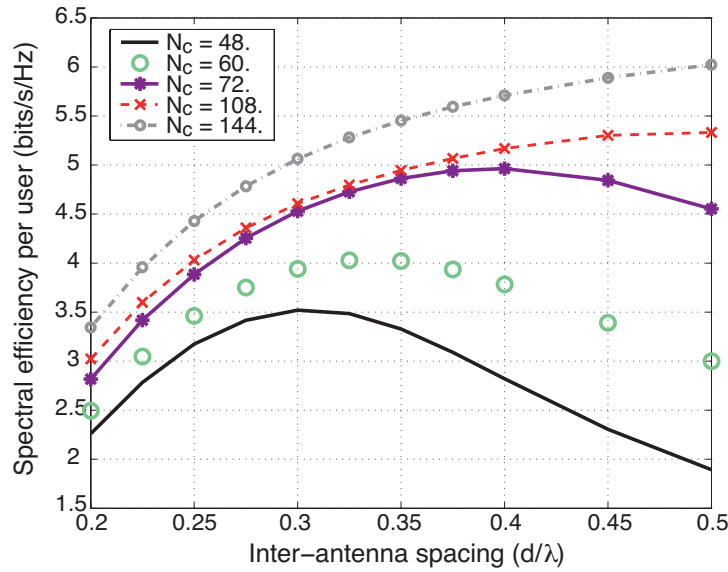


**Figure 6.7:** Spectral efficiency per user ( $S_k$ ) vs. inter-antenna distance ( $d/\lambda$ ).  $N = 144$ ,  $K = 12$  and SNR = 10 dB.

The impact of varying the inter-antenna distance on the spectral efficiency per user can be clearly seen in Fig. 6.7, where an identical setup to that of Fig. 6.6 has been considered. Fig. 6.7 characterizes the trade-off that arises by varying the inter-antenna distances: while the proposed scheme reduces the CSI approximation errors for small inter-element spacings, the loss produced by a larger spatial correlation can harm the spectral efficiency. In this line, the results of Fig. 6.7 allow determining the optimal inter-antenna distance for a given ratio of antennas with CSI ( $N_c/N$ ).

The number of real flops during the precoding stage and the global communication per frame are depicted in Fig. 6.8(a) and (b) respectively for increasing levels of  $N_c$ . The results of this figure show the notable complexity savings that can be experienced when the proposed incomplete CSI scheme is employed. Specifically, it can be seen that the number of precoding-related operations of the proposed scheme can be dramatically reduced w.r.t. a system with the same number of antennas but full CSI acquisition. This translates to a significant reduction of the global complexity as depicted in Fig. 6.8(b). The global complexity reduction can be explained by noting that the complexity of the precoding process accounts for a significant part of the global signal processing load, hence maximizing the benefits of the incomplete CSI scheme.

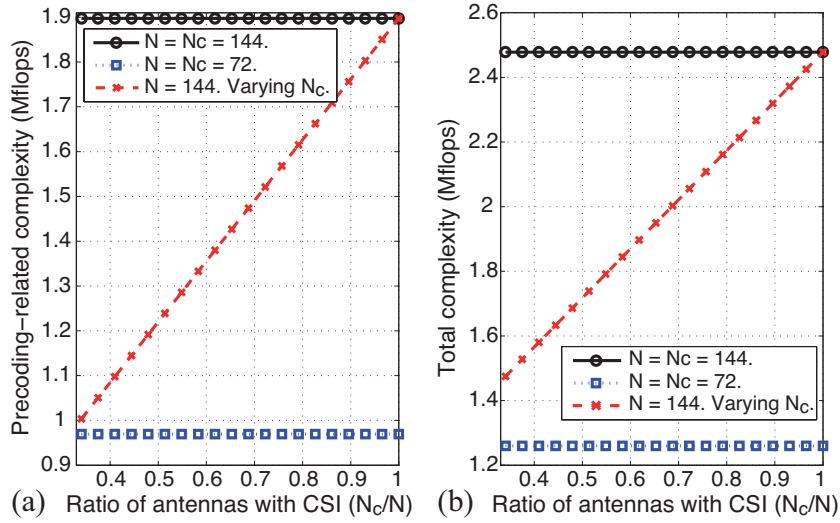


**Figure 6.8:** (a) Precoding-related complexity and (b) total complexity per frame for increasing  $N_c$ .  $K = 12$  users,  $\eta_{\text{coh}} = 140$ ,  $\eta_{\text{tr}} = K = 12$  and  $\eta_{\text{dl}} = 7 \times 14$ .

Fig. 6.9 depicts the energy efficiency metric (6.34) for increasing levels of spectral efficiency and  $L_h = L_v = 3.3\lambda$ . The results of this figure have been obtained by fixing the total noise power  $B\sigma^2$  to 10 dBm for reference, by setting the total system bandwidth to  $B = 20$  MHz, and by computing the transmission power required to achieve a given spectral efficiency [1]. Moreover, since the circuit power consumption varies depending on the total transmission power [5], a linear interpolation of the data shown in Table 6.2 has been performed to estimate the approximate power consumed by the RF chains. For simplicity, it has been considered that the analog signal combining and splitting processes do not introduce any additional losses, i.e., the considered schemes have the same transmission power. It should be remarked that, although dynamic power losses appear in the power combining process [248], determining the additional power consumption required by the transmission chains is intricate due to the possibility of designing different solutions for their compensation as studied in Chapter 8.

The results of Fig. 6.9 show that, under a moderate antenna correlation, deactivating half of the antennas during the pilot training stage constitutes the most energy-efficient alternative for a wide range of spectral efficiencies. In particular, it can be seen that using the proposed scheme is beneficial for low and intermediate spectral efficiencies. Instead, conventional massive MIMO strategies become more energy-efficient for large spectral

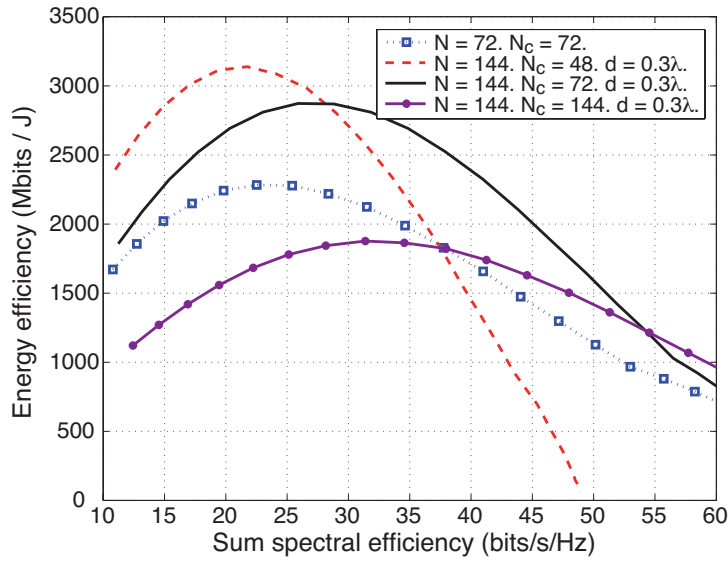


**Figure 6.9:** Energy efficiency vs. sum spectral efficiency for  $L = 10.9\lambda^2$ .  $N = 144$  and  $N = 72$ ,  $K = 12$ .

efficiencies. This behaviour can be explained by noting that the energy efficiency benefits of the proposed scheme are especially noticeable when the circuit power consumption strongly influences the total power consumption. Note that this can potentially occur in massive BSs due to the significant increase in the number of RF components required when compared with traditional BSs [60,61]. In these cases, reducing the number of RF chains is beneficial for the global energy efficiency as shown in Fig. 6.9. As higher spectral efficiencies are required, the dominant factor in the total power consumption is the power consumed by the power amplifiers following (6.35), which is not affected by the reduced number of RF chains offered by the proposed strategy. Nevertheless, it should be noted that the incomplete CSI schemes are capable of offering significant flexibility benefits as well as reductions of the signal processing complexity, hence extending their range of application to high spectral efficiencies where the computational load is expected to be cumbersome [78].

The effect of the percentage of active antennas during the training stage on the energy efficiency metric is shown in Fig. 6.10 and Fig. 6.11 for microcell and femtocell BSs respectively. The power consumption values from Table 6.2 have been employed for each of the scenarios. The results are shown for  $\text{SNR} = 10$  dB and a varying inter-antenna distance  $d$ . From the results of these figures it can be concluded that

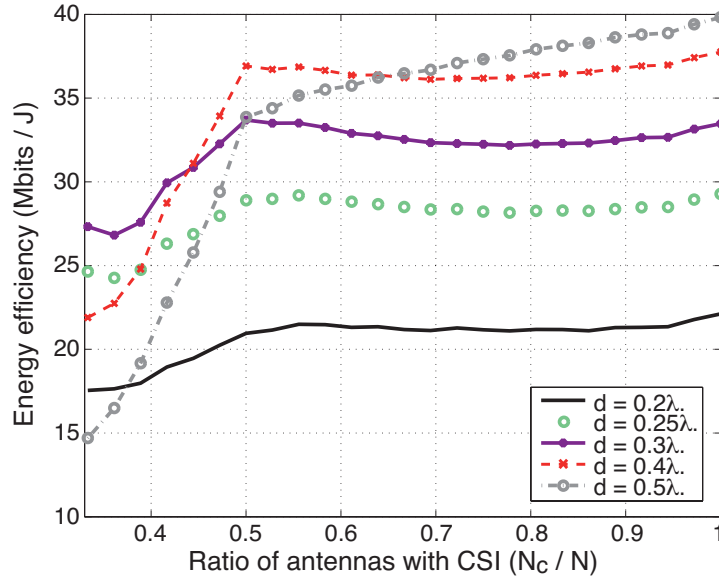


**Figure 6.10:** Energy efficiency vs. ratio of antennas with CSI ( $N_c/N$ ) for a micro-cell scenario and varying inter-antenna distance  $d$ .  $N = 144$ ,  $K = 12$  and  $\text{SNR} = 10$  dB.

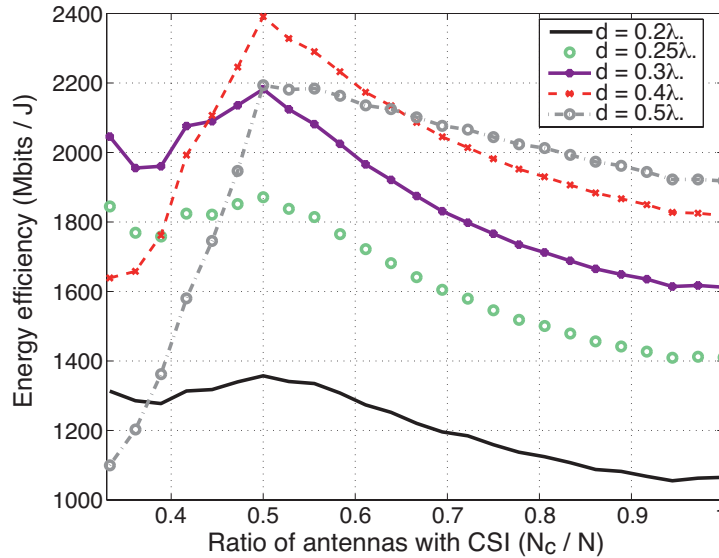


**Figure 6.11:** Energy efficiency vs. ratio of antennas with CSI ( $N_c/N$ ) for a femto-cell scenario and varying inter-antenna distance  $d$ .  $N = 144$ ,  $K = 12$  and  $\text{SNR} = 10$  dB.

reducing the number of active antennas during the training stage and the inter-antenna spacing can be beneficial from an energy efficiency perspective. Specifically, Fig. 6.10 shows that a large percentage of the maximum energy efficiency attained for  $d = 0.5\lambda$  and  $N_c = N = 144$  can be obtained by acquiring CSI for half of the antennas and  $d = 0.3\lambda$ . Note that in this second case the size of the deployed massive antenna array

is reduced w.r.t. the case of  $d = 0.5\lambda$ . Moreover, Fig. 6.11 shows that the energy efficiency is maximized for the femtocell scenario when  $N_c = N/2 = 72$  antennas are active during the CSI acquisition process and the distance between antennas is  $d = 0.4\lambda$ . Intuitively, this occurs because the small loss in the achievable rates is compensated by the substantial reduction experienced in the power consumption of the RF components and the DSP.

## 6.8 Conclusions

In this chapter, a low-complexity scheme to exploit the inter-antenna correlation that arises in space-constrained massive MIMO BSs has been presented. The proposed strategy reduces the required number of RF chains by deactivating a number of antennas during the CSI acquisition stage. Subsequently, the CSI for the remaining neighbour antennas is obtained by averaging the information acquired. This is also extended to the transmission stage, where a reduced RF chain approach is illustrated. Overall, the results presented in this chapter confirm that the proposed scheme is able to approximately preserve the performance of tightly-packed BSs, while simultaneously reducing the computational complexity and enhancing the energy efficiency. Specifically, it has been shown that systems with inter-antenna distances in the range  $d = 0.3 - 0.4\lambda$  can halve the number of RF chains w.r.t. the number of antennas, and still achieve a large percentage of the rates attained by a full RF-chain system with  $d = 0.5\lambda$ , at low to intermediate SNRs for the scenarios considered in this chapter.

*Critique:* In the context of incomplete CSI acquisition, the consideration of alternative and more intricate channel models that capture the behaviour realistic propagation environments seems of interest for an accurate assesment of its potential benefits [249]. Indeed, the performance results shown in this chapter should be affected by the consideration of mutual coupling, which would generally reduce the performance of space-constrained systems [104, 235]. It is also apparent that there exists a physical limit in the number of antenna elements that can be implemented in a fixed physical space, when the individual antenna dimensions are considered. Moreover, it is intuitive

that the proposed strategies for determining the antennas with instantaneous CSI and for interpolation are intrinsically sub-optimal. This is because the essential objective of this chapter is provide a low-complexity approach. However, more complex strategies with enhanced performance for distributing the CSI could also be devised. These alternative strategies could also account for non-stochastic CSI error models different from that considered in Sec. 6.4, since realistic least squares (LS) and minimum square error (MMSE) criteria are conventionally employed for channel estimation [72].



## Chapter 7

# Low-Complexity Large Scale Antenna Systems: Reduced-Connectivity Antenna Selection

### 7.1 Introduction

Large scale antenna systems (LSAS) motivate the design of novel digital and analog signal processing strategies, since the economic cost, power consumption, and hardware and digital signal processing complexities of systems with a dedicated RF chain per antenna might become burdensome [13,20,74]. For this reason, this chapter concentrates on the selection of a reduced number of antennas based on their channel conditions, which has been posed as a feasible alternative for reducing the complexity in both small and large scale MIMO systems [23,117,118].

As already highlighted in Sec. 2.3.1, the classical literature of antenna selection (AS) has concentrated on the development of low-complexity selection algorithms and on analyzing their performance [23,117–128]. Related literature has also focused on the study

of the acquisition of channel state information (CSI) [129–131] and the energy efficiency improvements [132–134] of AS systems. A number of practical implementation aspects are also raised in [135, 136]. More recently, the implementation of AS as a means of reducing the excessive number of radio frequency (RF) chains in LSAS has also attracted considerable interest [21, 137–146]. Particularly relevant in this context are the results presented in [21, 146, 148] and Chapter 8 of this Thesis, which illustrate that a large portion of the full-RF massive MIMO rates can be attained via AS in realistic propagation scenarios, hence motivating the practical application of AS in LSAS. However, none of the above-mentioned works presents a comprehensive analysis of a critical aspect: the design of the RF switching matrix that implements the AS.

The RF switching matrix represents the hardware components required in AS for interconnecting the RF chains with their selected antennas in implementations with a reduced number of RF chains [118, 135]. Indeed, the colossal growth of antenna numbers in LSAS also increases the complexity of RF switching, hence making these components a significant performance factor. In spite of acknowledging the crucial importance of this component [118], the impact of the switching network on the performance and energy efficiency of AS has been commonly ignored in the related literature. Only recently, the consideration of the insertion losses (ILs) and the complexity of switching matrices in LSAS have been considered in [147] and [146]. Specifically, [147] considers a switching network that only connects each RF chain to predefined subsets of antennas for reducing the complexity of switching between the large number of antennas required at millimeter wave frequencies. Similarly, [146] proposes to implement the switching matrix via binary switches to alleviate the ILs. However, this comes at the expense of reducing the input-output connectivity of the resultant switching architecture, which is partially-connected (PC). Still, these works do not perform a thorough and detailed analysis of the hardware implications behind their designs and only focus on specific implementations such as binary switching matrices.

Considering the above, this chapter generalizes the above-mentioned works to arbitrary switching architectures and concentrates on providing a detailed analysis of switching networks to characterize their influence in AS systems. In particular, this chapter

presents a number of specific hardware implementations of switching matrices that are optimized under different criteria such as the number of internal connections or the power losses. In this context, an accurate characterization of their ILs is provided, since they are critical for LSAS due to the large number of inputs (RF chains) and outputs (antennas) required. Moreover, architectures with limited connectivity are considered as a means for reducing the complexity of the fully-flexible (FF) switching networks, which instead facilitate the selection of any plausible subset of antennas and attain the maximum theoretical performance of AS. The performance loss introduced due to the limited connectivity for power-based (PB) AS systems is also determined in this chapter, since PB-AS can offer a superior performance when practical CSI acquisition procedures are considered. Altogether, the results and generalized designs considered in this chapter provide a comprehensive view of the impact of RF switching matrices on the performance, hardware architecture and energy efficiency of AS systems.

## 7.2 Preliminaries

### 7.2.1 Downlink System Model

Consider a time-division duplex (TDD) multi-user MIMO system comprised of a base station (BS) with  $N$  transmit antennas and  $K$  single-antenna mobile stations (MSs) such as that introduced in Chapter 2. The BS incorporates  $K \leq M \leq N$  RF chains to convey  $K$  independent data symbols to the MSs via AS. Similarly to (2.1), the composite signal  $\mathbf{y} \in \mathbb{C}^{K \times 1}$  received by the MSs can be expressed as

$$\mathbf{y} = \sqrt{\rho} \mathbf{H}_{[\mathcal{M}]} \mathbf{x} + \mathbf{n}, \quad (7.1)$$

where the relevant variables have been already defined in Sec. 2.1,  $\mathbf{n} \in \mathbb{C}^{K \times 1} \sim \mathcal{CN}(\mathbf{0}, \mathbf{I}_K)$  and  $\mathbf{H}_{[\mathcal{M}]} \in \mathbb{C}^{K \times M}$  is a submatrix of  $\mathbf{H}$  built by selecting the columns specified by the set  $\mathcal{M} \subseteq \{1, \dots, N\}$  with cardinality  $|\mathcal{M}| = M$ . Here,  $\mathcal{A} \subseteq \mathcal{B}$  denotes that  $\mathcal{A}$  is a subset of  $\mathcal{B}$ . Moreover,  $\mathbb{E} \{\mathbf{x}^H \mathbf{x}\} = K$  and  $\rho$  represents the average transmission power per mobile terminal.

### 7.2.2 Antenna Selection Benchmarks

The capacity  $C$  of the downlink system described in (7.1) is given by [250]

$$C = \max_{\mathbf{P}} \left( \frac{\eta_{\text{dl}}}{\eta_{\text{coh}}} \right) \log_2 \det \left( \mathbf{I}_K + \rho \mathbf{P} \mathbf{H}_{[\mathcal{M}]} (\mathbf{H}_{[\mathcal{M}]})^{\text{H}} \right), \quad (7.2)$$

where  $\eta_{\text{dl}}$  is the number of symbols dedicated to downlink transmission and  $\eta_{\text{coh}}$  denotes the number of symbols where the channel remains constant, as shown in Fig. 2.4. Moreover,  $\mathbf{P} \in \mathbb{R}^{K \times K}$  is a diagonal power allocation matrix satisfying  $\sum_{i=1}^K \mathbf{P}_{i,i} = K$ . A conventional criterion for AS consists in maximizing the system's capacity  $C$ , which results in the optimization problem [121, 148]

$$\begin{aligned} \mathcal{P}_{7.1} : \quad & \underset{\mathbf{S}, \mathbf{P}}{\text{maximize}} \quad \log_2 \det \left( \mathbf{I}_K + \rho \mathbf{P} \mathbf{H} \mathbf{S} \mathbf{H}^{\text{H}} \right) \\ & \text{subject to} \quad \sum_{i=1}^N \mathbf{S}_{i,i} = M, \\ & \quad \quad \quad \mathbf{S}_{i,i} \in \{0, 1\}, \quad \forall i \in \{1, \dots, N\}, \end{aligned} \quad (7.3)$$

where  $\mathbf{S} \in \mathbb{B}^{N \times N}$  is a diagonal binary matrix satisfying

$$\mathbf{S}_{i,i} = \begin{cases} 1, & \text{if } i \in \mathcal{M}, \\ 0, & \text{otherwise.} \end{cases} \quad (7.4)$$

The optimization problem  $\mathcal{P}_{7.1}$  is not convex due to the binary constraints  $\mathbf{S}_{i,i} \in \{0, 1\}, \forall i \in \{1, \dots, N\}$  [211]. However, these constraints can be relaxed to the weaker  $0 \leq \mathbf{S}_{i,i} \leq 1$ , hence turning  $\mathcal{P}_{7.1}$  into the convex optimization problem [134, 146, 148]

$$\begin{aligned} \mathcal{P}_{7.2} : \quad & \underset{\mathbf{S}, \mathbf{P}}{\text{maximize}} \quad \log_2 \det \left( \mathbf{I}_K + \rho \mathbf{P} \mathbf{H} \mathbf{S} \mathbf{H}^{\text{H}} \right) \\ & \text{subject to} \quad \sum_{i=1}^N \mathbf{S}_{i,i} = M, \\ & \quad \quad \quad 0 \leq \mathbf{S}_{i,i} \leq 1, \quad \forall i \in \{1, \dots, N\}. \end{aligned} \quad (7.5)$$

The final solution is attained by selecting the antennas corresponding to the  $M$  largest diagonal entries in  $\mathbf{S}$ . At this point it should be noted that  $\mathcal{P}_{7.2}$  can also have additional

constraints depending on the specific architecture of the RF switching matrix, since there might be specific antenna combinations that cannot be simultaneously selected due to having a limited input-output connectivity [146]. For ease of exposition, this section assumes that  $\mathcal{P}_{7.2}$  is solved while satisfying these constraints and leave their detailed definition for Sec. 7.4.

In resemblance with [148], one can compute the system's capacity for AS by first optimizing (7.5) over  $\mathbf{S}$  while setting  $\mathbf{P} = \mathbf{I}_K$ , which produces  $\tilde{\mathbf{S}}^*$ . Subsequently, the user power allocation matrix  $\tilde{\mathbf{P}}^*$  is computed by solving  $\mathcal{P}_{7.2}$  with  $\tilde{\mathbf{S}}^*$  fixed. This is a convex optimization problem with a waterfilling-type solution [251]. Note that this procedure is particularly efficient for large  $\rho$ 's, since the optimal power allocation matrix  $\mathbf{P}^* \approx \mathbf{I}_K$  in  $\mathcal{P}_{7.2}$  [250]. Moreover, this chapter also considers the practical linear zero-forcing (ZF) precoder, whose sum rates can be obtained as the resultant value of the objective function in the optimization problem [148]

$$\begin{aligned} \mathcal{P}_{7.3} : \quad & \underset{\mathbf{D}}{\text{maximize}} \quad \left( \frac{\eta_{\text{dl}}}{\eta_{\text{coh}}} \right) \sum_{i=1}^K \log_2 (1 + \rho \mathbf{D}_{i,i}) \\ & \text{subject to} \quad \sum_{i=1}^K \mathbf{D}_{i,i} \left( \left( \mathbf{H} \tilde{\mathbf{S}}^* \mathbf{H}^H \right)^{-1} \right)_{i,i} = K, \end{aligned} \quad (7.6)$$

where  $\mathbf{D} \in \mathbb{R}^{K \times K}$  is the diagonal power allocation matrix for ZF. The solution to  $\mathcal{P}_{7.3}$  can also be obtained via conventional water-filling [76]. Note that while  $\tilde{\mathbf{S}}^*$  obtained from  $\mathcal{P}_{7.2}$  does not necessarily maximize  $\mathcal{P}_{7.3}$ , this choice adopted in [146, 148] is supported by the results in [126], where it is shown that employing  $\tilde{\mathbf{S}}^*$  has a slight impact on the resultant system's performance when compared with other AS methods specifically designed for linear precoders.

### 7.2.3 Channel State Information Acquisition for AS Systems

The optimization problems  $\mathcal{P}_{7.2}$  and  $\mathcal{P}_{7.3}$  defined in Sec. 7.2.2 can only be solved provided that knowledge of the channel response  $\mathbf{H}$  is available at the BS. However, CSI acquisition poses a major challenge in AS systems with reduced RF chains since, as opposed to full RF chains systems, the CSI acquisition requires multiplexed training

slots to obtain full CSI for all transmit antennas.

### 7.2.3.1 Instantaneous CSI Acquisition for full-RF systems ( $M = N$ )

The conventional training stage in TDD systems where  $M = N$  consists of the transmission of orthogonal training sequences from the users to the BS throughout  $K \leq \eta_{\text{tr}} \leq \eta_{\text{coh}}$  training symbols [74, 252]. Considering channel reciprocity, the signal received at the BS  $\mathbf{Y}_{\text{tr}} \in \mathbb{C}^{N \times \eta_{\text{tr}}}$  can be expressed as [74, 252]

$$\mathbf{Y}_{\text{tr}} = \mathbf{H}^H \mathbf{\Theta} + \bar{\mathbf{N}}, \quad (7.7)$$

where the interpretation of the relevant variables is given in (2.19) and  $\bar{n}_{i,j} \sim \mathcal{CN}(0, \sigma_{\text{tr}}^2)$ . The communication channel  $\mathbf{H}$  can be directly estimated from (7.7) via least-squares (LS) estimation by correlating the received signal with the known unitary pilot sequences [84, 85]

$$\hat{\mathbf{H}}^H = (\mathbf{H}^H \mathbf{\Theta} + \mathbf{N}) \mathbf{\Theta}^H = \mathbf{H}^H + \mathbf{N} \mathbf{\Theta}^H. \quad (7.8)$$

Minimum mean square error (MMSE) estimation is also commonly applied provided that the channel statistics are known at the BS [85].

### 7.2.3.2 Instantaneous CSI Acquisition for reduced-RF systems ( $M < N$ )

In contrast with the full-RF system considered in (7.7), the AS system considered in this chapter only implements  $M \leq N$  RF chains. This constraint entails that only  $M$  signals from the antenna ports can be processed simultaneously, i.e. the training signal received after  $K$  training symbols reads as

$$\tilde{\mathbf{Y}}_{\text{tr}} = (\mathbf{H}_{[\mathcal{M}]})^H \mathbf{\Theta} + \tilde{\mathbf{N}}, \quad (7.9)$$

where  $\tilde{\mathbf{Y}}_{\text{tr}} \in \mathbb{C}^{M \times \eta_{\text{tr}}}$  and  $\tilde{\mathbf{N}} \in \mathbb{C}^{M \times \eta_{\text{tr}}}$  is comprised of independent and identically distributed (i.i.d.) entries following  $\tilde{n}_{i,j} \sim \mathcal{CN}(0, \sigma_{\text{tr}}^2)$ . As a result, only partial CSI  $\mathbf{H}_{[\mathcal{M}]}$  of the overall channel matrix  $\mathbf{H}$  can be derived from (7.9). This entails that a

multiplexed training stage is required to estimate the channels of all  $N$  antennas [129]. Indeed, the minimum number of training symbols required to estimate the channel in AS systems with a reduced number of RF chains is given by

$$\eta_{\text{tr}}^{\text{AS}} = K \times \left\lceil \frac{N}{M} \right\rceil, \quad (7.10)$$

where  $\lceil \cdot \rceil$  rounds to the highest closer integer. While this extended training might have a negligible impact on the attainable sum rates of slowly varying channels with large  $\eta_{\text{coh}}$ , their influence can instead be significant for fast varying channels, a trade-off that will be explicitly studied in Sec. 7.7 for LSAS. The resultant number of symbol periods dedicated to downlink data transmission is given by

$$\eta_{\text{dl}} = \eta_{\text{coh}} - \eta_{\text{ul}} - \eta_{\text{tr}} = \eta_{\text{coh}} - \eta_{\text{ul}} - \left( K \times \left\lceil \frac{N}{M} \right\rceil \right), \quad (7.11)$$

where  $\eta_{\text{ul}}$  refers to the number of symbols employed for uplink data transmission, as illustrated in Fig. 2.4.

### 7.2.3.3 Power-Based AS (PB-AS) for reduced-RF systems ( $M < N$ )

An elegant solution to the CSI acquisition problem in AS systems consists in adopting a selection decision hinging on the norm of the channel entries. With this purpose, let  $\bar{\mathbf{h}} = \left[ \|\mathbf{h}_1\|^2, \dots, \|\mathbf{h}_N\|^2 \right] \in \mathbb{R}^{1 \times N}$  be a vector comprising the channel power measured per antenna element, where  $\mathbf{h}_i$  denotes the  $i$ -th column of  $\mathbf{H}$ . The diagonal selection matrix  $\mathbf{S}$  defined in (7.4) can be obtained as

$$\begin{aligned} \mathcal{P}_{7.4} : \underset{\mathbf{S}}{\text{maximize}} \quad & \bar{\mathbf{h}}\mathbf{S} \\ \text{subject to} \quad & \sum_{i=1}^N \mathbf{S}_{i,i} = M, \\ & \mathbf{S}_{i,i} \in \{0, 1\}, \forall i \in \{1, \dots, N\}, \end{aligned} \quad (7.12)$$

This strategy is commonly referred to as power-based (PB) or norm-based AS. The solution to the PB-AS of  $\mathcal{P}_{7.4}$  is straightforward for the case of FF architectures, i.e.

[23]

$$\tilde{\mathbf{S}}^* = \max_M \|\mathbf{h}_i\|^2, \quad (7.13)$$

where  $\max_M(\cdot)$  selects the largest  $M$  entries. While sub-optimal, PB-AS is capable of reducing the amount of time resources spent for CSI acquisition in systems where RF power meters instead of full RF chains are attached to each antenna port [129]. This is because a) the channel power information can be acquired from the prior uplink stage and b) this information can be subsequently employed for AS as per (7.12). Therefore, the number of pilot symbols employed for downlink transmission  $\eta_{\text{dl}}$  for the case of PB-AS can be expressed as

$$\eta_{\text{dl}} = \eta_{\text{coh}} - \eta_{\text{ul}} - \eta_{\text{tr}} = \eta_{\text{coh}} - \eta_{\text{ul}} - K, \quad (7.14)$$

since instantaneous CSI is only required for the  $M$  antennas chosen for data transmission and  $\eta_{\text{tr}} = K$  [74] is considered.

#### 7.2.4 Sources of Losses in the RF Switching Matrices of AS

The design of the RF switching matrix in AS plays a fundamental role in the overall system performance [118]. Among the multiple technical aspects that should be considered from a system-level design perspective, the most relevant ones are:

- *Insertion losses (ILs)*. RF switching matrices introduce ILs that generally grow with the number of input and output ports [253, 254]. This is a critical parameter for LSAS, where both the number of RF chains and antennas are significantly large [11, 12, 69, 146].
- *Coupling between ports*. The coupling of the switching matrix determines the fraction of the signals that appear at a specific port, but were intended for other ports. This parameter depends on the network of connections inside the switching matrix and the power leakage of the internal switching devices (e.g., FET transistors or electromechanical switches) [255].

- *Transfer function balance.* The transfer function of each input-output combination between RF chain and antenna element should be ideally identical to ensure that the baseband model (4.1) accurately characterizes the system's operation [118].

From the above three sources of losses, this chapter concentrates on the ILs. This is because a) transfer function imbalances can be compensated via calibration prior to the normal system operation [118] and b) coupling between internal switching ports can be in the order of  $-20$  to  $-30$  dB, hence effectively making unintentional power transfers between nearby ports negligible [256]. Instead, the ILs introduced by switching matrices with a large number of input and output ports can be in the order of 2-3 dB [254], hence dominating the overall performance loss. For this reason, Sec. 7.3 firstly explores a number of implementations of conventional FF switching matrices, with emphasis on the number of switching components required and the associated ILs. Subsequently, PC switching matrices with an arbitrary number of input (RF chains) and output (antennas) ports are introduced in Sec. 7.4 as a means for reducing both the ILs and the hardware complexity of FF designs.

### 7.3 Fully-Flexible (FF) Switching for Antenna Selection

RF switching matrices in conventional AS have two essential requirements: a) connecting each RF chain to the antenna ports (full flexibility) and b) allowing bidirectional switching for uplink-downlink operation [118, 253]. These characteristics promote the implementation of the so-called blocking switching matrices, where the interconnection between the input and the output ports is performed by concatenating a number of switches of smaller size [253, 254]. An illustrative example of a blocking switching matrix is shown in Fig. 7.1(a), where the block diagram of a  $4 \times 8$  switching matrix can be observed. This figure shows that a large switching matrix is comprised of two main switching stages (represented by the dashed boxes in the figure) with multiple switches of smaller size: one stage at the RF-chain ports, referred to as RF-chain switching stage in the sequel, and a subsequent stage at the antenna ports, referred to as antenna switching stage.

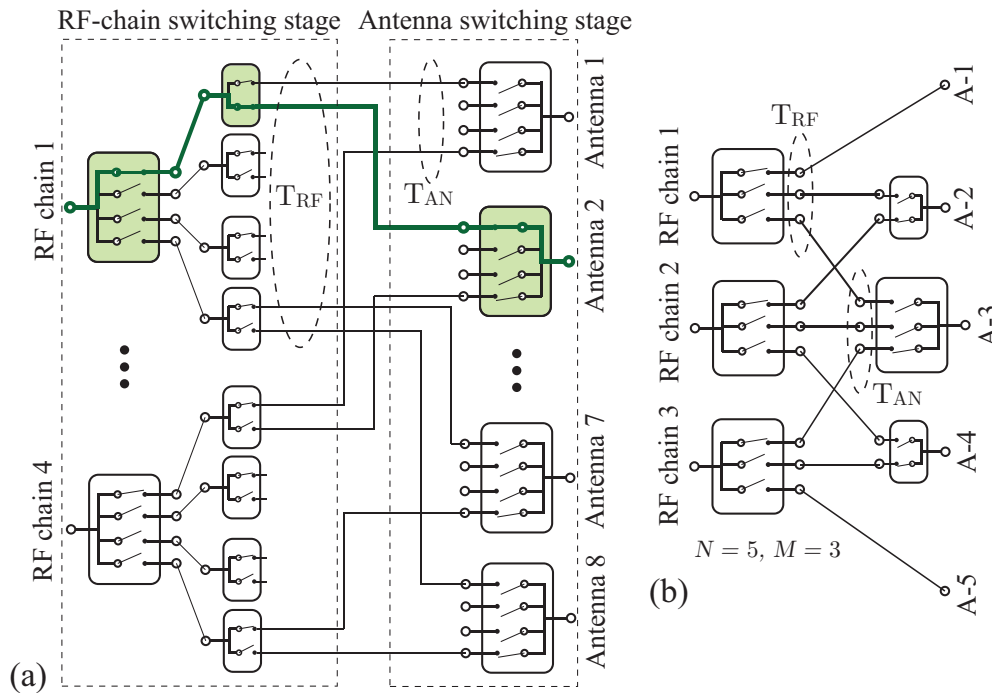


**Figure 7.1:** Block diagrams of FF architectures: (a) a conventional  $4 \times 8$  switching matrix with each input port connected to every output port (FF-FC) and (b) a switching matrix minimizing the number of internal connections (FF-MC).

Each of the above two switching stages is comprised by a number of smaller switches with a smaller number of ports, which will be referred to as *basic switches* in the following. Indeed, the RF-chain switching stage of Figure 7.1(a) illustrates that several of these basic switches can be concatenated to produce the desired number of ports [254]. The basic switches considered in this chapter conventionally follow the nomenclature SPXT (single-pole X-throw) which refers to the number of separate ports with independent signals that the basic switch can control (poles) and the number of different signal paths that the switch allows for each pole (throws) [256, 257]. For instance, a SP3T switch is capable of routing one signal from or towards three different ports (throws). The range of basic switches is usually SP2T-SP10T and their cost and ILs generally grow with the number of output ports [256, 257]. Without loss of generality, the SP2T-SP4T basic switches detailed in Table 7.1 are considered for the illustrative architectures shown in this chapter [256].

Conventional AS systems consider FF switching matrices between the  $M$  RF chains and the  $N$  antenna ports, which allows any possible combination of  $M$  antennas to

**Table 7.1:** Basic SPXT switches

<i>Switch type</i>	<i>Model</i> [256]	<i>Insertion loss</i>
SP2T	PE42422	$L_2 = 0.25$ dB
SP3T	PE42430	$L_3 = 0.45$ dB
SP4T	PE42440	$L_4 = 0.45$ dB

be simultaneously selected. However, a number of implementations for the design of switching matrices with varying complexity and IL can be implemented. Importantly, different architectures may result in RF-chain and antenna switching stages with different number of ports (throws). An accurate characterization of the maximum number of throws per switching stage is crucial, since they determine overall IL of the critical signal path, i.e. the signal path with largest power losses.

With the above purpose, let  $T_{\text{RF}}$  and  $T_{\text{AN}}$  be the maximum number of throws per RF chain ( $T_{\text{RF}}$ ) in the RF-chain switching stage or per antenna ( $T_{\text{AN}}$ ) in the antenna switching stage, as represented in Figure 7.1(a). Let  $\mathcal{T}$  denote the set with elements in decreasing order given by the number of throws in the basic switches, i.e.,  $\mathcal{T} = \{4, 3, 2\}$  for the basic switches considered in Table 7.1.  $\mathcal{T}_j$  corresponds to the  $j$ -th entry in  $\mathcal{T}$  and the cardinality of  $\mathcal{T}$  is  $|\mathcal{T}| \triangleq N_s$ . Intuitively,  $N_s$  refers to the number of different basic switches considered, i.e.  $N_s = 3$  for the basic switches of Table 7.1. The total IL measured in dB of the critical signal path  $L$  for a given switching architecture can be computed as

$$L = \sum_{j=1}^{N_s} \left( S_{\mathcal{T}_j}^{\text{RF}} + S_{\mathcal{T}_j}^{\text{AN}} \right) \times L_{\mathcal{T}_j} = \sum_{j=1}^{N_s} S_{\mathcal{T}_j} \times L_{\mathcal{T}_j}, \quad (7.15)$$

where  $S_{\mathcal{T}_j}^{\text{RF}}$  and  $S_{\mathcal{T}_j}^{\text{AN}}$  represent the number of consecutive basic switches with  $\mathcal{T}_j$  throws that the signals cross in the RF-chain and in the antenna switching stages, respectively, and  $L_{\mathcal{T}_j}$  denotes the IL in dB introduced by a basic switch with  $\mathcal{T}_j$  throws. For instance,  $L_2 = 0.25$  dB,  $L_3 = 0.45$  dB and  $L_4 = 0.45$  dB for the basic switches considered in Table 7.1. Moreover,  $S_{\mathcal{T}_j} \triangleq S_{\mathcal{T}_j}^{\text{RF}} + S_{\mathcal{T}_j}^{\text{AN}}$  refers to the total number of switches with  $\mathcal{T}_j$  throws in the critical signal path of the overall switching matrix.

The number of basic switches with  $\mathcal{T}_j$  throws crossed by the transmit signals in the RF-chain and antenna switching stages can be iteratively computed as<sup>1</sup>

$$S_{\mathcal{T}_j}^{\{\text{RF}, \text{AN}\}} = \text{fact} \left( Q_{\mathcal{T}_j}^{\{\text{RF}, \text{AN}\}}, \mathcal{T}_j \right), j \in \{1, \dots, N_s\}, \quad (7.16)$$

where  $\text{fact}(a, b)$ ,  $b < a$  denotes the number of times  $b$  appears in the integer factorization of  $a$  and  $Q_{\mathcal{T}_j}^{\{\text{RF}, \text{AN}\}}$  is given by

$$Q_{\mathcal{T}_j}^{\{\text{RF}, \text{AN}\}} = \begin{cases} T_{\{\text{RF}, \text{AN}\}}, & \text{if } j = 1, \\ Q_{\mathcal{T}_{j-1}}^{\{\text{RF}, \text{AN}\}} / \max \left( \mathcal{T}_{j-1}^{(S_{\mathcal{T}_{j-1}}^{\{\text{RF}, \text{AN}\}})}, 1 \right), & \text{otherwise.} \end{cases} \quad (7.17)$$

In plain words,  $\mathcal{T}_j^{S_{\mathcal{T}_j}}$  represents the number of throws obtained by  $S_{\mathcal{T}_j}$  subsequent switching stages comprised of basic switches with  $\mathcal{T}_j$  throws, as described in the illustrative example below.

*Illustrative example:* Let us illustrate the procedure for computing the IL in (7.15) for a system with  $T_{\text{RF}} = Q_4^{\text{RF}} = 8$  and  $T_{\text{AN}} = 4$ . This can correspond to a system with  $M = 4$  and  $N = 8$ , as shown in Figure 7.1(a). In this case, multiple basic switches from Table 7.1 are required at the RF-chain switching stage for connecting the RF chains with the  $N = 8$  antennas. Specifically, since  $Q_4^{\text{RF}} = 8$  as per (7.17), the number of consecutive SP4T switching stages is  $S_4^{\text{RF}} = \text{fact}(8, 4) = \text{fact}(4 \times 2, 4) = 1$  as per (7.16). Substituting the above values in (7.17) for  $j = 2$  results in  $Q_3^{\text{RF}} = Q_4^{\text{RF}} / \mathcal{T}_1^{S_4^{\text{RF}}} = 8/4 = 2$ . Consequently,  $S_3^{\text{RF}} = \text{fact}(2, 3) = 0$ . Since no SP3T switches are required,  $Q_2^{\text{RF}} = 2$  as per (7.17) for  $j = 3$ , which entails that an additional stage of SP2T ( $S_2^{\text{RF}} = 1$ ) switches is required for implementing the  $T_{\text{RF}} = 8$  throws required for transmission per RF chain. Overall, the transmit signal of each RF chain must always cross one SP4T ( $S_4^{\text{RF}} = 1$ ) and one SP2T ( $S_2^{\text{RF}} = 1$ ) basic switches, as explicitly illustrated in Figure 7.1(a) by the coloured signal path. This figure also shows that only one SP4T ( $S_4^{\text{AN}} = \text{fact}(4, 4) = 1$ ) switch is required per antenna element. More intricate examples are also provided in Table 7.2 for the  $N = 32$ ,  $M = 6$  case.

---

<sup>1</sup>For simplicity, it has been considered that  $T_{\text{RF}}$  and  $T_{\text{AN}}$  can be factorized into the integers contained in  $\mathcal{T}$ .

**Table 7.2:** Insertion losses introduced by the fully-flexible architectures in an AS system with  $N = 32$  and  $M = 6$ 

<i>Parameter</i>	<i>FF-FC</i>	<i>FF-MC</i>	<i>FF-ML</i>
$T_{\text{RF}}$	32	27	32
$T_{\text{AN}}$	6	6	6
$Q_{\{4,3,2\}}^{\text{RF}}$ as per (7.17)	$Q_{\{4,3,2\}}^{\text{RF}} = \{32, 2, 2\}$	$Q_{\{4,3,2\}}^{\text{RF}} = \{27, 27, 0\}$	$Q_{\{4,3,2\}}^{\text{RF}} = \{32, 2, 2\}$
{SP4T, SP3T, SP2T} basic switches required per RF chain ( $S_{\{4,3,2\}}^{\text{RF}}$ )	$S_{\{4,3,2\}}^{\text{RF}} = \{2, 0, 1\}$	$S_{\{4,3,2\}}^{\text{RF}} = \{0, 3, 0\}$	$S_{\{4,3,2\}}^{\text{RF}} = \{2, 0, 1\}$
$Q_{\{4,3,2\}}^{\text{AN}}$ as per (7.17)	$Q_{\{4,3,2\}}^{\text{AN}} = \{6, 6, 2\}$	$Q_{\{4,3,2\}}^{\text{AN}} = \{6, 6, 2\}$	$Q_{\{4,3,2\}}^{\text{AN}} = \{6, 6, 2\}$
{SP4T, SP3T, SP2T} basic switches required per antenna ( $S_{\{4,3,2\}}^{\text{AN}}$ )	$S_{\{4,3,2\}}^{\text{AN}} = \{0, 1, 1\}$	$S_{\{4,3,2\}}^{\text{AN}} = \{0, 1, 1\}$	$S_{\{4,3,2\}}^{\text{AN}} = \{0, 1, 1\}$
Total number of {SP4T, SP3T, SP2T} basic switches ( $S_{\{4,3,2\}}$ )	$S_{\{4,3,2\}} = \{2, 1, 2\}$	$S_{\{4,3,2\}} = \{0, 4, 1\}$	$S_{\{4,3,2\}} = \{2, 1, 2\}$
Total IL in dB ( $L$ ) as per (7.15). $L_{\mathcal{T}_j}$ given by Table 7.1.	$L = 2 \times 0.45 + 1 \times 0.45 + 2 \times 0.25 = 1.85$ dB	$L = 4 \times 0.45 + 1 \times 0.25 = 2.05$ dB	$L = 2 \times 0.45 + 1 \times 0.45 + 2 \times 0.25 = 1.85$ dB

Considering the above, this chapter explores three implementations for the design of FF switching matrices:

1. *Architecture 1. Conventional FF architecture with full connectivity (FF-FC).* This architecture is illustrated in Fig. 7.1(a), where it can be seen that each RF chain is connected to every antenna port. In this particular case

$$T_{\text{RF}} = N, \text{ and } T_{\text{AN}} = M. \quad (7.18)$$

2. *Architecture 2. FF architecture with minimum connectivity (FF-MC).* This architecture minimizes the maximum number of ports at the RF-chain and antenna switching stages. The block diagram of this architecture is shown in Fig. 7.1(b) for an illustrative  $3 \times 5$  RF switching matrix. Here, it can be seen that there are additional constraints regarding the connectivity of each antenna. For instance, Fig. 7.1(b) shows that the first RF chain does not connect to antenna ports  $A-4$  and  $A-5$ . In spite of this, a full flexibility is guaranteed provided that

$$T_{\text{RF}} = N - M + 1, \text{ and } T_{\text{AN}} = \min(M, T_{\text{RF}}). \quad (7.19)$$

Overall, the FF-MC architecture selects the basic switches such that  $T_{\text{RF}}$  and  $T_{\text{AN}}$

are minimized, while ensuring that any combination of antennas can be simultaneously activated. For instance, Table 7.2 shows that, for the  $6 \times 32$  switching matrix, the  $T_{\text{RF}} = 32$  ports from the FF-FC switching architecture can be reduced to  $T_{\text{RF}} = 27$  ports when the FF-MC architecture is employed. Hence, this architecture aims to minimize the number of connections to simplify the hardware design and possibly the hardware monetary cost.

3. *Architecture 3. FF architecture with minimum losses (FF-ML).* The FF-MC architecture does not guarantee that the ILs are minimized, since designing networks with larger  $T_{\text{RF}}$  or  $T_{\text{AN}}$  might actually reduce the total IL. This counter-intuitive behaviour is illustrated in Table 7.2 for an AS system with  $N = 32$  and  $M = 6$ , where it can be observed that minimizing the  $T_{\text{RF}}$  and  $T_{\text{AN}}$  as per the FF-MC architecture does not minimize the total IL. This is because the ILs introduced by the basic switches vary depending on their number of ports as per Table 7.1, an effect particularly noticeable for large  $T_{\text{RF}}$  and  $T_{\text{AN}}$ . In contrast, the FF-ML architecture selects the  $T_{\text{RF}}$  and  $T_{\text{AN}}$  that minimize the IL by relaxing (7.19) into

$$T_{\text{RF}} \geq N - M + 1, \text{ and } T_{\text{AN}} \geq \min(M, T_{\text{RF}}). \quad (7.20)$$

Note that while the different design criteria considered above guarantee full flexibility, their IL can still be as significant as 2-3 dB for LSAS. For instance, it can be shown that a system with  $N = 128$  and  $M = 76$  introduces ILs of  $L = 2.95$ ,  $L = 3.2$  and  $L = 3.4$  dB for the FF-ML, FF-MC and FF-FC switching architectures, respectively. For this reason, the following section concentrates on reducing the complexity of RF switching matrices at the expense of reducing their flexibility.

## 7.4 Partially-Connected Switching Architectures and Resulting AS Constraints

The significant IL and complexity of the FF matrices introduced for LSAS motivate the design of alternative low-complexity switching architectures [146]. This

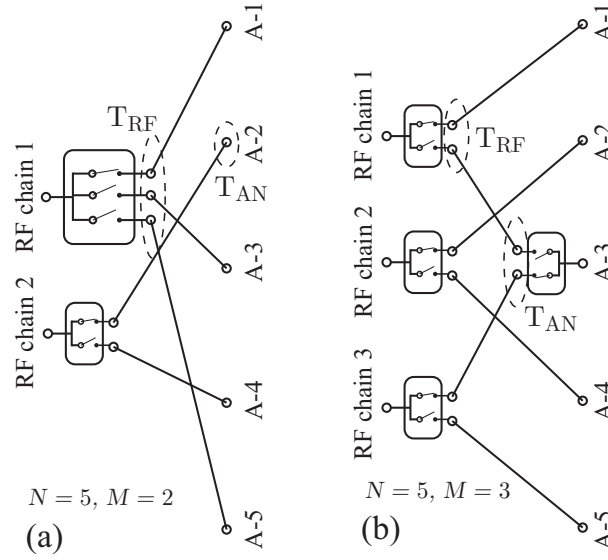


**Figure 7.2:** Illustrative block diagrams for the PC switching architectures of (a)  $\lfloor \frac{N}{M} \rfloor \geq 2$  and (b)  $\lfloor \frac{N}{M} \rfloor < 2$ .

section considers a switching architecture with partial connectivity, referred to as partially-connected (PC) architecture, with arbitrary  $N$  and  $M$  for alleviating the above-mentioned concerns. Specifically, the PC architecture is designed to reduce the number of internal connections and basic switches, i.e.

$$T_{\text{RF}} = \left\lceil \frac{N}{M} \right\rceil, \text{ and } T_{\text{AN}} = \begin{cases} 1, & \text{if } \lfloor \frac{N}{M} \rfloor \geq 2, \\ 2, & \text{otherwise,} \end{cases} \quad (7.21)$$

where the maximum number of throws per RF chain in the RF-chain switching stage,  $T_{\text{RF}}$ , is defined to guarantee the essential constraint of connecting every antenna to at least one RF chain. Moreover, (7.21) shows that there are two specific cases depending on the ratio  $\frac{N}{M}$  and whose practical implications are considered in the following:

1. *Case for  $\lfloor \frac{N}{M} \rfloor \geq 2$ .* PC switching schemes satisfying this condition are those where each antenna is connected to a single RF chain ( $T_{\text{AN}} = 1$ ). Accordingly, basic switches SP3T or with a larger number of outputs have to be employed at the RF-chain switching stage to ensure that all antennas can be employed for transmission. An illustrative example is shown in Figure 7.2(a), where  $N = 5$  and  $M = 2$ . In this architecture, it can be observed that one SP3T must be

implemented at the RF-chain switching stage for guaranteeing that every antenna is connected to one RF chain. Note that this architecture also comprehends the particular case  $N/M = 2$  considered in [146], where only binary (SP2T) switches are required to ensure antenna connectivity.

2. *Case for  $\lfloor \frac{N}{M} \rfloor < 2$ .* In these architectures each antenna might be connected to more than one RF chain ( $T_{AN} = 2$ ). Accordingly, employing basic switches SP2T suffices to guarantee connectivity for all  $N$  antennas. A specific switching architecture satisfying  $\lfloor N/M \rfloor < 2$  is shown in Figure 7.2(b) for  $N = 5$  and  $M = 3$ . This figure shows that at least one antenna is connected to more than one RF chain, hence introducing additional ILs in the output switching stage when compared with the case  $\lfloor N/M \rfloor \geq 2$ . However, incorporating additional RF chains simultaneously enhances the rates, which results in a relevant trade-off that will be studied in Sec. 3.5.

#### 7.4.1 Optimization constraints for AS with Instantaneous CSI

Overall, the above PC architectures impose a limited flexibility in the antenna selection procedure, since the simultaneous selection of certain antenna combinations is not implementable. In this context, the specific restrictions introduced by the partial connectivity should be considered when defining the optimization problem  $\mathcal{P}_{7.1}$  for selecting the antennas as per Sec. 7.2.2. With this purpose, let  $\overline{\mathcal{N}} = \{1, \dots, N\}$  and  $\overline{\mathcal{M}} = \{1, \dots, M\}$  be sets indexing the antennas and the RF chains, respectively. The antenna subsets  $\mathcal{N}^i, i \in \{1, \dots, S_{\text{cons}}\}$  are defined as disjoint sets of antennas sharing at least one common RF chain, i.e.  $\mathcal{N}^1 \cup \mathcal{N}^2 \cup \dots \cup \mathcal{N}^{S_{\text{cons}}} = \overline{\mathcal{N}}$  and  $\mathcal{N}^i \cap \mathcal{N}^j = \emptyset, \forall i, j \in \{1, \dots, S_{\text{cons}}\}$ . Here,  $\emptyset$  denotes the empty set and  $S_{\text{cons}}$  denotes the number of constraints detailed below. Similarly,  $\mathcal{M}^i \subset \overline{\mathcal{M}}, i \in \{1, \dots, S_{\text{cons}}\}$  represent disjoint sets of RF chains sharing at least one common antenna. For the illustrative example of Figure 7.2(b), the sets  $\mathcal{M}^i$  are defined as  $\mathcal{M}^1 = \{1, 3\}$ , since these RF chains inter-connect antennas  $\mathcal{N}^1 = \{1, 3, 5\}$ , and  $\mathcal{M}^2 = \{2\}$ , which inter-connects antennas  $\mathcal{N}^2 = \{2, 4\}$ . Intuitively, the cardinality of the antenna groups sharing different RF chains ( $S_{\text{cons}}$ ) also represents the additional

number of constraints required in  $\mathcal{P}_{7.1}$  to account for partial connectivity, which is given by

$$S_{\text{cons}} = M - N_{\text{ov}}, \quad (7.22)$$

where  $N_{\text{ov}}$  represents the number of antennas with the possibility of connecting to more than one RF chain. This is because the partial connectivity architecture imposes an additional constraint for every subset of antennas  $\mathcal{N}^i \subset \overline{\mathcal{N}}, i \in \{1, \dots, S_{\text{cons}}\}$ , interconnected with their corresponding subset of RF chains  $\mathcal{M}^i \subset \overline{\mathcal{M}}, i \in \{1, \dots, S_{\text{cons}}\}$ . For instance, Figure 7.2(b) shows that only two out of antennas  $\mathcal{N}^1 = \{1, 3, 5\}$  can be simultaneously active, since these antennas are only connected to two RF chains ( $|\mathcal{M}^1| = 2$ ). Similarly, only one antenna out of antennas  $\mathcal{N}^2 = \{2, 4\}$  can be active because they share a single RF chain ( $|\mathcal{M}^2| = 1$ ).

Without loss of generality, this chapter considers that each RF chain is connected to antennas physically separated as shown in Figure 7.2(a) and Figure 7.2(b)<sup>2</sup>. Based on the above, the distance between antennas inter-connected to a given RF chain  $N_{\text{dist}}$  can be defined as

$$N_{\text{dist}} = \begin{cases} M, & \text{if } \lfloor N/M \rfloor \geq 2, \\ N - M, & \text{otherwise.} \end{cases} \quad (7.23)$$

For instance, Figure 7.2(a) and (b) show that each RF chain connects to antennas separated by  $N_{\text{dist}} = M = 2$  and  $N_{\text{dist}} = N - M = 2$  indices, respectively. Similarly, the distance between the RF chains connected to a given subset of antennas  $M_{\text{dist}}$  is given by

$$M_{\text{dist}} = \begin{cases} 1, & \text{if } \lfloor N/M \rfloor \geq 2, \\ N - M, & \text{otherwise.} \end{cases} \quad (7.24)$$

For example, Figure 7.2(b) shows that RF chains  $\mathcal{M}^1 = \{1, 3\}$ , which inter-connect antennas  $\mathcal{N}^1 = \{1, 3, 5\}$ , are separated by  $M_{\text{dist}} = N - M = 2$  because RF chain  $\mathcal{M}^2 = 2$  is situated in-between. Accordingly,  $\mathcal{N}^i$  and  $\mathcal{M}^i$  for the non-adjacent antenna

---

<sup>2</sup>This consideration is motivated by the results obtained in [146] for real propagation environments, where it was shown that inter-connecting a given RF chain to non-adjacent antennas provides a better performance than the connection to adjacent antennas.

connectivity considered in this chapter can be expressed as

$$\mathcal{N}^i = \left\{ i, i + N_{\text{dist}}, \dots, i + \left( \left\lceil \frac{N - i + 1}{N_{\text{dist}}} \right\rceil - 1 \right) N_{\text{dist}} \right\}, \quad (7.25)$$

where each RF chain connects to antennas with indices separated by  $N_{\text{dist}}$  and

$$\mathcal{M}^i = \left\{ i, i + M_{\text{dist}}, \dots, i + \left( \left\lceil \frac{M - i + 1}{M_{\text{dist}}} \right\rceil - 1 \right) M_{\text{dist}} \right\}, \quad (7.26)$$

where each antenna connects to RF chains with indices separated by  $M_{\text{dist}}$ . Considering the above, the convex AS optimization problem for general PC architectures can be formulated as

$$\mathcal{P}_{7.5} : \underset{\mathbf{S}, \mathbf{P}}{\text{maximize}} \log_2 \det (\mathbf{I}_K + \rho \mathbf{P} \mathbf{H} \mathbf{S} \mathbf{H}^H) \quad (7.27a)$$

$$\text{subject to } \sum_{i=1}^N \mathbf{S}_{i,i} = M, \quad (7.27b)$$

$$0 \leq \mathbf{S}_{i,i} \leq 1, \quad \forall i \in \{1, \dots, N\}, \quad (7.27c)$$

$$\sum_{j \in \mathcal{N}^i} \mathbf{S}_{j,j} = |\mathcal{M}^i|, \quad \forall i \in \{1, \dots, S_{\text{cons}}\}, \quad (7.27d)$$

where w.r.t.  $\mathcal{P}_{7.2}$  it can be seen that additional constraints due to PC have been added as per (7.27d). Similarly to  $\mathcal{P}_{7.2}$ , the final solution to the AS can be obtained by choosing the  $M$  largest entries in the solution of  $\mathcal{P}_{7.5}$  compliant with the partial connectivity constraints.

#### 7.4.2 Optimization constraints for AS with Power-Based CSI

The specific RF switching architecture selected also determines the procedure for performing AS based on the channel power at each of the antenna ports. Indeed, the solution to select the antennas is not straightforward as per the case of FF RF switching in (7.13), since additional constraints due to the partial connectivity must be incorporated to  $\mathcal{P}_{7.4}$ . As a result, the convex optimization problem for PB-AS under limited

connectivity can be expressed as

$$\mathcal{P}_{7.6} : \underset{\mathbf{S}}{\text{maximize}} \quad \bar{\mathbf{h}}\mathbf{S}, \quad (7.28a)$$

$$\text{subject to} \quad \sum_{i=1}^N \mathbf{S}_{i,i} = M, \quad (7.28b)$$

$$0 \leq \mathbf{S}_{i,i} \leq 1, \forall i \in \{1, \dots, N\}, \quad (7.28c)$$

$$\sum_{j \in \mathcal{N}^i} \mathbf{S}_{j,j} = |\mathcal{M}^i|, \forall i \in \{1, \dots, S_{\text{cons}}\}, \quad (7.28d)$$

where the sets  $\mathcal{N}^i$  and  $\mathcal{M}^i$  are defined in (7.25) and (7.26), respectively, and it can be seen that new constraints are added w.r.t.  $\mathcal{P}_{7.4}$  as per (7.28d). The final solution is obtained by selecting the  $M$  largest entries satisfying the optimization constraints.

Similarly to the simplification of (7.13), the solution to  $\mathcal{P}_{7.6}$  also admits a straightforward implementation. Specifically, the optimal solution can be obtained by combining the  $|\mathcal{M}^i|$  largest entries of  $\bar{\mathbf{h}}_{[\mathcal{N}^i]}$  for each sub-array, i.e.,  $\mathcal{M} = \bigcup_{i \in \{1, \dots, S_{\text{cons}}\}} \max_{|\mathcal{M}^i|} \bar{\mathbf{h}}_{[\mathcal{N}^i]}$ .

### 7.4.3 Implications of Reducing Connectivity

The additional constraints introduced to the optimization problems  $\mathcal{P}_{7.2}$  in  $\mathcal{P}_{7.4}$  have a number of practical system-level implications that can be described as follows:

- *Insertion losses.* The ILs introduced will be smaller in the design with partial switching connectivity due to the smaller number of basic switches required to implement the switching matrix. For instance, in the example of Table 7.2 for  $M = 6$  and  $N = 32$ , the ILs are reduced to  $L = 0.7$  dB, since  $T_{\text{RF}} = 6$  and  $T_{\text{AN}} = 1$ , i.e. at most two basic switches (SP2T and SP3T) are required per RF chain.
- *Power-based AS.* The complexity order of solving  $\mathcal{P}_{7.4}$  and  $\mathcal{P}_{7.6}$  for the FF and PC switching networks is  $\mathcal{O}(N \log(N))$  and  $\mathcal{O}(\max(|\mathcal{N}^i|) \cdot \log(\max(|\mathcal{N}^i|)))$ , respectively [258]. Note that multiple independent instances of the sorting algorithm are required for solving the optimization problem  $\mathcal{P}_{7.6}$ , although each of these instances have a reduced complexity when compared with that required for solving

$\mathcal{P}_{7.4}$ , since  $|\mathcal{N}^i| < N, \forall i$ . Overall, the substantial hardware complexity savings demonstrated in Sec. 7.7 motivate the employment of PC RF switching architectures.

- *System performance.* Limiting the connectivity affects the number of possible antenna combinations that can be selected. Due to its importance, this aspect is studied in Sec. 7.5, where the performance loss w.r.t. FF architectures is characterized for the relevant case of PB-AS.
- *Baseband signal processing.* The digital signal processor (DSP) must account for the reduced connectivity in order to perform the precoding / detection operations. This is because the order of the antenna channels might be different from the conventional order at the antenna ports. Note that this might also happen for FF architectures minimizing the number of connections (FF-MC) and the power losses (FF-ML). For instance, consider the architecture shown in Fig. 7.2(a) and assume that antennas  $\mathcal{N}^2 = 2$  and  $\mathcal{N}^1 = 5$  are those that maximize capacity. For correct symbol-to-antenna mapping, the DSP should be aware that the channel employed for precoding/detection might have a different order w.r.t. the conventional antenna port order, since now the first RF chain will be connected to antenna port 5 whereas the second RF chain will be connected to antenna port 2.
- *Analog hardware complexity.* The employment of a reduced number of basic switches and connections can reduce cross-coupling between hardware components that are physically close, the time required for calibrating the input-output transfer function and the overall economic cost for implementing the switching matrix.

#### 7.4.4 Practical Hardware Implementation for PB-AS in LSAS

The solution advocated in [129] for reducing the CSI acquisition time in PB-AS is based on implementing analog power estimators at each antenna as shown in Fig. 7.3(a), i.e.  $N_{\text{PM}} = N$ , where  $N_{\text{PM}}$  refers to the number of power meters. Note that the speed and resolution requirements of the analog-to-digital converters (ADCs) required in the parallel power-meter chains can be relaxed due to the non-sensitive nature of the power

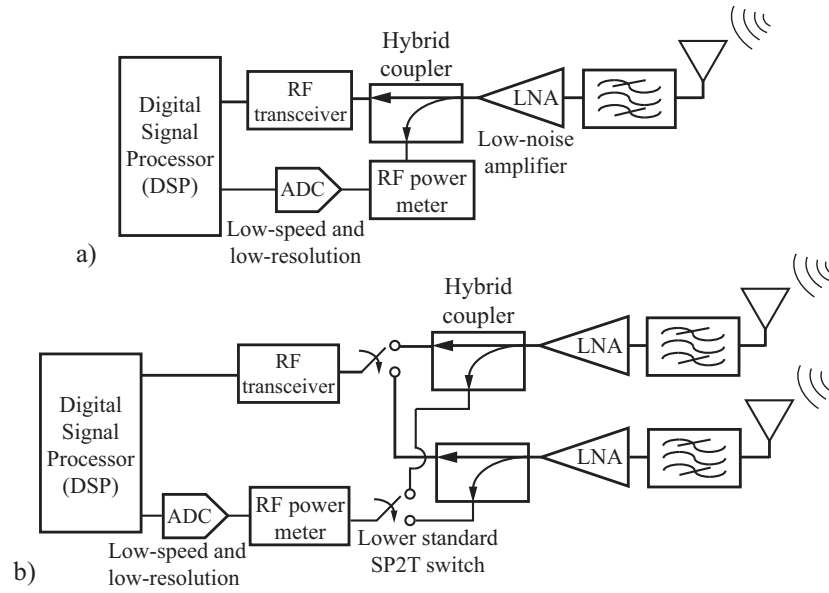


**Figure 7.3:** Block diagram of different hardware implementations for measuring channel power. (a) One parallel power meter chain per antenna and (b) limited number of power meter chains with additional switches.

measurements. Nevertheless, additional data ports are required at the digital signal processor (DSP) to acquire this data.

The excessive number of antenna implemented in LSAS also motivate the implementation of a considerable number of RF chains, even when AS is implemented [148]. Since each RF chain also captures the channel power information during the uplink data stage, this entails that the solution illustrated in Fig. 7.3(a) acquires a significant amount of redundant data. This redundancy is eliminated in the architecture considered in Fig. 7.3(b), where only  $N_{\text{PM}} = N - M$  power meters are required. The particular example shown in Fig. 7.3(b) corresponds to an architecture with  $N = 2M$ . When compared with the scheme of Fig. 7.3(a), it can be seen that, while an additional RF switches are required, the number of parallel power-meter chains and data ports at the DSP can be substantially reduced. Since the implementation with additional RF switches is expected to be less economically demanding than the solution with additional power meters, the former constitutes an attractive alternative for implementing AS in LSAS.

## 7.5 Performance Analysis: Degradation due to Limited Switching Connectivity

The partial connectivity architecture presented in Sec. 7.4 reduces the IL introduced by the switching matrix at the expense of limiting the number of antenna combinations that can be simultaneously selected, which entails a loss in performance. This section characterizes this loss by following the intuitive approach adopted in [123] for PB-AS. The reasons for focusing on the simpler PB-AS are twofold: a) its reduced CSI acquisition time as detailed in Sec. 7.2.3 by use of RF power meters, and b) the negligible performance loss introduced by this scheme when compared with the selection based on instantaneous CSI for the channels considered in this chapter. Indeed, it will be shown in Sec. 7.7 that, due to the above, PB-AS outperforms AS based on instantaneous CSI in terms of sum rates when CSI acquisition overheads are considered.

### 7.5.1 Ergodic Capacity Approximation for FF-AS

The analysis developed in [123] essentially relies on approximating  $\mathbf{H}_{[\mathcal{M}]}$  in (7.2) by a matrix  $\mathbf{V} \in \mathbb{C}^{K \times M}$  with entries following an identical distribution but with each column of the having different variances, i.e.

$$\mathbf{H}_{[\mathcal{M}]} \approx \mathbf{V}_{f(\mathbf{C})} = \mathbf{T}\mathbf{\Gamma}_{f(\mathbf{C})}, \quad (7.29)$$

where  $\mathbf{T} \in \mathbb{C}^{K \times M}$  is a matrix whose entries follow the same distribution of those from  $\mathbf{H}$ ,  $\mathbf{A}_{f(\mathbf{C})}$  indicates that  $\mathbf{A}$  is a function of the specific switching connectivity and  $\mathbf{\Gamma} \in \mathbb{R}^{M \times M}$  is a diagonal matrix whose definition is considered in the following. Specifically, let  $B_c = \sum_i^K |h_{c,i}|^2 = \|\mathbf{h}_c\|^2$  denote the norm of the  $c$ -th column of  $\mathbf{H}$  and define  $B_{t:N}$  as the  $t$ -th smallest column norm of  $\mathbf{H}$  as per  $\mathcal{W} = \{B_{1:N} < B_{2:N} < \dots < B_{N:N}\}$ . Then, the diagonal entries of  $\mathbf{\Gamma}$  are given by [123]

$$\theta_{i,i} = \mathbb{E}[B_{t_i:N}] / \sqrt{K}, \quad t_i \in \{1, \dots, N\}. \quad (7.30)$$

The definition of the indices  $t_i$  is straightforward and deterministic for the case of FF switching networks, since the PB-AS will always select the antennas corresponding to the largest column norms of  $\mathbf{H}$ , i.e.

$$\mathbf{\Gamma} = \text{diag} \left( \sqrt{B_{N:N}}, \sqrt{B_{N-1:N}}, \dots, \sqrt{B_{N-M+1:N}} \right) / \sqrt{K}. \quad (7.31)$$

A simpler approximation of the resultant channel in (7.29) can be obtained by averaging the power scaling (PS) factors of the selected ordered statistics in (7.30), which for FF switching networks yields

$$\tilde{P}_{\text{FF}} = \frac{1}{KM} \sum_{i=1}^M \mathbb{E}_{\mathbf{H}} [B_{N-i+1:N}], \quad (7.32)$$

where  $\mathbb{E}_{\mathbf{H}}$  denotes that the expectation is taken over the small-scale fading parameters of the random channel  $\mathbf{H}$ . For the case of uncorrelated Rayleigh flat-fading channels, the first moment of the  $t$ -th ordered random variable  $B_{t:N}$  is given by [259, 260]

$$\begin{aligned} \mathbb{E}_{\mathbf{H}} [B_{t:N}] &= \frac{N!}{(M-1)!(t-1)!(N-t)!} \sum_{r=0}^{t-1} (-1)^r \binom{t-1}{r} \\ &\times \sum_{s=0}^{(K-1)(N-t+r)} a_s (N-t+r) \frac{(K+s)!}{(N-t+r+1)^{K+s+1}}, \end{aligned} \quad (7.33)$$

where  $a_s (N-t+r)$  represent the polynomial coefficient of  $x^s$  in the expansion

$$\left( \sum_s \frac{x^s}{s!} \right)^N = a_0 x + a_1 x^2 + a_2 x^3 + \dots + a_N x^N. \quad (7.34)$$

Note that  $a_s (N-t+r)$  can be recursively computed from  $a_1(\cdot)$  [259, 260]. The resultant ergodic capacity with the PS approximation can be subsequently expressed as [123]

$$C_{\text{PS-FF}} = \mathbb{E}_{\mathbf{T}} \left[ \log_2 \det \left( \mathbf{I}_K + \rho \tilde{P}_{\text{FF}} \mathbf{T} \mathbf{T}^H \right) \right], \quad (7.35)$$

where the expectation over  $\mathbf{T}$  has been analytically derived in [261–263] for different correlated and uncorrelated communication channels.

### 7.5.2 Ergodic Capacity Approximation for PC-AS

While the approximation in (7.35) accurately characterizes the ergodic capacity attainable by FF schemes, an optimal PB-AS cannot be guaranteed under limited connectivity in general, since selecting the antenna combination with the largest column norms of  $\mathbf{H}$  might not be feasible due to the additional constraints imposed in the optimization problem. Moreover, note that selecting some combinations of ordered column norms is more probable than selecting others, since the probability that the  $t$ -th ordered coefficient  $B_{t:N}$  is not chosen is different for every  $t \in \{1, \dots, N\}$  as per the specific input-output connectivity in the implemented switching matrix. This entails that (7.31) and (7.32) are not longer valid for PC networks. For this reason (7.32) can be further approximated by taking into consideration the probability of selecting a given subset of the ordered set  $\mathcal{W} = \{B_{1:N} < B_{2:N} < \dots < B_{N:N}\}$ .

With the above purpose, let  $\mathcal{G}^j, j \in \left\{1, \dots, \binom{N}{M}\right\}$  of cardinality  $|\mathcal{G}^j| = M$  be discrete sets containing a given combination of ordered column norms of  $\mathbf{H}$ . For instance, in the architecture shown in Fig. 7.2(a), the relevant sets  $\mathcal{G}^j$  with non-zero probability of being selected following a PB criterion are  $\mathcal{G}^1 = \{1, 2\}$ ,  $\mathcal{G}^2 = \{1, 3\}$  and  $\mathcal{G}^3 = \{1, 4\}$ . Note that the antenna with the largest power can always be selected even under partial connectivity restrictions. Moreover, let  $T_j \in \{0, 1\}$  be a binary random variable that determines whether the specific combination of columns of  $\mathbf{H}$  determined by  $\mathcal{G}^j$  is selected or not. Intuitively, the limited connectivity restricts a given combination of antennas  $\mathcal{G}^j$  to be selected with a given probability. This entails that, in contrast with (7.32), the expectation in (7.30) must also be taken with respect to the discrete random variables  $T_j$ . Therefore, the performance of PB-AS for PC switching architectures can be approximated by employing

$$\tilde{P}_{\text{PC}} = \frac{1}{KM} \mathbb{E}_{T_j} \left[ \sum_{i=1}^M \mathbb{E}_{\mathbf{H}} \left[ B_{\mathcal{G}^j_i:N} \right] \right], \quad (7.36)$$

where  $\mathcal{A}_i$  refers to the  $i$ -th entry of a set  $\mathcal{A}$  and the outer expectation is taken over the set of random discrete variables  $T_j$ . Closed-form expressions for the inner expectation in (7.36) are already available for multiple channels such as those with Rayleigh flat-fading

as per (7.33) [123]. Instead, the outer expectation corresponds to that of a discrete random variable, which is given by

$$\tilde{P}_{\text{PC}} = \frac{1}{KM} \sum_{j=1}^{\binom{N}{M}} \left( \sum_{i=1}^M \mathbb{E}_{\mathbf{H}} \left[ B_{\mathcal{G}_i^j:N} \right] \right) \times P(T_j) = \sum_{j=1}^{\binom{N}{M}} \left( \hat{P}_j \times P(T_j) \right), \quad (7.37)$$

where  $P(T_j)$  refers to the probability of jointly selecting the ordered channel columns determined by  $\mathcal{G}^j$ . The probabilities associated with selecting  $\mathcal{G}^j$  can be computed depending on the specific switching connectivity between the RF chains and the antenna ports, and the particular channel characteristics. Specifically,  $P(T_j)$  can be decomposed by following the chain rule of probability

$$P(T_j) = P \left( \bigcap_{i=1}^M \text{selecting } \mathcal{G}_i^j \right) = \prod_{i=1}^M P \left( \text{selecting } \mathcal{G}_i^j \mid \bigcap_{r=1}^{i-1} \text{selected } \mathcal{G}_r^j \right), \quad (7.38)$$

where  $\cap$  denotes the intersection of events. To simplify the derivation of the joint probabilities in (7.38), this chapter concentrates on channels  $\mathbf{H}$  adopting the form [11]

$$\mathbf{H} = \mathbf{R}^{\frac{1}{2}} \mathbf{Z}, \quad (7.39)$$

where  $\mathbf{R} \in \mathbb{C}^{K \times K}$  is the deterministic channel covariance matrix and  $\mathbf{Z} \in \mathbb{C}^{K \times N}$  is a matrix of i.i.d. random variables following  $\mathbf{z}_{i,j} \sim \mathcal{CN}(0, 1)$ . Note that  $\mathbf{R}$  is a diagonal matrix with diagonal entries characterizing the large scale channel fading if the users are placed sufficiently apart as detailed in (2.11) [11].

The above assumption entails that the probability of finding the  $t$ -th ordered statistic  $B_{t:N}, t \in \{1, \dots, N\}$  at a given antenna is equal for all antenna elements  $\mathcal{N}$ , which makes computing the probabilities in (7.38) straightforward for a given connectivity matrix  $\mathbf{C}$ . An example of this derivation for  $N = 5$  and  $M = 2$  is provided in Appendix F for completeness. Once the probabilities of selecting a given ordered channel column combination  $P(T_j)$  in (7.37) are determined, an approximation to the analytical ergodic capacity of AS systems with PC switching matrices can be expressed as

$$C_{\text{PS-PC}} \approx \mathbb{E}_{\mathbf{T}} \left[ \log_2 \det \left( \mathbf{I}_K + \rho \tilde{P}_{\text{PC}} \mathbf{T} \mathbf{T}^H \right) \right]. \quad (7.40)$$

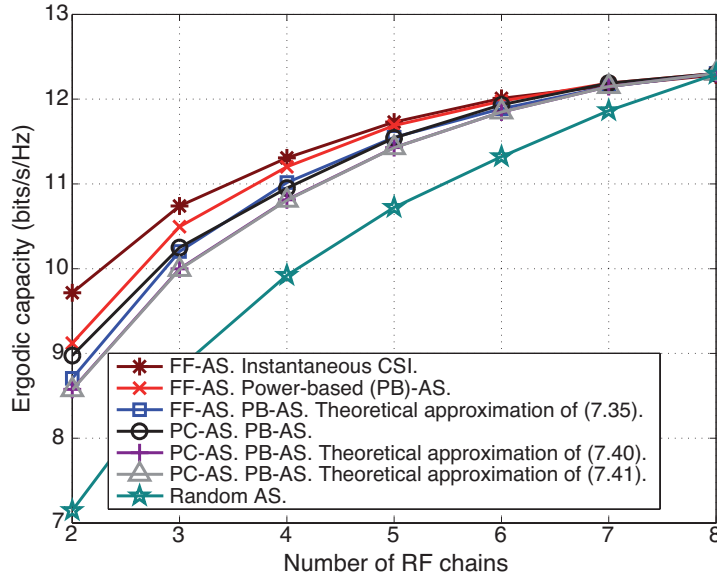


**Figure 7.4:** Theoretical and simulated ergodic capacities (bits/s/Hz) vs.  $M$ .  $N = 8$ ,  $K = 2$  and  $\rho = 10$  dB.

An alternative approximation to the ergodic capacity of PC switching matrices can be derived by directly computing the expectation of the capacity over both the discrete random variables  $T_j$  and  $\mathbf{T}$ . In this particular case, the approximation of the ergodic capacity is given by

$$C_{\text{PS-PC}} \approx \sum_{j=1}^{\binom{N}{M}} \mathbb{E}_{\mathbf{T}} \left[ \log_2 \det \left( \mathbf{I}_K + \rho \hat{P}_j \mathbf{T} \mathbf{T}^H \right) \right] \times P(T_j), \quad (7.41)$$

where  $\hat{P}_j$  is defined in (7.37).

The accuracy of the derived approximations can be observed in Fig. 7.4, which represents the ergodic capacity attained by the schemes considered in this chapter against increasing  $M$  for a system with  $N = 8$ ,  $K = 2$  and  $\rho = 10$  dB. Here, a small-scale MIMO setup is considered for illustrative reasons since, as shown in Sec. 7.7, the differences between the switching architectures vanish for large  $N$ . This figure also considers an uncorrelated Rayleigh flat-fading channel and ignores the overheads associated with CSI acquisition. In spite of this unfavourable assumption for the PB criterion, it can be seen that the PB-AS approaches the performance attained of the instantaneous CSI-based AS for different values of  $M$ , an observation consistent with previous works [23, 123].

Fig. 7.4 also shows that only a slight performance loss is experienced for the switching architecture with partial connectivity w.r.t. the FF scheme, which is also coherent with the results obtained for  $N = 2M$  in the real propagation channels of [146]. The slight performance loss can be explained by noting that, in general, there exists a large probability of selecting antennas with significant channel powers, even if these are not strictly the largest ones as shown in Appendix F. This result combined with those obtained in Sec. 7.7 motivate the employment of PB-AS with partial connectivity, especially for LSAS where the ILs introduced by the switching matrices can be significant. Moreover, Fig. 7.4 shows that the proposed approximations in (7.40) and (7.41) are able to capture the performance loss produced by the partial connectivity architecture, hence validating the approach adopted in this section.

## 7.6 Energy Efficiency with Insertion Losses

As highlighted throughout this Thesis, the enhancement of the communication's energy efficiency is a key driver for considering AS implementations in LSAS due to the possibility of reducing the number of RF chains simultaneously active [61, 146, 148]. This comes, however, at the expense of introducing additional ILs in the RF switching stage, hence posing an energy efficiency trade-off that this chapter aims at characterizing. The energy efficiency measured in bits/Joule/Hz can be expressed as [4, 57, 61, 116]

$$\varepsilon = \frac{R_{\text{sum}}}{P_{\text{tot}}} = \frac{R_{\text{sum}}}{P_{\text{PA}} + MP_{\text{dyn}} + P_{\text{LO}}}, \quad (7.42)$$

where  $R_{\text{sum}}$  refers to the sum rates in bits/s/Hz and  $P_{\text{tot}}$  is the total system power consumption, which is decomposed as described in Sec. 2.1.3. Specifically,  $P_{\text{PA}} = \frac{P_t}{\eta}$  is the power consumed by power amplifiers (PAs) with efficiency  $\eta$  to produce an output signal of  $P_t$  Watts. Moreover,  $P_{\text{dyn}}$  is the power consumed by the analog circuitry required in each of the RF chains, and  $P_{\text{LO}}$  denotes the power consumed by the local oscillator.

To explicitly account for the impact of the ILs on the system's energy efficiency,

this chapter incorporates  $L_{\text{IL}}$  directly in  $P_t$  above, that is, the RF switching matrix is placed after the power amplifiers in the transmission chain [117, 118]. This entails that power amplifiers in systems with AS will be required to produce output signals with larger power to compensate for the ILs of the switching stage, i.e.  $P_t^{\text{AS}} = P_t^{\text{no-AS}} \times L_{\text{IL}}$  [117, 118]. While other hardware solutions such as placing the switching matrices before the power amplifiers are certainly feasible, considering the impact of the ILs on the resultant system's energy efficiency also becomes more intricate. This is because precise knowledge of the power amplifiers response, which is non-linear and component-dependent, would be required to quantify the additional power required per RF chain. Instead, the above consideration facilitates providing meaningful insights on the trade-offs that arise when employing AS with the switching architectures considered in this chapter, as shown in the following.

## 7.7 Results and Discussion

This section presents numerical results for characterizing the performance of the switching architectures considered in this chapter. In particular, AS schemes based on both PB and instantaneous CSI decisions are considered under uncorrelated Rayleigh flat-fading channels. Moreover, this section shows the sum rates attained via dirty paper coding (DPC) and for the more practical ZF precoder. The focus is placed on characterizing the impact of varying the number of RF chains to provide guidelines for determining their optimal number in AS systems implementing the realistic switching architectures considered here. The results are obtained for LSAS, since the ILs and complexity of the FF switching networks are critical in these systems due to both the large number of RF chains and antennas deployed. For simplicity and without loss of generality, the results obtained in the following consider that the power losses introduced by the switching matrices correspond to those of the input-output combination with largest IL, i.e. the critical signal path.

Fig. 7.5 represents the sum rates of the schemes considered in this chapter against increasing number of RF chains  $M$  in a system with  $N = 128$ ,  $K = 16$  and  $\rho = 15$

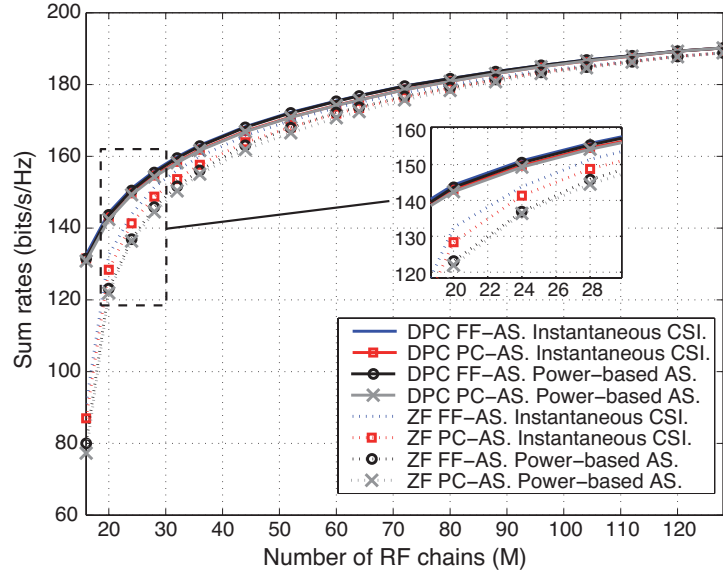


**Figure 7.5:** Sum rates (bits/s/Hz) vs.  $M$  for DPC and ZF with FF and PC switching matrices.  $N = 128$ ,  $K = 16$ ,  $\rho = 15$  dB and  $\eta_{\text{dl}}/\eta_{\text{coh}} = 1$ .

dB. The instantaneous CSI is assumed to be acquired at no cost, i.e.  $\eta_{\text{dl}}/\eta_{\text{coh}} = 1$  is considered, while the impact of CSI acquisition is explained in subsequent results. It can be observed that ZF approaches the performance of DPC as  $M$  grows, due to the favourable propagation conditions experienced by LSAS [11, 12, 69]. The results of Fig. 7.5 also show that there exists a very slight penalty when employing PB-AS against the AS based on instantaneous CSI in LSAS, a phenomenon already observed for small scale MIMO systems and for LSAS in realistic propagation environments [23, 148]. Interestingly, it can also be observed that, independently of  $M$ , the performance of PC-AS approaches that of the FF selection. This occurs because, while not being able to select the optimal antenna combination due to a limited switching connectivity, there are numerous antennas combinations with a similar performance due to the large number of antennas (channels) available to perform the selection.

The results of Fig. 7.6 illustrate the impact of considering a limited channel coherence time and the need for training in AS for the same simulation of parameters of Fig. 7.5 with  $\eta_{\text{coh}} = 200$ . This corresponds to a fast-varying communication channel [13]. Without loss of generality, Fig. 7.6 considers that 70% of the remaining time resources after channel estimation are allocated to downlink transmission, i.e.  $\eta_{\text{dl}} = 0.7 \times (\eta_{\text{coh}} - \eta_{\text{tr}})$  in (7.2), (7.6), (7.27a) and (7.28a), where  $\eta_{\text{tr}}$  is given by (7.11) and (7.14) for full-CSI and

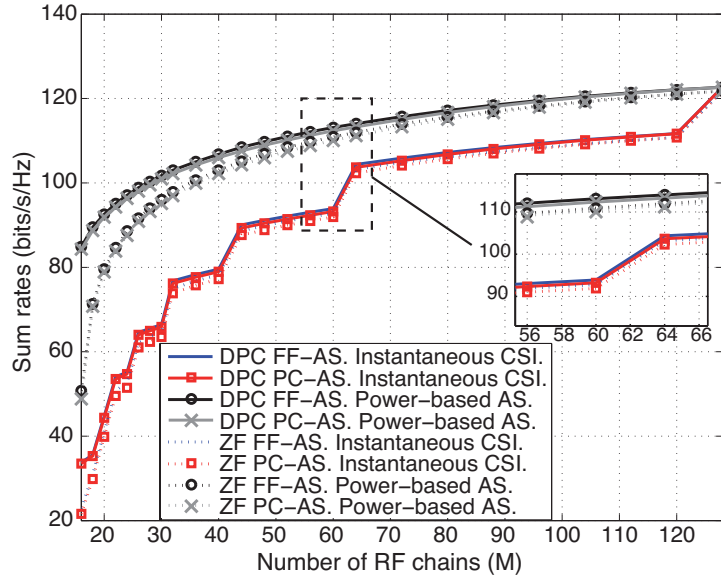


**Figure 7.6:** Sum rates (bits/s/Hz) vs.  $M$  for DPC and ZF with FF and PC switching matrices.  $N = 128$ ,  $K = 16$ ,  $\rho = 15$  dB and  $\eta_{\text{coh}} = 200$ .

PB-AS, respectively. Fig. 7.6 critically shows that full CSI acquisition becomes suboptimal and PB-AS becomes a more attractive approach when a realistic channel coherence time is considered. This is because acquiring the instantaneous CSI to perform the selection requires a larger training period, which results in a performance loss particularly significant for reduced  $M$ . Instead, PB-AS can employ the  $N_{\text{PM}} = N - M$  power meters integrated in the analog stage for estimating the channel powers and, exploiting channel reciprocity, for performing the selection without requiring accurate CSI for all antennas. The results of Fig. 7.6 also indicate the most efficient ranges for selecting  $M$  in the instantaneous CSI-based decision without power meters, since sudden rate variations can be observed for increasing  $M$  due to the different training times required as per (7.10). Specifically, the stepwise behaviour is a direct consequence of  $\eta_{\text{tr}}$  being an integer multiple of  $K$  in (7.10), as per the multiplexed training operation detailed in Sec. 7.2.3.

The results of Fig. 7.7 illustrate the sum rates against increasing values of  $N$  for a system with  $M = 32$ ,  $K = 16$ ,  $\rho = 15$  dB and  $\eta_{\text{coh}} = 200$ . It can be observed that increasing  $N$  does not always provide higher attainable rates for the case of instantaneous CSI acquisition due to the larger training time required when  $M$  is fixed. Instead, it can be observed that PB-AS strictly enhances the sum rates as  $N$  grows. Moreover,

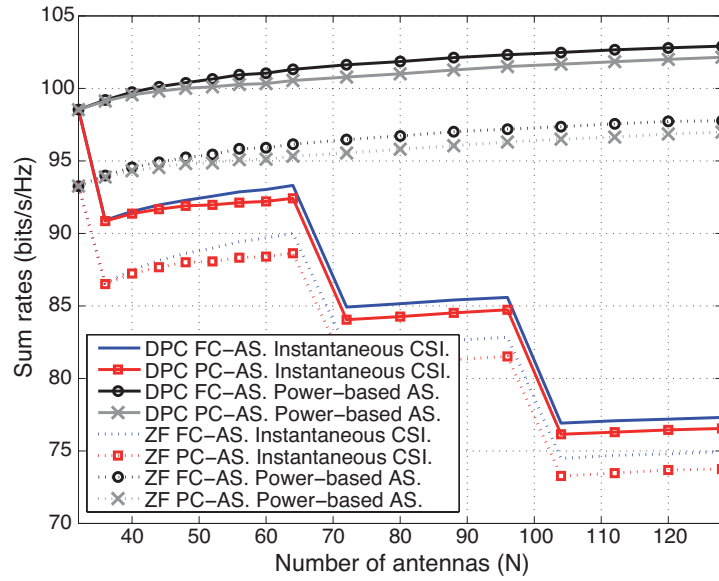


**Figure 7.7:** Sum rates (bits/s/Hz) vs.  $N$  for DPC and ZF with FF and PC switching matrices.  $M = 32$ ,  $K = 16$ ,  $\rho = 15$  dB and  $\eta_{\text{coh}} = 200$ .

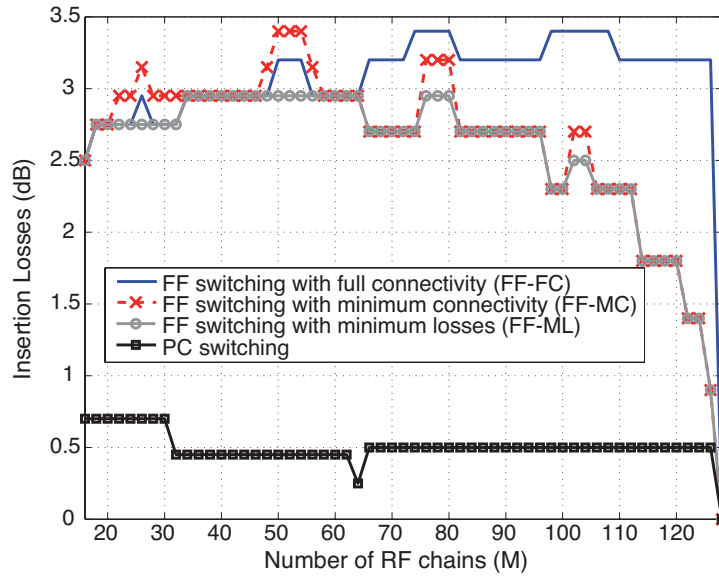


**Figure 7.8:** Insertion losses (dB) introduced by different switching architectures vs.  $M$ .  $N = 128$  and basic switching losses given in Table 7.1.

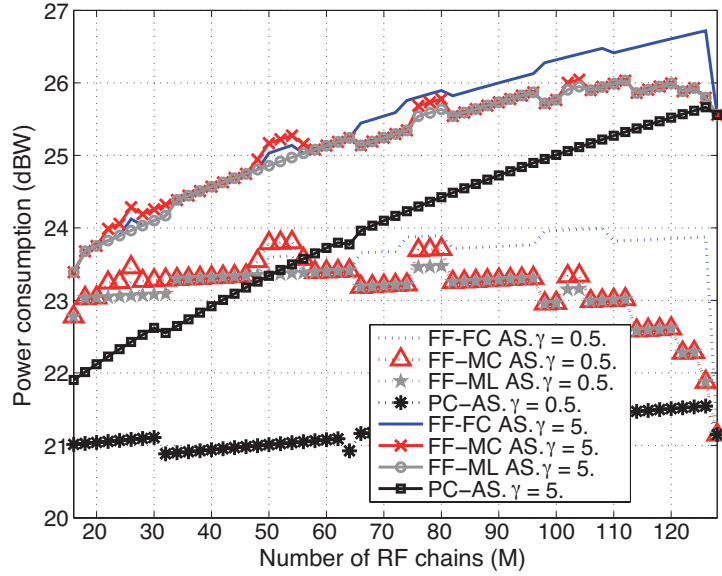
Fig. 7.7 also shows that the performance differences between FC and PC switching are approximately preserved independently of  $N$ . Similarly to Fig. 7.6, the stepwise trend is produced by the multiplexed training operation in (7.10).

Fig. 7.8 represents the ILs of (7.15) introduced by the FF and PC switching architectures considered in this chapter for  $N = 128$  and increasing  $M$ . The basic switches described in Table 7.1 are considered for implementing the switching network. The re-

sults of Fig. 7.8 clearly show the benefits of considering PC architectures when compared with the FF schemes, which motivates their employment when simultaneously considering their small performance loss depicted in Fig. 7.5-7.7. For instance, the ILs can be reduced by up to 2.5 dB for  $M = N/2$ , which is the point with minimal IL for the PC network and the specific case considered in [146]. This can be explained by noting that  $T_{RF} = 2$  and  $T_{AN} = 1$  for  $M = N/2$ . Instead, implementing a larger  $M$  requires additional RF switches at the output stage of the switching network as illustrated in Fig. 7.2(b), hence introducing additional losses in the critical signal path. However, note that considering a larger number of RF chains might also be required in realistic systems for satisfying specific sum rate requirements.

Fig. 7.8 also shows that there are non-desirable areas where the power losses can be substantially increased, if a FF architecture is preferred. As expected, the architecture designed to minimize the power losses (FF-ML) introduces smaller ILs than those with different criteria. Indeed, it can be observed that there are points where minimizing the number of connections as per FF-MC also entails larger IL than both FF-ML and the architecture with complete input-output connectivity (FF-FC). This counter-intuitive behaviour can be explained by detailing the number of basic RF switches required at the input switching stage, which is explicitly detailed in Table 7.2 for the illustrative case of  $N = 32$  and  $M = 6$ . Overall, the results of Fig. 7.8 provide meaningful insights for the design of AS systems, since it can be observed that the ILs of different switching architectures do not follow a monotonic trend with  $M$ . This behaviour, not considered in the related literature, arises due to the differences in the ILs of the basic switches and the specific number of ports  $T_{RF}$  and  $T_{AN}$  required at the input and output of the switching matrices as analyzed in Sec. 7.3.

The total system power consumption  $P_{\text{tot}}$  in (7.42) is shown in Fig. 7.9 against increasing values of  $M$ . Here,  $N = 128$ ,  $P_t = 30$  dBm and  $P_{\text{dyn}} = \gamma (P_t/100)$ , i.e.  $\gamma$  indicates the relative power consumption of each RF chain when compared with the total transmission power. This approach is adopted to make the conclusions independent of the specific transmission power, since the relative power consumption of the RF chains when compared with the power consumed by the power amplifiers strongly depends on



**Figure 7.9:** Total system's power consumption vs.  $M$  with  $N = 128$ ,  $P_t = 30$  dBm and  $P_{\text{dyn}} = \gamma(P_t/100)$  for  $\gamma = \{0.5, 5\}$ .

the transmission power [5, 60]. Fig. 7.9 considers  $\gamma = 0.5$ , which corresponds to a setup where the PA power consumption generally dominates the total power consumption, and  $\gamma = 5$ , where the circuitry power consumption dominates instead. Note that the circuitry power consumption generally dominates in realistic systems such as those of macro BSs with  $P_t = 46$  dBm [5, 60] and  $P_{\text{dyn}} = 1$  W [4], which results in  $\gamma = 2.5$ .

The results of Fig. 7.9 illustrate the importance of reducing the ILs in the switching stage, since substantial power savings over FF-AS can be attained when employing the PC architecture. Moreover, it can be observed that employing AS might be unfavourable in systems where the power consumed by the PAs dominates ( $\gamma = 0.5$ ), since the additional PA power required to compensate for the additional ILs is not counterbalanced by the savings in the power consumption of the RF circuitry. In other words, the most energy efficient option for FF-AS as per (7.42) may well be a MIMO system with  $N = M$ , since the power consumption is reduced for  $N = M$  and the attainable rates grow with  $M$ . Instead, significant enhancements in the total system power consumption can be attained via PC-AS in systems where the RF power consumption dominates, hence motivating their implementation in these setups.

The energy efficiency  $\varepsilon$  in (7.42) is shown vs.  $M$  in Fig. 7.10 for a ZF precoding system

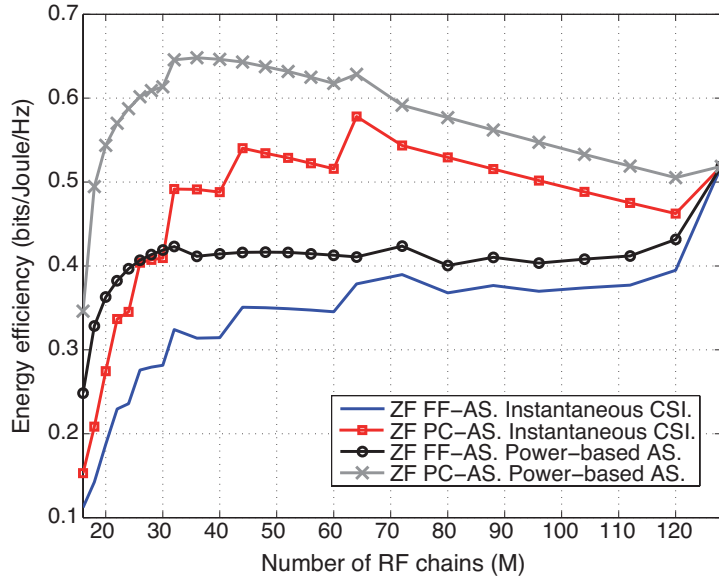


**Figure 7.10:** Energy efficiency  $\varepsilon$  vs.  $M$  for a ZF precoding system with  $N = 128$ ,  $P_t = 46$  dBm,  $\eta_{\text{coh}} = 200$  and  $\rho = 15$  dB.

with  $N = 128$ ,  $K = 16$ ,  $\rho = 15$  dB,  $\eta_{\text{coh}} = 200$ ,  $P_t = 46$  dBm,  $\eta = 0.38$ ,  $P_{\text{dyn}} = 1$  W and  $P_{\text{LO}} = 2$  W [4, 5, 57, 60]. Fig. 7.10 illustrates the benefits of employing both a switching network with limited connectivity and relying on power estimates for performing the AS decision. Specifically, it can be observed that the energy efficiency of the power-based PC-AS is maximized for  $M \approx 32$ , which can be explained by noting a) the significantly reduced ILs when compared with smaller  $M$  in Fig. 7.8 and b) that a large portion of the maximum attainable sum rates for  $M = 128$  is already obtained for  $M \approx 32$  as shown in Fig. 7.6. Note that, in spite of their reduced energy efficiency, the range  $M > 40$  is still of interest, since some systems may pose specific sum rate constraints that should be met. Overall, Fig. 7.10 demonstrates the importance of considering the ILs in the switching stage for energy-efficient system design.

## 7.8 Conclusions

This chapter has characterized the impact of implementing different RF switching architectures in AS systems. The hardware features of a number of conventional FF switching designs and RF switching matrices with reduced connectivity have been specified. This chapter has also characterized the performance loss introduced by these

reduced-complexity architectures as well as relevant differences that should be considered when implemented in combination with power-based AS. Altogether, the results obtained in this chapter motivate the employment of PC switching networks, particularly for LSAS, in combination with power-based AS.

*Critique:* It should be noted that the theoretical performance analysis performed in this chapter is only applicable to communication channels without correlation at the BS and, therefore, a natural extension should consider more general channel models. Moreover, the ideal assumption of having ideal hardware components in the parallel power measurement chains has been adopted. Since low-quality components might be employed in realistic implementations for minimizing the cost of these parallel chains, accounting for hardware non-idealities seems necessary for determining the affordable limits in the degradation of the power measurements.



## Chapter 8

# Realistic Large Scale Antenna Systems: Channel Measurements and Hybrid Precoding Revisited under Realistic RF Modeling

### 8.1 Introduction

The substantial increase in the number of antennas has motivated the development of strategies such as those considered in Chapters 6 and 7 of this Thesis, where the essential objective consists in reducing both the hardware and the signal processing complexity challenges involved in the design of future communications systems. However, a vast number of the conclusions that motivate the development of LSAS and low-complexity analog-digital precoding systems for mmWave rely on theoretical assumptions that have not been verified or do not hold in practice. For instance, the related literature conventionally considers that massive MIMO channels adhere to the Rayleigh fading model [11, 12, 69], or that there are no power losses in the analog stage of hybrid precoding systems [20, 147, 193, 195, 264]. These observations motivate the contents introduced in this chapter, which aim at bridging the gap between theoretical and practical commu-

nications systems with a large number of antennas.

Pursuing the above-mentioned objective, this chapter commences by providing a detailed description of measured large scale communication channels, whose analysis has also constituted the focus of [21, 148, 265–267] and references therein. While this related literature has mostly concentrated on evaluating the performance of linear precoding in LSAS, this chapter complements and expands the conclusions derived in previous works by relying on the measurements acquired in Bell Labs Stuttgart. Multiple aspects of the radio channel such as inter-antenna correlation, average power received per antenna and channel sparsity are studied. Moreover, the operation of reduced-RF designs is evaluated in realistic propagation channels. Overall, particular focus is placed on assessing the feasibility of reducing both the hardware and signal processing complexities of LSAS.

Subsequently, this chapter concentrates on hybrid analog-digital precoding and detection schemes, which are essential in mmWave systems due to the reduced number of degrees of freedom offered by the communication channel and the need of providing substantial beamforming gains [193]. However, the related literature generally disregards the practical implications of signal processing in the RF domain [20, 147, 193, 195, 264], which have been partly considered in [197, 268]. Instead, this chapter characterizes the impact of considering realistic analog beamforming networks (ABFN) in the performance of hybrid precoding schemes, hence providing useful insights for their design and evaluation in practical systems.

## 8.2 Channel Measurements: Campaign and Analysis

The contents of this section aim at describing the technical parameters of the measurements acquired by Dr. Vijay Venkateswaran and Dr. Pawel Rulikowski from Bell Labs Dublin in cooperation with Bell Labs Stuttgart.

### 8.2.1 Measurement Campaign

The measurement setup is comprised of a BS array with  $N = 64$  antennas and a single-antenna mobile station (MS). The outdoor measurements were taken in the

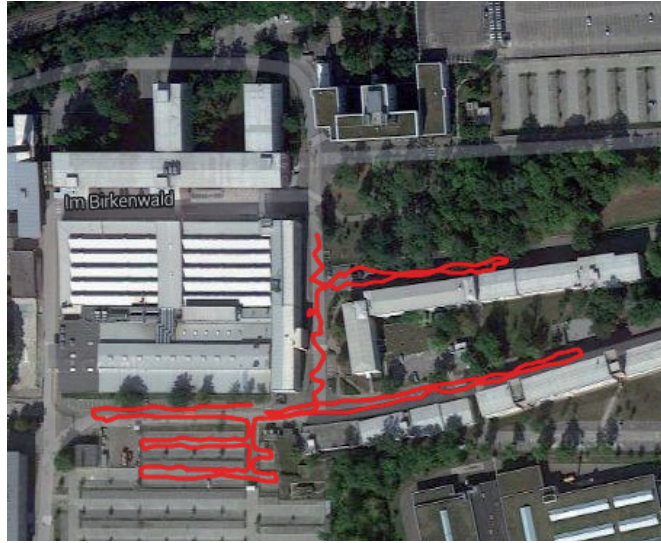


**Figure 8.1:** Overview of the measurement area in Bell Labs Stuttgart.

surroundings of the BL Stuttgart headquarters as illustrated Fig. 8.1. The red trace in Fig. 8.1 represents the route followed by the MS throughout the set of measurements, where a total of  $K = 14$  different outdoor user positions separated by 5 – 10 metres were recorded. The outdoor positions are subsequently combined to generate a multi-user channel matrix, where each measurement represents an independent single-antenna user [21, 148]. In each MS position,  $N_{\text{pos}} = 9$  consecutive channel measurements were acquired and classified according to the relative position between the MS and the BS into:

- 5 different user positions of line-of-sight (LOS) with a strong direct transmission path.
- 5 different user positions of LOS with a significant number of multipath components (partially blocked transmission).
- 4 different user positions of non-line-of-sight (NLOS) transmission.

As shown in Sec. 8.2.2, a number of channel metrics such as the number of significant eigenvalues in the channel covariance matrix are coherent with this classification. The results shown throughout this chapter are generally classified following the above channel categorization.

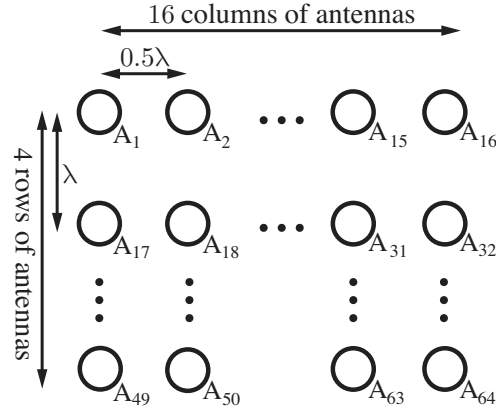


**Figure 8.2:** Schematic of the rectangular base station antenna array with  $N = 64$  antennas.

The BS array is arranged in a rectangular topology as shown in Fig. 8.2. The antenna elements are directional patch antennas with a 3 dB beamwidth of  $115^\circ$ . The antennas are distributed in  $M_v = 4$  rows, which each row comprised of  $M_h = 16$  antenna elements. The inter-antenna spacing between adjacent rows of antennas is  $\lambda$ , whereas the neighbouring column elements are separated by  $0.5\lambda$ . Here,  $\lambda \approx 11.5$  cm represents the wavelength. The mutual coupling between adjacent antenna elements is below  $-20$  dB and they follow a  $\pm 45^\circ$  cross-polarization. The measurements were acquired at an operational frequency of 2.6 GHz occupying an approximate bandwidth of  $B = 18$  MHz. A total of  $N_{\text{sub}} = 300$  subcarriers with a bandwidth of  $B_{\text{sub}} = 60$  kHz are allocated in the operational bandwidth.

The acquisition of the channel measurements is performed in an iterative manner by simultaneously collecting the CSI of a group of  $N_g = 8$  antennas over a time span per group of  $T_g = 10$  msec. This is required due to the limited number of RF chains ( $M = 8$ ) available in the measurement setup. A blank period of  $T_b = 10$  msec, where no CSI is acquired, is placed between different antenna group measurements. Based on the above, an instantaneous realization of the global channel vector is acquired every  $T_{\text{array}} = (T_g + T_b)(N/N_g) = 160$  msec. This procedure is subsequently repeated for a number of channel acquisitions  $g$ , and the resultant channel estimate is obtained by taking the expectation of the instantaneous channel realizations over an acquisition time of  $T_{\text{meas}} = gT_{\text{array}}$ . The time span,  $T_{\text{meas}}$ , over which the expectation is taken is con-

sidered to be smaller than the channel coherence time, which seems sensible due to the static position of the MS and the lack of moving scatters in the surroundings. However, the measurement procedure suffers from uncertainty, since the number of instantaneous channel realizations  $g$  employed for computing the resultant channel estimates is unknown.

### 8.2.2 Measurements Analysis

The acquired channel measurements are normalized in order to remove the path loss effect and to perform a meaningful comparison with previously published results. Specifically, the average channel power satisfies  $\mathbb{E} \left\{ \|\mathbf{h}_{l,k}\|^2 \right\} = N$ , where  $\mathbf{h}_{l,k} \in \mathbb{C}^{1 \times N}$  denotes the baseband downlink communication channel for the  $l$ -th subcarrier of the  $k$ -th user, and the expectation is taken over all  $N = 64$  antennas and  $N_{\text{sub}} = 300$  subcarriers [21]. In the following the subcarrier index,  $l$ , is omitted for ease of notation and the channel subindex is left to denote the user number. The composite downlink communication channel  $\mathbf{H} \in \mathbb{C}^{K \times N}$  can be subsequently expressed as  $\mathbf{H} = [\mathbf{h}_1^T, \mathbf{h}_2^T, \dots, \mathbf{h}_K^T]^T$ .

The acquired channel measurements are normalized in order to remove the path loss effect and to perform a meaningful comparison with previously published results. Specifically, the average channel power satisfies  $\mathbb{E} \left\{ \|h_{l,k,n}\|^2 \right\} = 1$ , where  $h_{l,k,n} \in \mathbb{C}^{1 \times N}$  denotes the baseband downlink communication channel between the  $n$ -th antenna at the BS and the  $k$ -th user, for the  $l$ -th subcarrier. The expectation in the previous expression is taken over all  $N = 64$  antennas and  $N_{\text{sub}} = 300$  subcarriers of each measurement instance [21]. In the following the subcarrier index,  $l$ , is omitted for ease of notation and the channel subindex of  $\mathbf{h}_k \in \mathbb{C}^{1 \times N}$  is left to denote the user number. The composite downlink communication channel  $\mathbf{H} \in \mathbb{C}^{K \times N}$  can be subsequently expressed as  $\mathbf{H} = [\mathbf{h}_1^T, \mathbf{h}_2^T, \dots, \mathbf{h}_K^T]^T$ .

#### 8.2.2.1 LOS and NLOS Measurement Classification

Fig. 8.3 validates the classification of the measurements in LOS and multipath-dominant links performed based on the physical location of both the BS and the MSs.

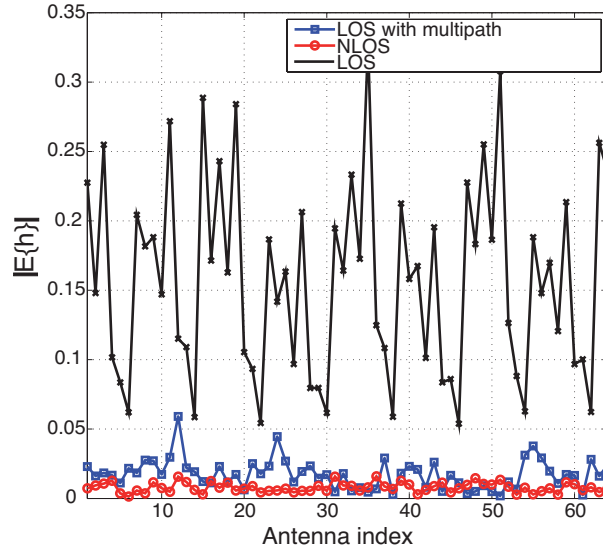


**Figure 8.3:**  $|\mathbb{E}\{\mathbf{h}_l\}|$  vs. BS antenna index.

The results represent the average channel gain  $|\mathbb{E}\{\mathbf{h}_l\}|$  for varying BS antenna indices. The expectation is taken over all  $N_{\text{sub}} = 300$  subcarriers and  $N_{\text{pos}} = 9$  consecutive channel measurements recorded for a given user position, hence resulting in a total of 2700 distinct communication channels. Fig. 8.3 shows that  $|\mathbb{E}\{\mathbf{h}_l\}| \neq \mathbf{0}$  for the LOS-dominant communication channels, whereas  $|\mathbb{E}\{\mathbf{h}_l\}| \approx \mathbf{0}$  for the cases of LOS with multipath and NLOS. This behaviour is consistent with the theoretical characterization of LOS and NLOS communication channels, where the non-zero mean of a channel with arbitrary statistics entails that there might be LOS propagation [85, 150]. The theoretical implications of having non-zero mean channels should be considered, since a large number of channel models assume  $|\mathbb{E}\{\mathbf{h}_l\}| = \mathbf{0}$  for deriving their conclusions [150, 238]. It should be noted that, although present, the effect of the LOS component in the channels classified as LOS with multipath components is not significant, i.e., a behaviour similar to that experienced by NLOS channels is expected.

### 8.2.2.2 Temporal Stability

The analysis of the temporal stability in the acquired measurements for static positions of both the BS and the MS is performed in Fig. 8.4. Here, the instantaneous normalization  $\|\mathbf{h}_k\|^2 = N$  has been employed to provide a meaningful comparison. A

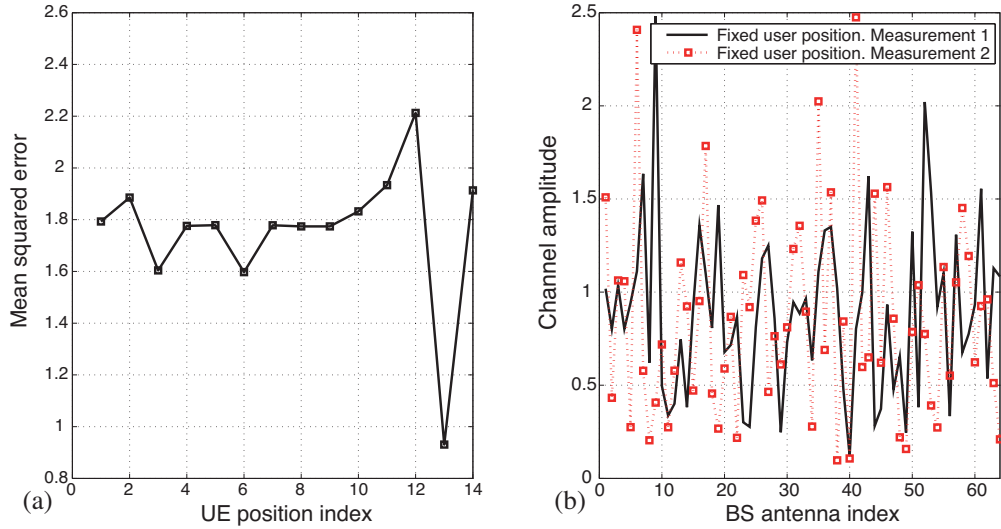


**Figure 8.4:** (a) MSE vs. measurement position index and, (b)  $|\mathbf{h}_k|$  vs. BS antenna index for two consecutive measurements with identical BS and MS physical positions and a randomly selected subcarrier.

slight variation in the channel coefficients of consecutive measurements could be expected for approximately static environments without moving particles in the surroundings [21]. However, Fig. 8.4(a) shows that the mean squared error (MSE)<sup>1</sup> between all the measurements acquired in a given physical position and a randomly selected channel realization in the same position adopts a significantly high value for all  $K = 14$  positions. Note that Fig. 8.4(a) represents the MSE averaged over the  $N_{\text{sub}} = 300$  OFDM subcarriers,  $N = 64$  antennas and  $N_{\text{pos}} = 9$  measurements taken in the same physical location. These results indicate that there exist significant differences in the channel coefficients of consecutive measurements. This difference can be explicitly seen in Fig. 8.4(b), which shows the magnitude of the channel coefficients,  $|\mathbf{h}_k|$ , of two consecutive channel responses for a random subcarrier index and physical location  $k \in \{1, \dots, K\}$ . Specifically, Fig. 8.4(b) shows that the amplitude of the channel coefficients substantially differs for consecutive channel measurements acquired in the same physical location. These notable temporal variations should be taken into account when considering the accuracy of the acquired measurements since, for instance, there exists no guarantee that the required relationship  $T_{\text{coh}} > T_{\text{meas}}$  is satisfied throughout the measurements.

<sup>1</sup>The employment of the mean squared error (MSE) as a metric to measure correlation is motivated by the limited number of consecutive measurements acquired in the same physical position. In this context, other metrics such as statistical correlation could be misleading due to the insufficient number of acquired samples.

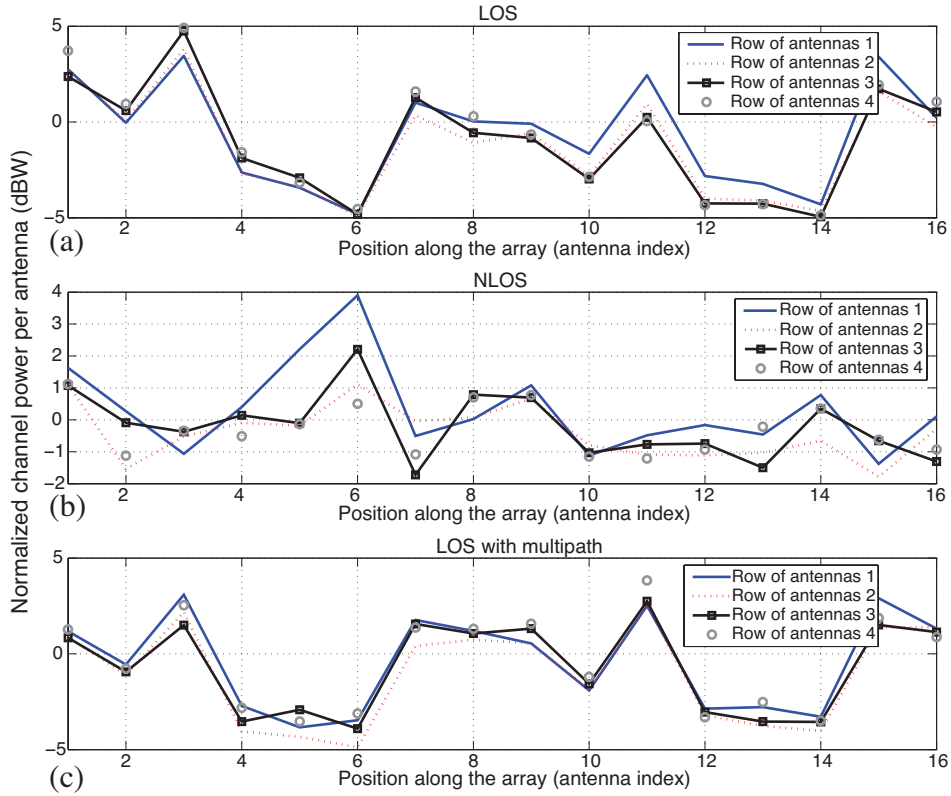


**Figure 8.5:** Normalized channel power (dBW) vs. column antenna index for the  $M_v = 4$  rows of the BS planar array for (a) LOS, (b) NLOS and, (c) LOS with multipath scenarios.

Still, a number of results and conclusions derived in this chapter seem to be consistent with other existing literature results, which suggests that the measurement procedure was valid. This uncertainty should be resolved in future measurement setups for the sake of accuracy.

### 8.2.2.3 Spatial Power Variation along the Antenna Array

The results of Fig. 8.5 show the variation of the normalized channel power in dBW for different BS antennas. This figure considers a composite channel comprised of  $K = 4$  simultaneous users with similar transmission characteristics, namely, LOS, NLOS and LOS with multipath, and it represents the average channel power for the  $N_{\text{sub}} = 300$  system subcarriers. For visual convenience, the normalized channel power is shown for each row of antennas, where each row has  $M_h = 16$  antennas as depicted in Fig. 8.2. Note that the results shown of this figure can be directly compared with those of Fig.

1(c) and (d) in [148].

Fig. 8.5 shows that there exists a substantial variation in the channel power of different antennas. This has direct implication in the objective of reducing the number of RF chains, since it suggests the possibility of directly deactivating the antennas that do not significantly contribute towards the communication. This phenomenon was already observed in [148], where the power variations of uniform linear array (ULA) are instead smoother than in the measurements acquired in this work. This spatial fading could be produced by the larger antenna aperture of LSAS, which makes antennas placed farther apart to receive signals from different scattering clusters [269]. Considering that the horizontal inter-antenna spacing is identical in both scenarios, providing a sensible explanation for this phenomena requires further investigation. Interestingly, Fig. 8.5(a) shows that the relative power variation is closer to 10 dB in the scenarios with strong LOS transmission, which is larger than in the NLOS scenario shown in Fig. 8.5(b), where the largest power variation is smaller than 7 dB. The larger power variation observed in the LOS setup is consistent with the results of [148]. Moreover, the results of Fig. 8.5 indicate that the power of the communication channels is similar for vertically collocated antennas, which suggests that their channels might be correlated. Note that this effect is more pronounced for the scenarios with LOS components.

#### 8.2.2.4 Channel Statistical Properties

The correlation between multiantenna channels is explicitly represented in Fig. 8.6, where the magnitude of the entries in the channel covariance matrix  $|\mathbf{R}_k| = |\mathbb{E}\{\mathbf{h}_k^H \mathbf{h}_k\}|$  of a random user  $k \in \{1, \dots, K\}$  experiencing a NLOS condition is shown. The spatial covariance matrix  $\mathbf{R}_k$  is a function of the physical scattering media and the antenna geometry [80, 270, 271]. Note that, although not shown for brevity, a similar structure can also be observed for the communication channels with LOS components and other users. To obtain this figure, each of the subcarriers are considered as independent channel realizations [21] and sharing similar channel statistics. This strong assumption is adopted due to the limited number of channel measurements and will be removed in future studies. Fig. 8.6 shows that there exists a significant inter-antenna correlation

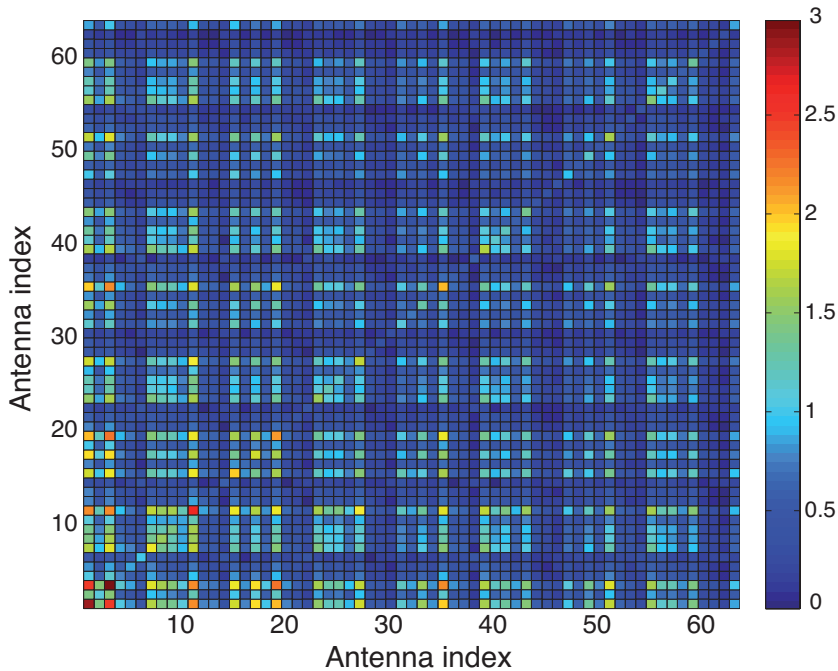


**Figure 8.6:** Magnitude of the entries of the channel covariance matrix  $\mathbf{R}_k = \mathbb{E} \{ \mathbf{h}_k^H \mathbf{h}_k \}$  of a randomly selected user  $k$  with NLOS propagation.

that mostly depends on the relative physical position between radiating elements as indicated by the peaks in the off-diagonal elements of  $\mathbf{R}_k$ . Furthermore, this correlation also exists in the elevation domain (between different rows of antennas) in spite of the increased inter-antenna distance  $\lambda$  to prevent this effect. For instance, it can be seen that there is a substantial correlation between antenna elements 1 and 17, which are vertically adjacent as shown in Fig. 8.2. This suggests a lack of scattering clusters in the elevation domain. The significant power variations experienced in the diagonal entries are also consistent with the results shown in Fig. 8.5.

The impact of both the inter-element correlation and the inter-antenna channel power variations on the eigenvalue distribution of the channel covariance matrices is shown in Fig. 8.7. This figure considers  $K = 4$  users and a separable Kronecker channel model to derive the global channel covariance matrices of the LOS, NLOS and LOS with multipath scenarios considered in this chapter, since it has been shown to provide a compelling approximation in realistic scenarios [150, 272]<sup>2</sup>. Fig. 8.7(a) shows the summatory function of the ordered eigenvalues for the acquired channels, whereas Fig.

<sup>2</sup>It should be noted that the accuracy of the Kronecker channel representation does not affect the conclusions derived in this section.

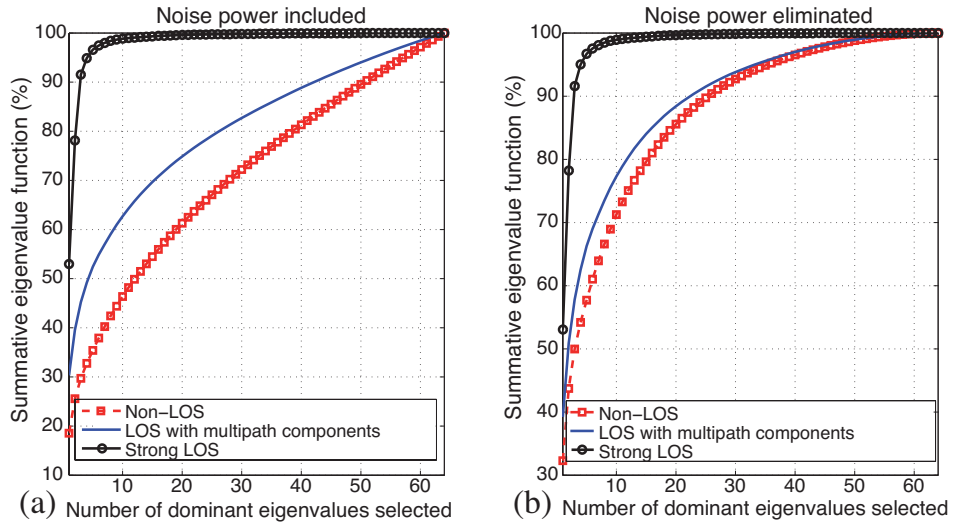


**Figure 8.7:** Summative eigenvalue function (%) of the channel covariance matrices vs. number of selected eigenvalues of the acquired measurements with (a) noise, and (b) without noise.

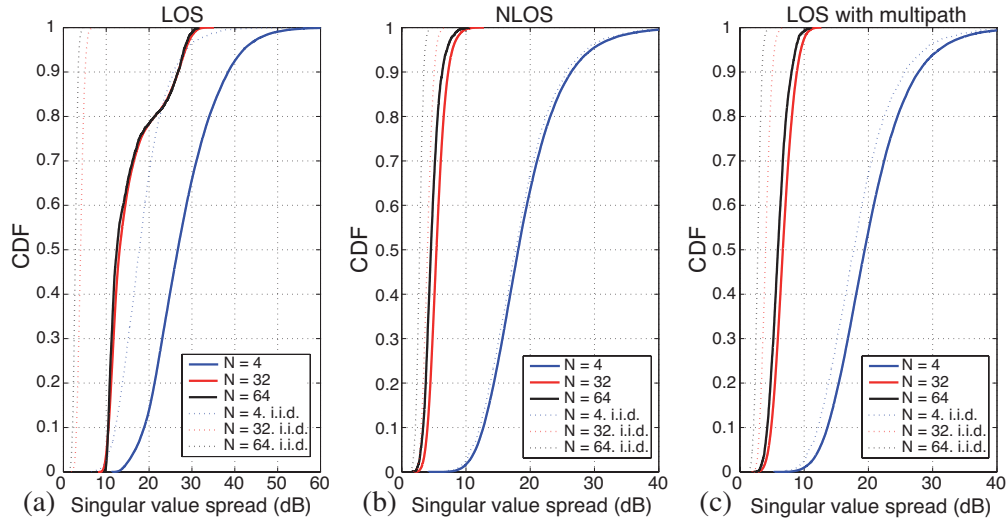
8.7(b) is obtained by eliminating the eigenvalue part that is assumed to correspond to the measurement noise. For this, the practical consideration that the smallest channel eigenvalue corresponds to noise in the measurement setup has been adopted. The results demonstrate that a reduced percentage of eigenvalues represent a significant proportion of the cumulative total, which hints the possibility of employing more intricate MIMO techniques for reducing the number of RF chains [103]. As expected, this effect is more pronounced for the LOS scenario when compared with the other setups, where the eigenvalues are more distributed.

Fig. 8.8 shows the cumulative distribution function (CDF) of the channel singular value spread,  $\bar{\kappa}$ , for the different communication channels considered in this chapter and  $K = 4$  simultaneous users. The singular value spread is defined as [21]

$$\bar{\kappa} = \frac{\lambda_{\max}^2(\mathbf{H})}{\lambda_{\min}^2(\mathbf{H})}, \quad (8.1)$$

where  $\lambda_{\max}$  and  $\lambda_{\min}$  denote the maximum and minimum singular values of the channel matrix  $\mathbf{H} \in \mathbb{C}^{K \times N}$ , respectively. The above singular value spread can be obtained as the result of the channel singular value decomposition

$$\mathbf{H} = \mathbf{U}\mathbf{\Sigma}\mathbf{V}^H, \quad (8.2)$$



**Figure 8.8:** CDF of the singular value spread  $\bar{\kappa}$  for (a) LOS, (b) NLOS and (c) LOS with multipath scenarios.  $K = 4$ .

where the unitary matrices  $\mathbf{U} \in \mathbb{C}^{K \times K}$  and  $\mathbf{V} \in \mathbb{C}^{N \times N}$  contain the left and right singular vectors of  $\mathbf{H}$  respectively, and the entries of the diagonal matrix  $\mathbf{\Sigma} \in \mathbb{C}^{K \times N}$  correspond to the channel singular values  $\lambda_k, k \in \{1, \dots, K\}$ . The singular value spread can be employed to measure the difficulty of spatially multiplexing the users to be simultaneously served [21]. In other words,  $\bar{\kappa} \approx 1$  indicates that the users have approximately orthogonal communication channels, whereas  $\bar{\kappa} \gg 1$  indicates that the users are difficult to separate spatially.

The results of Fig. 8.8 show that there exists some degradation w.r.t. ideal Rayleigh fading channels in the attainable singular value spreads for a large number of antennas, which is coherent with the results derived in [21]. The results are obtained for  $N = \{4, 32, 64\}$  antennas allocated at the BS and  $P = 20$  random antenna combinations per channel realization have been employed to compute the resultant CDF for the cases  $N = \{4, 32\}$ . The loss in channel orthogonality is particularly noticeable for the LOS scenario, where the degradation is larger than 5 dB independently of the number of BS antennas employed. Still, the results corroborate that a good spatial separation can be achieved when increasing the number of antennas in the considered scenario with  $K = 4$  users, a conclusion shared with [21], whose results can be directly compared with the ones presented here.

### 8.3 LSAS with a Reduced Number of RF Chains in Realistic Propagation Scenarios

The previous section shows that the measured large scale microwave channels have a certain degree of sparsity due to the existing inter-antenna correlation and the large channel power variations along the antenna array. The exploitation of channel sparsity for reducing the number of RF chains has attracted considerable attention in the past few years [80, 114, 192, 193, 273–275]. The exposition of this section is divided depending on the domain where the channel sparsity is observable: 1) AS strategies that exploit the sparsity in the antenna domain via  $\mathbf{H}$ , and 2) the more generic eigenspace schemes that exploit the limited number of channel degrees of freedom. Note that the concept of degrees of freedom employed in [149, 150] differs from the conventional one that refers to the number of parallel data streams that can be simultaneously sustained. Specifically, [149] employs this term to refer to the number of non-zero entries (or non-negligible ones) of the equivalent channel matrix when expressed in the virtual domain, while it also corresponds to the number of entries with non-negligible variances in the independent matrix  $\mathbf{H}_{\text{ind}} \in \mathbb{C}^{K \times N}$  of the more generic Unitary-Independent-Unitary (UIU) channel model [150]

$$\mathbf{H}_{\text{ind}} = \mathbf{U}_{\text{R}}^{\text{H}} \mathbf{H} \mathbf{U}_{\text{T}}. \quad (8.3)$$

Here, the columns of  $\mathbf{U}_{\text{R}} \in \mathbb{C}^{K \times K}$  and  $\mathbf{U}_{\text{T}} \in \mathbb{C}^{N \times N}$  are unitary matrices ( $\mathbf{U}_{\text{R}} \mathbf{U}_{\text{R}}^{\text{H}} = \mathbf{I}_K$  and  $\mathbf{U}_{\text{T}} \mathbf{U}_{\text{T}}^{\text{H}} = \mathbf{I}_N$ ) given by the eigenvectors of  $\mathbb{E} \{ \mathbf{H} \mathbf{H}^{\text{H}} \}$  and  $\mathbb{E} \{ \mathbf{H}^{\text{H}} \mathbf{H} \}$ , respectively [150]. The entries of  $\mathbf{H}_{\text{ind}}$  are zero-mean, i.i.d. and can have different variances. In general, a channel is deemed to be sparse if a large number of entries in  $|\mathbf{H}_{\text{ind}}|$  are zero or negligible when compared with the largest ones.

*Remark:* It can be shown that  $\mathbf{U}_{\text{T}}$  can be approximated as a submatrix of the discrete Fourier transform (DFT) matrix for the case of critically spaced ( $d = 0.5\lambda$ ) uniform linear antenna arrays with a large number of antennas [80, 273]. Indeed, the unitary DFT matrix,  $\mathbf{E}_{\text{DFT}} \in \mathbb{C}^{N \times N}$ , forms a basis for the  $N$ -dimensional spatial signal space in this particular case. For this reason, discrete lens antenna arrays such as

Continuous Aperture Phased MIMO (CAP-MIMO) that perform this transformation in the analog domain are proposed to be employed at millimeter wave frequencies [273]. Note that this strategy requires the employment of RF switching matrices as described in Chapter 7, since only a subset of antenna feeders should be employed depending on the specific propagation conditions.

### 8.3.1 Antenna Selection (AS)

The results shown in Fig. 8.5 and Fig. 8.6 indicate that there exist substantial differences in the channel power of the antennas allocated at the BS. This effect seems intrinsic to LSAS, since the power variation is more pronounced for large antenna apertures. This motivates the selection of a reduced subset of antennas for transmission based on the instantaneous CSI [148], which constitutes the subject of this section.

Fig. 8.9 shows the attainable achievable rates with zero forcing (ZF) precoding and AS when a limited number of active RF chains are considered and  $K = 4$  users with similar channel conditions and equal power allocation are simultaneously served. Here, the AS is based on choosing the antennas with largest average channel power over all communication subcarriers, i.e. the power-based AS described in Chapter 7. To facilitate direct comparison with [148], the downlink system model for AS follows the model already introduced in Sec. 7.2, i.e.

$$\mathbf{y} = \sqrt{\rho K} \mathbf{H}_{[\mathcal{M}]} \mathbf{x} + \mathbf{n}, \quad (8.4)$$

where the involved variables have been already introduced in Sec. 2.1 and Sec. 7.2,  $\mathcal{M}$  denotes the subset of antennas selected, and  $\rho = -5$  dB as per [148]. Note that the cardinality of  $\mathcal{M}$  represents the number of active RF chains  $M$ . Although suboptimal, this strategy is able to achieve a significant performance of the near-optimal convex selection at a significantly reduced complexity [148]. The results of Fig. 8.9 show that the performance improvements offered by AS strongly depend on the propagation scenario, which is coherent with the results obtained in [148]. Specifically, it can be seen that relative performance gains close to 15% for the LOS scenarios can be achieved when

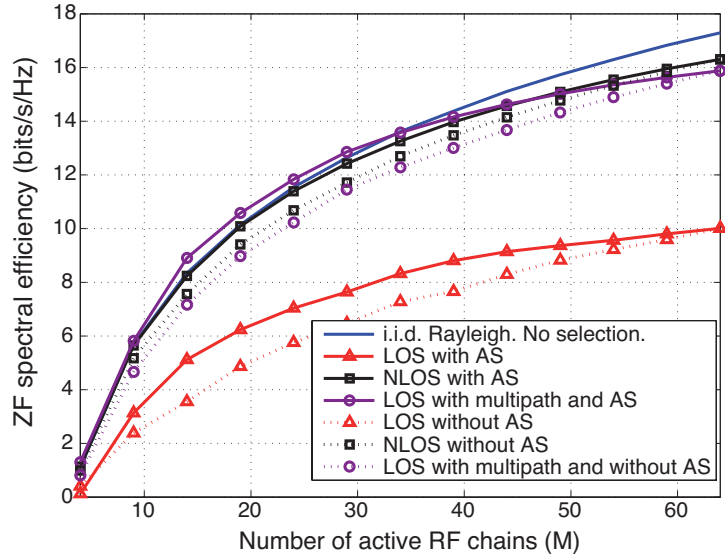


**Figure 8.9:** Ergodic spectral efficiency with ZF precoding (bits/s/Hz) vs.  $M$  with and without AS for LOS, LOS with multipath and NLOS channels.

$M = 32$  RF transceivers are active, whereas these gains are reduced to 4% and 10% for the NLOS and LOS with multipath scenarios respectively. Based on these results and those obtained in [148], it can be concluded that a sensible selection of the active transceivers can provide noticeable performance improvements. Moreover, these performance gains or, equivalently, the reduction in the number of RF transceivers required to achieve a given performance are more significant for larger number of antennas at the BS [148].

At this point it should be pointed out that energy-efficient LSAS should probably not rely on activating a fixed number of antennas but rather on adapting the number of simultaneously active antennas, based on the system load and propagation conditions. This is because, for a given number of users, a large percentage of the maximum achievable rates might be obtained by employing a reduced number of RF transceivers and antennas. A clear example of this observation can be seen in Fig. 8.9, where more than 75% of the maximum achievable rates obtained with  $M = N = 64$  active antennas can be achieved by just activating  $M = 32$  antennas for all considered scenarios. In other words, a large percentage of the maximum achievable rates can be achieved by simple deactivating a number of antennas, even without optimizing the active subset as in traditional AS. Indeed, this observation applies to a large variety of scenarios such

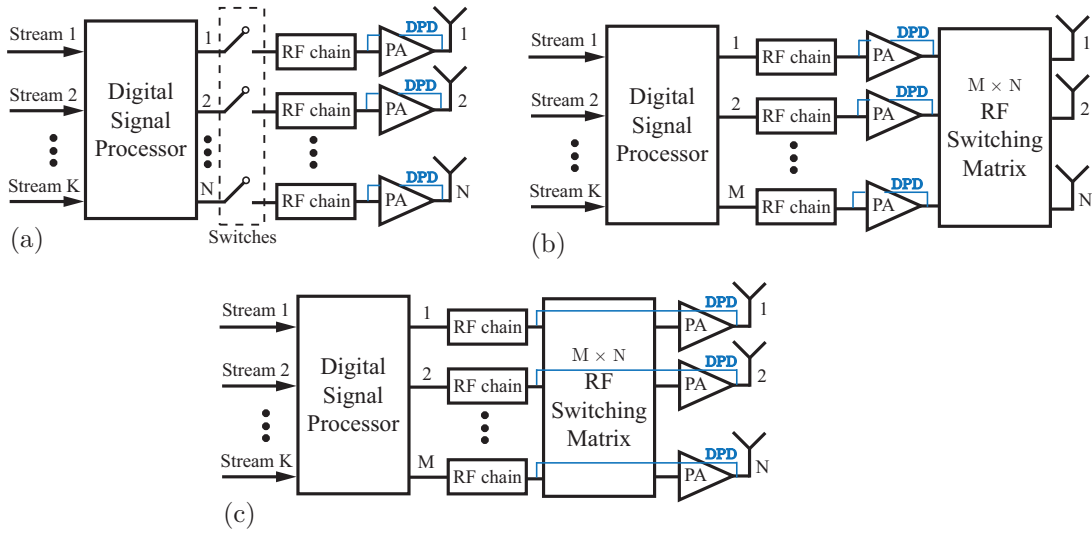


**Figure 8.10:** Different implementations of the AS scheme. (a)  $N$  RF chains and  $N_{\text{PA}} = N$  PAs, (b)  $M < N$  RF chains and  $N_{\text{PA}} = M$  PAs and, (c)  $M < N$  RF chains and  $N_{\text{PA}} = N$  PAs.

those shown in [11, 21, 81, 148].

While intuitively simple, a real implementation of the AS concept has several hardware and system-related impediments. From the hardware point of view, the main technical complication of performing an AS with a reduced number of RF transceivers is the implementation of a large number of RF switches, which can be particularly complex for the considered system dimensions and might induce signal quality losses as detailed in Chapter 7 [148]. This is the reason why [148] focuses on a solution with  $M = N$  RF chains and single-pole single-throw (SPST) switches that are activated and deactivated depending on the selected antenna (see Fig. 8.10(a)). While this alternative is more flexible due to the possibility of employing a different number of antennas depending on system conditions such as the user load, the design of an efficient RF switching matrix should not be discarded due to the potential of reducing the number of RF transceivers as detailed in Chapter 7. This alternative design is schematically shown in Fig. 8.10(b) and (c), where it can be seen that the switching matrix is allocated after the  $M < N$  RF transceivers in the chain. For convenience, the power amplifiers (PAs) have been separated from the RF transceivers, since their location can have a significant impact in the system design and resultant performance.

The number of amplifiers could be increased to  $N_{\text{PA}} = N$  and placed after the switch-

ing matrix to minimize the RF switching losses as shown in Fig. 8.10(c). This contrasts with the design shown in Fig. 8.10(b), where the switching operation is performed after the signals are amplified for transmission. This solution would also place less stringent linearity requirements in the switching matrix, since the digital predistortion technique employed in the PA could be extended to the switching matrix for mitigating the signal degradation as explicitly represented in Fig. 8.10(c). The selection of one alternative or the other depends on a number of parameters such as the specific power requirements, the number of antennas and RF transceivers available, the economical cost, etc.

### 8.3.2 Eigenspace Selection

This section aims at reducing the number of RF chains based on the sparsity on the equivalent channel  $\mathbf{H}_{\text{ind}}$  in (8.3). This type of channel sparsity does not only rely on exploiting the low power of the communication channels from a subset of antennas, but also on other aspects such as the inter-antenna correlation or the limited number of physical scatterers. Similarly to (8.4) and incorporating (8.3), the signals received by the mobile stations after linear precoding can be equivalently expressed as [273]

$$\mathbf{y} = \sqrt{\rho K} \mathbf{H} \mathbf{F} \mathbf{u} + \mathbf{n} = \sqrt{\rho K} \mathbf{H} (\mathbf{U}_T)_{[\tilde{\mathcal{M}}]} \mathbf{F}_{\text{BB}} \mathbf{u} + \mathbf{n} = \sqrt{\rho K} \tilde{\mathbf{H}}_{\text{ind}} \mathbf{F}_{\text{BB}} \mathbf{s} + \mathbf{n}, \quad (8.5)$$

where  $\mathbf{F} \in \mathbb{C}^{N \times K} = \mathbf{F}_{\text{RF}} \mathbf{F}_{\text{BB}}$  is the analog-digital precoding matrix and  $\mathbf{u} \in \mathbb{C}^{K \times 1}$  are the user symbols. In the previous expression,  $\mathbf{F}_{\text{BB}} \in \mathbb{C}^{M \times K}$  represents the digital baseband precoding matrix and  $\mathbf{F}_{\text{RF}} \in \mathbb{C}^{N \times M}$  characterizes the analog signal processing as detailed in Sec. 8.4.1. Moreover,  $\mathbf{F}_{\text{RF}} = (\mathbf{U}_T)_{[\tilde{\mathcal{M}}]} \in \mathbb{C}^{N \times M}$  represents a submatrix of  $\mathbf{U}_T$  in (8.3) built by selecting the columns with largest norm  $\tilde{\mathcal{M}}$  of the equivalent channel  $\mathbf{H}_{\text{ind}} = \mathbf{H} \mathbf{U}_T$ . In the previous expression, it has been considered that  $\mathbf{U}_R \approx \mathbf{I}_K$ , which occurs when the users are sufficiently separated and it has been verified in the measurements [81]. The above selection is referred to as eigenspace selection in the following, since the selection is performed based on the equivalent channel  $\mathbf{H}_{\text{ind}} = \mathbf{H} \mathbf{U}_T$ .

Ideally, the semi-unitary matrix  $(\mathbf{U}_T)_{[\tilde{\mathcal{M}}]}$  could be implemented in the analog domain via phase shifting networks as schematically represented in Fig. 8.11, hence effectively

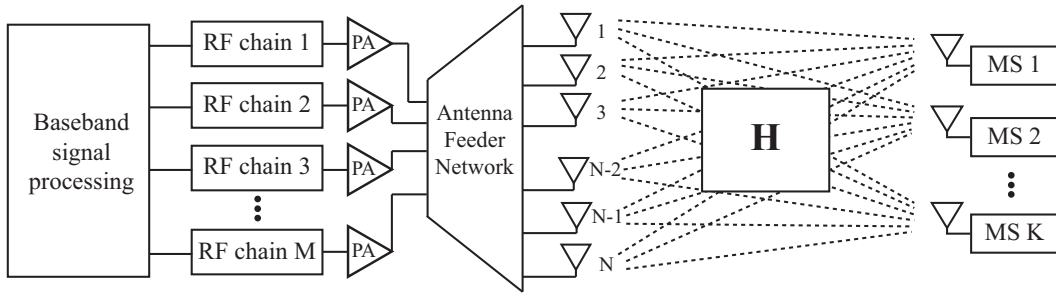


**Figure 8.11:** Block diagram of a transceiver architecture with a reduced number of RF chains via phase shifting network.

requiring  $M \leq N$  RF chains for transmission [196]<sup>3</sup>. Intuitively,  $|\widetilde{\mathcal{M}}| = M$  represents the selected number of distinct angles of arrival (AoA) of the signals impinging into the large scale antenna array when a ULA with an excessive number of antennas is implemented at the BS [80, 103, 149, 150]. Under the same model, the total number of distinct angles of arrival (AoA) is given by  $N_{\text{arrival}}$ .

The above observations are supported by the results shown Fig. 8.12, where the ergodic achievable rates of a BS serving (a)  $K = 4$  users and (b)  $K = 8$  users experiencing both NLOS and LOS with multipath channels are shown for increasing number of active RF chains. The results have been obtained for an average SNR per user of  $\rho = -5$  dB in (8.5) [148], ZF precoding in the baseband, and assuming that the channel statistics do not vary for the  $N_{\text{sub}} = 300$  subcarriers and the  $N_{\text{pos}} = 9$  consecutive channel measurements acquired in each user position. While it is acknowledged that the above are strong assumptions, they are enforced by the limited number of available measurements. It is also remarked that the eigenspace selection does not correspond to physically separated beams as considered in [103], since the more generic formulation developed in [150] is leveraged to derive the equivalent channel representation and select the channel eigendirections that result on the largest received power as per (8.5) [148]. Fig. 8.12 shows that the rates attainable via AS can be further enhanced by employing eigenspace selection, and that the performance differences are maximized for an intermediate number of active RF chains. Note that the eigenspace selection strategy

<sup>3</sup>While realizable, RF signal processing performing variable modifications of the signal amplitudes such as those necessary for implementing  $\mathbf{F}_{\text{RF}} = (\mathbf{U}_{\text{T}})_{[\widetilde{\mathcal{M}}]}$  are not practical. This is because both variable power splitters and phase shifters are required in general. Therefore, the results shown in the following constitute an upper bound of the realistic performance that can be achieved with more realistic hardware designs.

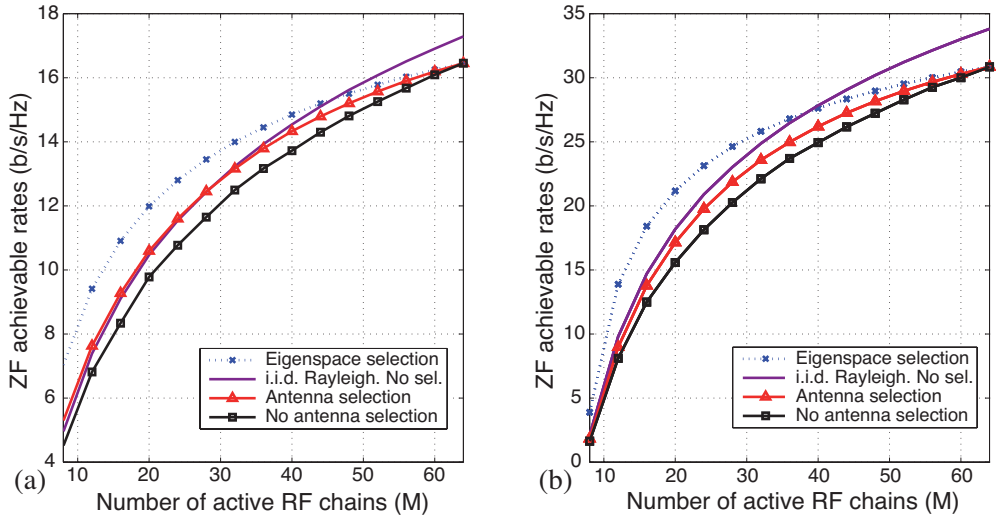


**Figure 8.12:** Ergodic ZF achievable rates vs.  $M$  for different reduced-RF schemes and  $\rho = -5$  dB. (a)  $K = 4$  users and (b)  $K = 8$  users.

requires either the implementation of a lens combined with an RF selection procedure similar to that of AS when the unitary matrices  $\mathbf{U}_T$  in (8.3) are fixed (e.g., ULAs with a large number of antennas), or the design of an analog feeder network comprised of phase shifters together with power splitters and combiners as detailed in Sec. 8.4.

At this point it should be noted that, in spite of its potential benefits, performing signal processing operations in the RF domain to reduce the number of RF chains introduces a number of challenges that are conventionally ignored in the related literature [20, 147, 193, 195, 264]. For this reason, the following section aims at providing a realistic model for hybrid analog-digital precoding systems.

## 8.4 Hybrid Analog-Digital Precoding Revisited under Realistic RF Modeling

Up to this point, the conventional assumption adopted in the literature relying on that no power losses are experienced in the RF stage of hybrid precoding systems has been followed [20, 147, 193, 195, 264]. However, this section proposes to model the ABFN as a bank of elementary RF components. The S-parameter representation of fully-connected ABFN (FC-ABFN), comprised of power combiners, power dividers and phase

shifters, reveals that there are significant power losses even when ideal components are considered – a feature commonly ignored in the related literature and that promotes the implementation of alternative ABFN [197, 248]. Subsequently, the insertion losses (ILs) found in real analog hardware components are incorporated for assessing the effective performance of hybrid precoding systems. The models and results presented in this section are supported by the detailed electromagnetic study of hybrid architectures implemented in [197] and provide a realistic framework for performing a fair comparison between hybrid schemes and fully-digital solutions.

### 8.4.1 Hybrid Precoding Systems

Consider a BS comprised of  $N$  antennas transmitting towards  $K \leq N$  single-antenna users. As already introduced in (2.1) and throughout this Thesis, this system can be characterized as

$$\mathbf{y} = \mathbf{H}\mathbf{x} + \mathbf{n} = \mathbf{G}^H\mathbf{x} + \mathbf{n}, \quad (8.6)$$

where the relevant variables are defined in Sec. 2.1. Here,  $\mathbf{g}_k^H$  collects the frequency-flat channel gains between the BS antennas and the  $k$ -th user, where  $\mathbf{g}_k = \mathbf{R}_k^{\frac{1}{2}}\mathbf{z}_k$  denotes the  $k$ -th column of  $\mathbf{G} \in \mathbb{C}^{N \times K}$  [80]. Here,  $\mathbf{z}_k \in \mathbb{C}^{N \times 1} \sim \mathcal{CN}(\mathbf{0}, \mathbf{I}_N)$  and  $\mathbf{R}_k \in \mathbb{C}^{N \times N}$  represents the channel covariance matrix. The transmitted signal in hybrid analog-digital precoding systems can be decomposed as [193]

$$\mathbf{x} = \mathbf{F}\mathbf{s} = \mathbf{F}_{\text{RF}}\mathbf{F}_{\text{BB}}\mathbf{u}, \quad (8.7)$$

where  $\mathbf{u} \in \mathbb{C}^{K \times 1} \sim \mathcal{CN}(\mathbf{0}, \frac{1}{K}\mathbf{I}_K)$  comprises the modulated data symbols and  $\mathbf{F} \in \mathbb{C}^{N \times K}$  is the composite precoding matrix. Here,  $\mathbf{F}_{\text{BB}} \in \mathbb{C}^{M \times K}$  is the digital baseband precoding matrix and  $\mathbf{F}_{\text{RF}} \in \mathbb{C}^{N \times M}$  characterizes the ABFN. An illustrative example of a hybrid precoding system is shown in Fig. 2.13. The signal-to-interference-plus-noise ratio (SINR) of the  $k$ -th user is given by [215]

$$\gamma_k = \frac{|\mathbf{g}_k^H \mathbf{f}_k|^2}{\sum_{i \neq k} |\mathbf{g}_k^H \mathbf{f}_i|^2 + \sigma^2}, \quad (8.8)$$

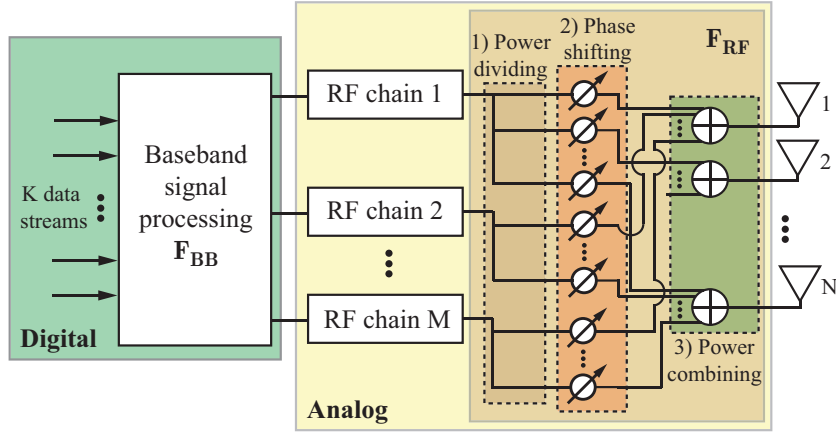


**Figure 8.13:** Block diagram of a hybrid precoding system comprised of digital precoding and a fully-connected analog beamforming network (FC-ABFN).

where  $\mathbf{f}_k \in \mathbb{C}^{N \times 1}$  represents the  $k$ -th column of  $\mathbf{F}$ . The ergodic sum rates in bits per second can be expressed as [215]

$$R = BS_e = B \sum_{k=1}^K \mathbb{E} \{ \log_2 (1 + \gamma_k) \}, \quad (8.9)$$

where  $B$  denotes the system bandwidth and  $S_e$  represents the sum spectral efficiency.

At this point it should be noted that traditional hybrid system models normalize the composite precoding matrix  $\mathbf{F}$  for satisfying a specific sum power constraint and subsequently apply additional constraints to the RF precoder  $\mathbf{F}_{\text{RF}}$ . Instead, this section aims at deriving the constraints of the RF precoder  $\mathbf{F}_{\text{RF}}$  based on a S-parameter analysis of the specific hardware implementation of the ABFN. Specifically,  $\|\mathbf{F}_{\text{BB}}\|_{\text{F}}^2 = K$  is imposed and  $\bar{\rho} \triangleq \frac{K}{\sigma^2}$ . The above constraints guarantee a fair comparison between hybrid and fully digital systems ( $\mathbf{F}_{\text{RF}} = \mathbf{I}_N$ ).

#### 8.4.2 Fully-Connected Analog Beamforming Network

The architecture of a FC-ABFN is shown in Fig. 8.13, where three stages can be clearly identified: a first one comprised of power dividers where each of the  $M$  input signals is divided into  $N$  equal-power outputs characterized by the matrix  $\mathbf{F}_{\text{D}} \in \mathbb{C}^{(M \cdot N) \times M}$ , a subsequent one where  $M \cdot N$  signals are phase shifted represented

by  $\mathbf{F}_{\text{PS}} \in \mathbb{C}^{(M \cdot N) \times (M \cdot N)}$ , and a final stage where  $M$  signals are combined with power combiners and coupled to  $N$  antenna ports characterized by  $\mathbf{F}_{\text{C}} \in \mathbb{C}^{N \times (M \cdot N)}$ . Based on the above and in order to offer a complete view of the ABFN's behaviour, the analog beamforming matrix is decomposed as [197]

$$\mathbf{F}_{\text{RF}} = \mathbf{F}_{\text{C}} \cdot \mathbf{F}_{\text{PS}} \cdot \mathbf{F}_{\text{D}}. \quad (8.10)$$

At this point it is noted that  $\mathbf{F}_{\text{RF}}$  is inherently defined by  $\mathbf{F}_{\text{PS}}$ , since both  $\mathbf{F}_{\text{C}}$  and  $\mathbf{F}_{\text{D}}$  are fixed as shown in the following. A common design criterion for  $\mathbf{F}_{\text{PS}}$  consists in selecting phase shifting values according to the transmit array response vectors at the angles of departure from the transmitter [193, 197]. However, in general the specific phase shifting values  $\mathbf{F}_{\text{PS}}$  can be obtained following multiple design criteria whose exhaustive description is out of the scope of this Chapter, since they do not modify the conclusions derived in the following [20, 80, 192, 193].

Note that the decomposition in (8.10) is performed in the RF domain. Therefore, an accurate description of their operation should be based on understanding the RF characteristics of the specific components. For this reason the signal distribution in  $\mathbf{F}_{\text{RF}}$  is defined based on the S-parameter representation of the hardware components involved in  $\mathbf{F}_{\text{C}}$ ,  $\mathbf{F}_{\text{PS}}$  and  $\mathbf{F}_{\text{D}}$ . Specifically,  $\mathbf{F}_{\text{D}}$ , which is comprised of Wilkinson power dividers [248], can be modeled following a block diagonal structure

$$\mathbf{F}_{\text{D}} = \sqrt{\frac{1}{L_{\text{S}}N}} \begin{pmatrix} \mathbf{1}_N & \mathbf{0}_N & \dots & \mathbf{0}_N \\ \mathbf{0}_N & \mathbf{1}_N & \dots & \mathbf{0}_N \\ \vdots & \vdots & \ddots & \vdots \\ \mathbf{0}_N & \mathbf{0}_N & \dots & \mathbf{1}_N \end{pmatrix}, \quad (8.11)$$

where  $L_{\text{S}}$  corresponds to the substrate power loss [248], and  $\mathbf{1}_T \in \mathbb{N}^{T \times 1}$  and  $\mathbf{0}_T \in \mathbb{N}^{T \times 1}$  represent the all-ones and all-zeros vectors respectively. In the sequel the substrate losses are referred to as *static* power losses, since they only depend on the loss tangent and the dielectric constant [248]. The phase shifting network matrix  $\mathbf{F}_{\text{PS}}$  is a diagonal

matrix characterized by

$$\mathbf{F}_{\text{PS}} = \sqrt{1/L_{\text{PS}}} \cdot \text{diag}([f_{1,1}, f_{2,1}, \dots, f_{N,M}]), \quad (8.12)$$

where  $L_{\text{PS}}$  denotes the static power losses introduced by each phase shifter, and the coefficient  $f_{i,j}, \forall i \in \{1, \dots, N\}$  and  $j \in \{1, \dots, M\}$  corresponds to the  $i, j$ -th phase shift of  $\mathbf{F}_{\text{RF}}$  normalized to satisfy  $\|f_{i,j}\| = 1$ . The combining matrix  $\mathbf{F}_{\text{C}}$  can be expressed as

$$\mathbf{F}_{\text{C}} = \sqrt{\frac{1}{L_{\text{CM}}}} [\text{diag}(\mathbf{1}_N), \dots, \text{diag}(\mathbf{1}_N)]. \quad (8.13)$$

With respect to the losses in the combining stage, there are two dominant factors: First,  $L_{\text{C}}$  represents the static power losses introduced by the power combiners. Secondly, the S-parameter representation of passive RF components reveals additional losses in the form of the scaling coefficient  $1/\sqrt{M}$  in (8.13). In other words, the adaptive nature of  $\mathbf{F}_{\text{BB}}$  and the data symbols produce phase and amplitude mismatches in the signals at the input of the power combiners, hence introducing a loss in the signal combining process - an aspect not often considered in the related literature. This loss is referred to as *dynamic* power loss and it should be remarked that it arises even for lossless (ideal) analog hardware components [248]. The consideration of the dynamic power losses entails that, in contrast with fully-digital precoding, the power amplifiers will have to compensate for substantial signal-dependent losses in order to guarantee a given transmission power. Indeed, (8.13) manifest power losses that scale linearly with  $M$  in ideal FC-ABFN.

### 8.4.3 DFT Analog Beamforming Networks via Butler Matrices

While fully-connected networks allow designing arbitrary ABFN, the above discussion has revealed that power combiners introduce substantial power losses. To alleviate these losses, 4-port hybrid directional couplers can be considered instead of power combiners [248]. 4-port hybrid couplers can be seen as a variation of 2-point DFT, hence enabling the implementation of higher order DFTs in the RF domain by stacking multi-

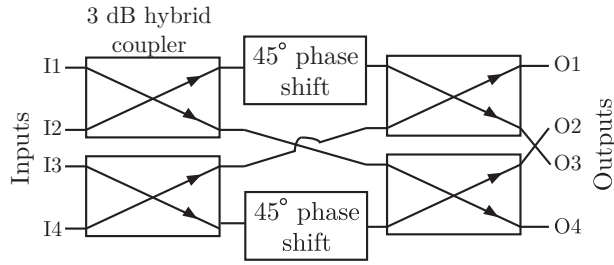


**Figure 8.14:** Block diagram of a  $4 \times 4$  Butler matrix.

ple hybrid couplers and phase shifters consecutively [80, 154]. Indeed a variation of this approach, commonly referred to as Butler matrix, has been employed to generate orthogonal beams with minimal loss [80, 154]. An illustrative example of a  $4 \times 4$  Butler matrix is shown in Fig. 8.14, where the conventional structure comprised of  $N_{\text{HYB}} = \log_2(N)$  and  $N_{\text{PS}} = \log_2(N) - 1$  ( $N \geq 2$ ) hybrid coupling and phase shifting subsequent stages can be observed, respectively. Based on the above,  $\mathbf{F}_{\text{RF}}$  can be expressed in the case of Butler matrices as

$$\mathbf{F}_{\text{RF}} = \frac{1}{\sqrt{(L_{\text{PS}})^{N_{\text{PS}}} (L_{\text{HYB}})^{N_{\text{HYB}}}}} \mathbf{E}_{\text{DFT}}^{(M)}, \quad (8.14)$$

where  $L_{\text{HYB}}$  are the static power losses introduced by each hybrid power coupler and  $\mathbf{E}_{\text{DFT}}^{(M)} \in \mathbb{C}^{N \times M}$  is a submatrix of the  $\mathbf{E}_{\text{DFT}} \in \mathbb{C}^{N \times N}$  DFT matrix [80]. For ULAs,  $\mathbf{E}_M$  is defined by approximating  $\mathbf{R}_k$  by a circulant matrix  $\mathbf{C}_k$  and selecting the eigenvectors corresponding to its largest eigenvalues, since the eigenvectors of  $\mathbf{C}_k$  form a DFT matrix [80]. For simplicity, this chapter ignores the additional static ILs introduced by the switching matrix required in Butler-based designs, since a detailed analysis of these power losses is intricate and can be found in Chapter 7.

#### 8.4.4 Static Insertion Losses (IL)

The IL introduced by the additional RF components employed for hybrid beamforming should be incorporated into a realistic system model for deriving the additional power gains required in the RF stage and preserving the same output power of a fully digital precoding solution. Illustrative values of these signal-independent losses are shown in Table 8.1. It should be highlighted that, in general, the IL introduced in the mmWave band grow with the frequency of operation and that the values of Table 8.1 correspond

**Table 8.1:** Orientative insertion losses (IL) of the hardware components employed in the design of analog beamforming networks.

-	mmWave	Sub 5 GHz
Three-port power dividers / combiners ( $\bar{L}_{\{S,C\}}$ )	0.6 dB [276]	0.5 dB [277]
Hybrid couplers	0.5 dB [278]	0.15 dB [279]
Phase shifters	0.5 dB [280]	3.5 dB [281]

to the Ka frequency band.

In the following it is considered for simplicity that the  $(T + 1)$ -port power combiners and dividers required in large ABFN are built by concatenating  $\log_2(T)$  three-port structures [248]. Therefore, the overall static losses for the splitting and combining stages are given by  $L_{S,\text{dB}} = \bar{L}_S \log_2(N)$  and  $L_{C,\text{dB}} = \bar{L}_C \log_2(M)$ , where both  $\bar{L}_S$  and  $\bar{L}_C$  are provided in Table 8.1.

#### 8.4.5 Energy Efficiency

While reducing the number of RF transceivers, hybrid precoding schemes simultaneously incur in additional power losses as detailed in Sec. 8.4.2 and 8.4.3. A relevant reason for reducing the number of active RF chains is enhancing the transmission's energy efficiency, which constitutes the main subject of study in this Thesis. In coherence with the models introduced in Sec. 2.1.3, this chapter defines the energy efficiency as [4]

$$\epsilon = \frac{R}{P_{\text{tot}}} = \frac{B \sum_{k=1}^K \mathbb{E}[\log_2(1 + \gamma_k)]}{P_{\text{PA}} + MP_{\text{dyn}} + P_{\text{LO}}} \text{ bits/Joule}, \quad (8.15)$$

where  $P_{\text{tot}}$  expressed in Watts (W) refers to the total power employed for transmission and  $P_{\text{PA}} = P_{\text{out}}/\eta$  denotes the power consumed by a power amplifier with efficiency  $\eta = 0.39$  to produce a signal output power of  $P_{\text{out}} = 40$  W [4]. Note that the effective output power of realistic hybrid precoding schemes will be reduced when compared with their fully-digital counterparts due to both dynamic and static power losses. Moreover,  $P_{\text{dyn}} = 1$  W and  $P_{\text{LO}} = 2$  W denote the power consumed by each RF chain and the frequency synthesizer respectively, derived by elaborating the values in [4].

### 8.4.6 Results and Discussion

This section characterizes the performance and energy efficiency of realistic ABFN. Although the conclusions derived in the following can be applicable to a vast number of hybrid precoding designs, this section concentrates on the precoding scheme referred to as joint spatial division and multiplexing (JSDM) [80], since it admits both fully-connected and DFT-based designs. A ULA is considered and the one-ring channel correlation model for microwave frequencies is adopted, where the  $i, j$ -th entry of  $\mathbf{R}_k$  is given by [80]

$$\{\mathbf{R}_k\}_{i,j} = \frac{1}{2\Delta} \int_{-\Delta}^{\Delta} e^{j\frac{2\pi}{\lambda}d(i-j)\cos(\vartheta+\theta)} d\vartheta, \quad (8.16)$$

where  $d$ ,  $\Delta$  and  $\lambda$  denote the inter-antenna spacing, angular spread and the wavelength respectively. Moreover,  $\theta$  represents the central azimuth angle between the BS and the users. Similarly to [80],  $d = 0.5\lambda$ ,  $\Delta = 15^\circ$  and three user groups comprised of  $K_g = 4$  single-antenna users each with  $\theta_1 = -45^\circ$ ,  $\theta_2 = 0^\circ$  and  $\theta_3 = 45^\circ$  are considered. ZF precoding with perfect channel state information is implemented in the digital domain and  $b_g$  is defined as the number of RF chains in the ABFN dedicated to serve the users in group  $g$ , which depends on the eigenvalues of  $\mathbf{R}_k$  [80]. Without loss of generality, asymmetric power ratios at the output of the power dividers and a sub 5 GHz transmission are considered in this section, since the general conclusions and observations derived in this chapter are independent of the operating frequency. However, note that propagation [20], static ILs and RF power consumption at mmWave frequencies is different from those below 5 GHz, which will shift the specific values shown in the sequel.

Fig. 8.15 considers  $N = 64$  and shows the sum spectral efficiency against increasing  $\bar{\rho}$  for a fully digital precoding system and a hybrid JSDM system implemented via both DFT and FC-ABFN ( $M = 32$ ). The results depicted in Fig. 8.15 characterize the performance loss experienced by the realistic FC-ABFN even when ideal analog hardware components are considered, which can be explained by the dynamic power losses introduced by the signal combiners. The performance degradation becomes even more pronounced when the static IL are considered, making a realistic DFT network outperform the FC-ABFN for a large range of  $\bar{\rho}$  thanks to its reduced hardware losses.

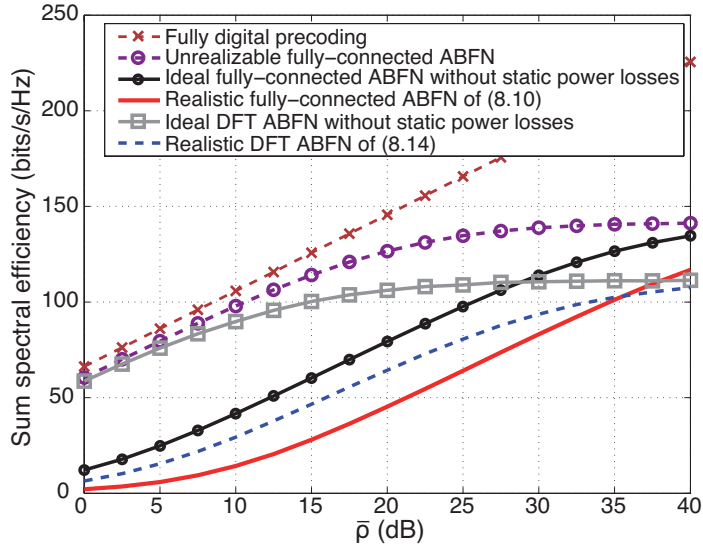


**Figure 8.15:** Sum spectral efficiency (bits/s/Hz) vs.  $\bar{\rho}$ .  $N = 64$ ,  $K_{\{1,2,3\}} = 4$ ,  $b_{\{1,3\}} = 10$  and  $b_2 = 12$ .

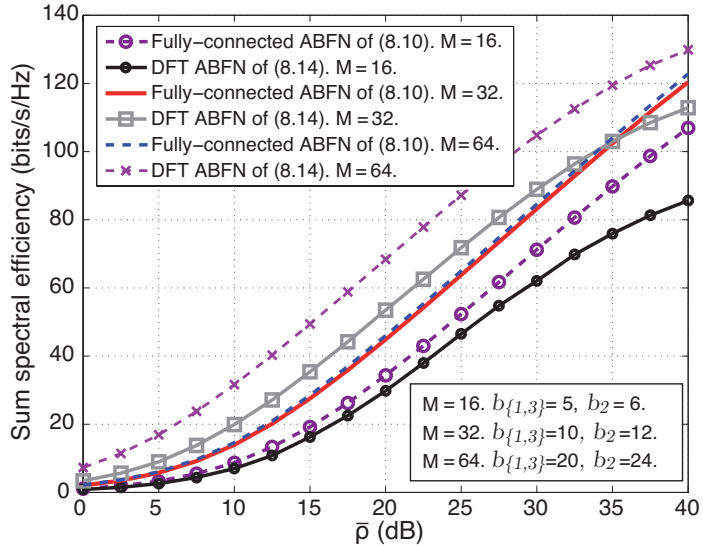


**Figure 8.16:** Sum spectral efficiency (bits/s/Hz) vs.  $\bar{\rho}$ .  $N = 128$ ,  $K_{\{1,2,3\}} = 4$  and varying number of RF chains.

In this context, the results of Fig. 8.15 also allow concluding that hybrid coupler based DFT ABFN designs will be more spectrally efficient than FC-ABFN for large  $M$ . This is because, as detailed in Sec. 8.4.2, the latter architecture introduces power losses that scale proportionally to  $M$  even when ideal analog hardware components are considered.

Fig. 8.16 shows the sum spectral efficiency of realistic hybrid precoding schemes against  $\bar{\rho}$  in a system with  $N = 128$  and different  $M$ . It can be observed that the relative performance between DFT-based designs and FC-ABFN depends on both  $M$

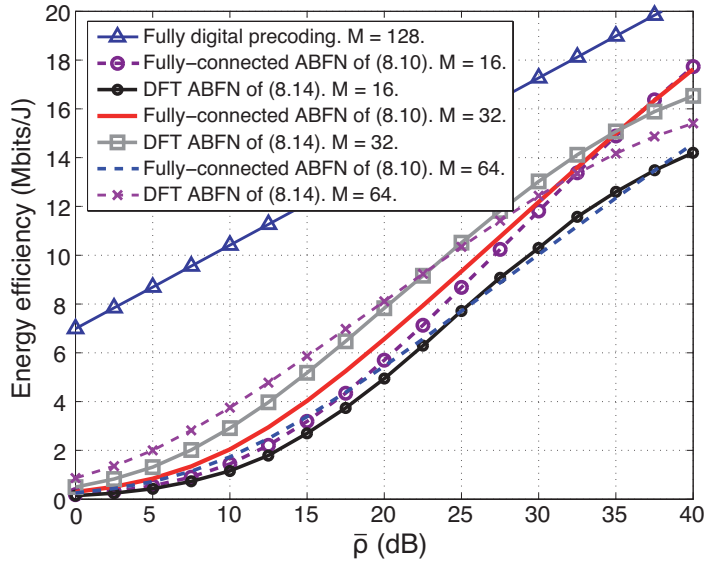


**Figure 8.17:** Energy efficiency (Mbits/Joule) vs.  $\bar{\rho}$ .  $N = 128$ ,  $K_{\{1,2,3\}} = 4$  and varying number of RF chains.  $B = 20$  MHz and  $P_{\text{out}} = 46$  dBm.

and  $\bar{\rho}$ . Moreover, Fig. 8.16 shows that a sensible selection of  $M$  should consider the power losses' impact on the performance. For instance, it can be seen that while  $M = 64$  offers significant performance benefits over other alternatives for the DFT-based implementations, both  $M = 32$  and  $M = 64$  offer a similar performance for the case of FC-ABFN. This can be explained by noting that while implementing a larger  $M$  allows for improved flexibility in the hybrid design [193], the network losses of FC-ABFN also grow with  $M$  as per (8.13), an aspect not quantified in the related literature.

Fig. 8.17 represents the energy efficiency of the systems considered in Fig. 8.16 with  $B = 20$  MHz. The energy efficiency trends allow characterizing the essential trade-off offered by hybrid schemes: while a large  $M$  generally allows an increased design flexibility [193], the overall power consumption is increased due to the additional analog hardware components required as detailed in Sec. 8.4.5. Overall, it can be observed that, while far from the fully digital system energy efficiency, hybrid schemes with reduced  $M$  are still capable of offering energy efficiency gains over those with large  $M$  for different  $\bar{\rho}$ 's, since their reduced power losses are able to compensate for their theoretical performance degradation.

## 8.5 Conclusions

In this chapter, a set of results and implications in the design of LSAS based on the set of measurements acquired in Bell Labs Stuttgart have been presented. In particular, the acquired measurements indicate that a) the communication channels of different antennas experience large power variations depending on their position, which suggests the possibility of selecting a subset of antennas for transmission without significant performance losses. Based on the acquired channel measurements and previous results, it has also been argued that b) employing a flexible scheme that deactivates a number of antennas depending on the communication conditions could significantly improve the system's energy efficiency. Moreover, it has been shown that c) the communication channels can be considered sparse depending on the specific characteristics of the propagation links between the BS and the mobile users. However, the results shown in this chapter indicate that channel sparsity is not a general characteristic of microwave channels. A number of alternatives to exploit channel sparsity, which is expected to be more significant at higher frequencies, and simplify the system design have been described. Overall, a larger number of controlled channel measurements is required to assess the feasibility of the reduced-RF alternatives considered in this chapter.

In line with the above, this chapter also describes the practical implications of employing ABFN in hybrid precoding systems when practical losses that are commonly ignored, are taken into account. In particular, this chapter has concentrated on understanding their impact on the data rates and the energy efficiency. The results shown here demonstrate that the performance of hybrid schemes critically depends on their hardware implementation and provide insights for an efficient design and evaluation. Specifically, it has been demonstrated that Butler-based designs provide a compelling alternative to FC-ABFN, since the latter ones introduce power losses that scale up with the number of RF chains.

*Critique:* It should be noted that the observations derived throughout this chapter hold for the case where the ABFN are adjacent to the antenna ports, which is the solution that minimizes the number of hardware components. Indeed, different conclusions could

be attained depending on the specific position of the ABFN. However, these would be component-dependent and, therefore, of reduced generality when compared with those presented in this chapter.

## Chapter 9

# Conclusions

Enhancing the energy efficiency of future wireless communications is essential both for guaranteeing a limited environmental impact and for their cost-effective deployment. Simultaneously, increasing the number of antennas seems necessary for satisfying the stringent spectral efficiency requirements posed by the vast amount of mobile devices to be simultaneously served. Accordingly, this Thesis has proposed and explored a number of strategies for enhancing the energy efficiency of multiple antenna communications systems, where a number of practical insights have been revealed.

### 9.1 Summary and Conclusions of the Thesis

This Thesis commenced by providing a general overview of energy-efficient multiple antenna systems in Chapter 2. Conventional precoding and detection schemes were introduced and classical strategies for reducing the hardware complexity of systems with a large number of antennas were presented. A number of shortcomings in these strategies were identified, hence motivating the research carried out throughout this Thesis.

- Chapter 3 proposed a power-efficient scheme for Tomlinson-Harashima precoding based on adjusting the user constellation symbols. It was shown that this technique is capable of providing significant power savings with moderate performance

losses, hence enhancing the energy efficiency of the communication. However, these improvements come at the cost of an increased signal processing complexity. Altogether, the central observations that can be derived from this chapter are:

- C3.1. The proposed strategy is particularly effective in small scale antenna systems, where the power consumption of the power amplifiers dominates the total system's power consumption and the additional signal processing load required is constrained.
  - C3.2. Systems with a large coherence time, small number of antennas and low-order modulations, where the power loss introduced by THP is larger, also motivate the employment of the proposed scheme. This is because the result of the symbol- and channel-dependent optimization problem can be collected in a lookup table.
- Improving performance of space shift keying (SSK) systems was the objective of Chapter 4, where a pre-scaling technique hinging on semidefinite relaxation (SDR) was designed. The results showed that transmission power savings in the order of several watts when compared with existing schemes could be achieved at a moderate complexity cost. The proposed scheme also accounts for imperfect channel state information (CSI) acquisition, hence ensuring a robust operation in realistic conditions. The following specific remarks can be derived from the results of this chapter:
- C4.1. The application of SDR for solving the pre-scaling problem in SSK is especially useful for systems with a small number of transmit antennas. This is a consequence of a) the direct dependence of the number of constraints on the number of transmit antennas and b) the degradation in the optimality of the solutions retrieved after relaxation, for problems with a large number of constraints [184, 210].
  - C4.2. The performance enhancements demonstrated by the proposed scheme motivate the acquisition of CSI at the transmitter, which is required for applying pre-scaling techniques in SSK. However, since SSK transmitters incorporate

a single radio frequency (RF) chain, the channel acquisition process could diminish the time spent for data transmission. This observation leads to the conclusion that pre-scaling strategies are particularly useful for systems with a small number of antennas and a large channel coherence time.

- The fundamentals behind compressive sensing (CS) were leveraged in Chapter 5 for devising a detector that improves the operation of spatial modulation (SM) in large scale multiple access channels. The proposed CS-based detector demonstrated signal-to-noise ratio gains in the order of 2 – 3 dB when compared with other schemes for the LSAS considered in this Thesis. These enhancements directly translate into energy efficiency improvements, hence motivating the incorporation of multiple antennas at the mobile terminals for facilitating a more energy-efficient data transmission. The central conclusions that can be extracted from the results obtained in this chapter are:

C5.1. Incorporating multiple antennas to the mobile terminals without increasing the number of RF chains and applying SM facilitates achieving spectral and energy efficiencies larger than those obtained with conventional multi-user MIMO systems with single-antenna mobile terminals. This conclusion holds true as long as the antennas at the mobile stations are not severely correlated and SM-specific detection algorithms are implemented.

C5.2. There exists a fundamental trade-off when the proposed detection algorithm is implemented: while extended channel coherence times facilitate incorporating a large number of antennas at the mobile stations due to the larger CSI acquisition time required by SM, it also diminishes the computational benefits of the proposed strategy when compared with conventional linear detectors. This is because the proposed algorithm performs an identical number of computations for every detection, whereas linear detectors concentrate their complexity at the beginning of the channel coherence time and subsequently perform low-complexity operations. Note, however, that the proposed detection algorithm always outperforms linear detectors for

the LSAS considered in this Thesis.

- The increasing correlation experienced by tightly packed antenna arrays was leveraged in Chapter 6 by incomplete CSI acquisition for reducing the complexity of LSAS and enhancing their energy efficiency. In particular, a simultaneous simplification in the hardware and signal processing was demonstrated by exploiting the large inter-antenna correlation existing in physically-constrained LSAS. The reduced number of RF chains required by the advocated scheme facilitates the deployment of LSAS in communication channels with severe correlation. The results of this chapter motivate the following critical observation:

C6.1. The proposed scheme is most useful in the low to mid SNR range and for inter-antenna spacings in the range of  $0.3\lambda - 0.4\lambda$  for the LSAS considered in this Thesis and without incorporating the effect of mutual coupling. These inter-antenna distances are those where a) there exists sufficient inter-antenna correlation for employing the proposed strategy without a significant performance degradation and b) the spectral efficiency is not severely reduced due to the increased correlation. Intuitively, these ranges should not be severely modified when the effect of mutual coupling is incorporated, since its impact is generally more pronounced for smaller inter-antenna distances [104].

- Chapter 7 concentrated on exploring the feasibility of employing simplified RF switching architectures in antenna selection (AS) systems. RF switching matrices designed with different optimization criteria such as the insertion losses (ILs) or the number of required hardware components were evaluated. Indeed, the results obtained in this chapter showed that the RF switching matrix design severely influences the energy efficiency of the communication system and motivate the following conclusions:

C7.1. RF switching architectures with a reduced connectivity are able to reduce both the ILs and number of hardware components required by conventional fully-flexible switching matrices, while showing negligible performance losses

in the considered LSAS. Indeed, power savings in the order of 2-3 dB were demonstrated in this chapter for the scenarios considered, values that hold when the RF switching matrix is implemented after the power amplifiers. However, it should be noted that this might not be the preferred alternative in realistic designs, since a larger number of power amplifiers placed after the switching matrix can be implemented if the overall power losses are reduced. The study of this alternative is, however, system-dependent, hence making its accurate characterization more challenging and the attainable conclusions of reduced generality.

C7.2. The deployment of AS in systems with a large number of antennas at the BS motivates the implementation of power-based AS in combination with partially-connected switching matrices, particularly in channels with a short coherence time. The above observation is motivated by the fact that AS systems require a larger CSI acquisition time that depends on the ratio between the number of antennas and RF chains, unless additional power meters for power-based AS are implemented.

- This Thesis concluded by analyzing the performance of practical LSAS in Chapter 8. The channel measurements acquired in Bell Labs were employed for characterizing signal propagation in LSAS, which demonstrated some sparsity that exhibits in the form of inter-antenna correlation and substantial variations in the power perceived by different antennas. Subsequently, this channel sparsity motivated the evaluation of schemes with a reduced number of RF chains. The power losses introduced by realistic hybrid precoding and detection systems were also characterized. Overall, the following insights can be derived from the research presented in this chapter:

C8.1. Reduced RF-chain schemes can be a compelling alternative for reducing the complexity in LSAS due to their limited performance losses when compared with designs with a dedicated RF chain per antenna. Note that this observation cannot be generalized, since systems with a larger number of users than

that considered in the measurements of this chapter will probably require fully digital precoding to guarantee favourable propagation conditions.

C8.2. Increasing the number of RF chains might not always be beneficial in hybrid precoding designs with analog signal processing. This aspect is critical for fully-connected beamforming networks due to the power losses introduced in their power combining stage, which were shown to scale linearly with the number of RF chains.

## 9.2 Future Work

As detailed above, the work and conclusions developed throughout this Thesis motivate further investigation in some research areas, which are identified and discussed in this section. In particular, the author would like to propose the following specific research lines for future work:

- **Enhancing the performance of pre-scaling strategies for space shift keying and spatial modulation.** The pre-scaling strategy developed in Chapter 4 aims at enhancing the minimum Euclidean distance at the received constellation. As another possibility, the direct consideration of alternative performance metrics such as the bit error rate could facilitate attaining further performance improvements, at the expense of complicating the algorithmic design and operation [208]. Moreover, some pre-scaling schemes such as the low-complexity constellation randomization pre-scaling advocated in [183] fundamentally rely on the statistical characteristics of the set of random pre-scaling vectors computed off-line for attaining a given performance. Therefore, an intuitive approach for enhancing the performance of this scheme could be based on incorporating prior knowledge about the particular channel statistics for ensuring that the set of candidate pre-scaling vectors lie closer to the optimal.
- **Spatial modulation in the multiple access accounting for realistic hardware constraints at the mobile and base stations:** The results and conclu-

sions derived in Chapter 5 motivate further research with the objective of assessing the realistic performance attainable by SM systems in the multiple access channel. For instance, a detailed study on the impact of spatial correlation and mutual coupling seems particularly significant, since the antennas might have to be tightly packed at the mobile terminals. Similarly, incorporating the additional power losses introduced by the symbol-speed RF switches required for transmission in SM seems an area where relevant contributions could be offered.

- **Incomplete CSI acquisition under different channel models and propagation conditions:** The scheme introduced in Chapter 6 was applied to exploit the inter-antenna correlation arising due to insufficient inter-antenna spacing. However, severe channel correlation can arise from a variety of propagation characteristics such as that of having a very narrow angular signal transmission. Therefore, the acquisition of incomplete CSI could be extended to more generic scenarios by accounting for the specific structure of the channel statistics. The employment of alternative channel models such as [249] also seems a relevant research line. Similarly, only activating a subset of antennas throughout the pilot training stage of highly correlated frequency division duplex systems constitutes an attractive alternative for enhancing their energy efficiency [242].
- **Impact of temporal channel correlation and power-based decision on the performance of antenna selection systems:** Conventionally, systems that implement the AS procedure based on the channel power rely on accurate power measurements as per Chapter 7. However, the power measurements in realistic AS systems that prefer not to extend the pilot training stage are based on uplink data and not on the ideal unitary training sequences indicated in [129]. Therefore, errors in the measured channel power could be produced, hence affecting the quality of power-based AS. Intuitively, these errors should depend on the length and received power of the uplink data and their analytical characterization seems of substantial interest. In a similar vein, the channel power measurements are intrinsically suboptimal, since they only depend on the channel impulse response of the previous uplink data stage [148]. Consequently, the temporal correlation of the

channel plays a fundamental role in the quality of the AS for the subsequent data transmission, i.e. if the channel varies rapidly, the channel power estimation might not be useful for performing an accurate AS. Based on the above, determining the limits in the temporal channel correlation for performing a reliable AS poses an appealing challenge for future research.

- **Reducing the number of antennas in LSAS via array thinning:** This future research line stems from the research project designed by Dr. Pawel Rulikowski and Dr. Vijay Venkateswaran in Bell Labs for reducing the hardware and signal processing complexity of LSAS detailed in Chapter 8. The essential idea consists in employing array thinning strategies for reducing the number of antennas without significantly harming the antenna array response [282–284]. Essentially, array thinning aims at removing a subset of antennas while satisfying a set of array-related requirements such as the maximum sidelobe level or the main lobe beamwidth. While array thinning strategies have been previously employed for reducing the number of antennas in massive radar applications, their application to millimeter wave frequencies is mostly unexplored [284]. In this context, there exists a clear energy efficiency trade-off that results from employing array thinning strategies and that should be studied since, while the overall system complexity can be reduced, the attainable performance might be simultaneously harmed.
- **Analytical study of the impact of power losses on the performance of hybrid analog-digital communications systems.** Chapter 8 presents a system model accounting for the power losses introduced by realistic designs involving analog signal processing. In real implementations, these power losses vary depending on the position of the analog beamforming network relative to the rest of the analog hardware components and they could be pre-compensated prior transmission. Therefore, understanding the additional power consumption required in realistic hybrid designs seems required for assessing their practical feasibility [197]. In a similar line, Chapter 8 demonstrates that increasing the number of RF chains simultaneously increases the power losses of the beamforming networks. Consequently, determining the optimal number of RF chains optimizing different

metrics such as the system's energy efficiency also seems an interesting topic for future research.

Overall, this Thesis has presented and analyzed a variety of energy-efficient designs, with particular emphasis on communications systems with a large number of antennas. It is hoped that the results and conclusions derived in this Thesis serve for deepening the understanding of the challenges and practical issues involved in the design of future multiple antenna systems as well as for enhancing their energy efficiency.



# Appendices

## Appendix A. Proof of Theorem 4.4.1

The proof of the theorem is based on exploiting the resemblance between the optimization constraints of  $\tilde{\mathcal{P}}_{4.1}$  and the robust beamforming designs developed in [216,285], and on reformulating the optimization constraints with the aid of the Lagrange dual function [216–218]. Specifically, the proof commences by reformulating the optimization constraints in the second line of (4.23), which constitute the optimal solution of the optimization problem for a given value of the optimization variable  $\mathbf{A}$

$$\begin{aligned} & \underset{\mathbf{\Delta}_{(k,m)} \in \mathcal{C}_{(k,m)}}{\text{minimize}} && \text{Tr} \left( \left( \tilde{\mathbf{E}}_{(k,m)} + \mathbf{\Delta}_{(k,m)} \right) \mathbf{A} \right) - d \\ & \text{subject to} && \tilde{\mathbf{E}}_{(k,m)} + \mathbf{\Delta}_{(k,m)} \succeq 0, \quad \|\mathbf{\Delta}_{(k,m)}\|_{\text{F}}^2 \leq \epsilon_{(k,m)}. \end{aligned} \quad (\text{A.1})$$

This is a convex optimization problem associated with a Lagrange dual function given by [211]

$$\begin{aligned} g(\lambda_{(k,m)}, \mathbf{B}_{(k,m)}) &= \inf_{\mathbf{\Delta}_{(k,m)}} \left\{ L(\mathbf{\Delta}_{(k,m)}, \lambda_{(k,m)}, \mathbf{B}_{(k,m)}) \right\} \\ &= \inf_{\mathbf{\Delta}_{(k,m)}} \left\{ \text{Tr} \left( \left( \tilde{\mathbf{E}}_{(k,m)} + \mathbf{\Delta}_{(k,m)} \right) \mathbf{A} \right) - d \right. \\ &\quad \left. + \lambda_{(k,m)} \left( \|\mathbf{\Delta}_{(k,m)}\|_{\text{F}}^2 - \epsilon_{(k,m)}^2 \right) - \text{Tr} \left( \left( \tilde{\mathbf{E}}_{(k,m)} + \mathbf{\Delta}_{(k,m)} \right) \mathbf{B}_{(k,m)} \right) \right\}, \end{aligned} \quad (\text{A.2})$$

where  $\inf \{\cdot\}$  denotes the infimum of a function,  $L(\mathbf{\Delta}_{(k,m)}, \lambda_{(k,m)}, \mathbf{B}_{(k,m)})$  is the Lagrangian, while  $\lambda_{(k,m)}$  and  $\mathbf{B}_{(k,m)}$  are dual variables [211]. The infimum of the La-

grangian in (A.2) can be obtained by finding the point satisfying

$$\frac{\partial L(\boldsymbol{\Delta}_{(k,m)}, \lambda_{(k,m)}, \mathbf{B}_{(k,m)})}{\partial \boldsymbol{\Delta}_{(k,m)}} = 0, \quad (\text{A.3})$$

which is achieved for [216]

$$\boldsymbol{\Delta}_{(k,m)} = \frac{\mathbf{B}_{(k,m)}^{\text{H}} - \mathbf{A}^{\text{H}}}{2\lambda_{(k,m)}}. \quad (\text{A.4})$$

Note that the particular structure of  $\boldsymbol{\Delta}_{(k,m)} \in \mathcal{C}_{(k,m)}$  detailed in Sec. 4.4 has to be considered, when defining the dual variable  $\mathbf{B}_{(k,m)}$  [217]. This is required for preserving the sparsity that arises in the constraint matrices of the proposed optimization problem  $\tilde{\mathbf{E}}_{(k,m)}$ . With this objective, the set  $\mathcal{T}_{(k,m)}$  is defined as

$$\mathcal{T}_{(k,m)} = \left\{ \{k_{(k,m)}, m_{(k,m)}\}, \{k_{(k,m)}, k_{(k,m)}\}, \{m_{(k,m)}, k_{(k,m)}\}, \{m_{(k,m)}, m_{(k,m)}\} \right\}. \quad (\text{A.5})$$

In these indices represented as  $\{a, b\}$ ,  $a$  refers to the row and  $b$  corresponds to the column of the indexed matrix. Moreover, let  $\mathcal{Q}_{(k,m)} = \{\{r, c\} \mid r, c \in 1, \dots, N\}$  denote the set containing all the indices of an  $(N \times N)$ -element matrix and  $\mathcal{S}_{(k,m)} = \mathcal{Q}_{(k,m)} - \mathcal{T}_{(k,m)}$ . Note that  $\mathcal{S}_j$  indexes the zero-valued entries of the  $j$ -th constraint matrix  $\tilde{\mathbf{E}}_{(k,m)}$ . Following the above argument, the following relationship must hold to preserve the structure of  $\boldsymbol{\Delta}_{(k,m)} \in \mathcal{C}_{(k,m)}$

$$\mathbf{B}_{(k,m)}|_{\mathcal{S}_{(k,m)}} = \mathbf{A}|_{\mathcal{S}_{(k,m)}}, \quad (\text{A.6})$$

where  $\mathbf{A}|_{\mathcal{S}_{(k,m)}}$  denotes the entries of the matrix  $\mathbf{X}$  determined by  $\mathcal{S}_{(k,m)}$ . This guarantees that  $\boldsymbol{\Delta}_{(k,m)} \in \mathcal{C}_{(k,m)}$  holds, since  $\mathbf{B}|_{\mathcal{S}_{(k,m)}} - \mathbf{A}|_{\mathcal{S}_{(k,m)}} = \mathbf{0}$ . For notational convenience,  $\mathcal{B}_{(k,m)}$  is defined as the set of matrices satisfying (A.6). Considering this and substituting (A.4) into (A.2), the Lagrange dual problem can be reformulated as [211]

$$\begin{aligned} \underset{\mathbf{B}_{(k,m)}, \lambda_{(k,m)}}{\text{maximize}} \quad & - \left( \text{Tr} \left( \tilde{\mathbf{E}}_{(k,m)} (\mathbf{B}_{(k,m)} - \mathbf{A}) \right) + \frac{\|\mathbf{B}_{(k,m)} - \mathbf{A}\|_{\text{F}}^2}{4\lambda_{(k,m)}} + \lambda_{(k,m)} \epsilon_{(k,m)}^2 + d \right) \\ \text{subject to} \quad & \mathbf{B}_{(k,m)} \succeq 0, \mathbf{B}_{(k,m)} \in \mathcal{B}_{(k,m)}, \lambda_{(k,m)} \geq 0. \end{aligned} \quad (\text{A.7})$$

At this point, note that (A.7) is an equivalent formulation of the optimization constraints in (A.1) because strong duality holds, i.e. the duality gap is zero and the bound provided by the Lagrange dual problem is tight [211]. This is because the (weaker) Slater condition that entails strong duality holds, if there exists a solution satisfying  $\tilde{\mathbf{E}}_{(k,m)} + \mathbf{\Delta}_{(k,m)} \succeq 0$  and  $\|\mathbf{\Delta}_{(k,m)}\|_{\text{F}} < \epsilon_{(k,m)}$ . Since  $\tilde{\mathbf{E}}_{(k,m)}$  is positive semidefinite by definition, the above condition is always satisfied and therefore there is no duality gap [211]. This entails that  $\tilde{\mathcal{P}}_{4.1}$  can be rewritten as

$$\begin{aligned} \tilde{\mathcal{P}}_{4.1} : \underset{\mathbf{A}, \mathbf{B}_{(k,m)}}{\text{maximize}} \quad & d \\ \text{s.t.} \quad & \max_{\mathbf{B}_{(k,m)} \in \mathcal{B}_{(k,m)}} - \left( \text{Tr} \left( \tilde{\mathbf{E}}_{(k,m)} (\mathbf{B}_{(k,m)} - \mathbf{A}) \right) + \epsilon_{(k,m)} \|\mathbf{B}_{(k,m)} - \mathbf{A}\|_{\text{F}} + d \right) \geq 0, \\ & \mathbf{B}_{(k,m)} \succeq 0, \mathbf{A} \succeq 0, \text{Tr}(\mathbf{A}) \leq (P_{\text{t}}N), \text{rank}(\mathbf{A}) = 1, \end{aligned} \quad (\text{A.8})$$

where the dual problem that determines the constraints in the second line of (A.8) has been already maximized w.r.t.  $\lambda_{(k,m)}$ . Finally, Theorem 4.4.1 is obtained by noting that the constraints determined by the maximum function are immediately satisfied for any feasible  $\mathbf{B}_{(k,m)} \in \mathcal{B}_{(k,m)}$  and by dropping the rank constraint, which completes the proof.

## Appendix B. Proof of Proposition 5.6.1

The large scale limit theory establishes that the condition number of a channel matrix  $\mathbf{G}_{\mathcal{L}} \in \mathbb{C}^{N \times |\mathcal{L}|}$  with entries  $g_{m,n} \sim \mathcal{CN}(0,1)$  independent and identically distributed (i.i.d.) converges almost surely in the asymptotic limit of transmit and receive antennas to [234, Theorem 7.3]

$$\Theta(\mathbf{G}_{\mathcal{L}}) \xrightarrow{N, |\mathcal{L}| \rightarrow \infty} \frac{1 + \sqrt{1/\beta(|\mathcal{L}|)}}{1 - \sqrt{1/\beta(|\mathcal{L}|)}} = \left| \frac{1 + \sqrt{\beta(|\mathcal{L}|)}}{1 - \sqrt{\beta(|\mathcal{L}|)}} \right|. \quad (\text{A.9})$$

Equation (A.9) provides a useful approximation to determine the maximum condition number of a Rayleigh channel with a large number of receive antennas [11]. This can be seen in Fig. 9.1, where the CDF of the condition number of a Rayleigh fading channel matrix with  $N = 128$  receive antennas is depicted. The number of columns is  $|\mathcal{L}| = 8$

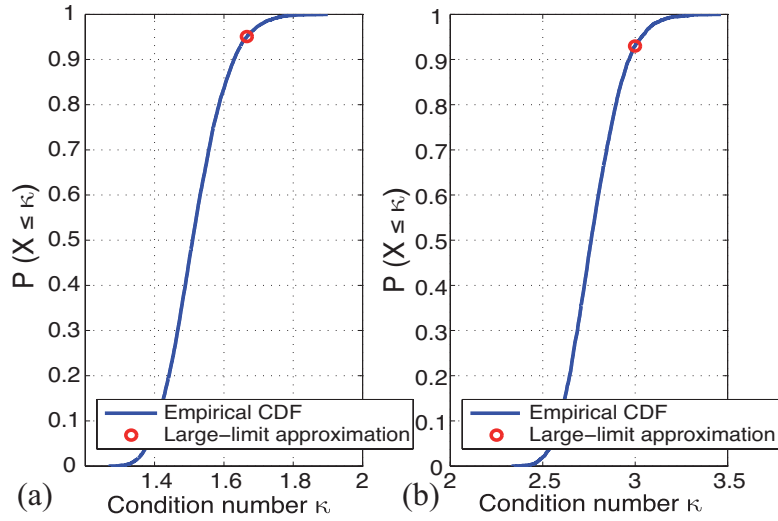


**Figure 9.1:** Empirical CDF and limit condition condition number for (a)  $N = 128$ ,  $|\mathcal{L}| = 8$  and (b)  $N = 128$ ,  $|\mathcal{L}| = 32$ .

and  $|\mathcal{L}| = 32$  for Figures 9.1(a) and (b) respectively. From the results of this figure it can be concluded that the condition number of the channel matrix is below the bound shown in (A.9) with a high probability. To conclude the argument, (A.9) is substituted into (5.23).

## Appendix C. Proof of Theorem 5.6.1

The first step to derive (5.29) is to note that the definition of the condition number  $\Xi$  used in [233] varies with respect to the one employed in [230, 234]. Attending to their relationship, which is shown in (5.19), the CDF of the standard condition number  $\Theta$  can be expressed as

$$F_{\Theta}(\theta) = P(\Theta \leq \theta) = F_{\Xi}(\theta^2). \quad (\text{A.10})$$

In plain words,  $F_{\Xi}(\theta^2)$  gives the probability that for a given constant  $\theta$ , the condition number of the LS matrix is below that value. The solution to the above expression can be immediately obtained via numerical integration [233]. Once the CDF of the standard condition number has been characterized, the number of iterations of the CG algorithm in the considered scheme can be determined. Particularly, by using (5.23) the probability that a given number of of LS iterations  $i_{\max}^{\text{LS}}$  achieves a relative error

reduction of  $\iota$  can be expressed as

$$P(i^{\text{LS}} \leq i_{\text{max}}^{\text{LS}}) = P\left(\Theta \leq \frac{2 \cdot i_{\text{max}}^{\text{LS}}}{\log\left(\frac{2}{\iota}\right)}\right). \quad (\text{A.11})$$

The proof is completed by substituting (A.11) into (A.10).

## Appendix D. Proof of Theorem 6.4.1

The proof of Theorem 6.4.1 relies on determining the error factor for the antennas with imperfect CSI and the antennas whose CSI is derived following the CSI averaging procedure described in Sec. 6.3. First, note that  $\Delta_k$  in (6.21) can be further decomposed as

$$\Delta_k = \frac{\mathbb{E}\left\{\sum_{n \in \mathcal{B}} |\bar{g}_{k,n}|^2 + \sum_{n \in \mathcal{C}} |\bar{g}_{k,n}|^2\right\}}{\mathbb{E}\left\{\sum_{n=1}^N |g_{k,n}|^2\right\}} \stackrel{(a)}{=} \frac{\sum_{n \in \mathcal{B}} \mathbb{E}\left\{|\bar{g}_{k,n}|^2\right\} + \sum_{n \in \mathcal{C}} \text{var}\left(\bar{g}_{k,n}\right)}{N}, \quad (\text{A.12})$$

where  $\bar{g}_{k,n}$  denotes the error of the channel from the  $n$ -th antenna of the BS to the  $k$ -th user and  $\text{var}(\cdot)$  denotes the variance of a random variable. In the above expression,  $\stackrel{(a)}{=}$  holds because it is considered that the channel for the  $n$ -th antenna without CSI is generated by following the averaging operation (6.15) and  $\mathbb{E}\{\hat{\mathbf{g}}_k\} = \mathbb{E}\{\mathbf{g}_k\} = \mathbf{0}$ , which entails that  $\text{var}(\bar{g}_{k,n}) = \mathbb{E}\{|\bar{g}_{k,n}|^2\}$ . Moreover, the channel coefficients of the physically-constrained model defined in (6.6) clearly satisfy  $\mathbb{E}\{|g_{k,n}|^2\} = 1$ .

The proof continues by placing the focus on the two terms found in the numerator of (A.12). In particular, it can be seen that the first term only involves the antennas with instantaneous CSI availability and accounts for the errors due to imperfect channel estimation. The factors of this term can be expressed as

$$\mathbb{E}\{|\bar{g}_{k,n}|^2\} = \tau_k^2 \mathbb{E}\left\{\left(\mathbf{A}_k|_{[\mathcal{D},n]}\right)^{\text{H}} \mathbf{q}_k \mathbf{q}_k^{\text{H}} \mathbf{A}_k|_{[\mathcal{D},n]}\right\} = \tau_k^2 \mathbf{R}_k|_{[n,n]}, \quad n \in \mathcal{B}, \quad (\text{A.13})$$

where  $\{\mathbf{A}_k\}_{[\mathcal{D},n]}$  denotes the  $n$ -th column of the transmit steering matrix  $\mathbf{A}_k$  defined in (6.7). Instead, the second term of the numerator in (A.12) characterizes the combination

of the errors introduced by having an inaccurate channel estimate and the averaging operation for the antennas without CSI. By combining (6.15) and (6.19) this factor can be re-expressed as

$$\text{var}(\bar{g}_{k,n}) = \text{var}\left(g_{k,n} - \frac{1}{M_n} \sum_{i=1}^{M_n} \hat{\mathbf{g}}_{k,\mathcal{B}_i^n}\right), \quad n \in \mathcal{C}, \quad (\text{A.14})$$

which corresponds to the variance of a subtraction of complex correlated random variables due to the compactness of the antenna array. This expression can be rewritten by iterative application of the statistical identities

$$\begin{aligned} \text{var}(X \pm Y) &= \text{var}(X) + \text{var}(Y) \pm 2 \text{Re}(\text{cov}(X, Y)), \\ \text{cov}(X \pm Y, Z) &= \text{cov}(X, Z) \pm \text{cov}(Y, Z), \end{aligned} \quad (\text{A.15})$$

where  $\text{cov}(\cdot, \cdot)$  denotes the covariance between two random variables and  $\text{Re}(\cdot)$  represents the real part of the argument. As a result,

$$\begin{aligned} \text{var}\left(g_{k,n} - \frac{1}{M_n} \sum_{i=1}^{M_n} \hat{\mathbf{g}}_{k,\mathcal{B}_i^n}\right) &= \text{var}(g_{k,n}) + \frac{1}{(M_n)^2} \sum_{i \in \mathcal{B}^n} \text{var}(\hat{g}_{k,i}) \\ &\quad - \frac{2}{M_n} \text{Re}\left(\sum_{i \in \mathcal{B}^n} \text{cov}(g_{k,n}, \hat{g}_{k,i})\right) + \frac{2}{(M_n)^2} \text{Re}\left(\sum_{i,j \in \mathcal{B}^n, i>j} \text{cov}(\hat{g}_{k,j}, \hat{g}_{k,i})\right), \quad n \in \mathcal{C}. \end{aligned} \quad (\text{A.16})$$

The terms involved in the above formulation can be further decomposed and given as a function of the true channel correlation matrix  $\mathbf{R}_k$ . With this purpose,  $\text{cov}(g_{k,n}, \hat{g}_{k,i})$  can be obtained as

$$\text{cov}(g_{k,n}, \hat{g}_{k,i}) = \text{cov}\left(g_{k,n}, \left(\sqrt{1 - \tau_k^2} g_{k,i} + \tau_k \bar{g}_{k,i}\right)\right) = \sqrt{1 - \tau_k^2} \mathbf{R}_k|_{[n,i]}, \quad (\text{A.17})$$

where it has been considered that  $\mathbf{z}_k$  is uncorrelated with  $\mathbf{q}_k$  in (6.20) [215]. The rest of the terms involved in (A.16) can be obtained similarly, and are omitted here for brevity. Finally, (6.22) is obtained by substituting (A.13) and (A.16) into (A.12), which completes the proof.

## Appendix E. Proof of Corollary 6.4.1.2

The objective of the proof is to show that the channel error factor  $\Delta_k$  is a monotonically increasing function of  $d$  for the physical channel model described in Sec. 6.2.2, i.e.,

$$\frac{\partial \Delta_k}{\partial d} = \frac{\partial}{\partial d} \left\{ \sum_{n \in \mathcal{C}} \left[ \underbrace{-\frac{2}{M_n} \operatorname{Re} \left( \sum_{i \in \mathcal{B}^n} \mathbf{R}_k|_{[n,i]} \right)}_{S_1} + \underbrace{\frac{2}{(M_n)^2} \operatorname{Re} \left( \sum_{i,j \in \mathcal{B}^n, i>j} \mathbf{R}_k|_{[j,i]} \right)}_{S_2} \right] \right\} > 0. \quad (\text{A.18})$$

Here, the terms independent of  $d$  and the factor  $\sqrt{1 - \tau_k^2}$  have been removed from (6.22), since  $\tau_k = 0$  when perfect CSI is considered as per (6.20). In the following the user index  $k$  is also dropped for notational convenience. The  $i, j$ -th entry of the channel correlation matrix  $\mathbf{R}$  for a ULA following the physical channel model described in Sec. 6.2.2 can be expressed as

$$\mathbf{R}|_{[i,j]} = \frac{1}{D} \sum_{m=1}^D e^{j2\pi d(j-i) \sin(\phi_m)}, \quad (\text{A.19})$$

where  $D$  denote the total number of angles of arrival (AoA) and  $\phi_m$  is the  $m$ -th azimuth AoA. In the following it is shown that

$$Q_n = \frac{\partial S_1}{\partial d} + \frac{\partial S_2}{\partial d} > 0, \quad \forall n \in \mathcal{C}, \quad (\text{A.20})$$

which in turn ensures that (A.18) holds. Here, since the real part of a function is not analytic, it is convenient to express  $S_1$  and  $S_2$  in (A.18) as

$$S_1 = -\frac{1}{M_n} \left( \sum_{i \in \mathcal{B}^n} \mathbf{R}|_{[n,i]} + \mathbf{R}|_{[i,n]} \right), \quad (\text{A.21})$$

and

$$S_2 = \frac{1}{(M_n)^2} \left( \sum_{i,j \in \mathcal{B}^n, i>j} \mathbf{R}|_{[j,i]} + \mathbf{R}|_{[i,j]} \right). \quad (\text{A.22})$$

For the case of ULAs and  $N/N_c \geq 2$ , the CSI for each of the  $|\mathcal{C}|$  antennas without CSI is obtained by averaging the CSI of the  $M_n = 2$  adjacent antennas. Note that

this is a consequence of the application of the basic CSI distribution pattern shown in Figure 6.1(b). Therefore,  $S_1$  can be re-expressed as

$$S_1 = - \left( \mathbf{R}|_{[n,i]} + \mathbf{R}|_{[i,n]} \right). \quad (\text{A.23})$$

Substituting (A.19) into (A.23) and differentiating w.r.t.  $d$  results in

$$\frac{\partial S_1}{\partial d} = \frac{4\pi}{D} \sum_{m=1}^D \sin(\phi_m) \sin(2\pi d \sin(\phi_m)), \quad (\text{A.24})$$

where it has been considered that  $(n - i) = 1$  because the CSI of the adjacent antennas is averaged, and  $\sin(\phi) = (e^{j\phi} - e^{-j\phi}) / 2j$ . Following a similar process while noting that the distance between the antennas with CSI used for averaging satisfies  $(i - j) = 2$  in (A.22),  $\frac{\partial S_2}{\partial d}$  can be expressed as

$$\begin{aligned} \frac{\partial S_2}{\partial d} &= \frac{2\pi}{D} \sum_{m=1}^D \sin(\phi_m) \sin(4\pi d \sin(\phi_m)) \\ &\stackrel{(a)}{=} \frac{4\pi}{D} \sum_{m=1}^D \sin(\phi_m) \sin(2\pi d \sin(\phi_m)) \cos(2\pi d \sin(\phi_m)), \end{aligned} \quad (\text{A.25})$$

where the trigonometric identity  $\sin(2\phi) = 2 \sin(\phi) \cos(\phi)$  has been employed in  $\stackrel{(a)}{=}$ . Subsequently, substituting (A.24) and (A.25) into (A.20),  $Q_n$  can be written as

$$Q_n = \frac{4\pi}{D} \sum_{m=1}^D \sin(\phi_m) \sin(2\pi d \sin(\phi_m)) (1 - \cos(2\pi d \sin(\phi_m))). \quad (\text{A.26})$$

To conclude, the small-angle approximations  $\sin(\phi) \approx \phi$  and  $\cos(\phi) \approx (1 - \phi^2/2)$  are incorporated into (A.26), which yields

$$Q_n = \frac{4\pi(2\pi d)}{D} \sum_{m=1}^D \phi_m^2 \left( \frac{(2\pi d \phi_m)^2}{2} \right) > 0, \quad (\text{A.27})$$

and completes the proof.

## Appendix F. Computation of the Joint Probabilities in (7.38)

This Appendix outlines the procedure for computing the probabilities  $P(T_j)$  in (7.38) for completeness. In particular, this is done for the PC architecture in Fig. 7.2(a) for reasons of illustration, where a scheme with  $M = 2$  and  $N = 5$  is considered. As detailed in Sec. 7.5, the sets containing the combinations of the ordered column norms with non-zero probability of being selected are  $\mathcal{G}^1 = \{1, 2\}$ ,  $\mathcal{G}^2 = \{1, 3\}$  and  $\mathcal{G}^3 = \{1, 4\}$ .  $P(T_1)$  is given by

$$P(T_1) = P\left(\text{selecting } \mathcal{G}_1^1 \cap \text{selecting } \mathcal{G}_2^1\right) = \quad (\text{A.28})$$

$$\stackrel{(a)}{=} P\left(\text{selecting } \mathcal{G}_1^1\right) P\left(\text{selecting } \mathcal{G}_2^1 | \text{selected } \mathcal{G}_1^1\right) \quad (\text{A.29})$$

$$\stackrel{(b)}{=} P\left(\mathcal{G}_1^1 = \{2, 4\}\right) P\left(\text{selecting } \mathcal{G}_2^1 | \mathcal{G}_1^1 = \{2, 4\}\right) \quad (\text{A.30})$$

$$+ P\left(\mathcal{G}_1^1 = \{1, 3, 5\}\right) P\left(\text{selecting } \mathcal{G}_2^1 | \mathcal{G}_1^1 = \{1, 3, 5\}\right) \quad (\text{A.31})$$

$$\stackrel{(c)}{=} \frac{2}{5} \times \frac{3}{4} + \frac{3}{5} \times \frac{2}{4} = \frac{3}{5}. \quad (\text{A.32})$$

In the above expressions,  $\stackrel{(a)}{=}$  is a direct application of (7.38),  $\stackrel{(b)}{=}$  divides the conditional probability of selecting the second antenna with the largest channel norm depending on whether the antenna with the largest norm were antennas  $\mathcal{G}_1^1 = \{1, 3, 5\}$  or antennas  $\mathcal{G}_1^1 = \{2, 4\}$  and  $\stackrel{(c)}{=}$  considers that the probability of finding  $B_{i:N}, i \in \{1, \dots, N\}$  at a given antenna port is equal for all antenna elements  $\mathcal{N}$ .

A similar procedure can be employed to compute  $P(T_3)$ , which reads as

$$P(T_3) = P\left(\text{selecting } \mathcal{G}_1^3 \cap \text{selecting } \mathcal{G}_2^3\right) = \quad (\text{A.33})$$

$$\stackrel{(a)}{=} P\left(\mathcal{G}_1^3 = \{1, 3, 5\}\right) P\left(\text{selecting } \mathcal{G}_2^3 | \mathcal{G}_1^3 = \{1, 3, 5\}\right) \quad (\text{A.34})$$

$$\stackrel{(b)}{=} \frac{3}{5} P\left(\text{not selecting } B_{2:N} \cap B_{3:N} | \mathcal{G}_1^3 = \{1, 3, 5\}\right) \quad (\text{A.35})$$

$$= \frac{3}{5} \times \frac{2}{4} \times \frac{1}{3} = \frac{1}{10}, \quad (\text{A.36})$$

where  $\stackrel{(a)}{=}$  and  $\stackrel{(b)}{=}$  hold because the only possibility of selecting the antenna with the  $\mathcal{G}_2^3 = 4$ -th largest norm is that the channels with the first, second and third largest norms are in antennas  $\{1, 3, 5\}$ . Finally,  $P(T_2) = 1 - P(T_1) - P(T_3) = \frac{3}{10}$ .



# List of References

- [1] S. Sesia, I. Toufik, and M. Baker, *LTE: The UMTS long term evolution*. Wiley, 2009.
- [2] G. Y. Li *et al.*, “Energy-efficient wireless communications: Tutorial, survey, and open issues,” *IEEE Wireless Commun.*, vol. 18, no. 6, pp. 28–35, Dec. 2011.
- [3] G. Fettweis and E. Zimmermann, “ICT energy consumption-trends and challenges,” in *Proceedings of the 11th Int. Symp. on Wireless Personal Multimedia Commun.*, vol. 2, no. 4, 2008, p. 6.
- [4] E. Björnson, L. Sanguinetti, J. Hoydis, and M. Debbah, “Optimal design of energy-efficient multi-user MIMO systems: Is massive MIMO the answer?” *IEEE Trans. on Wireless Commun.*, vol. 14, no. 6, pp. 3059–3075, June 2015.
- [5] G. Auer *et al.*, “D2. 3: Energy efficiency analysis of the reference systems, areas of improvements and target breakdown,” *INFSOICT-247733 EARTH (Energy Aware Radio and NeTwork TechNologies)*, *Tech. Rep.*, 2010.
- [6] J. G. Andrews *et al.*, “What will 5G be?” *IEEE Journal on Selected Areas in Commun.*, vol. 32, no. 6, pp. 1065–1082, June 2014.
- [7] M. Dohler, R. W. Heath, A. Lozano, C. B. Papadias, and R. A. Valenzuela, “Is the PHY layer dead?” *IEEE Commun. Mag.*, vol. 49, no. 4, pp. 159–165, April 2011.
- [8] J. Wu, S. Rangan, and H. Zhang, *Green communications: Theoretical fundamentals, algorithms and applications*. CRC Press, 2012.
- [9] C. Dorize, W. Van Heddeghem, F. Smyth, E. Le Rouzic, and B. Arzur. GreenTouch Draft Report on Baseline Power Consumption [*Online*]. Available: <http://www.greentouch.org>.
- [10] T. C. Group and G. e Sustainability Initiative (GeSI), “Smart 2020 report: Enabling the low carbon economy in the information age,” *Tech. Rep.*, 2008.

- [11] F. Rusek *et al.*, “Scaling up MIMO: Opportunities and challenges with very large arrays,” *IEEE Signal Process. Mag.*, vol. 30, no. 1, pp. 40–60, Jan. 2013.
- [12] K. Zheng *et al.*, “Survey of large-scale MIMO systems,” *IEEE Commun. Surveys Tutorials*, vol. 17, no. 3, pp. 1738–1760, thirdquarter 2015.
- [13] E. Björnson, E. G. Larsson, and T. L. Marzetta, “Massive MIMO: Ten myths and one critical question,” *IEEE Commun. Mag.*, vol. 54, no. 2, pp. 114–123, Feb. 2016.
- [14] C. Erdmann *et al.*, “A heterogeneous 3D-IC consisting of two 28nm FPGA die and 32 reconfigurable high-performance data converters,” in *IEEE Int. Solid-State Circuits Conf. Digest of Technical Papers (ISSCC)*, Feb. 2014, pp. 120–121.
- [15] A. Puglielli *et al.*, “Design of energy- and cost-efficient massive MIMO arrays,” *Proceedings of the IEEE*, vol. 104, no. 3, pp. 586–606, March 2016.
- [16] S. Rangan, T. S. Rappaport, and E. Erkip, “Millimeter-wave cellular wireless networks: Potentials and challenges,” *Proceedings of the IEEE*, vol. 102, no. 3, pp. 366–385, March 2014.
- [17] T. Bai, A. Alkhateeb, and R. W. Heath, “Coverage and capacity of millimeter-wave cellular networks,” *IEEE Commun. Mag.*, vol. 52, no. 9, pp. 70–77, Sept. 2014.
- [18] J. Jeganathan, A. Ghrayeb, L. Szczecinski, and A. Ceron, “Space shift keying modulation for MIMO channels,” *IEEE Trans. on Wireless Commun.*, vol. 8, no. 7, pp. 3692–3703, July 2009.
- [19] M. D. Renzo, H. Haas, A. Ghrayeb, S. Sugiura, and L. Hanzo, “Spatial modulation for generalized MIMO: Challenges, opportunities, and implementation,” *Proceedings of the IEEE*, vol. 102, no. 1, pp. 56–103, Jan. 2014.
- [20] W. Roh *et al.*, “Millimeter-wave beamforming as an enabling technology for 5G cellular communications: Theoretical feasibility and prototype results,” *IEEE Commun. Mag.*, vol. 52, no. 2, pp. 106–113, Feb. 2014.
- [21] X. Gao, O. Edfors, F. Rusek, and F. Tufvesson, “Massive MIMO performance evaluation based on measured propagation data,” *IEEE Trans. on Wireless Commun.*, vol. 14, no. 7, pp. 3899–3911, July 2015.
- [22] F. Boccardi, R. W. Heath, A. Lozano, T. L. Marzetta, and P. Popovski, “Five disruptive technology directions for 5G,” *IEEE Commun. Mag.*, vol. 52, no. 2, pp. 74–80, Feb. 2014.

- 
- [23] S. Sanayei and A. Nosratinia, “Antenna selection in MIMO systems,” *IEEE Commun. Mag.*, vol. 42, no. 10, pp. 68–73, Oct. 2004.
- [24] D. Tse and P. Viswanath, *Fundamentals of Wireless Communication*. Cambridge University Press, 2005.
- [25] C. Oestges and B. Clerckx, *MIMO wireless communications: From real-world propagation to space-time code design*. Academic Press, 2010.
- [26] G. H. Golub and C. F. Van Loan, *Matrix Computations*. JHU Press, 2012, vol. 3.
- [27] J. G. Proakis, “Digital communications.”
- [28] G. M. Miller, *Modern Electronic Communication*. Prentice-Hall, Inc., 1993.
- [29] L. Zheng and D. N. C. Tse, “Diversity and multiplexing: A fundamental tradeoff in multiple-antenna channels,” *IEEE Trans. on Inf. Theory*, vol. 49, no. 5, pp. 1073–1096, May 2003.
- [30] Y. Jiang, M. Varanasi, and J. Li, “Performance analysis of ZF and MMSE equalizers for MIMO systems: An in-depth study of the high SNR regime,” *IEEE Trans. on Inf. Theory*, vol. 57, no. 4, pp. 2008–2026, April 2011.
- [31] C. Windpassinger, R. F. H. Fischer, T. Vencel, and J. B. Huber, “Precoding in multiantenna and multiuser communications,” *IEEE Trans. on Wireless Commun.*, vol. 3, no. 4, pp. 1305–1316, July 2004.
- [32] Q. H. Spencer, C. B. Peel, A. L. Swindlehurst, and M. Haardt, “An introduction to the multi-user MIMO downlink,” *IEEE Commun. Mag.*, vol. 42, no. 10, pp. 60–67, Oct. 2004.
- [33] C. B. Peel, B. M. Hochwald, and A. L. Swindlehurst, “A vector-perturbation technique for near-capacity multiantenna multiuser communication-Part I: Channel inversion and regularization,” *IEEE Trans. on Commun.*, vol. 53, no. 1, pp. 195–202, Jan. 2005.
- [34] C. Masouros, “Correlation rotation linear precoding for MIMO broadcast communications,” *IEEE Trans. on Signal Process.*, vol. 59, no. 1, pp. 252–262, Jan. 2011.
- [35] C. Masouros and E. Alsusa, “Dynamic linear precoding for the exploitation of known interference in MIMO broadcast systems,” *IEEE Trans. on Wireless Commun.*, vol. 8, no. 3, pp. 1396–1404, March 2009.
- [36] —, “Soft linear precoding for the downlink of DS/CDMA communication systems,” *IEEE Trans. on Veh. Tech.*, vol. 59, no. 1, pp. 203–215, Jan. 2010.

- [37] S. M. Razavi, T. Ratnarajah, and C. Masouros, "Transmit-power efficient linear precoding utilizing known interference for the multiantenna downlink," *IEEE Trans. on Veh. Tech.*, vol. 63, no. 9, pp. 4383–4394, Nov. 2014.
- [38] G. Zheng, "Optimization in linear multiuser MIMO systems," Ph.D. dissertation, The University of Hong Kong, 2008.
- [39] B. M. Hochwald, C. B. Peel, and A. L. Swindlehurst, "A vector-perturbation technique for near-capacity multiantenna multiuser communication-Part II: Perturbation," *IEEE Trans. on Commun.*, vol. 53, no. 3, pp. 537–544, March 2005.
- [40] C. Masouros, M. Sellathurai, and T. Ratnarajah, "Computationally efficient vector perturbation precoding using thresholded optimization," *IEEE Trans. on Commun.*, vol. 61, no. 5, pp. 1880–1890, May 2013.
- [41] —, "Vector perturbation based on symbol scaling for limited feedback MISO downlinks," *IEEE Trans. on Signal Process.*, vol. 62, no. 3, pp. 562–571, Feb. 2014.
- [42] —, "A low-complexity sequential encoder for threshold vector perturbation," *IEEE Commun. Letters*, vol. 17, no. 12, pp. 2225–2228, Dec. 2013.
- [43] —, "Maximizing energy efficiency in the vector precoded MU-MISO downlink by selective perturbation," *IEEE Trans. on Wireless Commun.*, vol. 13, no. 9, pp. 4974–4984, Sept. 2014.
- [44] A. Li and C. Masouros, "A constellation scaling approach to vector perturbation for adaptive modulation in MU-MIMO," *IEEE Wireless Commun. Letters*, vol. 4, no. 3, pp. 289–292, June 2015.
- [45] T. K. Y. Lo, "Maximum ratio transmission," *IEEE Trans. on Commun.*, vol. 47, no. 10, pp. 1458–1461, Oct. 1999.
- [46] C. D. Meyer, *Matrix Analysis and Applied Linear Algebra*. Siam, 2000, vol. 2.
- [47] M. Costa, "Writing on dirty paper (corresp.)," *IEEE Trans. on Inf. Theory*, vol. 29, no. 3, pp. 439–441, May 1983.
- [48] B. Hassibi and H. Vikalo, "On the expected complexity of integer least-squares problems," in *IEEE Int. Conf. on Acoustics, Speech, and Signal Process. (ICASSP)*, vol. 2, May 2002, pp. II–1497–II–1500.
- [49] U. Erez and S. ten Brink, "A close-to-capacity dirty paper coding scheme," *IEEE Trans. on Inf. Theory*, vol. 51, no. 10, pp. 3417–3432, Oct. 2005.

- [50] R. Kannan, “Improved algorithms for integer programming and related lattice problems,” in *Proceedings of the fifteenth annual ACM symposium on Theory of computing*. ACM, 1983, pp. 193–206.
- [51] W. Yu, D. P. Varodayan, and J. M. Cioffi, “Trellis and convolutional precoding for transmitter-based interference presubtraction,” *IEEE Trans. on Commun.*, vol. 53, no. 7, pp. 1220–1230, July 2005.
- [52] E. C. Y. Peh and Y. C. Liang, “Power and modulo loss tradeoff with expanded soft demapper for LDPC coded GMD-THP MIMO systems,” *IEEE Trans. on Wireless Commun.*, vol. 8, no. 2, pp. 714–724, Feb. 2009.
- [53] J. Kang, H. Ku, D. S. Kwon, and C. Lee, “Tomlinson-Harashima precoder with tilted constellation for reducing transmission power,” *IEEE Trans. on Wireless Commun.*, vol. 8, no. 7, pp. 3658–3667, July 2009.
- [54] C. Liu, M. Li, and S. V. Hanly, “Power-efficient transmission design for MISO broadcast systems with QoS constraints,” in *Inf. Theory and Applications Workshop (ITA)*, Feb. 2013, pp. 1–7.
- [55] C. Masouros, M. Sellathurai, and T. Ratnarajah, “Interference optimization for transmit power reduction in Tomlinson-Harashima precoded MIMO downlinks,” *IEEE Trans. on Signal Process.*, vol. 60, no. 5, pp. 2470–2481, May 2012.
- [56] J. Kang, D. S. Kwon, and C. Lee, “Performance optimization of Tomlinson-Harashima precoder with tilted constellation,” *IEEE Commun. Letters*, vol. 14, no. 10, pp. 909–911, Oct. 2010.
- [57] J. Xu and L. Qiu, “Energy efficiency optimization for MIMO broadcast channels,” *IEEE Trans. on Wireless Commun.*, vol. 12, no. 2, pp. 690–701, Feb. 2013.
- [58] F. Heliot, M. A. Imran, and R. Tafazolli, “On the energy efficiency-spectral efficiency trade-off over the MIMO rayleigh fading channel,” *IEEE Trans. on Commun.*, vol. 60, no. 5, pp. 1345–1356, May 2012.
- [59] G. Miao, “Energy-efficient uplink multi-user MIMO,” *IEEE Trans. on Wireless Commun.*, vol. 12, no. 5, pp. 2302–2313, May 2013.
- [60] G. Auer *et al.*, “Cellular energy efficiency evaluation framework,” in *IEEE Veh. Tech. Conf. (VTC Spring)*, May 2011, pp. 1–6.
- [61] D. Ha, K. Lee, and J. Kang, “Energy efficiency analysis with circuit power consumption in massive MIMO systems,” in *IEEE Int. Symp. on Personal Indoor and Mobile Radio Commun. (PIMRC)*, Sept. 2013, pp. 938–942.

- [62] X. Wu, S. Sinanović, M. D. Renzo, and H. Haas, “Base station energy consumption for transmission optimised spatial modulation (TOSM) in correlated channels,” in *IEEE Int. Workshop on Computer Aided Modeling and Design of Communication Links and Networks (CAMAD)*, Sept. 2012, pp. 261–265.
- [63] H. Holtkamp, G. Auer, and H. Haas, “On minimizing base station power consumption,” in *IEEE Veh. Tech. Conf. (VTC Fall)*, Sept. 2011, pp. 1–5.
- [64] E. Björnson, J. Hoydis, M. Kountouris, and M. Debbah, “Massive MIMO systems with non-ideal hardware: Energy efficiency, estimation, and capacity limits,” *IEEE Trans. on Inf. Theory*, vol. 60, no. 11, pp. 7112–7139, Nov. 2014.
- [65] S. Cui, A. J. Goldsmith, and A. Bahai, “Energy-constrained modulation optimization,” *IEEE Trans. on Wireless Commun.*, vol. 4, no. 5, pp. 2349–2360, Sept. 2005.
- [66] W. Liu, S. Han, C. Yang, and C. Sun, “Massive MIMO or small cell network: Who is more energy efficient?” in *IEEE Wireless Commun. and Networking Conf. Workshops (WCNCW)*, April 2013, pp. 24–29.
- [67] E. Björnson, M. Kountouris, and M. Debbah, “Massive MIMO and small cells: Improving energy efficiency by optimal soft-cell coordination,” in *Int. Conf. on Telecommunications (ICT)*, May 2013, pp. 1–5.
- [68] S. K. Mohammed and E. G. Larsson, “Per-antenna constant envelope precoding for large multi-user MIMO systems,” *IEEE Trans. on Commun.*, vol. 61, no. 3, pp. 1059–1071, March 2013.
- [69] L. Lu, G. Y. Li, A. L. Swindlehurst, A. Ashikhmin, and R. Zhang, “An overview of massive MIMO: Benefits and challenges,” *IEEE Journal of Selected Topics in Signal Process.*, vol. 8, no. 5, pp. 742–758, Oct. 2014.
- [70] S. Yong and C.-C. Chong, “An overview of multigigabit wireless through millimeter wave technology: Potentials and technical challenges,” *EURASIP Journal on Wireless Commun. and Networking*, vol. 2007, no. 1, p. 078907, 2007. [Online]. Available: <http://jwcn.eurasipjournals.com/content/2007/1/078907>.
- [71] D. López-Pérez, M. Ding, H. Claussen, and A. H. Jafari, “Towards 1 Gbps/UE in cellular systems: Understanding ultra-dense small cell deployments,” *IEEE Commun. Surveys Tutorials*, vol. 17, no. 4, pp. 2078–2101, Fourthquarter 2015.
- [72] J. Hoydis, S. ten Brink, and M. Debbah, “Massive MIMO in the UL/DL of cellular networks: How many antennas do we need?” *IEEE Journal on Selected Areas in Commun.*, vol. 31, no. 2, pp. 160–171, Feb. 2013.

- [73] J. Vieira *et al.*, “A flexible 100-antenna testbed for massive MIMO,” in *GLOBE-COM Workshops*, Dec. 2014, pp. 287–293.
- [74] T. L. Marzetta, “Noncooperative cellular wireless with unlimited numbers of base station antennas,” *IEEE Trans. on Wireless Commun.*, vol. 9, no. 11, pp. 3590–3600, Nov. 2010.
- [75] S. Zarei, W. Gerstacker, R. R. Müller, and R. Schober, “Low-complexity linear precoding for downlink large-scale MIMO systems,” in *IEEE Int. Symp. on Personal Indoor and Mobile Radio Communications (PIMRC)*, Sept. 2013, pp. 1119–1124.
- [76] T. M. Cover and J. A. Thomas, *Elements of information theory*. John Wiley & Sons, 2012.
- [77] H. Prabhu, J. Rodrigues, O. Edfors, and F. Rusek, “Approximative matrix inverse computations for very-large MIMO and applications to linear pre-coding systems,” in *IEEE Wireless Commun. and Networking Conf. (WCNC)*, April 2013, pp. 2710–2715.
- [78] A. Kammoun, A. Müller, E. Björnson, and M. Debbah, “Linear precoding based on polynomial expansion: Large-scale multi-cell MIMO systems,” *IEEE Journal of Selected Topics in Signal Process.*, vol. 8, no. 5, pp. 861–875, Oct. 2014.
- [79] J. Jose, A. Ashikhmin, T. L. Marzetta, and S. Vishwanath, “Pilot contamination and precoding in multi-cell TDD systems,” *IEEE Trans. on Wireless Commun.*, vol. 10, no. 8, pp. 2640–2651, Aug. 2011.
- [80] A. Adhikary, J. Nam, J. Y. Ahn, and G. Caire, “Joint spatial division and multiplexing – The large-scale array regime,” *IEEE Trans. on Inf. Theory*, vol. 59, no. 10, pp. 6441–6463, Oct. 2013.
- [81] Z. Jiang, A. F. Molisch, G. Caire, and Z. Niu, “Achievable rates of FDD massive MIMO systems with spatial channel correlation,” *IEEE Trans. on Wireless Commun.*, vol. 14, no. 5, pp. 2868–2882, May 2015.
- [82] P. H. Kuo, H. T. Kung, and P. A. Ting, “Compressive sensing based channel feedback protocols for spatially-correlated massive antenna arrays,” in *IEEE Wireless Commun. and Networking Conf. (WCNC)*, April 2012, pp. 492–497.
- [83] X. Rao and V. K. N. Lau, “Distributed compressive CSIT estimation and feedback for FDD multi-user massive MIMO systems,” *IEEE Trans. on Signal Process.*, vol. 62, no. 12, pp. 3261–3271, June 2014.
- [84] H. Q. Ngo, E. G. Larsson, and T. L. Marzetta, “The multicell multiuser MIMO uplink with very large antenna arrays and a finite-dimensional channel,” *IEEE Trans. on Commun.*, vol. 61, no. 6, pp. 2350–2361, June 2013.

- [85] N. Shariati, E. Björnson, M. Bengtsson, and M. Debbah, “Low-complexity polynomial channel estimation in large-scale MIMO with arbitrary statistics,” *IEEE Journal of Selected Topics in Signal Process.*, vol. 8, no. 5, pp. 815–830, Oct. 2014.
- [86] H. Q. Ngo, E. G. Larsson, and T. L. Marzetta, “Energy and spectral efficiency of very large multiuser MIMO systems,” *IEEE Trans. on Commun.*, vol. 61, no. 4, pp. 1436–1449, April 2013.
- [87] S. L. H. Nguyen and A. Ghayeb, “Compressive sensing-based channel estimation for massive multiuser MIMO systems,” in *IEEE Wireless Commun. and Networking Conf. (WCNC)*, April 2013, pp. 2890–2895.
- [88] H. Yin, D. Gesbert, M. Filippou, and Y. Liu, “A coordinated approach to channel estimation in large-scale multiple-antenna systems,” *IEEE Journal on Selected Areas in Commun.*, vol. 31, no. 2, pp. 264–273, Feb. 2013.
- [89] R. R. Müller, M. Vehkaperä, and L. Cottatellucci, “Blind pilot decontamination,” *ITG-Fachbericht-WSA 2013*, 2013.
- [90] S. L. H. Nguyen and A. Ghayeb, “Precoding for multicell massive MIMO systems with compressive rank- $q$  channel approximation,” in *IEEE Int. Symp. on Personal Indoor and Mobile Radio Commun. (PIMRC)*, Sept. 2013, pp. 1227–1232.
- [91] A. Liu and V. Lau, “Hierarchical interference mitigation for massive MIMO cellular networks,” *IEEE Trans. on Signal Process.*, vol. 62, no. 18, pp. 4786–4797, Sept. 2014.
- [92] M. Li, S. Jin, and X. Gao, “Spatial orthogonality-based pilot reuse for multi-cell massive MIMO transmission,” in *Int. Conf. on Wireless Commun. Signal Process. (WCSP)*, Oct. 2013, pp. 1–6.
- [93] H. Huh, G. Caire, H. C. Papadopoulos, and S. A. Ramprasad, “Achieving “massive MIMO” spectral efficiency with a not-so-large number of antennas,” *IEEE Trans. on Wireless Commun.*, vol. 11, no. 9, pp. 3226–3239, Sept. 2012.
- [94] F. Fernandes, A. Ashikhmin, and T. L. Marzetta, “Inter-cell interference in non-cooperative TDD large scale antenna systems,” *IEEE Journal on Selected Areas in Commun.*, vol. 31, no. 2, pp. 192–201, Feb. 2013.
- [95] J. Zhang *et al.*, “Pilot contamination elimination for large-scale multiple-antenna aided OFDM systems,” *IEEE Journal of Selected Topics in Signal Process.*, vol. 8, no. 5, pp. 759–772, Oct. 2014.
- [96] T. Schenk, *RF imperfections in high-rate wireless systems: Impact and digital compensation*. Springer Science & Business Media, 2008.

- 
- [97] P. Z. Peebles, J. Read, and P. Read, *Probability, random variables, and random signal principles*. McGraw-Hill New York, 2001, vol. 3.
- [98] A. Pitarokoilis, S. Mohammed, and E. Larsson, “Uplink performance of time-reversal MRC in massive MIMO systems subject to phase noise,” *IEEE Trans. on Wireless Commun.*, vol. 14, no. 2, pp. 711–723, Feb. 2015.
- [99] U. Gustavsson *et al.*, “On the impact of hardware impairments on massive MIMO,” in *GLOBECOM Workshops*, Dec. 2014, pp. 294–300.
- [100] X. Zhang, M. Matthaiou, M. Coldrey, and E. Björnson, “Impact of residual transmit RF impairments on training-based MIMO systems,” *IEEE Trans. on Commun.*, vol. 63, no. 8, pp. 2899–2911, Aug. 2015.
- [101] C. Masouros, M. Sellathurai, and T. Ratnarajah, “Large-scale MIMO transmitters in fixed physical spaces: The effect of transmit correlation and mutual coupling,” *IEEE Trans. on Commun.*, vol. 61, no. 7, pp. 2794–2804, July 2013.
- [102] A. Ghosh, R. Ratasuk, B. Mondal, N. Mangalvedhe, and T. Thomas, “LTE-advanced: Next-generation wireless broadband technology [Invited Paper],” *IEEE Wireless Commun.*, vol. 17, no. 3, pp. 10–22, June 2010.
- [103] J. Brady, N. Behdad, and A. M. Sayeed, “Beamspace MIMO for millimeter-wave communications: System architecture, modeling, analysis, and measurements,” *IEEE Trans. on Antennas and Propagation*, vol. 61, no. 7, pp. 3814–3827, July 2013.
- [104] B. Clerckx, C. Craeye, D. Vanhoenacker-Janvier, and C. Oestges, “Impact of antenna coupling on  $2 \times 2$  MIMO communications,” *IEEE Trans. on Veh. Tech.*, vol. 56, no. 3, pp. 1009–1018, May 2007.
- [105] H. Q. Ngo, A. Ashikhmin, H. Yang, E. G. Larsson, and T. L. Marzetta, “Cell-free massive MIMO: Uniformly great service for everyone,” in *IEEE 16th Int. Workshop on Signal Process. Advances in Wireless Communications (SPAWC)*, June 2015, pp. 201–205.
- [106] C. A. Balanis, *Antenna Theory: Analysis and Design*. John Wiley & Sons, 2012.
- [107] J. Wallace and M. Jensen, “Mutual coupling in MIMO wireless systems: A rigorous network theory analysis,” *IEEE Trans. on Wireless Commun.*, vol. 3, no. 4, pp. 1317–1325, July 2004.
- [108] M. Morris and M. Jensen, “Network model for MIMO systems with coupled antennas and noisy amplifiers,” *IEEE Trans. on Antennas and Propagation*, vol. 53, no. 1, pp. 545–552, Jan. 2005.

- [109] N. Maleki, E. Karami, and M. Shiva, "Optimization of antenna array structures in mobile handsets," *IEEE Trans. on Veh. Tech.*, vol. 54, no. 4, pp. 1346–1351, July 2005.
- [110] R. Janaswamy, "Effect of element mutual coupling on the capacity of fixed length linear arrays," *IEEE Antennas and Wireless Propagation Letters*, vol. 1, no. 1, pp. 157–160, 2002.
- [111] C. Masouros and M. Matthaiou, "Space-constrained massive MIMO: Hitting the wall of favorable propagation," *IEEE Commun. Letters*, vol. 19, no. 5, pp. 771–774, May 2015.
- [112] S. Biswas, C. Masouros, and T. Ratnarajah, "Performance analysis of large multi-user MIMO systems with space-constrained 2D antenna arrays," *IEEE Trans. on Wireless Commun.*, vol. PP, no. 99, pp. 1–1, 2016.
- [113] G. Dahman, J. Flordelis, and F. Tufvesson, "Experimental evaluation of the effect of BS antenna inter-element spacing on MU-MIMO separation," in *IEEE Int. Conf. on Commun. (ICC)*, June 2015, pp. 1685–1690.
- [114] A. Sayeed and V. Raghavan, "Maximizing MIMO capacity in sparse multipath with reconfigurable antenna arrays," *IEEE Journal of Selected Topics in Signal Process.*, vol. 1, no. 1, pp. 156–166, June 2007.
- [115] Y. Pei, T.-H. Pham, and Y. C. Liang, "How many RF chains are optimal for large-scale MIMO systems when circuit power is considered?" in *IEEE Global Commun. Conf. (GLOBECOM)*, Dec. 2012, pp. 3868–3873.
- [116] H. Yang and T. L. Marzetta, "Total energy efficiency of cellular large scale antenna system multiple access mobile networks," in *IEEE Online Conf. on Green Commun. (GreenCom)*, Oct. 2013, pp. 27–32.
- [117] A. F. Molisch, "MIMO systems with antenna selection - an overview," in *Radio and Wireless Conf.*, Aug. 2003, pp. 167–170.
- [118] A. F. Molisch and M. Z. Win, "MIMO systems with antenna selection," *IEEE Microwave Mag.*, vol. 5, no. 1, pp. 46–56, March 2004.
- [119] S. Sanayei and A. Nosratinia, "Capacity of MIMO channels with antenna selection," *IEEE Trans. on Inf. Theory*, vol. 53, no. 11, pp. 4356–4362, Nov. 2007.
- [120] H. Zhang, H. Dai, Q. Zhou, and B. L. Hughes, "On the diversity order of spatial multiplexing systems with transmit antenna selection: A geometrical approach," *IEEE Trans. on Inf. Theory*, vol. 52, no. 12, pp. 5297–5311, Dec. 2006.

- 
- [121] A. F. Molisch, M. Z. Win, Y.-S. Choi, and J. H. Winters, "Capacity of MIMO systems with antenna selection," *IEEE Trans. on Wireless Commun.*, vol. 4, no. 4, pp. 1759–1772, July 2005.
- [122] A. Ghrayeb and T. M. Duman, "Performance analysis of MIMO systems with antenna selection over quasi-static fading channels," *IEEE Trans. on Veh. Tech.*, vol. 52, no. 2, pp. 281–288, March 2003.
- [123] P. J. Smith, T. W. King, L. M. Garth, and M. Dohler, "A power scaling analysis of norm-based antenna selection techniques," *IEEE Trans. on Wireless Commun.*, vol. 7, no. 8, pp. 3140–3149, Aug. 2008.
- [124] A. Gorokhov, D. A. Gore, and A. J. Paulraj, "Receive antenna selection for MIMO spatial multiplexing: Theory and algorithms," *IEEE Trans. on Signal Process.*, vol. 51, no. 11, pp. 2796–2807, Nov. 2003.
- [125] R. W. Heath and A. Paulraj, "Antenna selection for spatial multiplexing systems based on minimum error rate," in *IEEE Int. Conf. on Commun. (ICC)*, vol. 7, 2001, pp. 2276–2280.
- [126] R. W. Heath, S. Sandhu, and A. Paulraj, "Antenna selection for spatial multiplexing systems with linear receivers," *IEEE Commun. Letters*, vol. 5, no. 4, pp. 142–144, April 2001.
- [127] Y.-S. Choi, A. F. Molisch, M. Z. Win, and J. H. Winters, "Fast algorithms for antenna selection in MIMO systems," in *IEEE Veh. Tech. Conf. (VTC Fall)*, vol. 3, Oct. 2003, pp. 1733–1737.
- [128] A. Gorokhov, D. Gore, and A. Paulraj, "Receive antenna selection for MIMO flat-fading channels: Theory and algorithms," *IEEE Trans. on Inf. Theory*, vol. 49, no. 10, pp. 2687–2696, Oct. 2003.
- [129] A. B. Narasimhamurthy and C. Tepedelenlioglu, "Antenna selection for MIMO-OFDM systems with channel estimation error," *IEEE Trans. on Veh. Tech.*, vol. 58, no. 5, pp. 2269–2278, June 2009.
- [130] V. Kristem, N. B. Mehta, and A. F. Molisch, "Training for antenna selection in time-varying channels: Optimal selection, energy allocation, and energy efficiency evaluation," *IEEE Trans. on Commun.*, vol. 61, no. 6, pp. 2295–2305, June 2013.
- [131] —, "A novel, balanced, and energy-efficient training method for receive antenna selection," *IEEE Trans. on Wireless Commun.*, vol. 9, no. 9, pp. 2742–2753, Sept. 2010.

- [132] N. P. Le, F. Safaei, and L. C. Tran, "Antenna selection strategies for MIMO-OFDM wireless systems: An energy efficiency perspective," *IEEE Trans. on Veh. Tech.*, vol. 65, no. 4, pp. 2048–2062, April 2016.
- [133] O. K. Rayel, G. Brante, J. L. Rebelatto, R. D. Souza, and M. A. Imran, "Energy efficiency-spectral efficiency trade-off of transmit antenna selection," *IEEE Trans. on Commun.*, vol. 62, no. 12, pp. 4293–4303, Dec. 2014.
- [134] A. Dua, K. Medepalli, and A. J. Paulraj, "Receive antenna selection in MIMO systems using convex optimization," *IEEE Trans. on Wireless Commun.*, vol. 5, no. 9, pp. 2353–2357, Sept. 2006.
- [135] A. F. Molisch, N. B. Mehta, H. Zhang, P. Almers, and J. Zhang, "Implementation aspects of antenna selection for MIMO systems," in *Int. Conf. on Commun. and Networking in China*, Oct. 2006, pp. 1–7.
- [136] J. Ahmadi-Shokouh, S. H. Jamali, S. Safavi-Naeini, and G. Z. Rafi, "Switch loss and antenna directivity effects on MIMO antenna selection," in *Canadian Conf. on Electrical and Computer Engineering (CCECE)*, May 2008, pp. 641–646.
- [137] P. V. Amadori and C. Masouros, "Interference driven antenna selection for massive multi-user MIMO," *IEEE Trans. on Veh. Tech.*, to be published.
- [138] K. Dong, N. Prasad, X. Wang, and S. Zhu, "Adaptive antenna selection and Tx/Rx beamforming for large-scale MIMO systems in 60 Ghz channels," *EURASIP Journal on Wireless Communications and Networking*, vol. 2011, no. 1, pp. 1–14, 2011. [Online]. Available: <http://dx.doi.org/10.1186/1687-1499-2011-59>
- [139] H. Li, L. Song, and M. Debbah, "Energy efficiency of large-scale multiple antenna systems with transmit antenna selection," *IEEE Trans. on Commun.*, vol. 62, no. 2, pp. 638–647, Feb. 2014.
- [140] B. M. Lee, J. Choi, J. Bang, and B. C. Kang, "An energy efficient antenna selection for large scale green MIMO systems," in *IEEE Int. Symp. on Circuits and Systems (ISCAS)*, May 2013, pp. 950–953.
- [141] S. Mahboob, R. Ruby, and V. C. M. Leung, "Transmit antenna selection for downlink transmission in a massively distributed antenna system using convex optimization," in *Int. Conf. on Broadband, Wireless Computing, Communication and Applications (BWCCA)*, Nov. 2012, pp. 228–233.
- [142] M. Gkizeli and G. N. Karystinos, "Maximum-SNR antenna selection among a large number of transmit antennas," *IEEE Journal of Selected Topics in Signal Process.*, vol. 8, no. 5, pp. 891–901, Oct. 2014.

- 
- [143] R. Kataoka, K. Nishimori, N. Tran, and T. Imai, "Performance evaluation by antenna selection using real propagation channel on massive MIMO," in *IEEE International Workshop on Electromagnetics (iWEM)*, Aug. 2014, pp. 227–228.
- [144] M. Benmimoune, E. Driouch, W. Ajib, and D. Massicotte, "Feedback reduction and efficient antenna selection for massive MIMO system," in *IEEE Veh. Tech. Conf. (VTC Fall)*, Sept. 2015, pp. 1–6.
- [145] B. Fang, Z. Qian, W. Shao, and W. Zhong, "Raise: A new fast transmit antenna selection algorithm for massive MIMO systems," *Wireless Personal Communications*, vol. 80, no. 3, pp. 1147–1157, 2014. [Online]. Available: <http://dx.doi.org/10.1007/s11277-014-2077-4>.
- [146] X. Gao, O. Edfors, F. Tufvesson, and E. G. Larsson, "Multi-switch for antenna selection in massive MIMO," in *IEEE Global Commun. Conf. (GLOBECOM)*, Dec. 2015, pp. 1–6.
- [147] R. Méndez-Rial, C. Rusu, N. González-Prelcic, A. Alkhateeb, and R. W. Heath, "Hybrid MIMO architectures for millimeter wave communications: Phase shifters or switches?" *IEEE Access*, vol. 4, pp. 247–267, 2016.
- [148] X. Gao, O. Edfors, F. Tufvesson, and E. G. Larsson, "Massive MIMO in real propagation environments: Do all antennas contribute equally?" *IEEE Trans. on Commun.*, vol. 63, no. 11, pp. 3917–3928, Nov. 2015.
- [149] A. M. Sayeed, "Deconstructing multiantenna fading channels," *IEEE Trans. on Signal Process.*, vol. 50, no. 10, pp. 2563–2579, Oct. 2002.
- [150] A. M. Tulino, A. Lozano, and S. Verdu, "Impact of antenna correlation on the capacity of multiantenna channels," *IEEE Trans. on Inf. Theory*, vol. 51, no. 7, pp. 2491–2509, July 2005.
- [151] P. V. Amadori and C. Masouros, "Low RF-complexity millimeter-wave beamspace-MIMO systems by beam selection," *IEEE Trans. on Commun.*, vol. 63, no. 6, pp. 2212–2223, June 2015.
- [152] M. Bona, L. Manholm, J. P. Starski, and B. Svensson, "Low-loss compact Butler matrix for a microstrip antenna," *IEEE Trans. on Microwave Theory and Techniques*, vol. 50, no. 9, pp. 2069–2075, Sept. 2002.
- [153] M. Ueno, "A systematic design formulation for Butler matrix applied FFT algorithm," *IEEE Trans. on Antennas and Propagation*, vol. 29, no. 3, pp. 496–501, May 1981.

- [154] “Simplified design procedures for Butler matrices incorporating  $90^\circ$  hybrids or  $180^\circ$  hybrids,” *IEE Proceedings H - Microwaves, Antennas and Propagation*, vol. 134, no. 1, pp. 50–54, February 1987.
- [155] S. Vashist, M. Soni, and P. Singhal, “A review on the development of rotman lens antenna,” *Chinese Journal of Engineering*, vol. 2014, 2014.
- [156] M. R. Akdeniz *et al.*, “Millimeter wave channel modeling and cellular capacity evaluation,” *IEEE Journal on Selected Areas in Commun.*, vol. 32, no. 6, pp. 1164–1179, June 2014.
- [157] M. D. Renzo, H. Haas, and P. M. Grant, “Spatial modulation for multiple-antenna wireless systems: A survey,” *IEEE Commun. Mag.*, vol. 49, no. 12, pp. 182–191, Dec. 2011.
- [158] P. Yang *et al.*, “Single-carrier spatial modulation: A promising design for large-scale broadband antenna systems,” *IEEE Commun. Surveys Tutorials*, vol. PP, no. 99, pp. 1–1, 2016.
- [159] N. Serafimovski, S. Sinanović, M. Di Renzo, and H. Haas, “Multiple access spatial modulation,” *EURASIP Journal on Wireless Commun. and Networking*, vol. 2012, no. 1, pp. 1–20, 2012.
- [160] R. Y. Chang, S. J. Lin, and W. H. Chung, “Energy efficient transmission over space shift keying modulated MIMO channels,” *IEEE Trans. on Commun.*, vol. 60, no. 10, pp. 2950–2959, Oct. 2012.
- [161] K. Ntontin, M. D. Renzo, A. Perez-Neira, and C. Verikoukis, “Towards the performance and energy efficiency comparison of spatial modulation with conventional single-antenna transmission over generalized fading channels,” in *IEEE Int. Workshop on Computer Aided Modeling and Design of Communication Links and Networks (CAMAD)*, Sept. 2012, pp. 120–124.
- [162] A. Stavridis, S. Sinanovic, M. D. Renzo, H. Haas, and P. Grant, “An energy saving base station employing spatial modulation,” in *IEEE Int. Workshop on Computer Aided Modeling and Design of Communication Links and Networks (CAMAD)*, Sept. 2012, pp. 231–235.
- [163] S. Sugiura and L. Hanzo, “On the joint optimization of dispersion matrices and constellations for near-capacity irregular precoded space-time shift keying,” *IEEE Trans. on Wireless Commun.*, vol. 12, no. 1, pp. 380–387, Jan. 2013.
- [164] S. Sugiura, S. Chen, and L. Hanzo, “Coherent and differential space-time shift keying: A dispersion matrix approach,” *IEEE Trans. on Commun.*, vol. 58, no. 11, pp. 3219–3230, Nov. 2010.

- [165] J. Jeganathan, A. Ghrayeb, and L. Szczecinski, "Spatial modulation: optimal detection and performance analysis," *IEEE Commun. Letters*, vol. 12, no. 8, pp. 545–547, Aug. 2008.
- [166] M. Di Renzo and H. Haas, "Bit error probability of SM-MIMO over generalized fading channels," *IEEE Trans. on Veh. Tech.*, vol. 61, no. 3, pp. 1124–1144, March 2012.
- [167] P. Yang, M. Di Renzo, Y. Xiao, S. Li, and L. Hanzo, "Design guidelines for spatial modulation," *IEEE Commun. Surveys and Tutorials*, vol. 17, no. 1, pp. 6–26, Firstquarter 2015.
- [168] R. Y. Mesleh, H. Haas, S. Sinanovic, C. W. Ahn, and S. Yun, "Spatial modulation," *IEEE Trans. on Veh. Tech.*, vol. 57, no. 4, pp. 2228–2241, July 2008.
- [169] C. Masouros and L. Hanzo, "Dual layered MIMO transmission for increased bandwidth efficiency," *IEEE Trans. on Veh. Tech.*, vol. PP, no. 99, pp. 1–1, 2015.
- [170] A. Younis, S. Sinanovic, M. D. Renzo, R. Mesleh, and H. Haas, "Generalised sphere decoding for spatial modulation," *IEEE Trans. on Commun.*, vol. 61, no. 7, pp. 2805–2815, July 2013.
- [171] S. Sugiura, C. Xu, S. X. Ng, and L. Hanzo, "Reduced-complexity coherent versus non-coherent QAM-aided space-time shift keying," *IEEE Trans. on Commun.*, vol. 59, no. 11, pp. 3090–3101, Nov. 2011.
- [172] C. M. Yu *et al.*, "Compressed sensing detector design for space shift keying in MIMO systems," *IEEE Commun. Letters*, vol. 16, no. 10, pp. 1556–1559, Oct. 2012.
- [173] C. H. Wu, W. H. Chung, and H. W. Liang, "OMP-based detector design for space shift keying in large MIMO systems," in *IEEE Global Commun. Conf. (GLOBECOM)*, Dec. 2014, pp. 4072–4076.
- [174] P. Yang *et al.*, "Star-QAM signaling constellations for spatial modulation," *IEEE Trans. on Veh. Tech.*, vol. 63, no. 8, pp. 3741–3749, Oct. 2014.
- [175] M. D. Renzo and H. Haas, "On transmit diversity for spatial modulation MIMO: Impact of spatial constellation diagram and shaping filters at the transmitter," *IEEE Trans. on Veh. Tech.*, vol. 62, no. 6, pp. 2507–2531, July 2013.
- [176] M. Maleki, H. R. Bahrami, S. Beygi, M. Kafashan, and N. H. Tran, "Space modulation with CSI: Constellation design and performance evaluation," *IEEE Trans. on Veh. Tech.*, vol. 62, no. 4, pp. 1623–1634, May 2013.

- [177] K. Ntontin, M. D. Renzo, A. Perez-Neira, and C. Verikoukis, "Adaptive generalized space shift keying," *EURASIP Journal on Wireless Commun. and Networking*, vol. 2013, no. 1, pp. 1–15, 2013.
- [178] "Constellation design for spatial modulation," *Procedia Technology*, vol. 7, pp. 71 – 78, 2013, 3rd Iberoamerican Conf. on Electronics Engineering and Computer Science, {CIIECC} 2013.
- [179] X. Guan, Y. Cai, and W. Yang, "On the mutual information and precoding for spatial modulation with finite alphabet," *IEEE Wireless Commun. Letters*, vol. 2, no. 4, pp. 383–386, Aug. 2013.
- [180] C. Masouros, "Improving the diversity of spatial modulation in MISO channels by phase alignment," *IEEE Commun. Letters*, vol. 18, no. 5, pp. 729–732, May 2014.
- [181] C.-H. Wu, W.-H. Chung, and H.-W. Liang, "Improved generalized space-shift keying via power allocation," *IEEE Commun. Letters*, vol. 18, no. 7, pp. 1143–1146, July 2014.
- [182] M. Di Renzo and H. Haas, "Improving the performance of space shift keying (SSK) modulation via opportunistic power allocation," *IEEE Commun. Letters*, vol. 14, no. 6, pp. 500–502, June 2010.
- [183] C. Masouros and L. Hanzo, "Constellation-randomization achieves transmit diversity for single-RF spatial modulation," *IEEE Trans. on Veh. Tech.*, vol. PP, no. 99, pp. 1–1, 2016.
- [184] M.-C. Lee, W.-H. Chung, and T.-S. Lee, "Generalized precoder design formulation and iterative algorithm for spatial modulation in MIMO systems with CSIT," *IEEE Trans. on Commun.*, vol. 63, no. 4, pp. 1230–1244, April 2015.
- [185] M. Di Renzo and H. Haas, "Bit error probability of space-shift keying MIMO over multiple-access independent fading channels," *IEEE Trans. on Veh. Tech.*, vol. 60, no. 8, pp. 3694–3711, Oct. 2011.
- [186] L.-L. Yang, "Signal detection in antenna-hopping space-division multiple-access systems with space-shift keying modulation," *IEEE Trans. on Signal Process.*, vol. 60, no. 1, pp. 351–366, Jan. 2012.
- [187] T. Narasimhan, P. Raviteja, and A. Chockalingam, "Large-scale multiuser SM-MIMO versus massive MIMO," in *Inf. Theory and Applications Workshop (ITA)*, Feb 2014, pp. 1–9.
- [188] T. L. Narasimhan, P. Raviteja, and A. Chockalingam, "Generalized spatial modulation in large-scale multiuser MIMO systems," *IEEE Trans. on Wireless Commun.*, vol. 14, no. 7, pp. 3764–3779, July 2015.

- [189] J. Zheng, “Low-complexity detector for spatial modulation multiple access channels with a large number of receive antennas,” *IEEE Commun. Letters*, vol. 18, no. 11, pp. 2055–2058, Nov. 2014.
- [190] S. Wang, Y. Li, M. Zhao, and J. Wang, “Energy-efficient and low-complexity uplink transceiver for massive spatial modulation MIMO,” *IEEE Trans. on Veh. Tech.*, vol. 64, no. 10, pp. 4617–4632, Oct. 2015.
- [191] S. Wang, Y. Li, and J. Wang, “Multiuser detection in massive spatial modulation MIMO with low-resolution ADCs,” *IEEE Trans. on Wireless Commun.*, vol. 14, no. 4, pp. 2156–2168, April 2015.
- [192] A. Liu and V. Lau, “Phase only RF precoding for massive MIMO systems with limited RF chains,” *IEEE Trans. on Signal Process.*, vol. 62, no. 17, pp. 4505–4515, Sept. 2014.
- [193] O. El Ayach, S. Rajagopal, S. Abu-Surra, Z. Pi, and R. Heath, “Spatially sparse precoding in millimeter wave MIMO systems,” *IEEE Trans. on Wireless Commun.*, vol. 13, no. 3, pp. 1499–1513, March 2014.
- [194] R. W. Heath, N. González-Prelcic, S. Rangan, W. Roh, and A. M. Sayeed, “An overview of signal processing techniques for millimeter wave MIMO systems,” *IEEE Journal of Selected Topics in Signal Process.*, vol. 10, no. 3, pp. 436–453, April 2016.
- [195] A. Alkhateeb, J. Mo, N. González-Prelcic, and R. W. Heath, “MIMO precoding and combining solutions for millimeter-wave systems,” *IEEE Commun. Mag.*, vol. 52, no. 12, pp. 122–131, Dec. 2014.
- [196] V. Venkateswaran and A. J. van der Veen, “Analog beamforming in MIMO communications with phase shift networks and online channel estimation,” *IEEE Trans. on Signal Processing*, vol. 58, no. 8, pp. 4131–4143, Aug. 2010.
- [197] V. Venkateswaran, F. Pivit, and L. Guan, “Hybrid RF and digital beamformer for cellular networks: Algorithms, microwave architectures and measurements,” *IEEE Trans. on Microwave Theory and Techniques*, accepted for publication, 2016. [Online]. Available: <http://arxiv.org/abs/1510.02822>.
- [198] P. W. Wolniansky, G. J. Foschini, G. D. Golden, and R. A. Valenzuela, “V-BLAST: An architecture for realizing very high data rates over the rich-scattering wireless channel,” in *URSI Int. Symp. on Signals, Systems, and Electronics*, Sept. 1998, pp. 295–300.
- [199] A. Garcia-Rodriguez and C. Masouros, “Power loss reduction for MMSE-THP with multidimensional symbol scaling,” *IEEE Commun. Letters*, vol. 18, no. 7, pp. 1147–1150, July 2014.

- [200] T. F. Coleman and Y. Li, “An interior trust region approach for nonlinear minimization subject to bounds,” *SIAM Journal on Optimization*, vol. 6, no. 2, pp. 418–445, 1996.
- [201] J. J. Moré, *Numerical Analysis: Proceedings of the Biennial Conf.* Berlin, Heidelberg: Springer Berlin Heidelberg, 1978, ch. The Levenberg-Marquardt algorithm: Implementation and theory, pp. 105–116.
- [202] D. M. Bates and D. G. Watts, “Nonlinear regression: Iterative estimation and linear approximations,” *Nonlinear Regression Analysis and Its Applications*, pp. 32–66, 1988.
- [203] T. H. Lee, *The Design of CMOS Radio-Frequency Integrated Circuits.* Cambridge University Press, 2004.
- [204] D. Curd, “Power consumption in 65 nm FPGAs,” *White Paper: Virtex-5 FPGAs*, 2007.
- [205] M. Arakawa, “Computational Workloads for Commonly Used Signal Processing Kernels,” Massachusetts Institute of Technology (MIT), Cambridge, MA, USA, Tech. Rep. SPR-9, 2006.
- [206] K. Dufková, J.-Y. Boudec, L. Kencl, and M. Bjelica, *Proceedings of the Mobile Entity Localization and Tracking in GPS-less Environments: Second Int. Workshop, (MELT).* Springer, 2009, ch. Predicting User-Cell Association in Cellular Networks from Tracked Data, pp. 19–33.
- [207] C. Wang and R. D. Murch, “Adaptive downlink multi-user MIMO wireless systems for correlated channels with imperfect CSI,” *IEEE Trans. on Wireless Commun.*, vol. 5, no. 9, pp. 2435–2446, Sept. 2006.
- [208] P. Yang *et al.*, “Transmit precoded spatial modulation: Maximizing the minimum euclidean distance versus minimizing the bit error ratio,” *IEEE Trans. on Wireless Commun.*, vol. 15, no. 3, pp. 2054–2068, March 2016.
- [209] A. Garcia-Rodriguez, C. Masouros, and L. Hanzo, “Pre-scaling optimization for space shift keying based on semidefinite relaxation,” *IEEE Trans. on Commun.*, vol. 63, no. 11, pp. 4231–4243, Nov. 2015.
- [210] Z.-Q. Luo, W.-K. Ma, A.-C. So, Y. Ye, and S. Zhang, “Semidefinite relaxation of quadratic optimization problems,” *IEEE Signal Process. Mag.*, vol. 27, no. 3, pp. 20–34, May 2010.
- [211] S. Boyd and L. Vandenberghe, *Convex optimization.* Cambridge university press, 2004.

- 
- [212] N. D. Sidiropoulos, T. N. Davidson, and Z.-Q. Luo, "Transmit beamforming for physical-layer multicasting," *IEEE Trans. on Signal Process.*, vol. 54, no. 6, pp. 2239–2251, June 2006.
- [213] P. Biswas and Y. Ye, "Semidefinite programming for ad hoc wireless sensor network localization," in *Third Int. Symp. on Inf. Processing in Sensor Networks (IPSN)*, April 2004, pp. 46–54.
- [214] A. B. Gershman, N. D. Sidiropoulos, S. Shahbazpanahi, M. Bengtsson, and B. Ottersten, "Convex optimization-based beamforming," *IEEE Signal Process. Mag.*, vol. 27, no. 3, pp. 62–75, May 2010.
- [215] S. Wagner, R. Couillet, M. Debbah, and D. T. M. Slock, "Large system analysis of linear precoding in correlated MISO broadcast channels under limited feedback," *IEEE Trans. on Inf. Theory*, vol. 58, no. 7, pp. 4509–4537, July 2012.
- [216] I. Wajid, Y. C. Eldar, and A. Gershman, "Robust downlink beamforming using covariance channel state information," in *IEEE Int. Conf. on Acoustics, Speech and Signal Processing (ICASSP)*, April 2009, pp. 2285–2288.
- [217] B. K. Chalise and L. Vandendorpe, "Optimization of MIMO relays for multipoint-to-multipoint communications: Nonrobust and robust designs," *IEEE Trans. on Signal Process.*, vol. 58, no. 12, pp. 6355–6368, Dec. 2010.
- [218] I. Wajid, M. Pesavento, Y. C. Eldar, and D. Ciochina, "Robust downlink beamforming with partial channel state information for conventional and cognitive radio networks," *IEEE Trans. on Signal Process.*, vol. 61, no. 14, pp. 3656–3670, July 2013.
- [219] C. Xu, S. Sugiura, S. X. Ng, and L. Hanzo, "Spatial modulation and space-time shift keying: Optimal performance at a reduced detection complexity," *IEEE Trans. on Commun.*, vol. 61, no. 1, pp. 206–216, Jan. 2013.
- [220] D. L. Donoho, A. Maleki, and A. Montanari, "Message-passing algorithms for compressed sensing," *Proc. of the National Academy of Sciences*, vol. 106, no. 45, pp. 18 914–18 919, 2009.
- [221] Y. C. Eldar and M. Mishali, "Robust recovery of signals from a structured union of subspaces," *IEEE Trans. on Inf. Theory*, vol. 55, no. 11, pp. 5302–5316, 2009.
- [222] R. G. Baraniuk, V. Cevher, M. F. Duarte, and C. Hegde, "Model-based compressive sensing," *IEEE Trans. on Inf. Theory*, vol. 56, no. 4, pp. 1982–2001, 2010.
- [223] A. Younis, N. Serafimovski, R. Mesleh, and H. Haas, "Generalised spatial modulation," in *Conf. Record of the Forty Fourth Asilomar Conf. on Signals, Systems and Computers (ASILOMAR)*, Nov. 2010, pp. 1498–1502.

- [224] R. Zhang, L.-L. Yang, and L. Hanzo, "Generalised pre-coding aided spatial modulation," *IEEE Trans. on Wireless Commun.*, vol. 12, no. 11, pp. 5434–5443, Nov. 2013.
- [225] R. Baraniuk, "Compressive sensing [lecture notes]," *IEEE Signal Process. Mag.*, vol. 24, no. 4, pp. 118–121, 2007.
- [226] E. J. Candès and M. B. Wakin, "An introduction to compressive sampling," *IEEE Signal Process. Mag.*, vol. 25, no. 2, pp. 21–30, 2008.
- [227] E. Candès, "Compressive sampling," in *Proceedings of the Int. Congress of Mathematicians: Madrid, August 22-30, 2006: invited lectures*, 2006, pp. 1433–1452.
- [228] E. Candès, J. Romberg, and T. Tao, "Stable signal recovery from incomplete and inaccurate measurements," *Communications on pure and applied mathematics*, vol. 59, no. 8, pp. 1207–1223, 2006.
- [229] D. Needell and J. A. Tropp, "CoSaMP: Iterative signal recovery from incomplete and inaccurate samples," *Applied and Computational Harmonic Analysis*, vol. 26, no. 3, pp. 301–321, 2009.
- [230] A. Björck, *Numerical methods for least squares problems*. Siam, 1996.
- [231] L. Vandenberghe, "Applied numerical computing," University Lecture.
- [232] R. Hunger, "Floating point operations in matrix-vector calculus [*Available*]: <https://mediatum.ub.tum.de/doc/625604/625604.pdf>," Tech. Rep.
- [233] M. Matthaiou, M. McKay, P. Smith, and J. Nossék, "On the condition number distribution of complex Wishart matrices," *IEEE Trans. on Commun.*, vol. 58, no. 6, pp. 1705–1717, June 2010.
- [234] A. Edelman, "Eigenvalues and condition numbers of random matrices," Ph.D. dissertation, Yale University, 1988.
- [235] B. Clerckx, G. Kim, and S. Kim, "Correlated fading in broadcast MIMO channels: Curse or blessing?" in *IEEE Global Commun. Conf. (GLOBECOM)*, Nov. 2008, pp. 1–5.
- [236] B. T. Maharaj, J. W. Wallace, L. P. Linde, and M. A. Jensen, "Frequency scaling of spatial correlation from co-located 2.4 and 5.2 Ghz wideband indoor MIMO channel measurements," *Electronics Letters*, vol. 41, no. 6, pp. 336–337, March 2005.
- [237] A. Stavridis, S. Sinanovic, M. Di Renzo, and H. Haas, "Energy evaluation of spatial modulation at a multi-antenna base station," in *IEEE 78th Veh. Tech. Conf. (VTC Fall)*, Sept. 2013, pp. 1–5.

- [238] V. Raghavan and A. Sayeed, "Sublinear capacity scaling laws for sparse MIMO channels," *IEEE Trans. on Inf. Theory*, vol. 57, no. 1, pp. 345–364, Jan. 2011.
- [239] J. Zhang, L. Dai, M. Matthaiou, C. Masouros, and S. Jin, "On the spectral efficiency of space-constrained massive MIMO with linear receivers," in *IEEE Int. Conf. on Commun. (ICC)*, to be published.
- [240] S. Noh, M. Zoltowski, Y. Sung, and D. Love, "Pilot beam pattern design for channel estimation in massive MIMO systems," *IEEE J. of Sel. Topics in Signal Process.*, vol. 8, no. 5, pp. 787–801, Oct. 2014.
- [241] B. Lee, J. Choi, J. y. Seol, D. J. Love, and B. Shim, "Antenna grouping based feedback reduction for FDD-based massive MIMO systems," in *IEEE Int. Conf. on Commun. (ICC)*, June 2014, pp. 4477–4482.
- [242] B. Lee, J. Choi, J. Y. Seol, D. J. Love, and B. Shim, "Antenna grouping based feedback compression for FDD-based massive MIMO systems," *IEEE Trans. on Commun.*, vol. 63, no. 9, pp. 3261–3274, Sept. 2015.
- [243] L. Zheng, D. Tse, and M. Medard, "Channel coherence in the low-SNR regime," *IEEE Trans. on Inf. Theory*, vol. 53, no. 3, pp. 976–997, March 2007.
- [244] H. Yang and T. Marzetta, "Performance of conjugate and zero-forcing beamforming in large-scale antenna systems," *IEEE Journal on Selected Areas in Commun.*, vol. 31, no. 2, pp. 172–179, Feb. 2013.
- [245] K. F. Warnick and M. Jensen, "Optimal noise matching for mutually coupled arrays," *IEEE Trans. on Antennas and Propagation*, vol. 55, no. 6, pp. 1726–1731, June 2007.
- [246] A. Garcia-Rodriguez and C. Masouros, "Exploiting the tolerance of massive MIMO to incomplete CSI for low-complexity transmission," in *IEEE Global Communications Conf. (GLOBECOM)*, Dec. 2015.
- [247] H. Kim, C. B. Chae, G. de Veciana, and R. W. Heath, "A cross-layer approach to energy efficiency for adaptive MIMO systems exploiting spare capacity," *IEEE Trans. on Wireless Commun.*, vol. 8, no. 8, pp. 4264–4275, Aug. 2009.
- [248] D. M. Pozar, *Microwave Engineering*. John Wiley & Sons, 2009.
- [249] A. S. Y. Poon, R. W. Brodersen, and D. N. C. Tse, "Degrees of freedom in multiple-antenna channels: A signal space approach," *IEEE Trans. on Inf. Theory*, vol. 51, no. 2, pp. 523–536, Feb. 2005.
- [250] A. Goldsmith, S. A. Jafar, N. Jindal, and S. Vishwanath, "Capacity limits of MIMO channels," *IEEE Journal on Selected Areas in Commun.*, vol. 21, no. 5, pp. 684–702, June 2003.

- [251] S. Vishwanath, N. Jindal, and A. Goldsmith, “Duality, achievable rates, and sum-rate capacity of gaussian MIMO broadcast channels,” *IEEE Trans. on Inf. Theory*, vol. 49, no. 10, pp. 2658–2668, Oct. 2003.
- [252] T. L. Marzetta, “How much training is required for multiuser MIMO?” in *Asilomar Conference on Signals, Systems and Computers (ASILOMAR)*, Oct. 2006, pp. 359–363.
- [253] S. Nazemzadeh, “A guide to RF switching systems,” *The RF & Microwave Solutions Update*, pp. 34–44, June 2008.
- [254] Teledyne Coax Switches, “Coax switch matrix selection guide,” 2014. [Online]. Available: [http://www.teledynecoax.com/pdf/csm\\_selection\\_guide.pdf](http://www.teledynecoax.com/pdf/csm_selection_guide.pdf).
- [255] A. M. Niknejad, *Electromagnetics for high-speed analog and digital communication circuits*. Cambridge University Press, 2007.
- [256] Peregrine semiconductor, “Portfolio of RF switches.” [Online]. Available: <http://www.psemi.com/products/rf-switches>.
- [257] Skyworks Solutions, “Portfolio of RF switches.” [Online]. Available: [http://www.skyworksinc.com/products\\_switches.aspx](http://www.skyworksinc.com/products_switches.aspx).
- [258] C. H. Papadimitriou, *Computational complexity*. John Wiley and Sons Ltd., 2003.
- [259] S. S. Gupta, “Order statistics from the gamma distribution,” *Technometrics*, vol. 2, no. 2, pp. 243–262, 1960.
- [260] B. C. Arnold, N. Balakrishnan, and H. N. Nagaraja, *A first course in order statistics*. Siam, 1992, vol. 54.
- [261] E. Telatar, “Capacity of multi-antenna Gaussian channels,” *European Trans. on Telecommunications*, vol. 10, no. 6, pp. 585–595, 1999.
- [262] V. V. Veeravalli, Y. Liang, and A. M. Sayeed, “Correlated MIMO wireless channels: Capacity, optimal signaling, and asymptotics,” *IEEE Trans. on Inf. Theory*, vol. 51, no. 6, pp. 2058–2072, June 2005.
- [263] P. J. Smith, S. Roy, and M. Shafi, “Capacity of MIMO systems with semicorrelated flat fading,” *IEEE Trans. on Inf. Theory*, vol. 49, no. 10, pp. 2781–2788, Oct. 2003.
- [264] A. Alkhateeb, O. El Ayach, G. Leus, and R. Heath, “Channel estimation and hybrid precoding for millimeter wave cellular systems,” *IEEE Journal of Selected Topics in Signal Process.*, vol. 8, no. 5, pp. 831–846, Oct. 2014.
- [265] J. Hoydis, C. Hoek, T. Wild, and S. ten Brink, “Channel measurements for large antenna arrays,” in *International Symp. on Wireless Communication Systems (ISWCS)*, Aug. 2012, pp. 811–815.

- [266] C. Shepard, A. Javed, and L. Zhong, "Control channel design for many-antenna MU-MIMO," in *Proceedings of the 21st Annual International Conf. on Mobile Computing and Networking*. ACM, 2015, pp. 578–591.
- [267] S. Payami and F. Tufvesson, "Channel measurements and analysis for very large array systems at 2.6 GHz," in *6th European Conf. on Antennas and Propagation (EUCAP)*, March 2012, pp. 433–437.
- [268] P. Sudarshan, N. Mehta, A. Molisch, and J. Zhang, "Antenna selection with RF pre-processing: Robustness to RF and selection non-idealities," in *IEEE Radio and Wireless Conf.*, Sept. 2004, pp. 391–394.
- [269] S. Wu, C.-X. Wang, E.-H. Aggoune, M. Alwakeel, and Y. He, "A non-stationary 3-D wideband twin-cluster model for 5G massive MIMO channels," *IEEE Journal on Selected Areas in Commun.*, vol. 32, no. 6, pp. 1207–1218, June 2014.
- [270] I. Viering, H. Hofstetter, and W. Utschick, "Spatial long-term variations in urban, rural and indoor environments," in *COST273 5th Meeting*, 2002.
- [271] ———, "Validity of spatial covariance matrices over time and frequency," in *IEEE Global Telecommunications Conf. (GLOBECOM)*, Nov. 2002, pp. 851–855.
- [272] D. Chizhik *et al.*, "Multiple-input-multiple-output measurements and modeling in Manhattan," *IEEE Journal on Selected Areas in Commun.*, vol. 21, no. 3, pp. 321–331, April 2003.
- [273] A. Sayeed and J. Brady, "Beamspace MIMO for high-dimensional multiuser communication at millimeter-wave frequencies," in *IEEE Global Commun. Conf. (GLOBECOM)*, Dec. 2013, pp. 3679–3684.
- [274] A. Adhikary *et al.*, "Joint spatial division and multiplexing for mm-Wave channels," *IEEE Journal on Selected Areas in Commun.*, vol. 32, no. 6, pp. 1239–1255, June 2014.
- [275] J. Nam, A. Adhikary, J.-Y. Ahn, and G. Caire, "Joint spatial division and multiplexing: Opportunistic beamforming, user grouping and simplified downlink scheduling," *IEEE Journal of Selected Topics in Signal Processing*, vol. 8, no. 5, pp. 876–890, Oct. 2014.
- [276] Quinstar Technology Inc, "Power divider - QSP series." [Online]. Available: <http://quinstar.com>.
- [277] Anaren Corporation, "Power divider - PD2328J5050S2HF." [Online]. Available: <https://www.anaren.com>.

- [278] Millitech Inc, “Hybrid directional coupler - CSS-28.” [Online]. Available: <http://www.millitech.com>.
- [279] Anaren Corporation, “Hybrid coupler - X3C22E1-03S [Online].” [Online]. Available: <https://www.anaren.com>
- [280] Millitech Inc, “Phase shifter - VPS-28 [Online].” [Online]. Available: <http://www.millitech.com>.
- [281] Analog Devices, “Phase shifter - HMC928LP5E.” [Online]. Available: <http://www.analog.com/>
- [282] R. Jain and G. Mani, “Dynamic thinning of antenna array using genetic algorithm,” *Progress In Electromagnetics Research B*, vol. 32, pp. 1–20, 2011.
- [283] M. O. Binelo, A. L. De Almeida, and F. R. P. Cavalcanti, “MIMO array capacity optimization using a genetic algorithm,” *IEEE Trans. on Veh. Tech.*, vol. 60, no. 6, pp. 2471–2481, 2011.
- [284] R. L. Haupt, “Thinned arrays using genetic algorithms,” *IEEE Trans. on Antennas and Propagation*, vol. 42, no. 7, pp. 993–999, 1994.
- [285] M. Bengtsson and B. Ottersten, “Optimal and suboptimal transmit beamforming,” *Handbook of Antennas in Wireless Communications (L. C. Godara, ed.)*, 2001.